STUDY OF FLUID FLOW IN UNCONVENTIONAL RESERVOIR ROCKS: ASSESSING FLOW REGIMES, GEOMECHANICS AND CAPILLARY END EFFECTS

By

Rasoul Nazari Moghaddam

BSc., MSc.

Submitted for the degree of **Doctor of Philosophy** in

Petroleum Engineering

Heriot-Watt University

Institute of Petroleum Engineering

November 2016

ABSTRACT

Unconventional resources have received significant attentions as recent advances in technology has made it possible to economically produce from these reservoirs. While the economical production from these reservoirs have been initiated, the impact of the mentioned mechanisms on fluid flow are not well understood.

In this thesis, to study the effects of flow regimes and geomechanical stress on fluid flow in shale matrix, several experiments were performed at different pore pressure and net stress conditions. It was aimed to obtain a reliable model for prediction of matrix permeability during the production period when the pore pressure is decreasing and the net stress is increasing with time. For this purpose, the matrix permeability of several shale rock samples were measured at different conditions. In addition, the results of TOC, Helium porosimetry, XRD analysis, contact angle measurements, MICP test and SEM image analysis were used to characterize the shale sample under study.

In line with the experimental measurements, the corresponding flow equations were derived using Navier-Stokes (NS) equations with slip boundary conditions. The derived flow equations and the experimental results were used to obtain appropriate slip coefficients. Then the geo-mechanical effects on matrix permeability were considered. The experimental data were used to develop a model for permeability prediction at different pore pressure and net stress values. The proposed model was also validated using a set of experimental data in the literate.

Furthermore, the gas flow in micro and nanoscale systems was simulated using the Lattice Boltzmann method (LBM). After validation, the simulation results were compared with the scaled experimental data. From the comparison, Tangential Momentum Accommodation Coefficient (TMAC) for LBM simulation of gas flow in shale rocks was determined. Results obtained in this study are essential for using the LBM as a simulation technique for fluid flow modelling in shale rocks.

In addition to single phase flow studies, two-phase relative permeability of unconventional rocks were measured. It is shown that the Capillary End Effect (CEE) caused as result of ultra-high capillary pressure in shale formations, is the main artefacts that makes these measurements unreliable. In this thesis, a model is developed to correct the CEE during the steady-state relative permeability measurements. The proposed model was also evaluated by a set of artificially generated data and the experimental SS-kr data measured in the lab.

DEDICATION

To the memory of my father…

To my mother

&

To my wife

ACKNOWLEDGEMENT

I would like to express my deep gratitude to my supervisor Prof. Mahmoud Jamiolahmady (Jami) for his technical guidance, encouragement and support throughout my thesis work. I would also like to thank my second supervisor Prof. Mehran Sohrabi for his encouragement and technical comments.

The financial support of the Heriot-Watt University through the award of James-Watt Scholarship to conduct this work is sincerely acknowledged. This study was conducted as a part of the Unconventional Gas and Gas-condensate Recovery Project at Heriot-Watt University. This research project is sponsored by: Daikin, Dong Energy, Ecopetrol/Equion, ExxonMobil, GDF, INPEX, JX-Nippon, Petrobras, RWE, Saudi-Aramco and TOTAL, whose contribution is gratefully acknowledged.

I would like to thank Mr. Shaun Ireland, Mr. Pantelis Tsolis, Mr. Kamran Ahmed, Mr. Adam Sisson and Dr. Jim Buckman for their technical support in the laboratory.

I would also like to thank Dr. Jingsheng Ma, Mr Hamidreza Nasriani, Dr. Jalal Fahimpour, Dr. Jalal Foroozesh, Mr. Mojtaba Moradi and Mr. Payam Alikhani for their time for discussion and providing valuable comments.

I also wish to express my warmest thanks to Dr. Karl Stephen and Prof. Yu-Shu Wu for their time to review my PhD thesis and providing valuable technical comments.

Last but not least, I would like to express my sincere gratitude to my lovely wife for her unconditional support, understanding and encouragement during my PhD studies.

LIST OF PUBLICATIONS

- ✓ Nazari Moghaddam, R., Jamiolahmady, M.: Fluid Transport in Shale Gas Reservoirs: Simultaneous Effects of Stress and Slippage on Matrix Permeability, *International Journal of Coal Geology*, Volume 163, 1 June 2016, Pages 87–99.

- ✓ Nazari Moghaddam, R., Jamiolahmady, M.: Slip flow in Porous Media, *Fuel*, Volume 173, 1 June 2016, Pages 298–310.

- ✓ Nazari Moghaddam, R., Jamiolahmady, M.: Study of Slip Flow in Unconventional Shale Rocks Using Lattice Boltzmann Method: Effects of Boundary Conditions and TMAC, Under Review.

- ✓ Nazari Moghaddam, R., Jamiolahmady, M.: Steady State Relative Permeability Measurements of Tight and Shale Rocks Considering Capillary End Effect, Ready for submission.

- ✓ Nazari Moghaddam, R., Jamiolahmady, M.: Gas Flow Transport in Shale Matrix: Simultaneous Effects of Stress and Slippage on Matrix Permeability" SPE-180126-MS, *SPE EUROPEC*, 30 May-02 June 2016, Vienna, Austria.

- ✓ Nazari Moghaddam, R., Jamiolahmady, M.: Study of Slip Flow in Tight and Shale Gas Reservoirs Using Lattice Boltzmann Method, *SPE EUROPEC*, Jun 2017, Paris, France, Submitted.

TABLE OF CONTENTS

LIST OF FIGURES

LIST OF TABLES

LIST OF SYMBOLS

Nomenclature

n	coordination normal to the wall
L_s	Slip Length
k_B	Boltzmann constant (1.3805×10^{-23} J/K)
C_1	first-order slip coefficient
C_2	second-order slip coefficient
C_g	gas compressibility
u	velocity in x-direction
R	conduit radius
Q_p	flow rate of a pipe
Q_{Np}	flow rate of N pipe
L	length
P	pressure
D	Characteristic length
A	cross-sectional area
h	channel height
k	permeability
κ	Boltzmann constant
f	particle distribution function
f^{eq}	Boltzmann-Maxwell distribution function
t	time
ξ	particle velocity
m	molecular mass
c	lattice speed
c_s	speed of sound
t	time
T	temperature
K	absolute permeability
g	flow rate
S	saturation
F	liquid/gas flow rate ratio

Greek Letters

ρ	density
λ	mean free path of flowing gas
μ	viscosity
α	direction of velocity $\alpha = 1, \dots, 8, 9,$
Ω	collision term
σ_v	tangential momentum accommodation coefficient
γ	ratio of specific heats
φ	porosity
α_0	fitting parameter in B-K model equals to 1.358
α_1	fitting parameter in B-K model equals to 4.0
β	fitting parameter in B-K model equals to 0.4
ζ	second viscosity coefficient

Subscript

w	wall
app	apparent
non-slip	without slip
s	slip
D	dimensionless
p	pore
r	refers to r-direction
z	refers to z-direction
θ	refers to θ -direction
B	Boltzmann
w	wall
int	interstitial
avg	average
BK	Beskok and Karniadakis Model
o	oil
g	gas

c	capillary
out	outlet
Exp	experimental
CEE	capillary end effect

Superscript

1st	first order slip model
2nd	second order slip model
i	i-direction
j	j-direction

Abbreviations

Kn	Knudsen number
Re	Reynold number
Ma	Mach number
DSMC	direct simulation Monte Carlo
MD	molecular dynamic
LBE	Linearized Boltzmann equation
CL	Cercignani–Lampis
DGM	dusty gas model
B-K	Beskok and Karniadakis
KL	Knudsen Layer
TMAC	tangential momentum accommodation coefficient
MEMS	microelectromechanical systems
PDF	probability distribution function
UGR	unconventional gas reservoir
IP	information preservation
MFP	mean free path
N-S	Navier-Stokes
SRT	single relaxation time
TRT	two relaxation time
MRT	multi relaxation time
BB	bounce-back boundary condition
SR	specular reflection boundary condition

DR	diffusive reflection boundary condition
BSR	bounce back-specular reflection
lu	lattice unit
CEE	capillary end effect
SS	steady state
LGR	liquid gas ratio
Psi	pounds per square inch
cc	cubic centimetre
sur	surface
LMA	Levenberg–Marquardt algorithm
GNA	Gauss–Newton algorithm

Operators

div	divergence
∇	gradient vector field
∂	gradient operator

Chapter 1: Introduction

Based on the U.S. Energy Information Administration's (EIA) annual outlook for 2015, oil and natural gas will continue to be the main source of energy till 2040. It is predicted that natural gas consumption will increase to 29% by 2040. The main reason for this increase in natural gas consumption is the emergence of unconventional resources (EIA, 2015). This growing energy demand on one side and the continuance of fossil fuels as the main source of energy on the other side highlight the important role of the unconventional reservoirs in global energy markets in future. However, as unconventional reservoirs have only recently emerged, the physics of flow in these reservoirs is poorly understood. It is accepted that fluid flow in low-permeability unconventional reservoirs is a complex process and subject to more nonlinear physical processes compared to flow in conventional reservoirs.

Unconventional reservoirs are known as comprising a highly compacted sediment with low/ultralow matrix permeability and pore volumes. The average sizes of pores and throats are typically up to three orders of magnitude smaller than those in conventional rocks (Javadpour et al., 2007). Due to the presence of micro- and nanoscale flow conduits (micro and nanoscale pores and throats) the dynamics of flow is different compared to that in conventional rocks (Javadpour, 2009, Deng et al., 2014, Freeman et al., 2011). In these reservoirs, flow regimes are not the same as those in the conventional formations with micro and macro pores. Gas flow in the unconventional rocks can be at different flow regimes including "continuum", "slip", "transition" and "free-molecular flow". This means that, unlike the situation in the conventional reservoirs, a single flow equation (e.g. the Darcy Equation) is no longer valid for modelling of fluid flow in unconventional reservoir rocks. This is the first key difference for fluid flow modelling in unconventional rocks, which makes the predictions more complicated.

In addition to various flow regimes, rock mechanical properties are among the important factors that make the unconventional rocks (more specifically shale rocks) different from the conventional matrices. These rock mechanical properties are compressive strength, tensile strength, and elastic modulus. For shale formations, the values of these properties are much lower than those of the sandstones or carbonates (Yves et al., 2015). These different properties of shale rocks make the poroelasticity

effects more pronounced. As a result, shale matrices are extremely sensitive to the effective stress. The effective stress applied to the reservoir formation increases gradually due to the pore pressure decline during production. This variation of effective stress will have a great impact on matrix permeability and hence on fluid flow.

Capillary pressure is another factor that makes the fluid flow modelling difficult in unconventional rocks. Capillary pressure is significantly high in these formations compared to conventional matrices. In low-permeability unconventional rocks, the average size of pore/throat is much smaller than the average pore size in conventional rocks. Therefore, higher capillary pressure is expected to exist in the unconventional rocks. This higher capillary pressure can be several orders of magnitude greater than the capillary pressure in conventional rocks for the same fluid system. Such high capillary pressure can influence the two-phase flow in unconventional rocks. For example, during the relative permeability measurements, high capillary pressure can cause a significant liquid hold-up at the core outlet. This liquid hold-up (which is known as the capillary end effect) makes such measurements, using conventional set-up an procedures, incorrect and unreliable (Gupta and Maloney, 2015).

Another important mechanism, which affects the fluid flow is the sorption/desorption process (which includes both adsorption and absorption), which is mainly controlled by the rock composition, amount of organic materials and microstructure of the rock. This mechanism can act as a sink/source of hydrocarbon. In other words, gas adsorption on the solid surface of pores enhances the overall storage capacity of the rock compared to the same rock with only a free phase. The sorption/desorption process is pressure dependent. This means that, by decreasing pore pressure during the depletion, light hydrocarbons can be released from the organic matter. The released gas can flow towards the wellbore and provides not just additional gas for production but helps to sustain pressure (Heller and Zoback, 2014).

In addition to the mechanisms mentioned above, geometrical flow regimes around the wellbore are among the specific features of these reservoirs. In fact, commercial production from tight and shale reservoirs is not possible without special stimulation techniques, including hydraulic fracturing or horizontal well drilling. Flow around such fractures/wellbore system (e.g. fractures propagated around a horizontal well) is expected to create a complex sequence of geometrical flow regimes. These geometrical flow regimes can be linear, bi-linear, compound linear, radial or boundary dominated flow (Nobakht et al., 2013, Chen and Rajagopal, 1997). However, depending on extent of the

fractures, type of the well, geological formation and production time, some of these flow regimes may or may not be physically generated.

Finally, fluid confinement and deviation from bulk thermodynamic can be mentioned as another unconventional behaviour of these rock matrices. In conventional rocks, the pore and throat diameters are in the range of micrometres, which is several hundred times larger than the gas molecule diameter. In these systems, molecule-molecule collisions are known to be the dominant interactions governing fluid behaviour. However, in unconventional formations, the molecules are confined in the systems with average size in tens of nanometres (Curtis et al., 2011). In such systems, wall interactions with fluid cannot be negligible and even as significant as intermolecular interactions. These more frequent wall-molecule collisions can have a great impact on fluid properties and make them different from those measured on macro systems (Vishnyakov et al., 2001, Singh et al., 2009).

In this research, some of these unconventional mechanisms were investigated with an emphasis on shale rocks. Among them, flow regimes and their effect on fluid flow modelling were studied for unconventional gas reservoirs. Geomechanical effects of shale rocks were also investigated, as well as the effects of high capillary pressure in unconventional rocks. It should be noted that the sorption/desorption mechanism, geometrical flow regimes and fluid confinement effects were not studied in this research.

1.1 Problem Statement

1.1.1 Permeability Change with Reservoir Pressure

The unconventional rock matrices are usually made up of highly compacted sediment with an average grain radius in the range of nano- and micrometres. In the unconventional gas reservoirs, it has been reported that the gas flow regime may change depending on the size of flow conduit and reservoir pressure. Considering nano- and micro-pores in these rocks, the prediction of gas flow rate requires accurate determination of the flow regime in these systems. In other words, it depends on the pressure and the average size of pore/throats; thus the dominant flow regime should be determined and the corresponding appropriate flow equations should be used. In practice, it is unfeasible to incorporate all the governing equations in reservoir simulators. As an alternative, the Darcy equation is used with a variable permeability factor. This means that, to predict the

flow rate accurately, the permeability factor in the Darcy equation can be changed, depending on the existing flow regime. This permeability factor should be obtained such that the Darcy equation gives the same flow rate as calculated by the complex flow equations. Therefore, for accurate prediction of gas flow rate in tight and shale rocks, variable matrix permeability should be precisely estimated for different flow regimes. This suggests that reliable relationships for permeability prediction of shale and tight matrix are highly demanded for unconventional flow predictions by reservoir simulators.

During the reservoir depletion, the average reservoir pressure declines, which results in a change in the flow regime. Therefore, matrix permeability should be updated based on the current flow regime. As this flow regime can be predicted based on the dimensionless Knudsen number, which is the ratio of mean free path to characteristic dimension of the flow conduit, the permeability can also be correlated based on the current Knudsen number of the system.

1.1.2 Permeability Change with Net Stress

As mentioned previously, the rock mechanical properties of shale formations are significantly lower than those in the conventional rocks, which makes them very sensitive to the effective stress. The effective stress (or net stress) is a function of confining pressure, reservoir pore pressure and effective stress coefficient. Since the reservoir pore pressure can considerably change during the production period, the net stress applied to the reservoir rock can also change significantly with time. This net stress change has a great impact on matrix permeability during the production period. Since accurate estimation of permeability is required for flow rate predictions, the effects of net stress on matrix permeability should also be considered. It is noted that the permeability change as a result of net stress variation is not negligible in shale formations and can affect the predicted gas flow rate significantly.

1.1.3 Simultaneous Effects of Flow Regimes and Net Stresses on Permeability

As the pore pressure declines and the net stress increases in the shale formations, the matrix permeability reduces. Basically, this reduction in matrix permeability happens as a result of pore/throat volume shrinkage and reduction of the effective area to flow. This reduction of pore/throat size causes an overall reduction in rock permeability.

In addition to permeability reduction, this change in pore/throat size can affect the dominant flow regimes, and hence the corresponding flow rate. As mentioned above, for flow regime determination, the Knudsen number is used, which is a function of the characteristic size of the flow conduit and pore pressure. The flow regime can be changed if the flow conduit size (pore/throat average radius) is altered as a result of the net stress change.

Considering the variation of both flow regimes and net stress during the depletion period, it can be concluded that the gas flow rate can be affected significantly by these two effects. To account for these effects on gas flow rate, the permeability factor in the Darcy equation should be updated. Therefore, for accurate prediction of gas flow rate, both mechanisms should be considered simultaneously. In other words, a model is required to predict the matrix permeability at different flow regimes, while the effects of pore pressure and net stress are taken into account.

1.1.4 Slip and Tangential Momentum Accommodation Coefficients (TMAC)

Accurate flow rate predictions in tight and shale rocks requires gas flow modelling under the existing dominant flow regime. In these reservoirs, slip and transition flow regimes are usually dominant. Gas slippage on the wall surface, which happens in the non-Darcy flow regimes, makes the fluid flow modelling more complex. Among the available models, a solution of the N-S equation with slip boundary conditions is frequently used to find the gas flow rate. In this approach, slip boundary conditions are used to account for the gas slippage on the wall surfaces. However, choosing appropriate slip boundary conditions is still a big challenge. In other words, suitable slip coefficients are required before solving the N-S equation for fluid flow modelling in shale and tight rocks. The available slip coefficients in the literature have been developed for flow through the non-porous single channel at low pressures. Therefore, it is extremely important that accurate slip coefficients should be determined for porous media at high pressures, in order to use N-S equations.

In addition to the analytical solution of N-S equations (which is usually used at the larger scales) numerical simulation (at the smaller scales) can also be performed to study the flow behaviour in shale and tight gas reservoirs. Lattice Boltzmann method (LBM) is among the available techniques for simulation of fluid flow at the mesoscopic level. Lattice Boltzmann simulations are currently being used by many researchers to study the

fluid flow in shale and tight rocks. In this technique, gas slippage on the wall surface is usually taken into account by Tangential Momentum Accommodation Coefficients (TMAC). This factor is required to be determined before using the LBM technique for fluid flow modelling in shale and tight systems. It is noted that the reported TMACs in the literature have been measured for gas flow through non-porous channels at low pressures. Thus, measuring such coefficients in porous media is of great interest for simulation of fluid flow in unconventional shale and tight rocks.

1.1.5 Gas Flow Regimes in the Presence of Liquid Saturation

The liquid phase in unconventional rocks can be presented inside the pores/throats (as residual or flowing). Depending on several parameters, including rock surface wettability and heterogeneity, the liquid phase can occupy smaller pores/throats or co-exist in the larger pores/throats filled with gas. The presence of a liquid phase can reduce the effective available area for the gas to flow. Hence, it not only reduces the overall permeability of the gas but can also change the gas flow regime.

Despite some research studying the single phase gas flow regimes, the effect of presence of a liquid phase on gas flow regimes have rarely been investigated. Therefore, it is necessary to determine how the permeability factor should be changed to account for the effects of liquid phase on gas flow rate.

1.1.6 Relative Permeability Measurements of Shale and Tight Rocks

Relative permeability functions are among the main necessary input data for reservoir simulations. For almost all two-phase flow studies, relative permeability data need to be measured. Two-phase relative permeability measurements of conventional rocks have been extensively studied and several methods and procedures (including steady-state and unsteady-state methods) have been proposed. However, due to the various complex mechanisms, two-phase relative permeability measurements of unconventional rocks are extremely difficult and challenging. Ultra-low matrix permeability and porosity, non-Darcian flow regimes, stress-dependent permeability and experimental artefacts are among the main important factors, which make these measurements complicated and difficult to perform.

Tight and shale rocks are known as ultra-low permeability porous media. Simultaneous injection of liquid and gas (for SS-kr measurements) with high flow rates can generate a significant pressure drop across the core. This high-pressure drop can have several adverse effects on SS-Kr measurements. A large net stress gradient, experience of various flow regimes and variation of fluid properties along the core can occur if a high-pressure drop is applied to the core. On the other hand, injection at low flow rates can also make the experiment time-consuming, such that each single test can take several weeks to be completed. Therefore, an optimum injection rate should be used during the SS-kr measurements. In addition, the low pore volume of these rock samples makes all measurements subject to error. As the sample pore volume decreases, the measurement error increases. Thus, highly accurate facilities are also required for these measurements.

In addition to the mentioned difficulties, the capillary end effect (CEE) is the main challenge that makes the steady-state relative permeability measurements (SS-kr) problematic. The liquid can hold-up at the outlet of the core sample due to high capillary pressure in tight and shale rocks. This liquid hold-up can even be extended along the core and cover all parts of it. In this case, the measured data are unreliable, due to this experimental artefact. Hence, it is required to correct the experimental data for capillary end effects (CEE) during the SS-kr measurements in such tight matrices.

1.2 Objectives and Thesis Structure

Based on the available issues for fluid-flow modelling in unconventional rocks with an emphasis on shale rocks described in the previous section, the study objectives in this thesis can be summarised as follows:

- To develop a model for accurate matrix permeability prediction which considers the effects of pore pressure reduction and the effective stress increase during the production life.
- To measure slip coefficients in porous media at high pressure applicable for fluid flow in shale rocks
- To determine the appropriate TMAC value for Lattice Boltzmann simulation of gas flow in shale rocks.
- To develop a technique for capillary end-effect correction during the steady-state relative permeability measurements of shale rocks.

This thesis includes seven chapters started by the introduction as Chapter 1. In this chapter, a short introduction to fluid flow in the unconventional reservoirs has been presented. In the problem statement section, the challenging behaviours of the unconventional rocks have been briefly explained before presenting the study objectives and the thesis structure. In Chapter 2, an introduction concerning future energy demand and the use of unconventional resources is presented. Then unconventional mechanisms are briefly introduced and linked to the current study. Then, as the literature review, main findings of the previous studies are discussed and the contributions of this study are highlighted.

Chapter 3 presents the results of permeability measurements performed on different shale rocks (with permeability range of 600 nD to 0.5 mD) at different pore pressures and net stresses. In the first part of this chapter, the materials and methods are described and the results of characterisation tests including MICP, XRD, ESEM analyses and contact angle measurements are presented. In the second part, the results of apparent permeability measurements and Klinkenberg corrections are presented and the effects of pore pressure and net stress on matrix permeability are discussed.

Chapter 4 describes how the model was developed for matrix permeability prediction, based on the experimental data. First, the derivation of the NS equation with slip boundary conditions are described. It is then shown how the developed equations were used to determine the slip coefficients in porous media. In addition, the effects of net stress on matrix permeability are discussed and the final form of the model is presented. Finally, the results of the model verification are presented.

Chapter 5 presents the numerical simulation of gas flow in a pore/throat system using the Lattice Boltzmann method. In the first part of this chapter, the Lattice Boltzmann technique is briefly described and the slip boundary conditions considered in this part of the study are explained. These boundary conditions include Bounce-back (BB), Specular reflection (SR), Diffusive reflection (DR) and Bounce-back Specular reflection (BSR) boundary conditions. The validation of the LBM simulation results is then presented. For validation, the LBM results of gas flow with slippage in a single pipe were compared with the results obtained from other methods, including Information Preservation (IP) and Direct Simulation Monte Carlo (DSMC). In the second part, comparisons of the scaled experimental data with the LBM simulation results are presented and the TMAC values are discussed. Then, the results of gas flow modelling in a pore body/throat system are presented and compared with the experimental data.

Chapter 6 presents the results of the two-phase flow study conducted as part of this research. In the first part, experimental facilities and methods are described. Then the experimental results of two-phase relative permeability measurements for a tight sandstone and three shale samples are reported. In the second part, the capillary end effect (CEE) is explained as the main artefact during the steady state relative permeability measurements of shale and tight rock samples. Then a new technique is proposed for the correction of CEE. The reliability of the proposed method is first evaluated by a set of artificially generated experimental data. It is then shown that the proposed method can be used to correct the SS-kr data obtained during the conducted measurements.

Finally, a summary of the results and the main conclusions are presented in Chapter 7. This chapter also includes some recommendations for further investigations on the research areas discussed in this work.

It is noted that several experiments were performed during this research. However some of them were carried out by the external companies. In the following, the experiments were performed by the author and the external companies are listed.

The experiments performed by the author:

- Helium porosimetry
- Wettability measurements by contact angle
- Single phase absolute permeability measurements (steady state method)
- Single phase absolute permeability measurements (unsteady state method)
- Effective permeability measurements (two-phase)
- Experiments for stress-induced permeability hysteresis measurements
- Two-phase steady state relative permeability measurements
- Experiments for the effects of net stress on SS kr measurements

The following experiments were performed by the external companies:

- TOC and X-ray diffraction analysis (XRD) measurements by ALcontrol Laboratories and British Geological Survey.
- MICP and pore size distribution measurements by Core Laboratories.

Chapter 2: Unconventional Reservoirs

2.1 Future Energy Demand and Unconventional Resources

According to current projections of population growth, the world population will continue to grow until at least 2050. The estimated population, based on current growth trends, will be 9 billion in 2040 (UN, 2015). At the same time, as the population increases, incomes will rise, and with them the demand for energy. The EIA estimates that, in 2013, total world energy consumption was 5.67×10^{20} joules, equal to an average power consumption of 18.0 terawatts. It is projected that the global energy demand will grow by 37% by 2040. Currently, hydrocarbon liquids and gases are the primary sources of energy. However, the decline in oil and gas production from conventional resources increases the important role of the unconventional resources to meet the growing rate of energy demands in future.

Based on the U.S. Energy Information Administration's (EIA) annual energy outlook for 2015, oil and natural gas will continue to be the main source of energy until 2040.

Figure 2.1 shows the U.S total primary energy consumption. As shown in this figure, oil and natural gas supply 63% of America's energy and the EIA projects that they will provide 62% in 2040 (33% for oil and 29% for natural gas).

It is predicted that the natural gas consumption will increases by 2 %, from 27 % in 2013 to 29% in 2040. It is forecasted that the main reason for this increase in the natural gas consumption will be the emerging shale and tight gas reservoirs. Figure 2.2 shows the prediction of U.S dry natural gas production. As shown, shale gas and tight oil plays will be the largest source of dry gas production, at around 50% of the total production from 2013 till 2040 (EIA, 2015).

This growing energy demand and the need for fossil fuels as the main source of energy highlight the essential role of unconventional reservoirs in the global energy markets in future. Although the unconventional reservoirs have recently received attention as economical sources of hydrocarbon, our understandings of flow mechanisms are still poor and need to be developed. In fact, the physics of flow are different from those in the conventional reservoirs, due to the different nature of the media. Therefore, long-term production from these new emerging energy sources requires more fundamental scientific

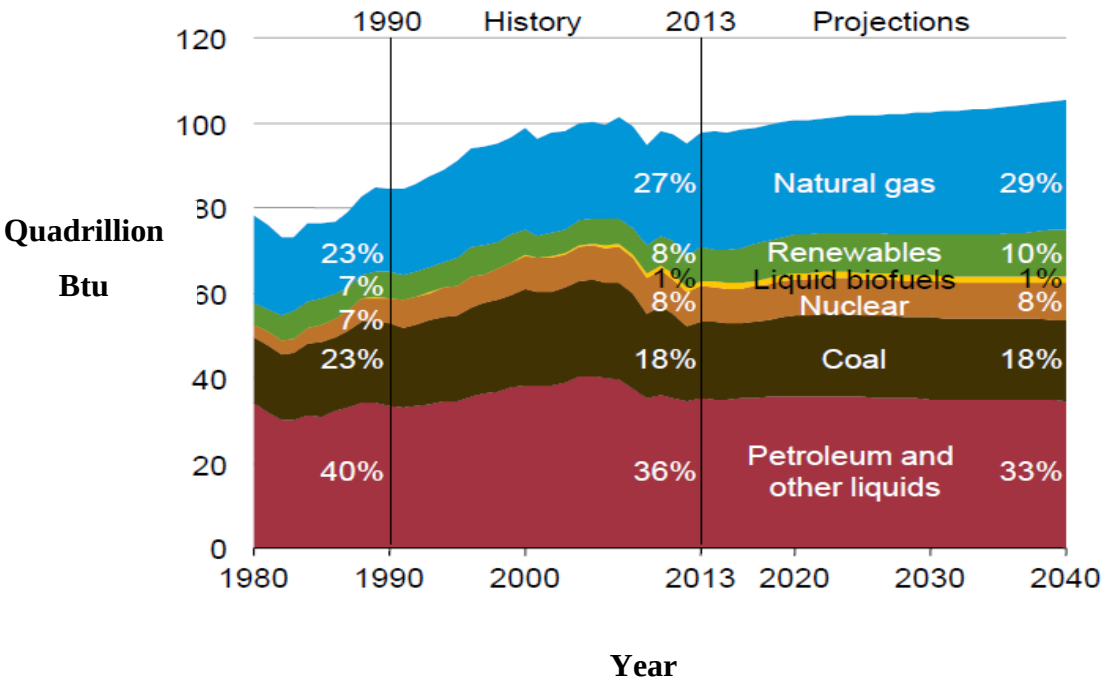

Figure 2.1: U.S primary energy consumption (Source: EIA, Annual Energy Outlook, 2015: Reference Case)

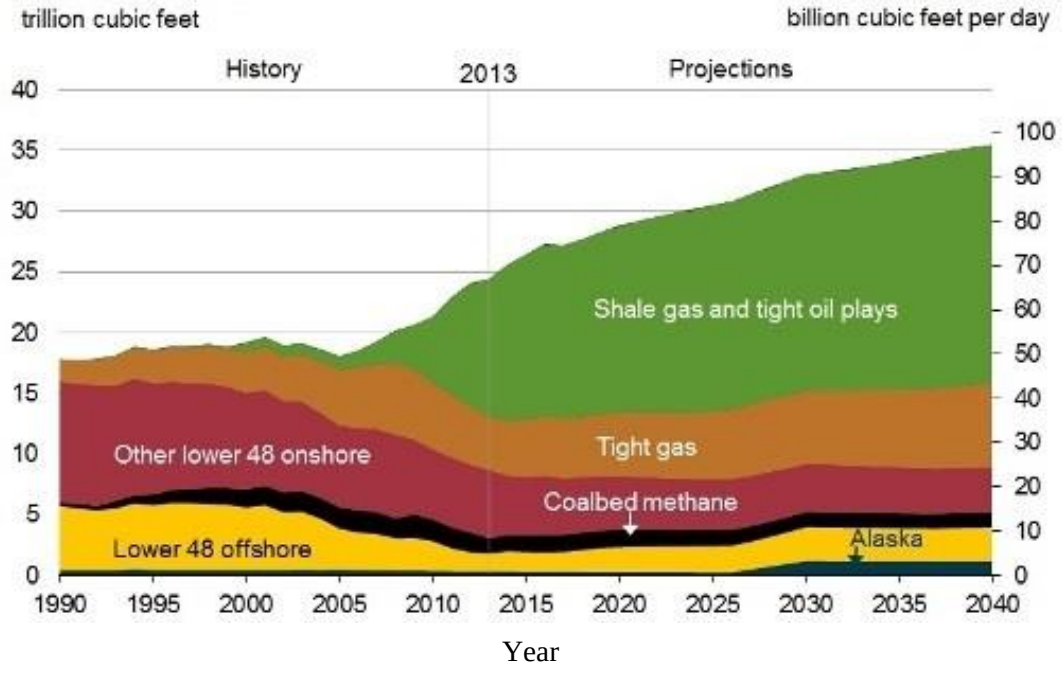

Figure 2.2: U.S dry natural gas production (EIA, Annual Energy Outlook, 2015: Reference Case.

research to increase the current understanding of flow behaviour and well performance in unconventional reservoirs.

2.2 Unconventional Reservoirs: Shale Gas, Tight Gas and Tight Oil

Conventional reservoirs contain hydrocarbon, which can be produced without any particular process such as hydraulic fracturing or horizontal well drilling. A conventional reservoir usually has high to medium matrix permeability and favourable storage porosity, in which one can conventionally drill a vertical well and produce at commercial flow rates. In these reservoirs, oil and gas flow naturally and there is no need for the reservoir stimulation. In addition, fewer wells are needed to drain the reservoir, since fluids can flow with relative ease.

Unconventional Reservoirs are those that cannot be produced at economic flow rates without special recovery processes. From the unconventional reservoirs, some forms of stimulation are required to obtain commercial production. The required stimulation includes hydraulic fracture treatment, horizontal and multilateral wellbores, and some other techniques to increase the effective contact areas between wellbore-formation or reduce flow resistance from reservoir to well (Wu, 2015).

Typical unconventional reservoirs are shale gas, tight gas, tight oil, coalbed methane and heavy oil. However, in this thesis, the term unconventional reservoirs refers to shale gas, tight gas and tight oil. To produce from these reservoirs, massive hydraulic fracturing is required. The fluids typically flow through matrix and fracture and are produced from the wellbore. Other unconventional resources such as heavy oil and tar sand, with different geological formations and extractive techniques are not the subject of this study.

2.2.1 Shale Gas Reservoirs

The term “Shale Gas” refers to natural gas that is trapped within shale formations. Shales are fine-grained sedimentary rocks that can be rich sources of petroleum and natural gas. Shales usually have low matrix permeability, so gas production in commercial quantities requires additional stimulation processes. Based on data collected by the Energy Information Administration Agency (EIA, 2013), China, Argentina, Algeria, the United States and Canada are the countries with highest shale gas resources with estimated "technically recoverable" gas reserves of 1115, 802, 707, 665 and 573 trillion cubic feet, respectively.

Commercial production from "Shale Gas" began from the Barnett Shale located in north-central Texas. The first commercial shale natural gas production was initiated by the Mitchell Energy and Development Corporation. In 2000, Mitchell Energy achieved a hydraulic fracturing technique that produced commercial volumes of shale gas (EIA, 2016). After this success, other companies started drilling wells in this formation so that by 2005, the Barnett Shale was producing 0.5 Tcf of natural gas per year. Later on, with additional confirmation provided by good results in the Fayetteville Shale in northern Arkansas, oil and gas companies started developing other shale formations, including Haynesville, Woodford, Eagle Ford, Marcellus and Utica shales (EIA, 2016).

Figure 2.3 presents the daily gas production from different U.S. shale reservoirs, indicating the growth of gas production from 2002 to 2016.

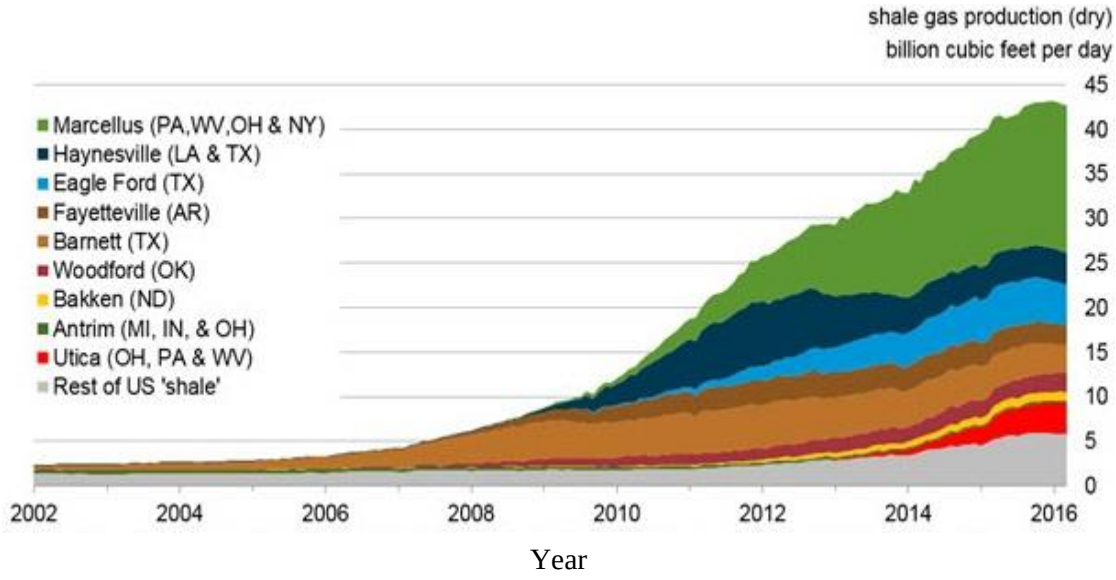

Figure 2.3: The growth of daily dry gas production from shale formations in the U.S (EIA, 2016).

2.2.2 Tight Gas Reservoirs

The term "Tight Gas" refers to natural gas reservoirs with low and ultra-low permeability matrices. Tight gas is typically trapped in sandstone or limestone formations that have abnormally low permeability or porosity. Similarly to the other unconventional reservoirs, tight gas requires additional effort to be extracted, because of the extremely tight formation in which it is located. Without stimulation techniques, gas from a tight formation would flow at very slow rates, making production uneconomical.

In these reservoirs, the size of the flow channels are in the range of micro and nano-scale. Although for the tight gas reservoirs, the range of pore/throat size is not the same as those for shale formations, similar processes (e.g. various flow regimes) have been observed in these formations because of the low matrix permeability and porosity. The Clinton, Medina, and Tuscarora formations in Appalachia (USA), Rotliegend in Germany and Netherlands and Berea sandstone in Michigan are examples of tight gas reservoirs around the world.

2.2.3 Tight Oil Reservoirs

The term "Tight Oil" reservoirs refer to all resources with low-permeability formations that produce oil. Tight oil is produced from low-permeability sandstones, carbonates (e.g., limestone), and shale formations. The industry uses the term tight oil production as it is a more encompassing term with respect to the different geological formations producing oil (EIA, 2016). Economical production from tight oil formations requires the same hydraulic fracturing or horizontal well technology used in the production of shale gas reservoirs.

Figure 2.4 shows the daily tight oil production rate reported by EIA in April 2016. As shown, daily production from tight oil reservoirs has increased for almost all formations from 2002. However, no increase in oil rate was recorded from 2015, which is mainly because of the global oil price reduction affecting the development of tight oil projects.

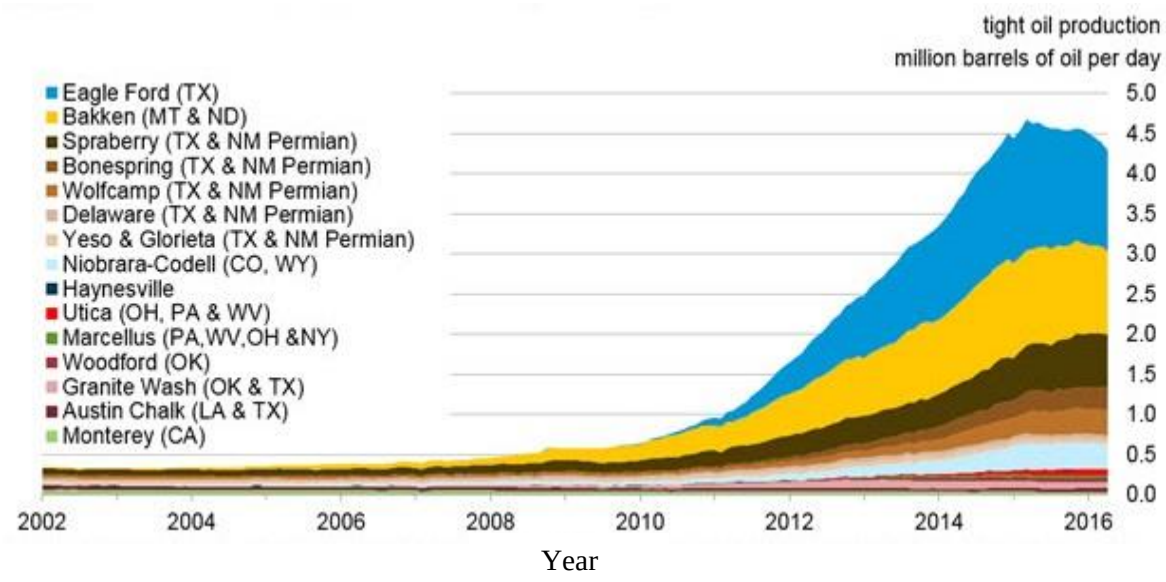

Figure 2.4: U.S tight oil production rate from 2002 to 2016.

In this thesis, the fluid flow in matrices of shale formations were studied, to gain a better understanding of flow mechanisms in "shale gas" and "shale oil" reservoirs. However, flow mechanisms in "tight gas" reservoirs (with carbonate or sandstone formations) can be similar to those for shale gas, due to the presence of micro- and nanopores involved in the production.

2.3 Unconventional Mechanisms in Shale and Tight Rocks

Fluid flow in low-permeability unconventional reservoirs is a more complex process and subject to more nonlinear physical processes compared to flow in conventional reservoirs. During the past decades, many researchers have studied fluid flow in conventional reservoirs, including sandstone and carbonate rocks. As a result, almost all the transport concepts and mechanisms involved have been extensively investigated for conventional sandstone and carbonate rocks. In the past, shale and other low-permeability formations were considered as non-reservoir layers. However, these days, unconventional reservoirs, made of these tight formations, can produce oil and gas at an economical level. In these formations, the physics of flow and transport concepts are significantly different compared to those in the conventional systems. The dominant effects of the co-existing unconventional mechanisms impose the need to develop the transport concepts in these formations and improve the flow characterisation techniques.

The main important unconventional mechanisms are 1) micro- and nanoscale flow regimes; 2) Geomechanical and poroelasticity effects; 3) High capillary pressure; 4) Sorption and desorption processes; 5) complex geometrical flow regimes and 6) Fluid confinement or deviations from bulk thermodynamic. In the following sub-sections these mechanisms are briefly described. However, only the first three mechanisms are investigated in this thesis.

2.3.1 Micro- and Nanoscale Flow Regimes

The shale/tight rock matrix is considered as a highly compacted sediment with an average grain radius in the range of nano- and micrometres. In these systems, the pore sizes are small enough to be comparable to the mean free path of the producing gas. Under these conditions, the behaviour of flow in nano- and microscale systems cannot be modelled based on the Navier-Stokes (N-S) equations, as their assumptions are not valid.

According to Gad-el-Hak (1999), the assumptions of N-S equations can only be valid when the three fundamental assumptions of the Newtonian framework (fluid with Newtonian viscosity), continuum approximation (mean free path much less than flow conduit dimensions), and thermodynamic equilibrium are satisfied (Gad-el-Hak, 1999). When the gas mean free path is comparable to the flow conduit dimensions, these are not satisfied and molecules' collisions with the wall surface should be taken into account, in addition to intermolecular collisions.

Considering nano- and micro-pores in unconventional rocks that are comparable to the mean free path of the producing gas, the Darcy equation (which can be derived from the N-S equation) with a constant permeability factor cannot be used for prediction of the flow rate. Therefore, other flow models, which may be much more complicated, are required for the flow behaviour predictions.

Gas flow in nano- and microscale conduits has been widely modelled based on rarefied gas dynamics. Rarefied gas dynamics is based on the kinetic approach to gas flows. The term rarefaction refers to the gas phase, when it is becoming less dense and the intermolecular collisions become less important. A key dimensionless parameter for considering the rarefaction effect is the Knudsen number, which is defined as the ratio of the mean free path (λ) to the flow conduit characteristic length (D), as expressed by:

$$Kn = \frac{\lambda}{D} \tag{2.1}$$

The rarefaction effect becomes more important as the Knudsen number increases. This increase in the Knudsen number could be as a result of increasing mean free path (i.e. under low-pressure conditions) or decreasing the characteristic length (similar to gas flow in nano- and micro-scale systems) or both.

Gas flow in unconventional rocks may experience other flow regimes than the continuum flow. Flow regimes are classified based on the Knudsen number of the system, as described below (Zhang et al., 2012c).

I. For $Kn < 10^{-2}$, flow is in the full continuum regime. The continuum and thermodynamic equilibrium assumptions are valid, and the flow can be described by N–S equations with conventional no-slip boundary conditions, as shown in Figure 2.5(a).

II. For $10^{-2} < Kn < 10^{-1}$, flow can be considered as the slip flow regime. The non-equilibrium effects (slip velocity and temperature jump) dominate near the walls but the continuum assumption within the fluid bulk is valid. This means that

the conventional boundary condition, i.e. no slip boundary condition, fails at the walls' flow path, as shown in Figure 2.5(b). Usually, the slip boundary models are applied to N–S equations to consider the gas slippage in this flow regime.

III. For $10^{-1} < Kn < 10$, flow is in the transition region between slip and free molecule flow, as shown in Figure 2.5(c).

IV. For $Kn > 10$, the free-molecular regime should be considered. In this regime, non-equilibrium effects dominate almost all the gas bulk flow. The collisions between the gas molecules and wall surfaces are dominant and the intermolecular collisions can be ignored, as shown in Figure 2.5(d).

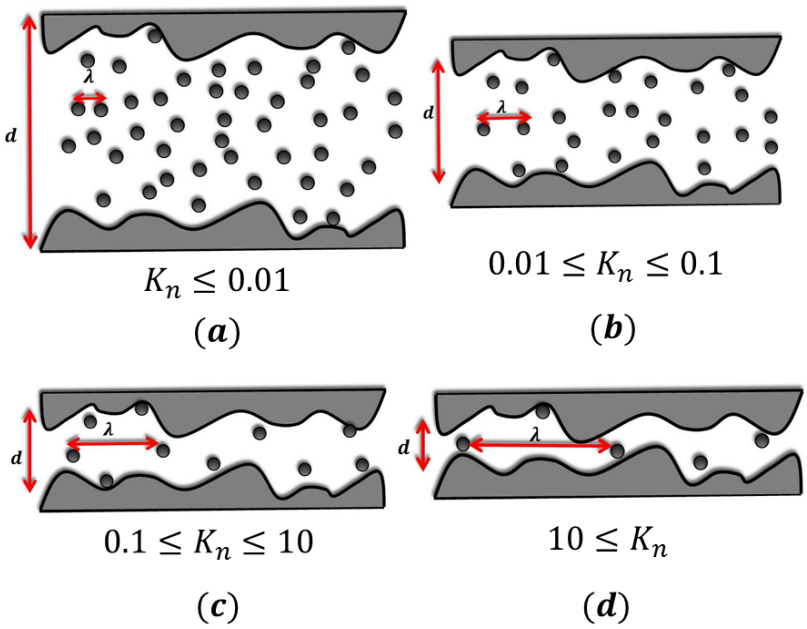

Figure 2.5: Schematic diagram of different flow regimes, showing mean free path (λ) and conduit length (d) and the corresponding Knudsen number range: (a) continuum flow, (b) slip flow, (c) transition flow and (d) free molecular flow.

As mentioned above, in the unconventional rocks the average size of pores/throats are typically up to three order of magnitude smaller than those in the conventional rocks (Javadpour et al., 2007). Due to the presence of micro- and nanoscale flow conduits, the calculated Knudsen numbers are high in these reservoir rocks. This means that the gas flow can be in a different flow regime, such as slip, transition or even free molecule flow (Javadpour, 2009, Deng et al., 2014, Freeman et al., 2011). In this condition, the Darcy equation, which is derived from Navier-Stokes equations (N-S equations), is not valid. In

addition, depending on the Knudsen number, the flow regime can change during the production period if the reservoir pressure declines. Therefore, unlike the case of conventional reservoirs, a single flow equation (e.g. the Darcy Equation) is no longer valid for modelling fluid flow during the production life. In unconventional reservoirs, the flow regime should be determined and appropriate equations should be used. This is the first key concept of fluid flow in unconventional rocks, which makes the flow rate predictions more complicated. In this study, flow regimes in unconventional rocks were investigated. Several experiments were performed for this purpose and the experimental results were used for modelling of the flow regimes.

2.3.2 Geomechanical and Poroelasticity Effects

In addition to the rarefied flow in the matrix, the presence of geomechanical effects or stress-dependent permeability is another active phenomenon which should be considered (Wu, 2015, Wang and Reed, 2009, Lei et al., 2007). In general, rock mechanical properties (such as compressive strength, tensile strength, and elastic modulus) in unconventional rocks are different from those of the conventional matrices. For shale formations, these properties are much lower in value than for the sandstones or carbonates (Yves et al., 2015). These different properties of shale rocks make the poroelasticity effects more pronounced, which needs to be considered during the fluid flow studies. For example, the shale matrices are extremely sensitive to the effective stress (Gutierrez et al., 2000, Jones and Owens, 1980, Gutierrez et al., 2014). It means that the absolute permeability of shale rocks can dramatically change by increasing the effective or net stress. In other words, during the production period, the net stress applied to the reservoir formation gradually increases due to the reduction of pore pressure with time. This variation of net stress will have great impacts on fluid flow and absolute permeability. These effects are significant and non-negligible on shale formations. In the conventional oil and gas reservoirs, the geomechanical effects on the rock permeability are generally small and have been mostly ignored in practice.

According to effective pressure law, most physical properties of porous media (e.g. porosity and permeability) are a function of effective or net stress. The net stress is related to the confining and pore pressures as follows:

$$\sigma_{net} = P_{conf} - \alpha P_{pore} \quad (2.2)$$

where σ_{net} is net stress, P_{conf} is confining stress, P_{pore} is pore pressure and α is effective pressure coefficient (Biot and Willis, 1957, Biot, 1956). In weak rocks such as shales, α is generally close to unity (Dewhurst and Siggins, 2006, Kwon et al., 2001), hence the net stress is the difference between the overburden pressure and the pore pressure.

In a shale matrix, the clay minerals are densely packed and nano-scale pore throats exist between the clay minerals. It is believed that the opening and closure of finely-distributed pore throats between the clay minerals are responsible for the strong stress dependency of shale permeability. In addition, the presence of micro-fractures is an additional factor accounting for the stress sensitivity (Dewhurst and Siggins, 2006, Gutierrez et al., 2014). In the past, it has been reported that the stress dependent permeability of non-shale rocks can be described by exponential relationships (Brace et al., 1968, Evans et al., 1997, Schmoker and Halley, 1982). In addition, it is reported in the literature that the permeability and porosity are not only dependent upon the stress, but also on the history of loading and unloading of the stresses. In other words, a hysteresis is observed when measuring stress-dependent permeability (Kwon et al., 2004, Lei et al., 2007).

To achieve an accurate modelling of flow, matrix permeability should be predicted taking into consideration its stress dependency. However, there are few published studies on the stress sensitivity of shale formations, since this requires repeated experiments at different stress levels, which are extremely time-consuming. In this study, several shale formations were used to examine the effects of the poroelastic properties of shale formations on fluid flow. In addition to the geomechanical effects on shale absolute permeability, the flow regimes can also be influenced by stress. This means that the flow regimes can change because of the change in conduit length scale due to the the net stress alteration. In this study, the poroelastic effects of shale rocks on both matrix permeability and gas flow regime were taken into account.

2.3.3 High Capillary Pressure

In unconventional rocks, the capillary pressure is significantly high compared to conventional matrix. In fact, the capillary pressure increases as the average size of the

system decreases. In low-permeability unconventional rocks, the average size of pores/throats is much smaller than the average pore size in conventional rocks. Thus, higher capillary pressure is expected in the unconventional rocks. In these formations, the capillary pressure should be taken into account, as it can be several orders of magnitude higher than the capillary pressure in conventional rocks for the same fluid system. Results of MICP measurements (mercury intrusion capillary pressure) performed on shale samples showed great capillary pressure, up to 70,000 psi (Al Hinai et al., 2014, Chalmers et al., 2012b). Such high capillary pressure can influence the two-phase flow in unconventional rocks. For example, during the relative permeability measurements, high capillary pressure can cause a significant liquid hold-up at the core outlet. This liquid hold-up, which is known as Capillary End Effect (CEE) is the main difficulty for laboratory measurements of relative permeability (kr) for tight and shale rocks. In other words, as the capillary pressure is significantly high in the unconventional porous media, the CEE is dominant that makes all kr measurements, incorrect and unreliable (Gupta and Maloney, 2015).

Liquid hold-up (or CEE) is generally created due to a discontinuity in capillary pressure at the core outlet. This discontinuity causes an accumulation of wetting phase at the end part of the core. As a result, the saturation distribution of the wetting phase along the core is not uniform, which influences the pressure drop and the calculated kr. Figure 2.6 shows a schematic of the saturation profile inside a core sample with a CEE region at the outlet. It should be noted that the main problem for the study of end effect is determination of the liquid saturation profile along the core. It has to be added that CEE is probably not important in large-scale reservoirs, i.e. it is important mainly for small-scale laboratory studies.

It should also be added that CEEs are more significant in tight/shale rock samples compared to the conventional rocks, because the capillary pressure is higher in the unconventional tight formations. One of the practical solutions to overcome the CEE during the kr measurements is to increase the injection rate, although this may not be always possible for unconventional rocks, because of their low/ultra low matrix permeability. Therefore, the capillary end effect may cover most of the core length during the steady state displacements. It happens because the length of the CEE region depends on the competition of the capillary and viscous forces. In other words, a lower rate (i.e.

low viscous force) in a porous medium with high capillary pressure results in a longer CEE length.

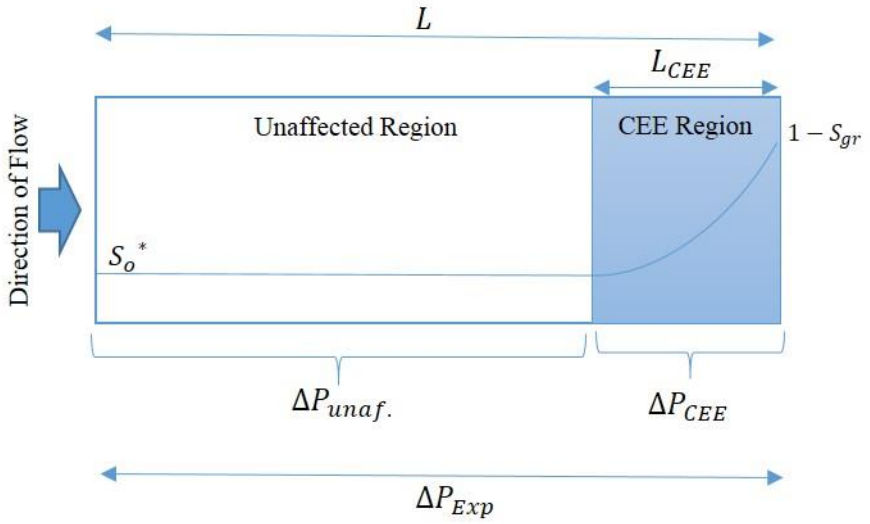

Figure 2.6: A schematic of saturation profile of the wetting phase inside the core during the steady state relative permeability measurement when the capillary end effect (CEE) is dominant.

In this study, capillary end effects were considered during the relative permeability measurements of unconventional rocks. Relative permeability measurements of unconventional rocks are extremely difficult, mainly due to the dominant CEE in such low-permeability matrices. It is therefore necessary to correct these measured kr data. In Chapter 6, these difficulties are discussed in more detail and the relative permeability data of three shale samples measured by the steady state method are presented. A new technique for correction of CEE is also presented and validated.

2.3.4 Sorption and Desorption

Another important mechanism which affects the flow in unconventional rocks is the sorption/desorption process (including both adsorption and absorption). This mechanism is mainly controlled by the rock composition, the amount of organic materials and the microstructure of the rock. The sorption/desorption process can act as a sink/source of hydrocarbon. In other words, gas adsorption on the solid surface of pores enhances the overall storage capacity of the rock relative to that if there were a free phase alone. The

sorption/desorption mechanism is a pressure dependent process. It means that, by decreasing pore pressure during the depletion, light hydrocarbons can be released and flow towards the wellbore, providing not just additional gas for production but helping to sustain pressure (Heller and Zoback, 2014).

The adsorption mechanism in shale formation is usually described through adsorption isotherms. The Langmuir isotherm is widely used to fit the experimental data of adsorption in shale samples. Several studies have reported that the Langmuir isotherm can describe gas adsorption in shale samples (Zhang et al., 2012a, Heller and Zoback, 2014). This mechanism can also have a great impact on gas production from unconventional shale reservoirs. As mentioned, the sorption/desorption mechanism is pressure dependent, hence the gas desorption rate can change during the production life, when the pore pressure changes. It is noted that the sorption/desorption mechanism is not reported for conventional reservoirs, mainly due to the lack of organic matter (adsorbent layer).

In this thesis, this mechanism is not investigated and the researcher tried to minimise its effect on the measurements by using nitrogen gas in the experiments. It is shown that for hydrocarbon-bearing rocks such as coal and shale, using nitrogen and helium has minimal effects on permeability measurements, due to their adsorption (Cui et al., 2009).

2.3.5 Geometrical Flow Regimes around Wellbore

As mentioned earlier, commercial production from tight and shale reservoirs is not possible without special stimulation techniques, including hydraulic fracturing or horizontal well drilling. As shown by Nobakht et al. (2013) the sequence of flow regimes is complex around multi-fractured horizontal wells and the proper interpretation of these geometrical flow regimes is highly demanded. Previous studies have shown that these geometrical flow regimes can be linear, bi-linear, early radial, compound linear, late radial and boundary dominated flow (Nobakht et al., 2013, Xie et al., 2014, Chen and Rajagopal, 1997). For example, Nobakht et al. highlighted the following flow regimes (from the signatures observed on the log-log derivative plot) for the case that the hydraulic fractures are equally-spaced along the horizontal well. In this case, after initial linear flow within the fractures, the flow regime may be replaced by a bilinear flow. The early bilinear flow may be observed as a result of linear flow within the fractures and linear flow in the formation perpendicular to the fractures. Then the bilinear flow period is followed by

early radial flow around the fractures. In the radial flow, the fractures behave independently, i.e. the production from each fracture is independent of the other fractures. The compound linear flow period occurs after the early radial flow. This is the period during which the fractures start to interact and interfere. This flow regime is then followed by pseudo-radial flow. Finally, just as for any closed reservoir, boundary-dominated flow is the last flow regime. It is noted that, the generated fractures may not be distributed uniformly alyaws and as a result, one or some of these flow regimes may not be physically generated.

This flow behaviour around the wellbore in the unconventional reservoirs makes the flow modelling more complicated compared to those in conventional reservoirs. These unconventional geometrical flow regimes are not considered in this thesis. In fact, geometrical flow regimes should be considered when modelling fluid flow (matrix to fracture) around the wellbore in the large reservoir scale, which is out of the scope of this study.

2.3.6 Fluid Confinement and Deviation from Bulk Thermodynamic

In conventional rocks, the pore and throat diameters are in the range of micrometres, which is several hundred times larger than gas molecule diameter. In these systems, molecule-molecule collisions are known to be the dominant interactions governing fluid behaviour. However, in unconventional formations, the molecules are confined in systems with an average size of tens of nanometres (Curtis et al., 2011). In such systems, wall interactions with fluid can be non-negligible, and even as significant as intermolecular interactions. These more frequent wall-molecule collisions can have a great impact on fluid properties and cause them to be different from those measured on macro systems (Vishnyakov et al., 2001, Singh et al., 2009). This shift in fluid properties can only be important in the pores with an average size of <10 nm (Sanaei et al., 2014). However, the level of this deviation and its overall effect on fluid flow is not well understood. The fluid confinement is also out of the scope of this work and it is not investigated in this thesis.

2.4 Literature Review

2.4.1 Analytical Models for Gas Flow in Unconventional Rocks

As mentioned before, when $Kn > 10^{-2}$, the prediction of N-S equations with no-slip boundary conditions fails. Under such conditions, other methods such as molecular dynamic (MD), direct simulation Monte Carlo (DSMC) or solution of linearized Boltzmann equation (LBE) are used to describe the flow at the molecular level. There are various published studies of the gas flow in nano- and micro-channels using LBE (Zhang et al., 2014, Fathi and Akkutlu, 2013, Niu et al., 2014), MD (Niu et al., 2014, Bird, 1994, Bhattacharya and Lie, 1991, Arya et al., 2003, Cao et al., 2006, Barisik and Beskok, 2014) and DSMC (Karniadakis et al., 2005, Tokumasu and Matsumoto, 1999). However, it has been shown in practice that the description of gas flow in micro- and nano-channels is also possible by solving N-S equations with modified boundary conditions for slip and transition flow regimes. Some researchers used the first order (Maxwell, 1879), 1.5-order (Mitsuya, 1993), and second-order slip boundary conditions (Burgdorfer, 1958, Hsia and Domoto, 1983). These studies show the application of N-S equations with the velocity-slip boundary conditions.

With regard to slip flow in shale gas reservoirs, almost all researchers have used the models that were originally developed for micro-electromechanical systems (MEMS). These models can be divided into two separate approaches. In the first approach, researchers have considered the Dusty Gas Model (DGM), which assumes a linear combination of the "viscous flow" and the "gas diffusion" to predict the overall flow rate in nanopores (Javadpour, 2009, Darabi et al., 2012, Deng et al., 2014, Guo et al., 2015, Javadpour et al., 2007). In the following paragraphs these works are briefly reviewed.

Javadpour et al. (2007) reported that the mathematical modelling of gas flow in nanopores is difficult, since the standard assumption of no-slip boundary conditions in the N-S equation breaks down at the nanometre scale. They showed theoretically that gas flow in nanopores deviates from the traditional flow models, i.e., Fick's law or Darcy's equation. They proposed to model the gas flow in nanopores assuming a diffusive transport regime with a constant diffusion coefficient and negligible viscous effects. They concluded that the diffusion coefficient obtained in their model is consistent with the Knudsen diffusivity and supports the slip boundary condition at the nanopore surfaces.

Subsequently, Javadpour (2009) proposed a model for gas flow in the nanopores of mud-rocks, based on Knudsen diffusion and slip flow. Using the proposed model, he

introduced a formulation for apparent permeability term that includes the complexity of flow in such systems. The proposed model converges to the Knudsen diffusion model when average pore size decreases (nanoscale pores) and it converges to the continuum model, when average pore size increases (i.e. in microscale pores). He concluded that at the nanoscale, permeability is not only a characteristic of the solid matrix, but the gas type and operating conditions affect gas permeation through the media.

Darabi et al. (2012) modified Javadpour's model to take into account the surface pore roughness effect. They also upscaled their model for using at a larger (centimetre) scale. They substituted $\frac{R_{nt}^2}{8}$ with Darcy permeability (k_∞) to take into account the effect of the pore network structure.

Deng et al. (2014) proposed a seepage model, by considering diffusion, slippage and desorption effects. They proposed a non-linear combination of slippage and diffusion terms, then adding a desorption term to the model. For slippage effects, they used a modified permeability adjustment factor derived from the equation of Beskok and Karniadakis (1991). To take into account the diffusion, they used Knudsen diffusivity, given by Civan (2010). For adsorption/desorption effects, they also used the Langmuir isothermal adsorption equation. Although their model considers slippage, diffusion and desorption, it is complicated to be used in commercial reservoir simulators.

Guo et al. (2015) conducted some experiments to study nitrogen flow through nanomembranes (with pore throat sizes 20 nm, 55 nm, and 100 nm). They proposed a mathematical model similar to Javadpour's formulation to characterise gas flow in nanopores. They extracted a new apparent permeability expression based on the proposed model.

In this approach, the gas flow rate in the shale matrix is mostly correlated with viscous flow and free molecular flow regime. However, recent experimental observations have shown that gas mostly encounters slip flow and transition flow in shale and tight gas reservoirs (Sinha et al., 2013, Ghanizadeh et al., 2014b, Heller et al., 2014, Yves et al., 2015) and rarely experiences free-molecular flow. In addition, as the Knudsen diffusivity is based on simple kinetic theory, the DGM model becomes inaccurate, when strong potential energy gradients exist (Niu et al., 2014, Bhatia et al., 2011, Bhatia and Nicholson, 2003).

In the second approach, researchers have considered the dominant flow regime distinguished by the Knudsen number and developed flow equations suitable for that flow

regime (Florence et al., 2007, Sakhaee-Pour and Bryant, 2012, Civan, 2010, Ziarani and Aguilera, 2012). Their works are mainly based on the Beskok-Karniadakis unified model (1999).

Florence et al. (2007) used field data from low permeability reservoirs and proposed a model to improve the predicted data from the Klinkenberg correction. They obtained an empirical correlation for average pore radius and proposed to use a "Pseudo Knudsen number". To develop the model, they used the Karniadakis and Beskok unified model (1999) and introduced three calibration coefficients. Although they tried to incorporate the porous media parameters (i.e. permeability and porosity), they used the slip model and slip coefficients which originally developed for nonporous media at low pressure.

Civan (2010) modified the model of Florence et al. by considering the effect of tortuosity in porous media. He used the same rarefaction coefficient proposed by Beskok-Karniadakis (1999) and obtained a new formulation for the Klinkenberg gas slippage factor. He compared the results of his model with the literature experimental data (Loyalka and Hamoodi, 1990) measured for single pipe at low pressure.

Sakhaee-Pour and Bryant (2012) considered the effect of gas slippage by applying the model appropriate to the flow regime, according to the Knudsen number (Kn). They concluded that for the slip flow regime, the first-order slip model is more suitable than the dusty gas model (DGM). For transition regime, they proposed the solution of Karniadakis et al. (2005), with some modifications. For free molecular flow, they considered the mass-flow rate modelled by Knudsen.

Ziarani and Aguilera (2012) proposed the "Knudsen's permeability correlation" obtained from the general slip model developed by Karniadakis and Beskok (1999) for all flow regimes. They evaluated the model by using data from the Mesaverde formation in the United States, reported by Byrnes et al. (2006). They concluded that the Knudsen permeability correlation is more accurate than Klinkenberg's model especially for extremely tight porous media with transition and free molecular flow regimes.

In almost all the models in the latter category, the proposed Beskok-Karniadakis unified model (1999) has been used with the same slip and tangential momentum accommodation coefficient (TMAC). These coefficients were originally determined based on Direct Simulation Monte Carlo (DSMC) for low-pressure gas flow in a single straight pipe. Although Beskok and Karniadakis (1999) used the experimental data to

verify their model, all the experiments were performed in a single channel at low pressure (Karniadakis et al., 2005).

To the best of the researcher's knowledge, there is no comprehensive study on the suitability of the reported slip models in the literature for shale/tight gas flow. As almost all available models for slip flow were developed for low-pressure non-porous media (for MEMS applications); thus, an investigation on these slip models for high pressure, porous media is highly valuable and sought after. However, some researchers tried to modify the available slip models, but they used the same slip coefficients (Florence et al., 2007). In other words, suitable slip coefficients should be obtained for porous media and used for the modelling of gas flow in shale matrix. It is noted that, despite several measurements of slip coefficients for different systems, there is no reported measurements for slip coefficients of gas in porous media. Hence, slip coefficients in the slip models are further critical parameters, which should be determined properly for accurate prediction of flow behaviour in shale rocks.

There are different proposed techniques in the literature to obtain slip coefficients: kinetic model based methods, the polynomial expansion approach, DSMC, the Lattice Boltzmann method and experimental measurements. However, experimental results in non-porous media have shown that there are significant discrepancies between the measured slip coefficients and the theoretical values in the literature (Zhang et al., 2012c). Several authors have tried to measure the slip coefficients and TMAC using various experimental setups. (Kuhlthau, 1949, Maurer et al., 2003). There are discrepancies between these measured values, as their measurements seem to be specific for the considered geometric microdevices. As mentioned, there is no reported value for the slip coefficients (or TMAC) for porous media, which can be used in the slip models for prediction of flow in shale/tight gas reservoirs. In this research, experimental data regarding gas flow in shale rocks were used to determine the slip coefficient and TMAC value in porous media. For this purpose, slip boundary conditions (first-order and second-order) were utilised in the N-S equations to capture the gas flow in the conducted experiments. From the experimental data, the slip coefficients and TMAC for porous media under study (shale rocks) were determined. The slip coefficients obtained were used in the solution of the N-S equation to develop a reliable model for prediction of shale matrix permeability.

2.4.2 LBM Simulation of Micro and Nanoscale Gas Flow

In addition to analytical and semi-analytical equations for prediction of flow in the non-continuum regimes, mesoscale simulation of gas flow in micro and nanosystems has also been used as an alternative. It is noted that almost all analytical and semi-analytical equations are originally developed based on simple geometries such as channels or tubes. Hence, for more complex flow path systems (e.g. porous media), the analytical solutions can give only approximate results. An accurate study of gas flow in such complex systems requires an appropriate simulation technique.

Recently, the Lattice Boltzmann Method (LBM) has received great attention for such applications. It solves a discretised form of the continuous Boltzmann equation, which is an accepted relationship for the modelling of evolution of gas flow based on the kinetic theory of gas particles, for a regular lattice. This technique is computationally efficient, as it deals with particle distribution functions. In fact, the intrinsic kinetic nature of the LBM makes it an attractive method for microfluidic flows with high Knudsen numbers, similar to the case of gas flow in shale and tight matrices. In the LBM, to take into account the slippage at the wall surface, the interaction of gas particles with the solid surface should be defined properly. Appropriate boundary conditions should be applied to obtain reliable results during the numerical simulation of slip flow by the LBM.

In the literature, different boundary conditions have been proposed for this purpose, such as bounce back (Nie et al., 2002), specular reflection (Lim et al., 2002, Succi, 2002), diffusive reflection and combinations of these (Sofonea and Sekerka, 2005). Sbragaglia and Succi (2005) derived analytical expressions for a broad class of boundary conditions for the slip flow and compared the corresponding results with numerical simulations. Sofonea and Serka (2005) also studied the effect of various boundary conditions including bounce back, specular reflective and diffusive reflection .

Some LBM simulations have been published recently regarding gas flow in tight and shale formations. Using LBM, Fathi et al. (2012) showed that inelastic collisions of gas molecules with the nano-capillary walls create a high kinetic energy molecular streaming effect on the fluid flow. This leads to dramatic changes in the fluid flow velocity profile. Fathi and Akkutlu (2013) performed LBM simulations with a Langmuir slip boundary condition to incorporate the slippage and the surface-transport mechanisms. They introduced the surface transport of the adsorbed phase as a moving wall in the model. Zhang et al. (2015) performed Lattice Boltzmann simulations and proposed a method to

estimate the matrix permeability of complex pore structures. They investigated various possible factors that affect shale gas flow characteristics and analysed the influence of each factor. Ren et al. (2015) applied the Langmuir isothermal adsorption equation with bounce-back/specular-reflection boundary conditions, to take into account the effects of surface diffusion, gas slippage and adsorbed layer (Ren et al., 2015). Ning et al. (2015) propose a method to incorporate inter-molecular and adsorptive forces into the generalised LBM algorithm to capture gas adsorptions in organic nano-pores (Ning et al., 2015).

In all the studies mentioned above, the strengths and deficiencies of LBM for simulation of gas flow in shale gas reservoirs have not been well addressed. In addition, the simulation results of LBM have never been scaled and compared with actual shale rock experimental data measured at high pressure. In this research, for the first time, various slip boundary conditions were employed in the LBM to consider the gas slippage in porous media. As the simulation results were compared with the scaled experimental data, the suitability of different boundary conditions for simulation of gas flow in shale rock was investigated. Furthermore comparison of the experimental data and simulation results were used to obtain appropriate TMAC value for LBM simulation of gas flow in shale rocks. The TMAC value is an important factor as the slippage intensity can be determined by this coefficient in shale matrices. Moreover, the simulation results of a single pipe and a pore/throat system were also compared with scaled the experimental data. The results of this study are presented in Chapter 5.

2.4.3 Geomechanical and Stress Effects

As mentioned, prediction of in-situ matrix permeability and how it evolves with depletion is essential for accurate production forecasting. The variation of rock permeability with effective stress has been studied extensively for sandstones and carbonates (Warpinski and Teufel, 1992, Al-Wardy and Zimmerman, 2004, Ghabezloo et al., 2009). Recently, several researchers have studied the stress dependency of the shale permeability. Kwon et al. (2001) measured the permeability of Wilcox shale at varying confining and pore pressures. They reported that shale permeability depends on both confining and pore pressure, with similar sensitivities. They obtained an effective pressure coefficient of 0.99 ± 0.06, which is indistinguishable from unity; i.e. $P_e = P_{conf} - P_{pore}$.

Lei et al. (2007) performed a laboratory study of stress-sensitive permeability and developed a correlation for permeability prediction at different effective stress values. They also used the results of electronic microscope scanning (SEM) analysis and constant-rate mercury injection tests. The found that the stress variation has small effect on rock porosity and a significant impact on rock permeability due to the higher sensitivity of pore throats to the stress. They concluded that the changes in formation permeability, caused by both elastic and plastic deformation, are permanent and irreversible.

Bustin et al. (2008) investigated the sensitivity of permeability to confining pressure at a single pore pressure. They reported that the level of stress-dependency of permeability depends on composition and fabric. They also concluded that the biogenic silica-rich shales are less sensitive to an increase in effective stress.

Dong et al. (2010) measured the stress dependent permeability and porosity of fine-grained sandstones and a silty-shale. They showed that the dependency of gas permeability on the stress can be better expressed using a power law function (Dong et al., 2010).

Chalmers et al. (2012) conducted some experiments to investigate the geological parameters controlling the matrix permeability of Devonian shales. They reported that permeability is a function of mineral distribution, pore size, and fabric.

Gut et al. (2014) investigated the use of the Constant Rate of Strain (CRS) consolidation test for measurement of continuous stress-dependent permeability, compressibility and poroelasticity of stiff and low-permeability shales. The concluded that the CRS test is useful to characterize stiff shale in terms of the compressibility, poroelasticity, and permeability.

Heller et al. (2014) performed an experimental study on intact shale samples. They measured matrix permeability at different pore pressures and net stress values. They concluded that the matrix permeabilities of gas shales are more sensitive to changes in confining pressure than to changes in pore pressure. Based on the data obtained, it was concluded that the effective permeability of shale rocks is significantly enhanced at low pore pressures (<1000 psi). They used the Klinkenberg correction to consider the slippage effects on flow.

Although some researchers performed permeability measurements at different net stress and various pore pressures, the effects of net stress on the pore/throat size and the

dominant flow regimes were not investigated. In other words, in the previous studies, the goemechnaicl effects were only investigated on apparent permeability and its effects on gas flow regimes were not examined. In this study, both stress and slippage effects on fluid flow were investigated experimentally and a model has been developed to take into account these effects on shale matrix permeability. In other words, first, an appropriate slip model was developed for gas flow in shale based on the experimental data. Then the geomechanical effects on both permeability and flow regimes were incorporated into the model.

2.4.4 Capillary End Effects

The capillary end effect has been extensively studied for many years. Leverett (1941) mentioned the boundary effect in porous materials (Leverett, 1941). Osoba et al. (1951) reported that there is no variation in kr at different rates in the absence of boundary effects (Osoba et al., 1951). They proposed using high flow rates to minimise the end effects. Rapaport and Leas (1953) studied effects of the core length and injection rate on the flooding behaviour. They concluded that the same flooding behaviour is obtained for different lengths, if the injection rates are properly adjusted. They added that the flooding behaviour dependency to the rate and length decreases as anyone of these factors increases in value. They also proposed a scaling criteria to determine the stabilisation of flooding (Rapoport and Leas, 1953).

In addition, there are several published papers, which propose that additional information should be obtained (e.g. in-situ saturation, independent measurement of capillary pressure, in-situ pressure measurements along the core) to correct measured relative permeability data for CEE. Haung and Honarpour (1988) proposed the use of kr-Pc relationships to correct the capillary end effects. However, their method is difficult to apply and may not be valid for rocks with unknown kr-Pc functions (Huang and Honarpour, 1998). Qadeer et al. (1991) developed a model, which consists of an optimisation algorithm to estimate the oil/water kr exponential functions from the unsteady state displacement experiments. However, in this approach, a Pc function is required and the match might not be unique (Qadeer et al., 1991). Virnovsky et al. (1995, 1998) proposed measuring Pc separately, which is then used to estimate saturation and kr data and correct CEE (Virnovsky et al., 1995, Virnovsky et al., 1998). Chen and Wood (2001) measured the in-situ saturation and pressure at different intervals along the core.

Although during the kr measurements the pressure can be recorded by internal taps, it is expensive and impractical for cores such as shale and tight samples, which are not long enough (Chen and Wood, 2001).

It is noted that all the studies mentioned above have been performed on conventional core samples. Recently, Gupta and Maloney (2015) proposed a technique to correct CEE by performing measurements at different flow rates. Although no additional information (e.g. in-situ saturation) is required in their method, they assumed a constant wetting phase kr along the core, which is open to question. In addition, they did not consider the variation of the length of the CEE region at different flow rates (Gupta and Maloney, 2015). In Chapter 6, this issue is discussed in detail and it is shown that the length of the CEE region is not constant and changes with the flow rate, which poses serious questions on the validity of the approach proposed by Gupta and Maloney (2015).

As indicated above, in most of the proposed methods for CEE correction, additional information such as in-situ saturation or in-situ pressure is required. In practice, it is difficult to have an in-situ pressure transducer on shale/tight samples, which are general small plugs. It is noted that the length of the shale/tight rock samples used in the displacement experiments are generally small, due to the ultralow permeability of these rock types. In addition, measurements of in-situ liquid saturation are very expensive and may not be accurate for such small samples. To date, there is no reported data on relative permeability measurements of shale rock samples corrected for capillary end effects. The previous theoretical and experimental studies were developed for conventional rock types. To the best of the author's knowledge, this is the first time that the relative permeabilities of shale samples have been measured, and the capillary end effects have been corrected, based on a proposed unique method. In this method, the fluid flow in the core is modelled at two separate regions of CEE zone and unaffected zone. Then, from the experimental data conducted at four different rates, the corrected relative permeability and liquid saturation can be obtained as discussed in Chapter 6.

Chapter 3: Experimental Study of Gas Flow in Shale Matrix: Permeability Measurements

3.1 Introduction

Gas production in shale reservoirs is attributed to the conductivity of the matrix and fracture systems. However, the long-term gas production from these reservoirs are known to be a function of fluid transport in the matrix (Bustin and Bustin, 2012, Swami and Settari, 2012). Many researchers have shown the importance of the matrix flow (Bustin et al., 2008, Kalantari-Dahaghi, 2011, Bustin and Bustin, 2012). However, the fluid flow in shale matrices can be affected by several simultaneous processes such as rarefaction flow, gas adsorption/desorption, and geomechanical effects, which were explained in the previous chapter. The impact of these unconventional mechanisms on fluid flow is not well understood. There are few studies in the literature that considered these effects to a limited extent, hence, more experimental works are required. For example, measurement of shale matrix permeability is still challenging mainly due to dominant roles of these processes during the measurements.

As mentioned before, there are some theoretical works on permeability modelling of systems with micro and nanopores (Javadpour, 2009, Civan, 2010, Deng et al., 2014, Florence et al., 2007, Freeman et al., 2011, Kazemi and Takbiri-Borujeni, 2015) but there are a few reported studies, which investigate these mechanisms experimentally.

Heller et al. (2014) performed an experimental study on intact shale samples. They measured matrix permeability at different pore pressures and net stress values. They concluded that the matrix permeability of gas shales are more sensitive to changes in confining pressure than changes in pore pressure. Based on the obtained data, the effective permeability of shale rocks is significantly enhanced at low pore pressures (<1000 psi). They used Klinkenberg correction to consider the slippage effects on flow.

Ghanizadeh et al. (2014) conducted a laboratory study examining the transport properties in the matrix of the Lower Toarcian Posidonia Shale. The main objective of their case study was to provide high-quality experimental data, when analysing the effects of different parameters (Ghanizadeh et al., 2014a). Firouzi et al. (2015) conducted pressure pulse decay experiments and measured the helium permeability and Klinkenberg

parameters of a shale core plug. They compared the measured permeabilities and the permeability predictions using Non-equilibrium molecular dynamics simulations indicating that the pulse-decay gas permeability is approximately two orders of magnitude greater than that calculated values by the MD simulation (Firouzi et al., 2014). Guo et al. (2015) presented an experimental study of nitrogen flow through nanomembranes. They proposed a new mathematical model to characterise gas flow in nanopores. In addition, they derived a new apparent permeability expression based on viscous flow and Knudsen diffusion. Ghanizadeh et al. (2015) conducted some experiments to characterise the porosity, pore size distribution and permeability of Montney and Bakken shale formations in Canada.

Recently, the stress dependency of shale matrix permeability have also been studied experimentally. Dong et al. (2010) measured the stress dependent permeability and porosity of fine-grained sandstones and silty shales. They showed that the dependency of gas permeability to the stress can be better expressed using a power law function. Chalmers et al. (2012) conducted some experiments to investigate the geological parameters controlling the matrix permeability of Devonian shales. They reported that permeability is a function of mineral distribution, pore size, and fabric. Gut et al. (2014) investigated the use of the Constant Rate of Strain (CRS) consolidation test for measurement of continuous stress-dependent permeability, compressibility and poroelasticity of stiff and low-permeability shales.

However, in all experimental studies mentioned above, the flow regimes and geomechanical effects are usually investigated separately. To the best of the author's knowledge, there is no experimental work studying the fluid flow in shale matrix considering combined effects of the rarefaction and geomechanics.

This chapter is focused on the experimental study of flow in the shale matrix. Different shale samples were used in this research and several rock characterization tests have been performed on these shale rocks to determine the mineralogy, pore size distribution and pore structures. Then, a series of steady state and unsteady state permeability measurements was performed to investigate the slippage and geomechanical effects on fluid flow in the matrix of these shale rocks.

3.2 Shale Rocks Characterization

This study was performed on three shale rock types of Eagle Ford, Pierre and Barnett. Prior to any dynamic experiments, the rock characterisation tests such as total organic carbon (TOC) measurements, X-ray diffraction (XRD) analysis, Mercury injection capillary pressure (MICP), Helium porosimeter, scanning electron microscope (SEM) tests and contact angle measurements were performed. Shale samples were provided by Kocurek Industries, all in 1.5 inch diameters. Shale rock samples were cut parallel to beddings. Figure 3.1 shows samples from Eagle Ford, Pierre and Barnett formations used in this study. It is noted that the total organic carbon (TOC) measurements, X-ray diffraction (XRD) analysis and Mercury injection capillary pressure (MICP) were performed by external companies.

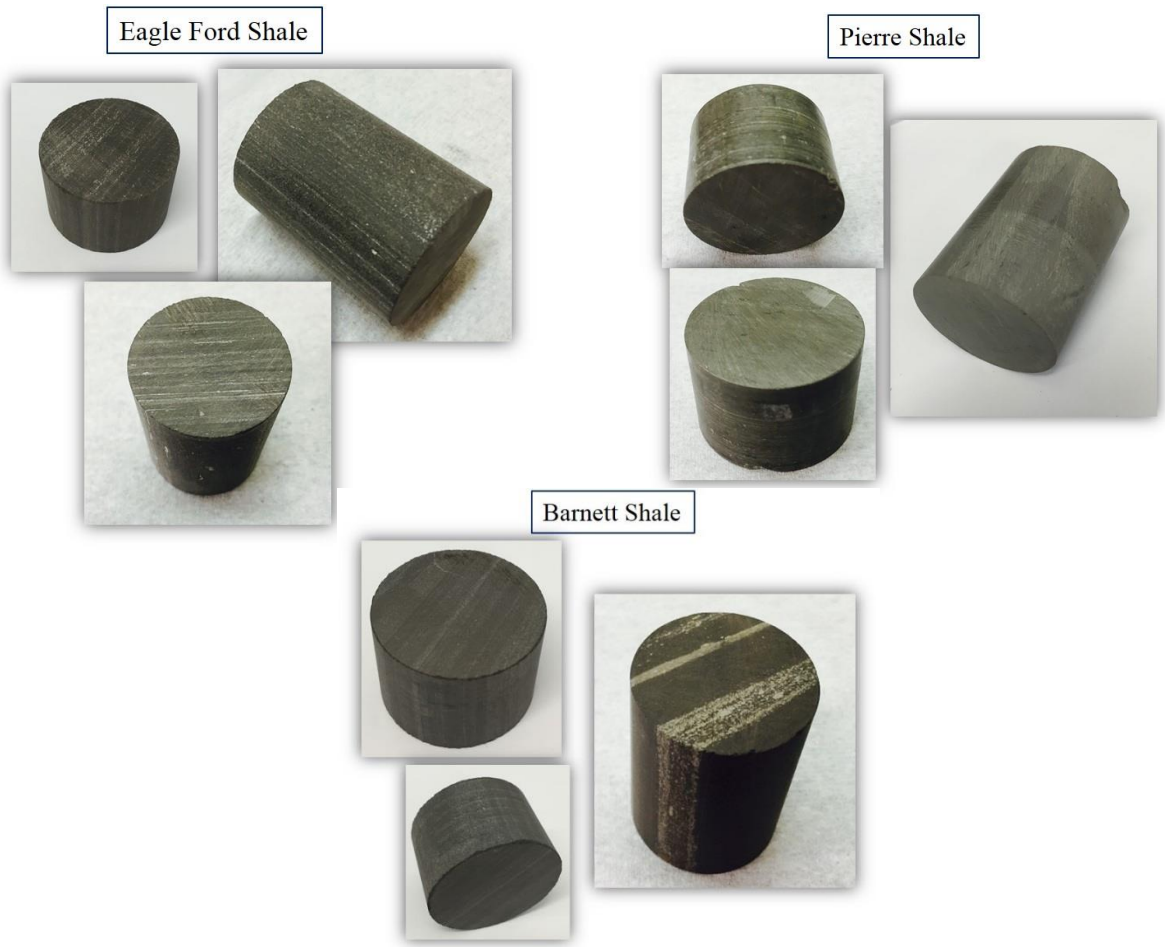

Figure 3.1: Samples from Eagle Ford, Pierre and Barnett shale formations used in this study.

3.2.1 Helium Porosimetry and TOC measurements

The porosities of shale samples were measured by Helium using Boyle's two cell method. All samples were dried before performing experiments. To remove the initial water, rock samples were placed in the oven at 105 ℃ overnight while connected to the vacuum pump. For porosity measurements, the overburden pressure was set at 500 psi and the tests were conducted at 100 psi. Several measurements were performed to obtain a reliable value for the porosity of each shale sample. Total organic carbon (TOC) analyses were carried out by ALcontrol Laboratories Ltd, Flintshire on 1 g portions of ball-milled material. The samples were firstly treated with hydrochloric acid to remove any inorganic carbon. The samples were then heated in a flow of oxygen in an ELTRA CS800 carbon/sulphur analyser. Any carbon present in the samples was therefore converted to carbon dioxide, which was measured by an infra-red detector. The percentage carbon was then calculated with respect to the original sample weight. The lower detection limit for the method is 0.2% TOC.

Table 3.1 presents the basic properties of shale samples including porosity and TOC.

Table 3.1: Basic properties of the three shale rock samples used for apparent permeability measurements at various pore and confining pressures.

Shale Sample	**Length (cm)**	**Porosity (%)**	**TOC (%)**	**Permeability Range (D)**	**Moisture Condition**
Eagle Ford (E1)	4.61	13.4	3.28	$\sim 10^{-4}$	Fully Dry
Pierre (P1)	2.54	31.6	0.50	$\sim 10^{-5}$	Fully Dry
Barnett (B1)	2.55	8.60	11.40	$\sim 10^{-6}$	Fully Dry

3.2.2 X-ray Diffraction Analysis (XRD)

Mineralogy of the shale samples were obtained from XRD analysis. Quantitative whole-rock XRD analyses were carried out by British Geological Survey (BGS) using a PANalytical X'Pert Pro series diffractometer equipped with a cobalt-target tube, X'Celerator detector and operated at 45kV and 40mA. The micronised powder samples were scanned from 4.5-85°2θ at 2.06°2θ/minute. Diffraction data were initially analysed using PANalytical X'Pert HighScore Plus version 4.5 software coupled to the latest version of the International Centre for Diffraction Data (ICDD) database.

The results of whole-rock powder XRD analyses are summarised in Table 3.2. The samples exhibit a range of different mineralogies. Eagle Ford sample is predominantly composed of calcite with major amounts of quartz and traces of clay minerals. Pierre and Barnett samples are all quartz-dominated with greater amounts of phyllosilicates/clay minerals.

Table 3.2 : Mineralogy of the shale samples obtained from whole-rock x-ray diffraction (XRD) analyses.

Shale Sample	**Silicates**			**Carbonates**			**Phyllosilicates/Clay minerals**				**Others**		
	Quarts	**Plagioclase**	**K-feldspar**	**Calcite**	**Dolomite**	**Siderite**	**Mica***	**Kaolinite**	**Chlorite**	**Smectite**	**Pyrite**	**Fluorapatite**	**Gypsum**
Eagle Ford	27.1	nd**	<0.5	68.4	nd	nd	1.0	1.6	nd	nd	<0.5	nd	1.2
Pierre	68.3	2.1	nd	0.6	nd	nd	15.9	<0.5	2.2	10.3	0.7	nd	nd
Barnett	55.3	nd	nd	nd	nd	1.1	32.0	1.0	2.0	nd	0.8	7.8	nd

* Undifferentiated mica species possibly including muscovite, biotite, illite, illite/smectite.

** Not detected

3.2.3 MICP and Pore Size Distribution

To measure the capillary pressure and pore size distribution of the shale samples ultrahigh pressure MICP tests were performed by Core Laboratories using Micromeritics Autopore V. For drainage, mercury (non-wetting phase) was injected into the core plug at increasing incremental pressures from 0.5 to 25.0 psi. In other words, a positive change in the value of mercury pressure was 0.5 psi at the beginning and 25 psi at higher pressures. At each pressure point, mercury intrusion was monitored while the pressure was held constant. Equilibrium was identified on a time basis. Monitoring the change in pressure over a specific period, (60 seconds), identifies equilibrium. If the pressure remains above 99.5% of the set injection pressure over this period then equilibrium is assumed. If the pressure drops below 99.5%, then the pressure is reset, and monitored again over the equilibration

time. This is repeated until equilibration is achieved at each pressure. The capillary pressure in these tests was increased up to 55000 psi. Figure 3.2 shows the measured capillary pressure of three shale samples of Eagle Ford, Pierre and Barnett. As illustrated, for Eagle Ford and Pierre samples, the mercury occupied almost all pores at 55000 psi. However, for Barnett shale, 40 % of pores remained unsaturated even at 55000 psi.

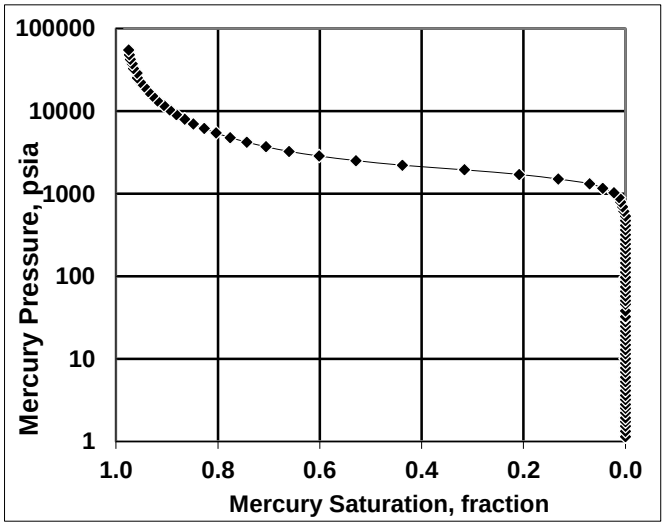

(a)

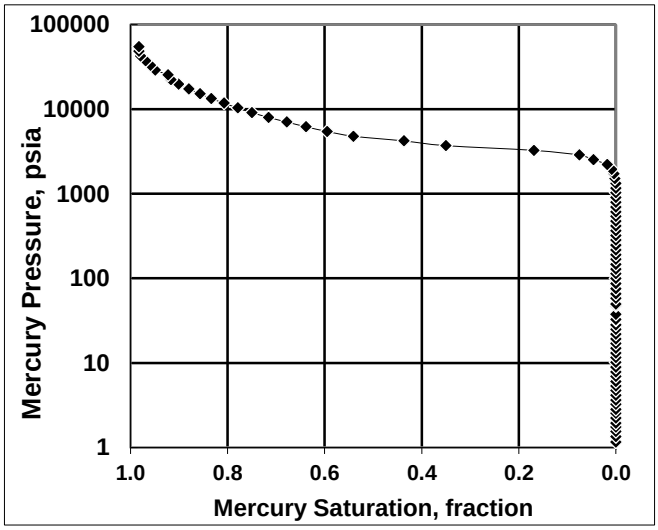

(b)

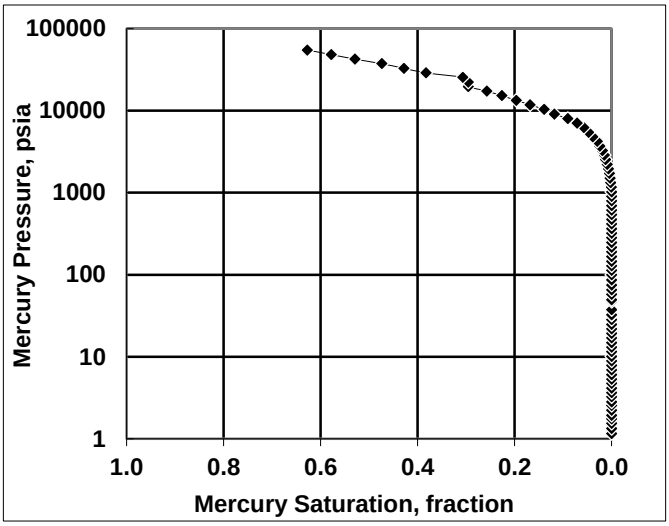

(c)

Figure 3.2: MICP capillary pressure of (a) Eagle Ford (b) Pierre and (c) Barnett rock samples.

In addition to capillary pressure, pore size distributions of these shale samples are calculated. The minimum pore throat radius at any mercy displacement pressure can be obtained using the following equation.

$$r = \frac{2\sigma \cos\theta}{P_c} \tag{3.1}$$

where σ is interfacial tension between air and mercury (485 dynes/cm) and θ is contact angle between air and mercury (140°). The fraction of pore volume injected (v) can be also obtained during the mercury displacement. Hence, a graph of fraction of pore volume injected (v) versus pore throat radius can be constructed. The differential of this plot gives a pore throat size distribution (PSD) function.

$$PSD = \frac{dv}{d\log(r)} \tag{3.2}$$

As mentioned in Chapter 2, the flow regimes can be recognised based on the dimensionless Knudsen number. For determination of the Knudsen number, flow "characteristic length" is required. In this study, an average of pore sizes is obtained from pore size distributions and used for the Knudsen number calculation. For average pore size estimation, the measured pore sizes were fitted by appropriate well-known probability distribution functions. These fitted probability functions were used since some of the pores remained unsaturated after the MICP test (e.g Barnett sample). Hence as

these fitted probability functions cover all pore sizes, it can be presumed that the smaller pores, which were not saturated in the test, have been taken into account. As shown in Figure 3.3, for Eagle Ford and Pierre, the normal distribution is the best probability function to describe the pore sizes. For Barnett, the Gamma distribution function is identified as the best probability function of the pore sizes. Table 3.3 shows the statistical parameters of the pore size distributions. The mean pore size of shale samples was used as an average flow conduit characteristic length for the Knudsen number calculation.

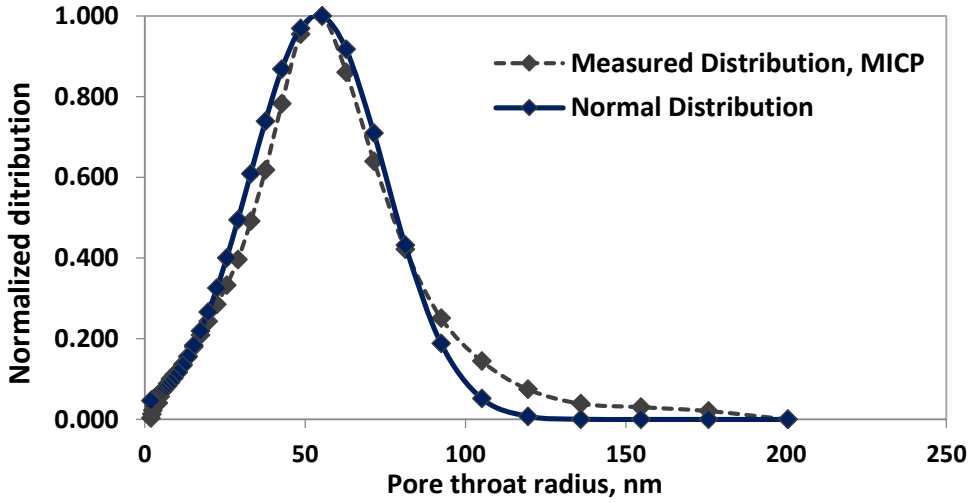

(a)

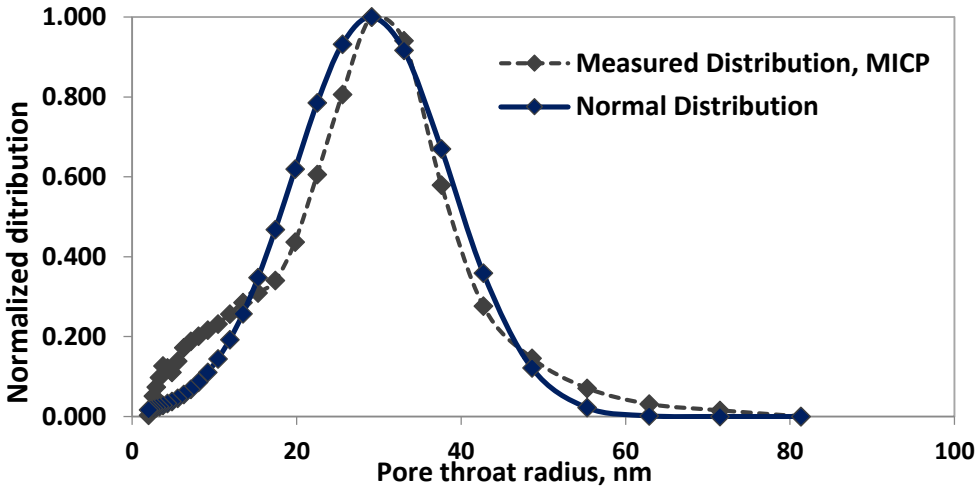

(b)

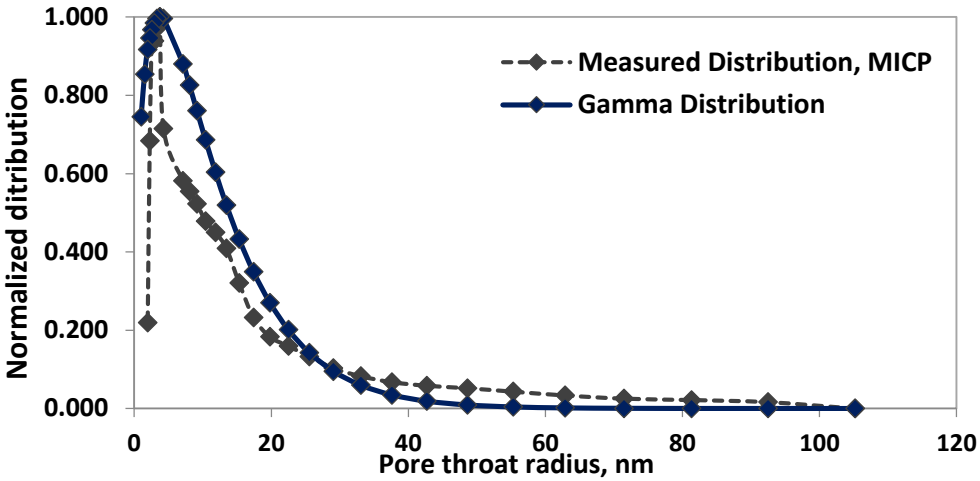

(c)

Figure 3.3: Pore size distribution of (a) Eagle Ford (b) Pierre and (c) Barnett rock samples. The best identified probability function is also shown for each sample.

Table 3.3: The statistical parameters of the distribution functions based on the measured MICP pore size distribution and best fitted probability function.

Shale sample	**Probability function**	**Mean (μ)**	**Standard Deviation (σ)**
Eagle Ford	Normal	54 nm	21 nm
Pierre	Normal	29.1 nm	9.5 nm
Barnett	Gamma	11.25 nm	9.2 nm

3.2.4 SEM Images and Pore Structure Analysis

In addition to the measured pore size distribution by MICP for all shale samples, void spaces and pore structure of the Eagle Ford shale matrix were studied by Scanning Electron Microscopy (SEM). Pore structures in shale matrix can give valuable information, while interpreting the stress-dependent matrix permeability. Generally, pore types in shale and mudrocks are classified into two main groups of nonorganic-matter-related pores (interparticle, intraparticle and intracrystalline) and organic-matter-related pores (Jennings et al., 2013, Loucks et al., 2010). Microfractures (MF) are also classified among the effective pores, which have a significant impact on the storage and flow capacity. It is noted that these microfractures could be the artefacts of post-coring stress release or sample preparation. However, naturally occurred microfractures are also

frequently observed in shale and mudrocks (Jennings et al., 2013, Kwon et al., 2004, Chalmers et al., 2012a, Wu et al., 2015) with a significant contribution to the flow (Wu et al., 2015).

Figure 3.4 shows the SEM images taken from the Eagle Ford shale sample. The SEM images were taken from the polished thin sections. As shown in this figure, several microfractures are detected as shown by the red arrows. These microfractures can play important roles in fluid transport. Moreover, the significant stress-dependent permeability of shale matrix can also be linked to these microfractures.

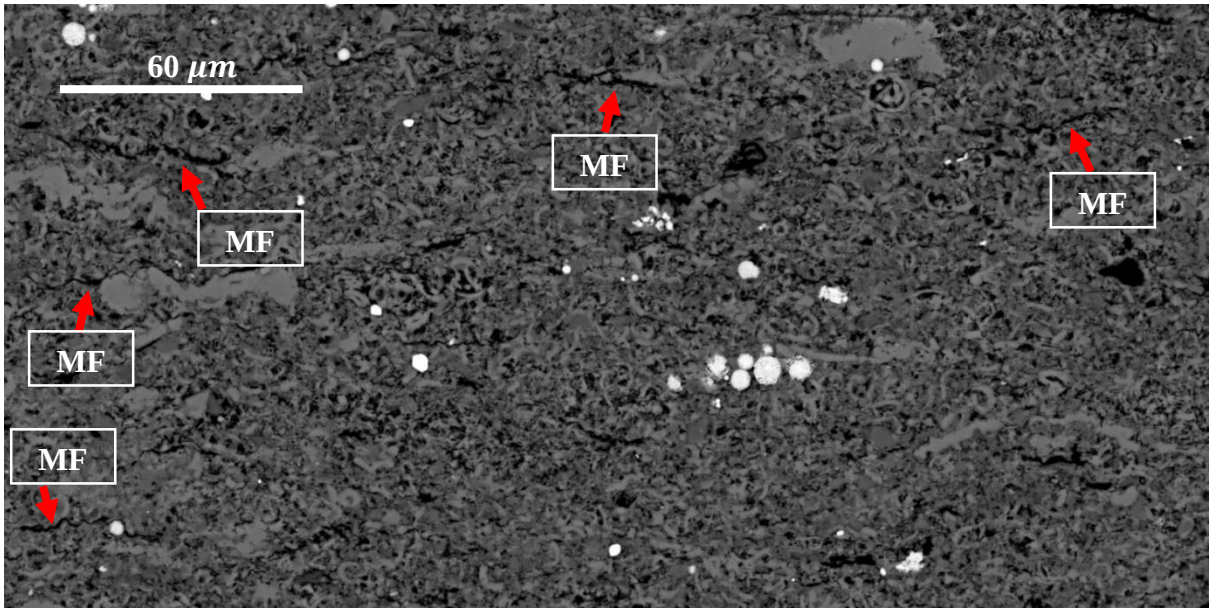

Figure 3.4: SEM image of Eagle Ford shale sample which shows the interparticle microfractures (MF) by red arrows.

In addition to MFs, other pore types including interparticle and intraparticle pores are observed in the Eagle Ford shale. Figure 3.5 presents more details about the available pores. These microfractures are mostly generated parallel to bedding (Kwon et al., 2004). In Figure 3.5 (a) a microfracture is illustrated with an approximate length of 60 μm. Interparticle (IP) pores are shown by the yellow arrows in Figure 3.5 (b). Interparticle pores can be found between grains and crystals, which are generally related to the primary pore network. Interparticle pores are the most common pore type found in the Eagle ford (Jennings et al., 2013). In Figure 3.5 (c), intraparticle (IT) pores are shown by the green arrows. Intraparticle pores are generally defined as the pores within a particle boundary, which can be primary (original pores within grains that are clustered together such as

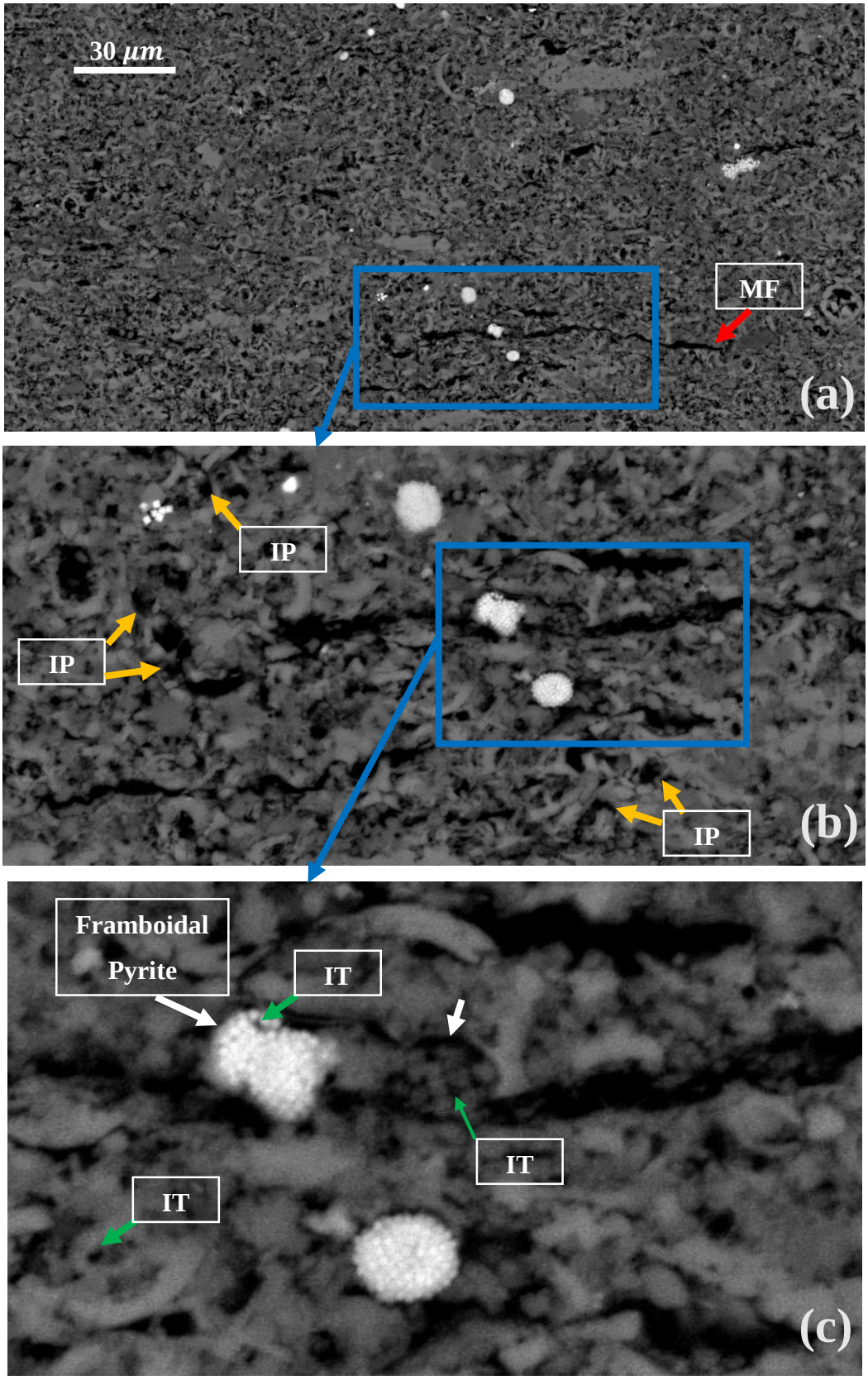

Figure 3.5: Presence of framboidal pyrite and finer sediments inside a microfracture (shown by white arrows) which decreases the possibility of fracture propagation during the core preparation.

pores within framboidal pyrite as shown in Figure 3.5 (c)) or secondary (dissolution pores) in origin. It is noted that these pore types are more common and can be easily detected.

Despite different pore types observed in the structure of Eagle Ford, it is believed that the microfractures have dominant contributions in both flow and stress-dependency behaviour of shale formations.

3.2.5 Wettability Evaluation by Contact Angle Measurements

The wettability of these shale rocks were evaluated by contact angle measurements at atmospheric pressure and room temperature. The KRUSS drop shale analyser of the gas-condensate recovery research team was used for this purpose (shown in Figure 3.6). Two fluid systems of water/air and Decane/air were used in these measurements. For each measurement, the same volume of liquid droplet was placed on the shale surface and the contact angles were recorded versus time. In addition, the base diameter of the droplets was recorded to evaluate the droplet's horizontal spreading. The results of water/air contact angles are shown in Figure 3.7. As seen, at the start of the experiments, water contact angles of 95, 49 and 48 were recorded for Eagle Ford, Pierre and Barnett shale samples, respectively. These values indicated a higher wetting tendency of Pierre and Barnett compared to Eagle Ford. These water wetting tendency of Pierre and Barnett can be assigned to their high clay contents of 30% and 35%, respectively.

In addition, it can be seen that the water droplet imbibed into the Pierre sample rapidly, while it was almost stable on Barnett shale. As the organic materials are hydrophobic, this difference can be interpreted based on TOC content of these shale samples, which are 0.5% for Pierre and 11.4% for Barnett shale. In addition, this different imbibition rate can be also linked to the matrix permeability of these shale samples. As shown by Nazari Moghaddam and Jamiolahmady (2015), the rate of imbibition is proportional to the permeability of the porous media. Hence, lower imbibition rate can be expected for Barnett shale which has a lower matrix permeability.

Furthermore, drop base diameter of Pierre shale sample showed horizontal spreading of water droplet on the rock surface. Lower TOC and higher clay content of this shale rock can be the main reasons for this strong wetting tendency with respect to water.

The contact angle of Decane/air system was also measured on all three shale rock samples. The decane droplet was used to evaluate the oleophilic tendency of shale rocks

under study. However, the contact angle measurement is only a simple method to indicate rock wettability qualitatively. In other words, a comparison can be made for wetting tendency of shale samples with respect to water and oil if the corresponding contact angles are available. It is also noted that, the contact angle value can slightly change from one point to another depending on the mineralogy, roughness and other parameters.

In these tests, the same procedure was followed for contact angle measurements of decane droplets. In all tests, the decane droplets were rapidly imbibed into the rock sample. This behaviour is usually assumed as a strong wetting tendency of rock with respect to the droplet and the contact angle is assumed to be zero. Comparing to the contact angles obtained for water droplet, it can be concluded that these shale samples are more oil-wet.

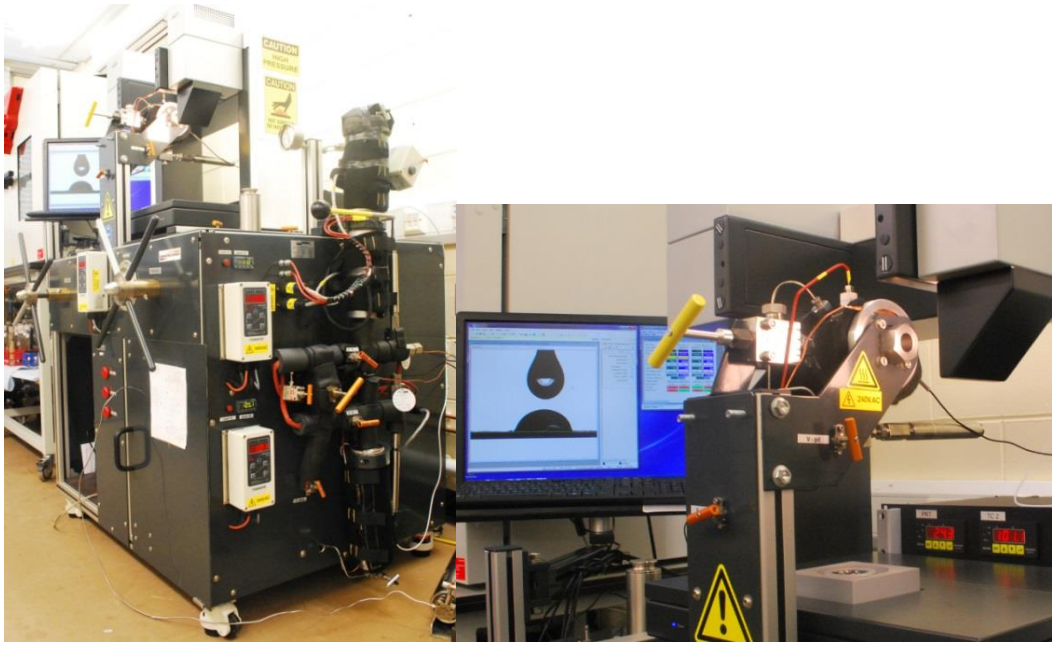

Figure 3.6: Kruss drop shape analysis system used for contact angle measurements of shale samples.

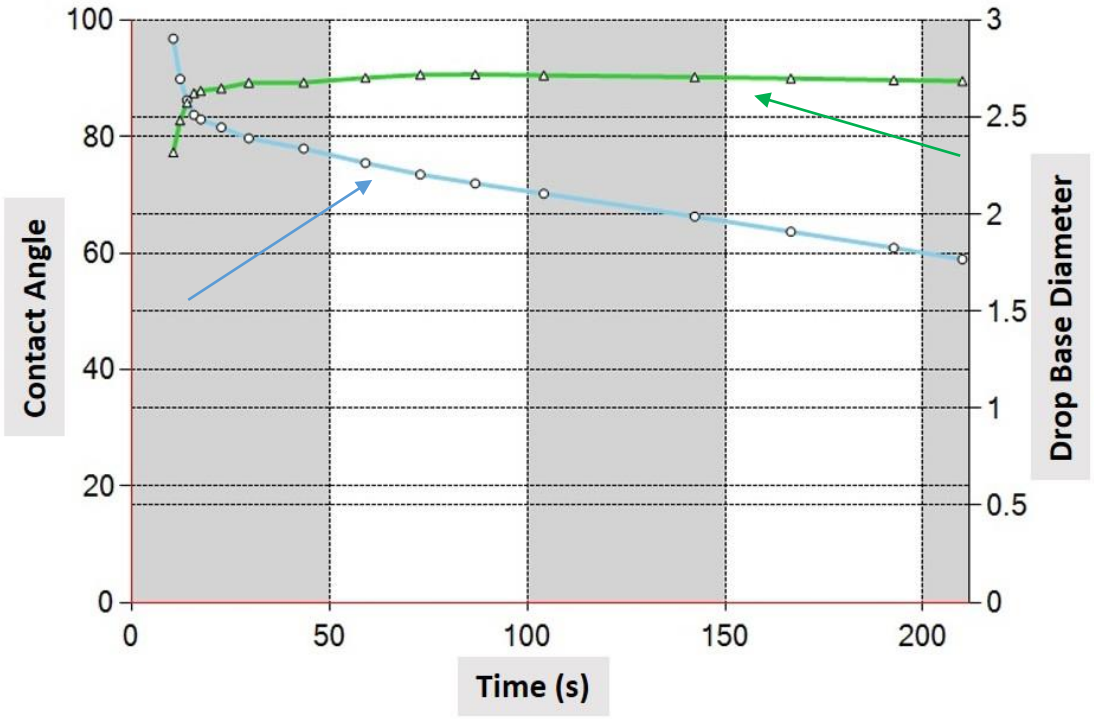
Contact Angle
Drop Base Diameter
Time (s)
0
20
40
60
80
100
0
0.5
1
1.5
2
2.5
3
0
50
100
150
200

(a)

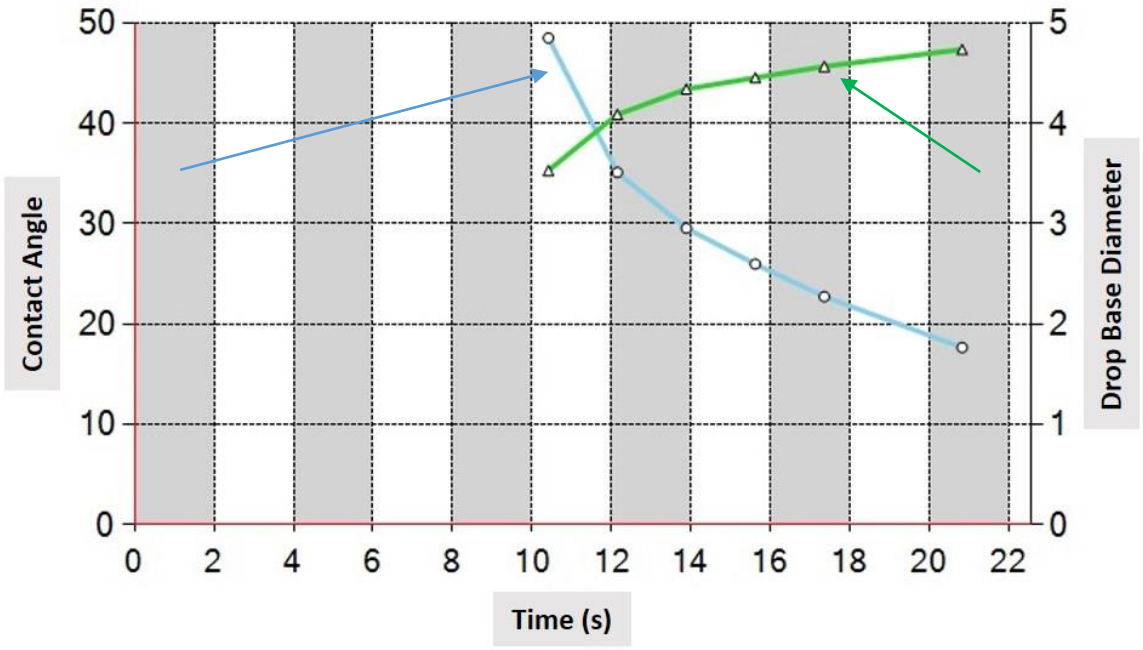
Contact Angle
Drop Base Diameter
Time (s)
0
10
20
30
40
50
0
1
2
3
4
5
0
2
4
6
8
10
12
14
16
18
20
22

(b)

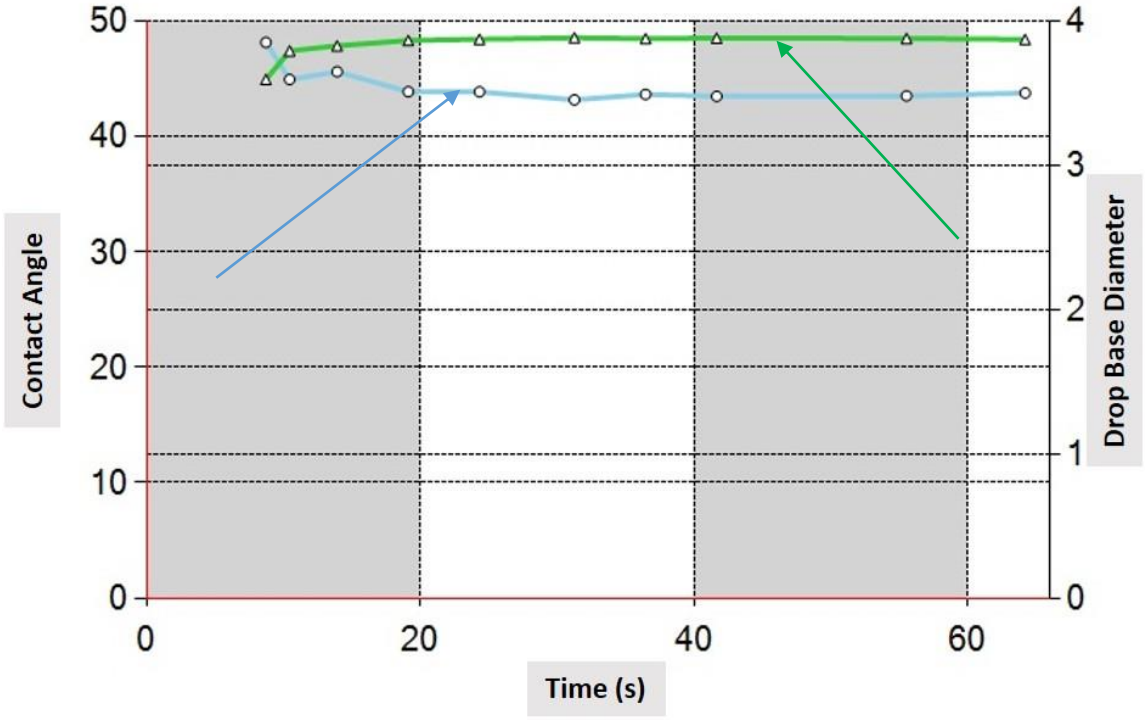

(c)

Figure 3.7: Contact angle and drop base diameter of water measured on Eagle Ford (a), Pierre (b) and Barnett (c) shale samples versus time.

3.3 Experimental Facilities and Procedure

3.3.1 Absolute Permeability Measurements (Single Phase)

For permeability measurements, two techniques of the steady and unsteady state were used. For shale samples with higher permeability (i.e. Eagle Ford) the steady state method was used while for shale rocks with lower permeability (Pierre and Barnett), the unsteady state technique was applied. The schematic diagrams of the experimental facilities for steady state and unsteady state methods are shown in Figure 3.8. It is noted that for both steady state and unsteady state techniques applied in this research, standard procedures were followed (RP40, 1998).

For hydrocarbon bearing rocks such as coal and shale, nitrogen and helium are commonly used and believed to have minimal effects on permeability measurements due to their adsorption properties (Cui et al., 2009). Nitrogen was used for all measurements in this research. The experiments were performed at a constant temperature of 60 °C inside the oven. The temperature fluctuation inside the oven was recorded for 24 hours,

which showed ± 0.1 ℃ variation. Prior to any experiment, a gas leakage test at high temperature was performed. The accuracy of the pressure transducers is ±0.015% FS and accurate Quizix pumps were used for displacement and applying the overburden pressure. It is believed that the stress equilibrium in such rocks is a slow viscoelastic dominated process. Thus adequate time is required to reach the equilibrium after each change. In this study, to reach the equilibrium, the permeability was measured 24 hours after changing the overburden pressure. The dead volumes of all lines and valves were measured based on the Boyle two cell method using nitrogen at low pressure. All fluid parameters, e.g. gas viscosity, were extracted from the NIST database (NIST, 2015).

In these measurements, pore pressures were designed in such a way to study rarefied flow when the Knudsen numbers were between 0.01 and 1. The apparent matrix permeability of all shale samples was measured at four different net stresses and five different pore pressures. Based on the calculated Knudson number, gas flow in these experiments were within the slip flow regime and a small part of the transition regime. It is noted that several researchers have theoretically studied the flow regimes in shale reservoirs including the free-molecule regimes (Darabi et al., 2012, Javadpour, 2009, Deng et al., 2014), however, recent experimental observations have shown that gas mostly encounters the slip and transition flow in shale/tight gas reservoirs (Sinha et al., 2013, Ghanizadeh et al., 2014b, Heller et al., 2014, Yves et al., 2015) and rarely experiences free-molecular flow.

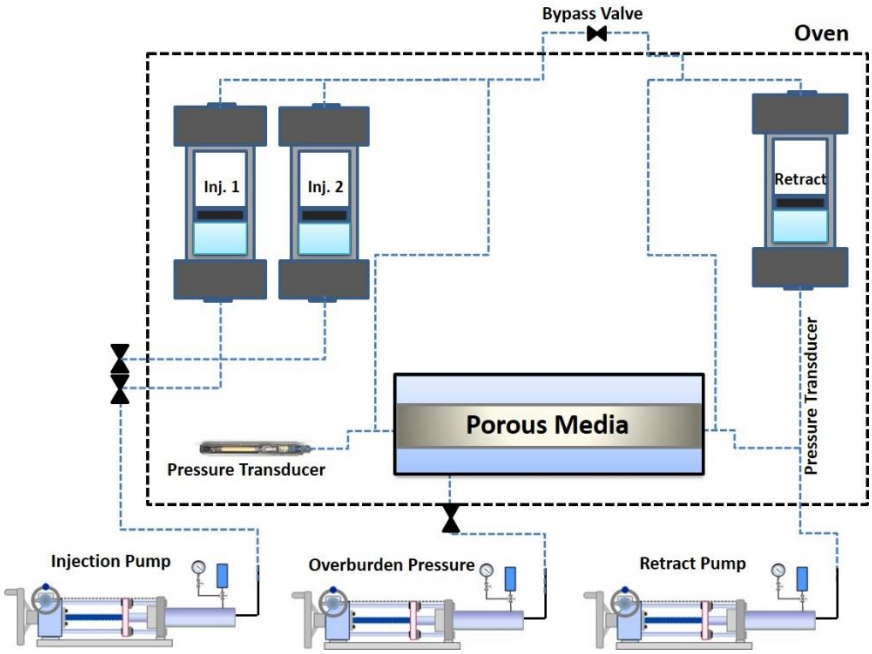

(a)

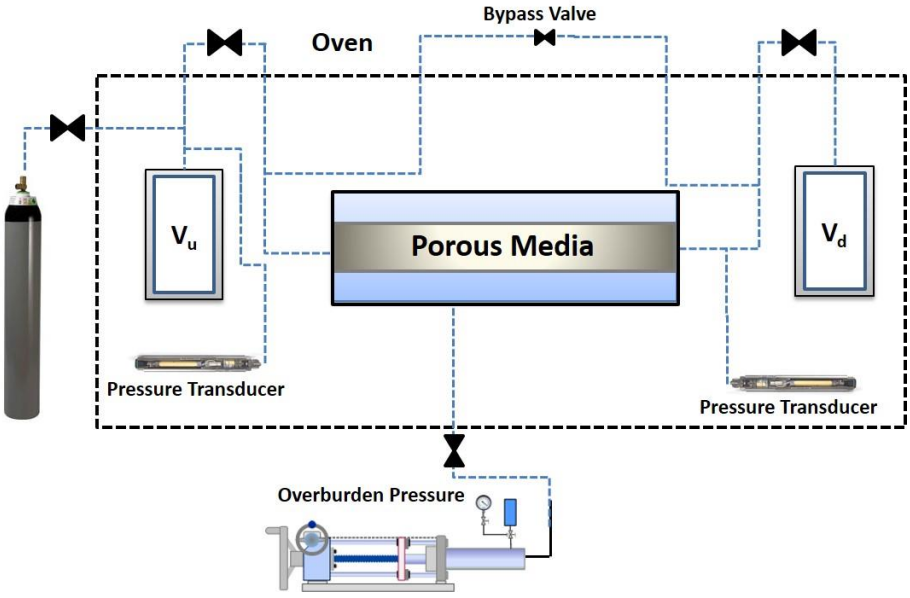

(b)

Figure 3.8: The schematic diagram of (a) steady state and (b) unsteady state pulse-decay setups used for the matrix permeability measurements in this study.

In this research, the analytical solution of the diffusivity equation for pulse-decay experiments was used to determine the rock permeability values (Dicker and Smits, 1988, Brace et al., 1968, Bourbie and Walls, 1982, Hsieh et al., 1981, Chen and Stagg, 1984, Jones, 1997). As recommended by Jones (Jones, 1997) an equal upstream and downstream reservoir volume was used to produce the desirable effects of maintaining a

constant mean pore pressure, which would ensure constant average fluid viscosity and compressibility. Darabi et al. (2012) have shown that the variations of μ and C_g with pressure across the core have a negligible effect on the solution of the unsteady state method (Darabi et al., 2012). In the unsteady-state experiments, the volumes of the upstream and downstream cells were equal to 40 cc. The pressure differences between two upstream and downstream cells at the beginning of the experiments were less than 10% of the average pressure.

In all permeability measurements, experiments were started from the highest pore pressure of 3000 Psi and completed at the lowest pore pressure of 250 Psi. The overburden pressure was also decreased step by step to obtain the desired net stress (difference in overburden and pore pressure). It is noted that as explained in Chapter 2, the effective stress coefficients is assumed to be unity for the shales under study, hence the term "effective stress" and "net stress" can be used interchangeably.

As the net stress effect is believed to be irreversible to a great extent, the experiments were started from the net stress of 500 and completed at the highest net stress (i.e 3000 psi) with two intermediate steps of 1000 and 2000 psi. This trend is also in agreement with what happens in reservoirs during their production life.

After these measurements, to evaluate the level of permeability hysteresis due to the net stress, the measurements were repeated starting from the highest net stress (3000 psi) and completed at the lowest net stress (500 psi).

3.3.2 Evaluation of the Facilities' Accuracy

As the permeability of the unconventional rocks are commonly below 0.1 mD, the permeability measurements are much more difficult compared to the permeability measurements of the conventional rocks. As mentioned, the unsteady state technique was used for the permeability measurements of the tighter shale samples, i.e. Pierre and Barnett. To evaluate the performance of the unsteady state setup, the reliability of the results was examined by performing both unsteady and steady state tests on an Eagle Ford rock sample. The results showed ± 2 % difference between steady state and unsteady state measurements. Although, this verification shows good agreement between steady and unsteady state techniques, but it is noted that this kind of evaluation can be performed only on the samples with higher permeability like Eagle Ford. For the tighter cores (e.g. Barnett), it is not practical to measure the permeability by the steady state technique. For this reason, the reliability of the unsteady state facilities was evaluated by using a standard

core. This standard core, which is a stainless steel cylinder with a single microchannel inside is shown in Figure 3.9. As seen, a solid glass is implemented into the centre of the core, which contains a long microchannel. For accurate measurement of the microchannel diameter, SEM images of the top and bottom of the standard core were taken. As shown in Figure 3.10, the average channel diameter is 3.15 μm. Using this value as the diameter of microchannel, the channel permeability is 310 mD and the whole core permeability is 2.13 nD.

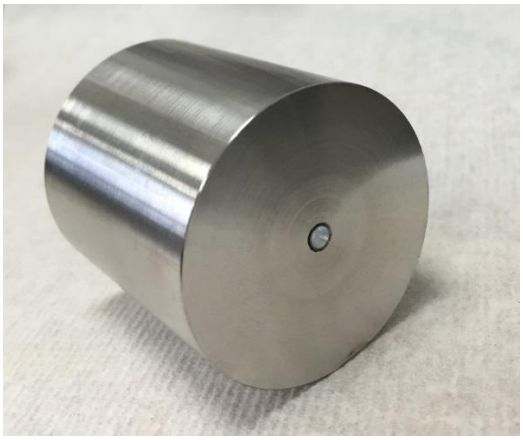

Figure 3.9: The standard core with a single microchannel used to evaluate the accuracy of the unsteady state setup.

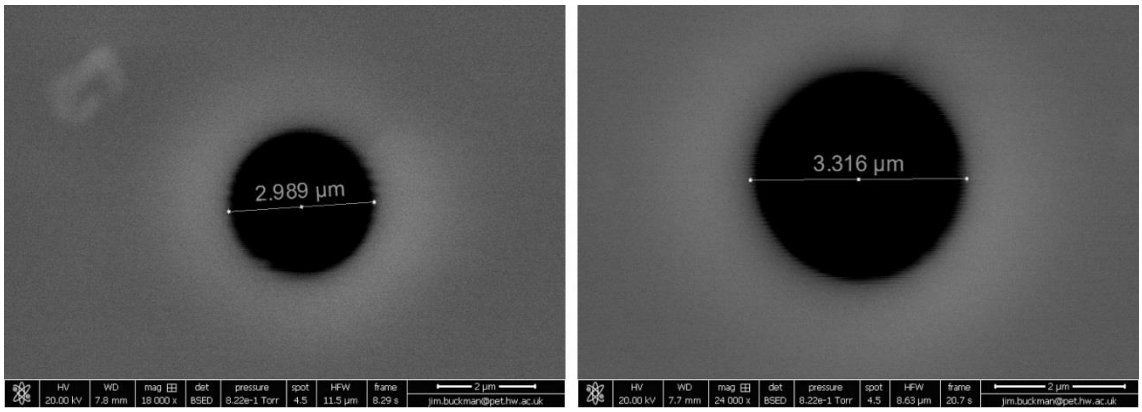

Figure 3.10: SEM images of the top and the bottom of the standard core used for the evaluation of permeability measurements facilities.

After analytical determination of the standard core permeability, it was loaded into the core holder in the unsteady state setup. The permeability measurements were repeated several times and the average value of 10.2 nD were obtained. Based on this result, the

error of the measurements was around 8 nD. It is noted that the lowest permeability measured in the study was 615 nD, which is much greater than the error of the facilities.

3.3.3 Effective permeability measurements (Two-phase)

Gas flow in shale matrix was also studied in the presence of irreducible liquid saturation to investigate the effects of gas slippage on shale matrix permeability, when the liquid phase exists in the system. In these measurements, a mixture of C4/N2 was used at the room temperature. To prepare the fluids, pure Nitrogen (N2) and Butane (C4) were mixed in the recombination cell and shaken for 24 hours to reach the equilibrium state. Then the liquid and gas phase were separated and collected in separate cells. All measurements were performed at the pressure of 1500 psi. Two shale samples from Eagle Ford (E2) and Pierre (P2) formations were used in this study. Basic properties of these shale samples are shown in Table 3.4. In these experiments, liquid saturations were calculated based on the material balance using an accurate HPHT sight glass. The accuracy of the sight glass which is shown in Figure 3.11 is 0.07 cc.

Table 3.4: Basic properties of the three shale rock samples used in this study

Shale Sample	**Length (cm)**	**Porosity (%)**	**Diameter (cm)**	**Abs. Permeability (μD)**	**Orientation wrt bedding**
Eagle Ford (E2)	5.08	13.1	3.8	20.8	Parallel to bedding
Pierre (P2)	5.1	31.7	3.78	6.5	Parallel to bedding

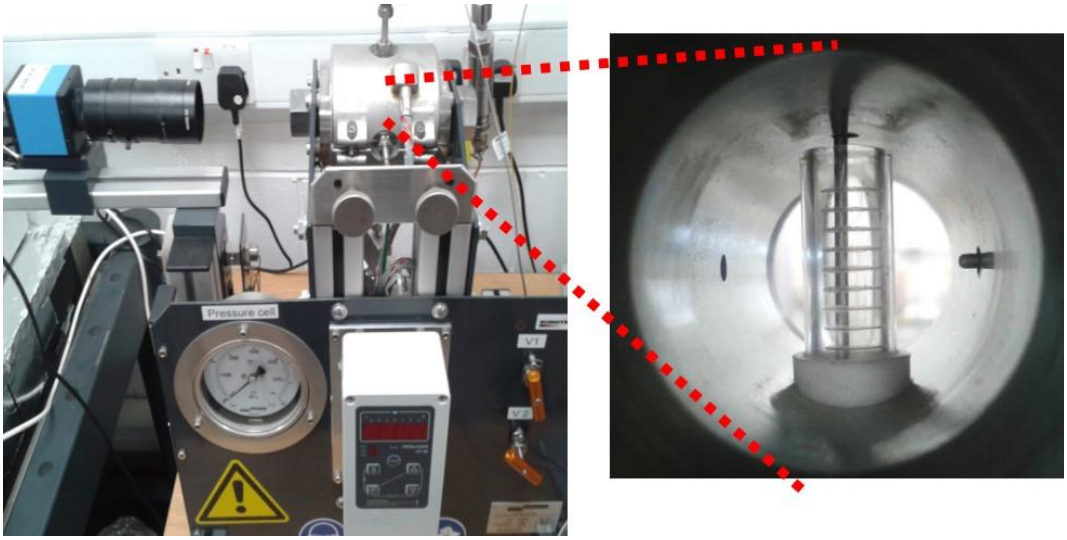

Figure 3.11: HPHT sight-glass equipped with a high-resolution camera and graduated test tube used for accurate measurement of produced fluids.

To reach the irreducible liquid saturation, the procedure was followed as below. First, equilibrated liquid butane was injected into the core, which was fully saturated with gas. After liquid breakthrough, several pore volumes of the liquid were injected. Then the liquid saturation of the sample was calculated. After that, equilibrated nitrogen was injected into the core to replace the liquid and reach the irreducible liquid saturation. Several pore volumes of the equilibrated nitrogen at different rate were injected until no liquid was produced. Finally, the irreducible liquid saturation was calculated based on the total liquid produced. After reaching the irreducible liquid saturation, the main experiment was started.

To study the gas flow in the presence of the liquid phase, the effective gas permeability of shale samples was measured at five different pore pressures of 1500, 1250, 1000, 750 and 500 psi. In all experiments, the net stress kept constant at 1000 psi. In other words, by changing the pore pressure, the overburden pressure was also modified to keep the net stress constant and equal to 1000 psi. For all measurements, the steady state technique was used.

3.4 Results and Discussion

3.4.1 Apparent Matrix Permeability (Single Phase)

In this section, the results of measured absolute permeability of shale samples are presented. Figure 3.12 shows apparent permeability versus pore pressures at different net stress for three cores of Eagle Ford (Figure 3.12a), Pierre (Figure 3.12b) and Barnett Shale (Figure 3.12c). The error of single phase permeability measurements was $\pm$ 3.2 % as calculated in Appendix 1. As shown in these figures, the apparent permeability is increased by a reduction of pore pressure. This enhancement is higher at the lower pore pressures which can be an indication that the gas slippage is more dominant, when the Knudsen number is high. The gas slippage is probably dominant in almost all cases, but to determine the slippage intensity, the non-slip permeability should be determined. From Figure 3.12, it can be also concluded that the apparent permeability decreases as the net stress increases. In fact, the flow conduit size (pore size) is decreased by increasing the net stress. However, the resultant permeability reduction is not the same for all shale samples. In addition, it is found that the strength of gas slippage is different at different net stress values.

Figure 3.13, includes the same data as those noted in Figure 3.12, but here the measured apparent permeabilities are plotted versus net stress. As shown in Figure 3.13, almost all core samples are sensitive to the net stress such that the permeability can be decreased up to 10 times from 500 to 3000 psi net stress. This significant stress sensitivity of shale permeability is probably observed due to the presence of microfracture inside the shale matrix. These microfractures, which have dominant contribution to flow, are more influenced by applied net stress compared to the other pore types (Kwon et al., 2004). However, it should be noted that the effect of stress on flow regime is not the same as its effect on matrix permeability.

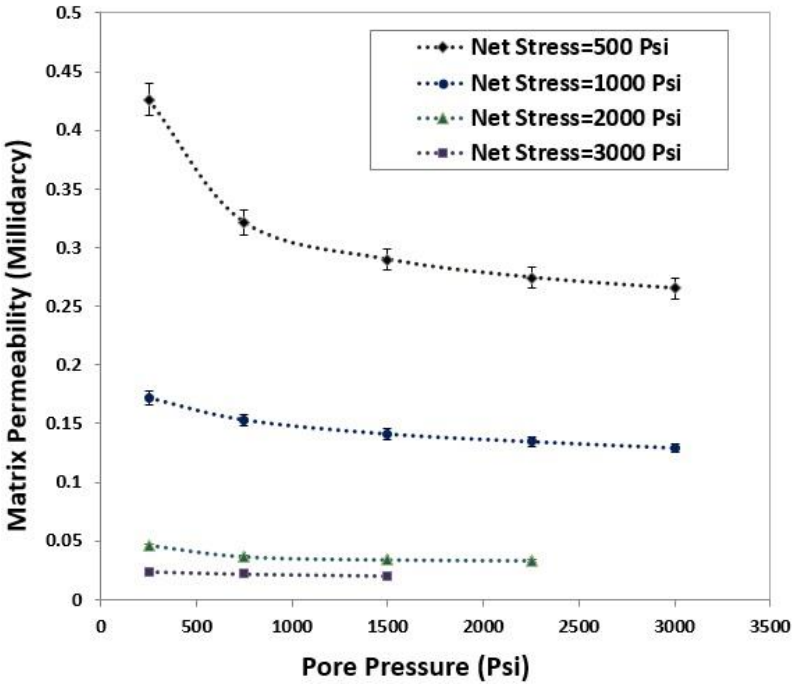
Net Stress=500 Psi
Net Stress=1000 Psi
Net Stress=2000 Psi
Net Stress=3000 Psi
Matrix Permeability (Millidarcy)
Pore Pressure (Psi)
0
0.05
0.1
0.15
0.2
0.25
0.3
0.35
0.4
0.45
0.5
0
500
1000
1500
2000
2500
3000
3500

(a)

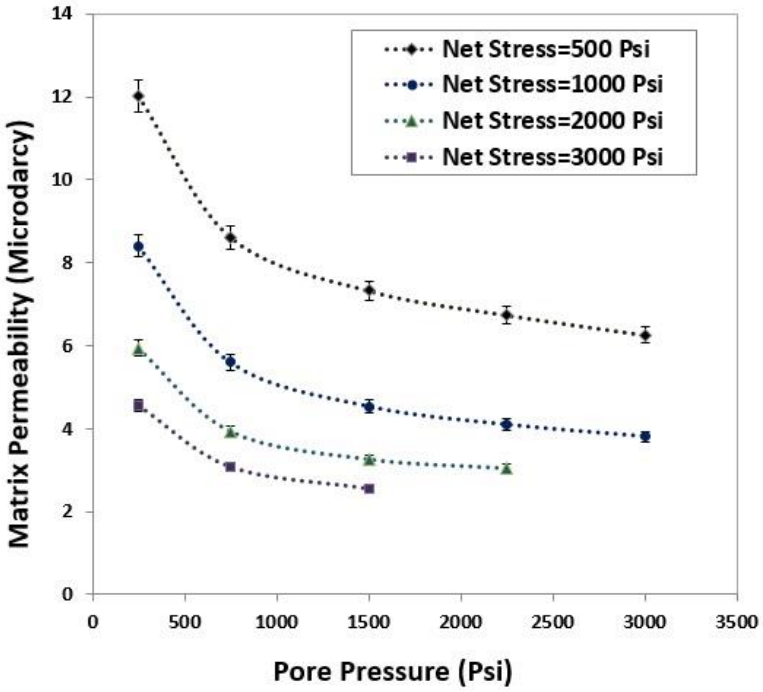
Net Stress=500 Psi
Net Stress=1000 Psi
Net Stress=2000 Psi
Net Stress=3000 Psi
Matrix Permeability (Microdarcy)
Pore Pressure (Psi)
0
2
4
6
8
10
12
14
0
500
1000
1500
2000
2500
3000
3500

(b)

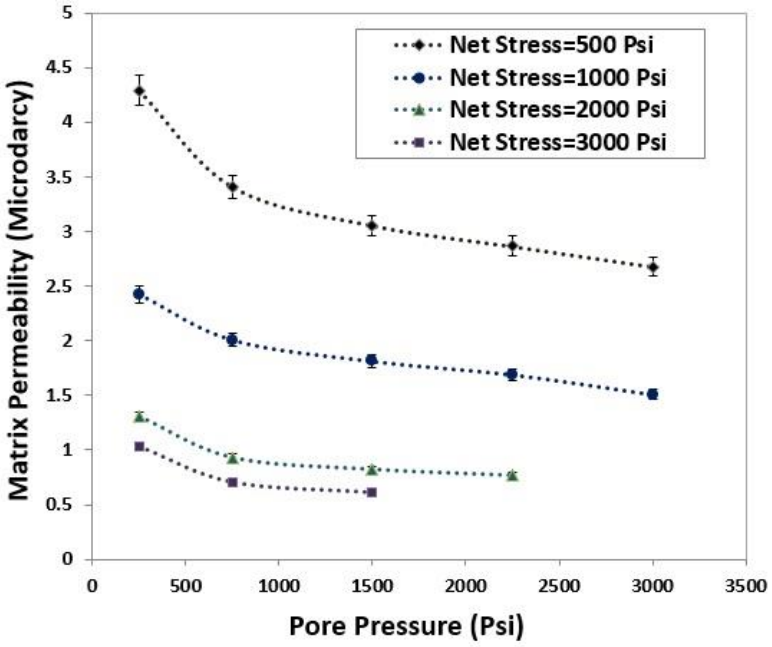

(c)

Figure 3.12: Measured apparent permeability versus pore pressure for (a) Eagle Ford, (b) Pierre and (c) Barnett shale cores at different net stresses.

It is noted that the geomechanical effect on permeability is not the same at all net stresses, i.e. the permeability reduction is more considerable at the lower net stresses. It means that the matrix permeability is more sensitive to the applied stress, when the pore pressure is close to the overburden pressure (early time of the production life). This sensitivity decreases gradually as the reservoir pore pressure decreases during the production period. In other words, as the pore pressure is reduced (higher Kn number) the slippage effect becomes more dominant and the geomechanical effects are less important. From Figure 3.13, it is also noted that the stress effects on the matrix permeability are not the same for all shale rocks, i.e. it is more for the shale sample with higher permeability. It is noted that the evaluation of the stress sensitivity of permeability with respect to the net stress is important as 1) the net stress changes during the production and hence the permeability changes; and 2) matrix permeability can change by depth as the effective stress changes. It is reported that, the permeability of shale samples, which are more sensitive to the effective stress show a steeper decline curve during the production compared to the less sensitive samples. Therefore, there is less risk associated with the less sensitive rocks if the reservoir is deep (Chalmers et al., 2012b).

Based on these results it can be concluded that during the production life of a reservoir, both (i) permeability reduction due to geomechanical effects and (ii) permeability enhancement due to gas slippage occur simultaneously in shale/tight gas reservoirs due to pore pressure reduction caused by gas production. As these two mechanisms play important roles, in a competitive manner, quantification of their effects on matrix permeability is required for the accurate prediction of matrix permeability. Thus to quantify the slippage effect, the reduction in average pore size due to the net stress alterations has to be considered as will be described in Chapter 4.

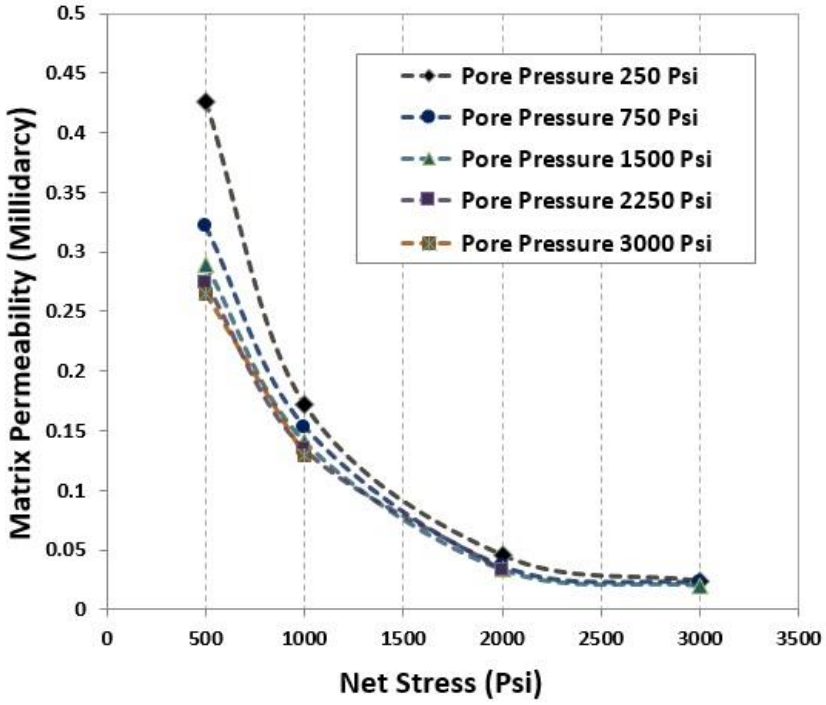

(a)

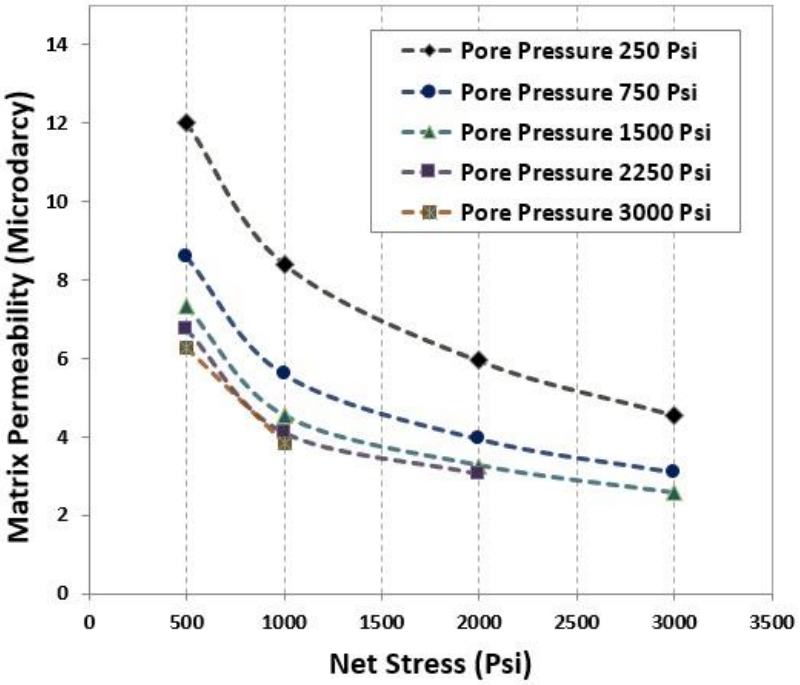

(b)

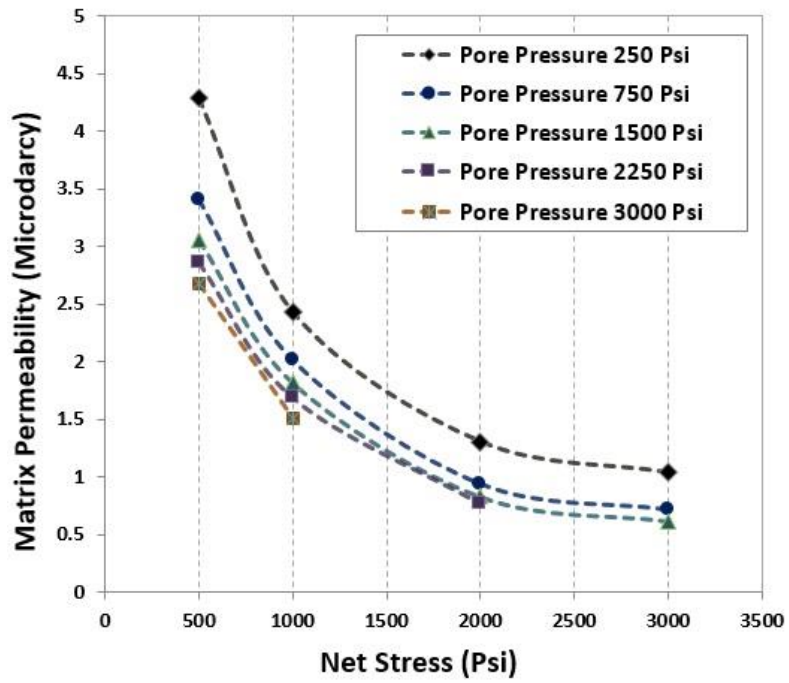

(c)

Figure 3.13: Measured apparent permeability versus net stress for (a) Eagle Ford, (b) Pierre and (c) Barnett shale cores at different pore pressures.

3.4.2 Non-slip Permeability Determination

Non-slip permeability is referred to the absolute permeability of rock, when the slippage effect is not dominant. Based on the Klinkenberg correction, this permeability is equal to the gas permeability at infinite gas pressure (Klinkenberg, 1941). In other words, the Klinkenberg correction, which is a first-order slip model, gives a non-slip permeability if the plot of measured permeability versus inverse pressure (1/P) is extrapolated linearly. In this study, non-slip permeability values were predicted using the measured permeability at the higher pressures (1500, 2250 and 3000 psi). The Klinkenberg correction method was used to find the permeability at infinite pressure (when $P \rightarrow \infty$ or $1/P \rightarrow 0$) by linear extrapolating the measured data. However, it will be shown in the next chapter that the measured values deviate from the Klinkenberg corrected straight line, particularly when the permeability of tighter cores were measured at the lower pressures. It means that the Klinkenberg correction can only be used, when the flow is in the slip regime and the non-slip permeability cannot be estimated by this model when the flow is in the transition regime. Therefore, in this study, the non-slip permeability for each core sample was obtained by extrapolation of the measured permeabilities at pressures higher than 1500 psi (i.e. experiments with Kn < 0.1 were used). It is evident that at higher pressures, the Knudsen number is low and the flow is in the slip regime. Therefore extrapolation of these measured values probably gives an accurate non-slip permeability.

From the data of Figure 3.14, corresponding to the net stress of 500 psi, the non-slip permeabilities are calculated as 0.240 md, 5.28 μd and 1.810 μd for Eagle ford, Pierre and Barnett shale rock samples, respectively. For the other net stresses, the non-slip permeabilities have also been calculated using the same procedure with results shown in Table 3.5 and Figure 3.15. As illustrated, the stress dependency of non-slip permeabilities follows an exponential relationship in the following form:

$$k_{non-slip} = k^0{}_{non-slip}[\exp(\alpha \times \Delta P)] \tag{3.3}$$

where $k^0{}_{non-slip}$ is the non-slip permeability at a reference net stress and α is a fitting parameter.

The exponential constants (α) of the best-fitted lines in this study are close to those reported in the literature for the similar measurements (Chalmers et al., 2012b, Zhang et al., 2015). For example, Zhang et al (2015) performed similar measurements for eight

shale samples and reported exponential constants from 0.05 to 0.12 MPa^{-1}, which is in the range of the values obtained here.

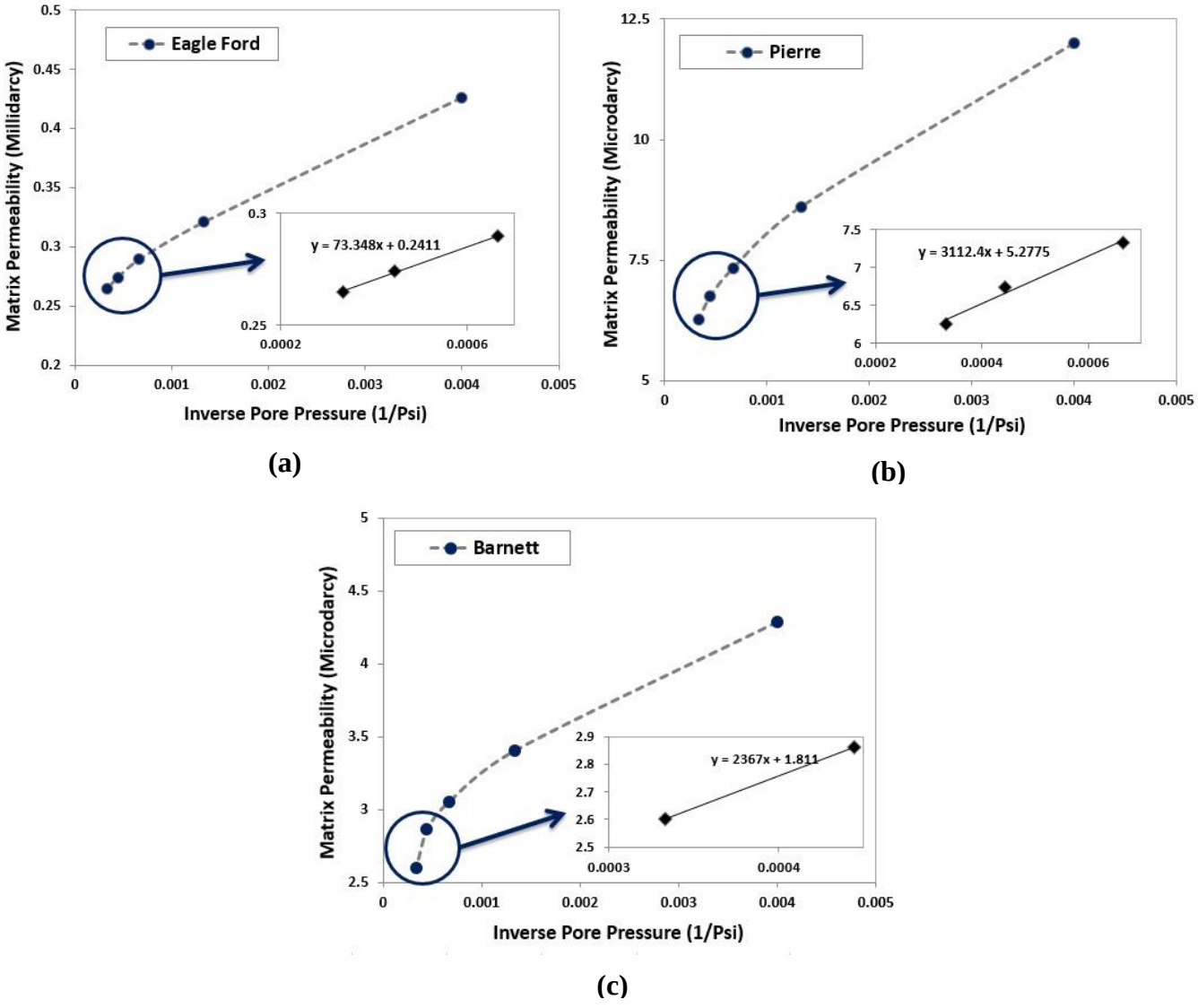

Figure 3.14: Measured permeability versus inverse pore pressure (a) Eagle Ford, (b) Pierre and (c) Barnett shale core plugs at the net stress of 500 psi. Measured permeability at high pressures (1500, 2250 and 3000 psi) are used for extrapolation to estimate non-slip permeability of each core plug; the lines connecting measured points are trend guides for the eye.

Table 3.5: The Klinkenberg corrected permeability (non-slip permeability) for three shale samples.

Net Stress (Psi)	**Non-slip Matrix Permeability (±3.2 %)**		
	Eagle Ford (mD)	**Pierre (μD)**	**Barnett (μD)**
500	0.24	5.3	1.81
1000	0.11	3	0.95
2000	0.03	2.1	0.45

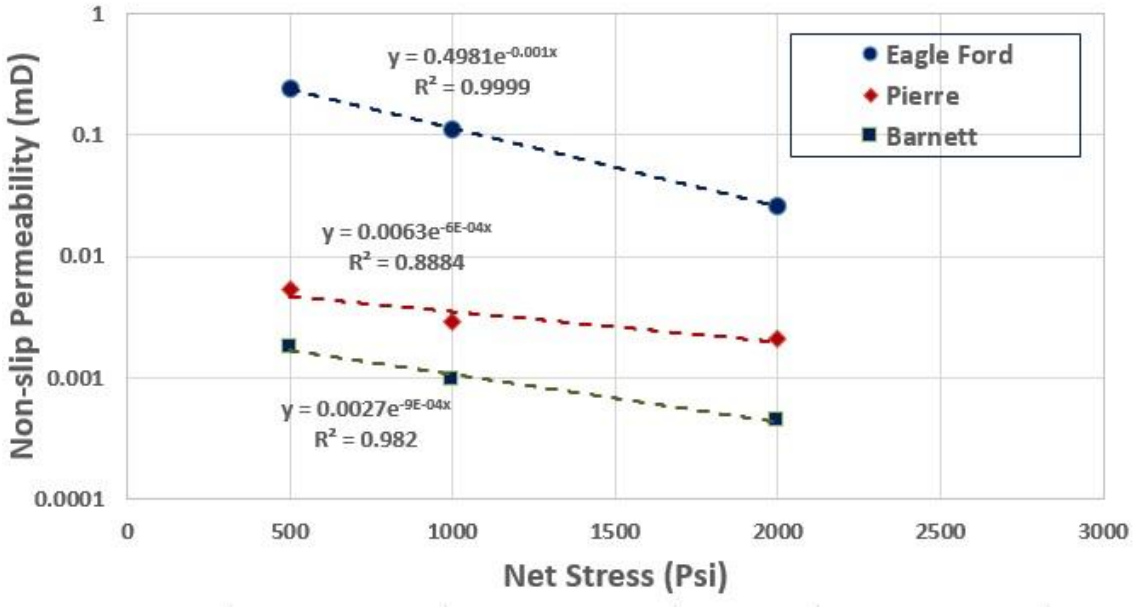

Figure 3.15: Non-slip permeability of three shale rock samples, calculated based on the Klinkenberg correction.

3.4.3 Stress-Induced Permeability Hysteresis

After single phase permeability measurements, the level of permeability hysteresis of the shale samples was evaluated. The results of apparent permeability measurements of Eagle Ford (E1) and Pierre (P1) shale at different net stress values are shown in Figure 3.16. These permeability measurements were started from the net stress of 500 psi and continued to the net stress of 3000 psi. Then the measurements were repeated while the net stress was decreased from 3000 psi to 500 psi.

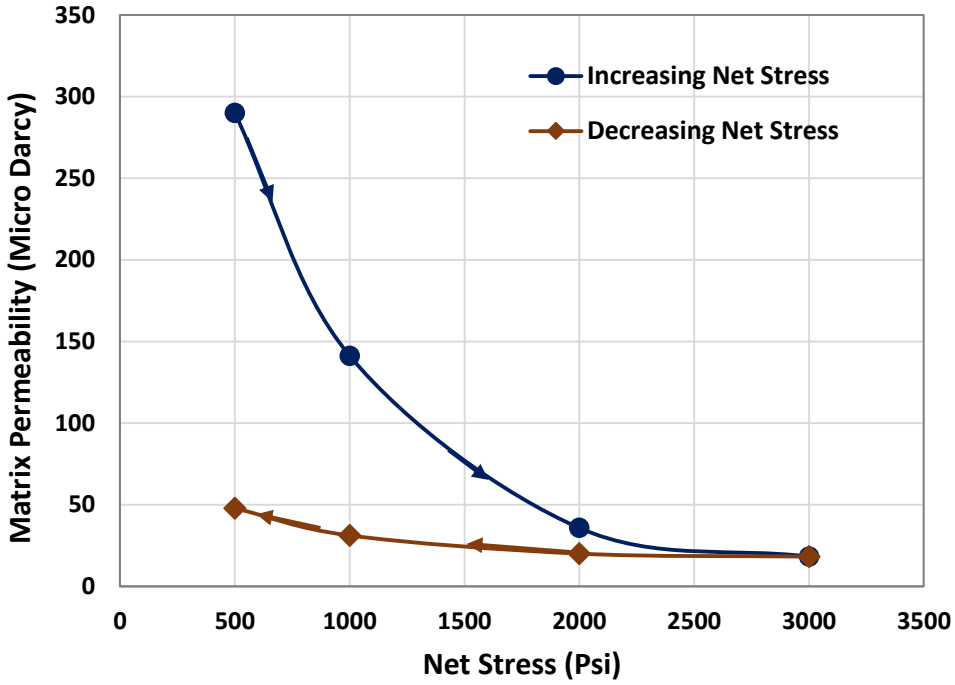

(a)

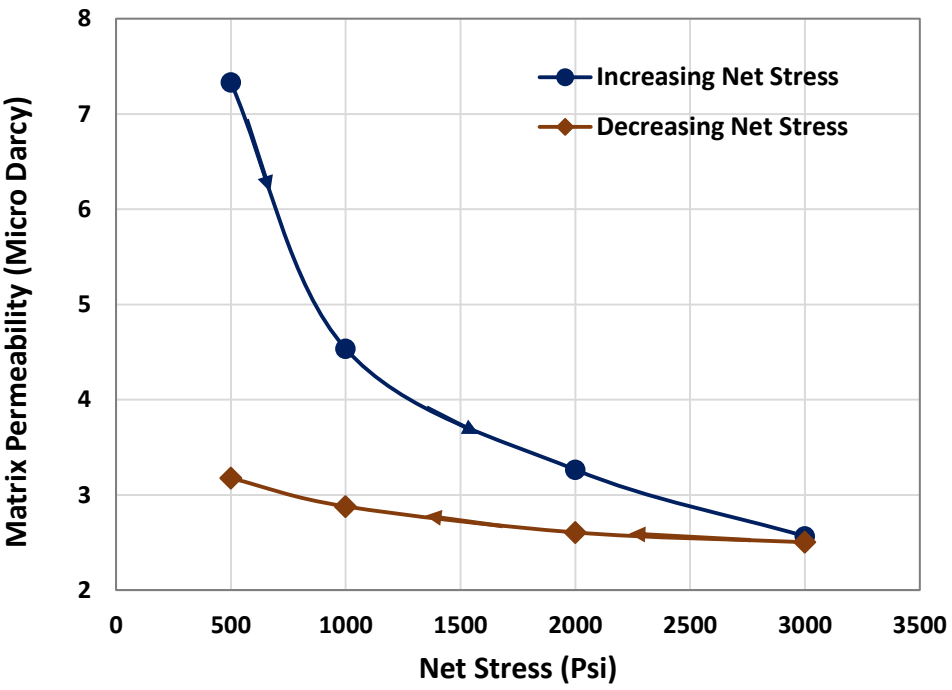

(b)

Figure 3.16: Stress-induced permeability hysteresis of Eagle Ford (a) and Pierre shale sample. All apparent permeabilities were measured at pore pressure of 1500 psi.

As seen in Figure 3.16, the measured matrix permeability was decreased by increasing the net stress to 3000 psi. The level of permeability reduction is much bigger for the Eagle Ford shale sample. For this rock, the permeability was decreased to 6 % of its original value, when the net stress increased to 3000 psi. For Pierre shale, the permeability reduction was less and it was reduced to 35% of its initial value, when the net stress increased to 3000 psi. This significant permeability reduction of Eagle Ford shale can be due to the presence of microfracture as shown in the SEM images of Eagle Ford shale sample (Figure 3.4). In addition, this stress sensitivity can be linked to the mineralogy of shale samples. Although, there is no explicit relation between rock mineralogy and the stress sensitivity, more stress sensitivity was observed for shale samples that exhibit a higher degree of anisotropy (Chalmers et al., 2012b). In addition, Chalmers et al. reported that samples with higher permeabilities (at a constant effective stress) are more likely to have a greater sensitivity to the changes in effective stress.

As mentioned, the matrix permeabilities were also measured again, when the net stress decreased to the initial value of 500 psi. As shown in Figure 3.16, the Eagle Ford and Pierre shale samples regained 16% and 43% of the original permeabilities when the net stress decreased again to 500 psi. As seen, the Eagle Ford and Pierre shale samples lost 84% and 57% of the original permeability. This significant hysteresis of Eagle Ford permeability can be assigned to the microfractures inside the rocks. These microfractures are extremely sensitive to the net stress and can be even closed permanently when the rock is exposed to a higher net stress. This permanent reduction of permeability and stress-induced permeability hysteresis have also been reported before (Lei et al., 2007).

The stress-induced permeability hysteresis of shale rocks should be considered when designing a production plan. Assuming such an irreversible permeability reduction, the well bottomhole pressure should not be decreased much below the initial reservoir pressure. In other words, an optimum value for drawdown pressure should be considered since the shale rock can be permanently damaged if a significant confining stress is applied to the reservoir layer due to the low pore pressure around the wellbore.

3.4.4 Effective Matrix Permeability (Two Phase)

In this section, the impact of liquid phase on the gas slippage is investigated. For this purpose, the effective permeability values of two shale samples were measured, when the liquid phase presents in the system. As mentioned before, two shale samples of Eagle

Ford (E2) and Pierre (P2) were used in this study. The residual liquid saturation of 0.57 and 0.44 were obtained for Eagle Ford and Pierre shale samples, respectively. It is noted that the maximum gas rate for displacing the liquid phase was 10 and 20 cc/hr for Eagle Ford and Pierre, respectively. In addition, for effective permeability measurements, the gas rate of 5 cc/hr was used. The results of effective permeability measurements at different pore pressures are shown in Figure 3.17. As illustrated, the effective gas permeability increases by decreasing the pore pressure. It is noted that, as the net stress was kept constant for all measurements (i.e. 1000 psi), the permeability enhancement is only due to the gas slippage. From these results, it can be concluded that the gas flow rate can be enhanced at lower pressures even in the presence of liquid phase, which occupies the pores. Using the Klinkenberg approach, the non-slip effective permeability were obtained as 12.1 μD and 1.9 μD for Eagle Ford and Pierre shale, respectively. Using these non-slip permeability, the permeability enhancement at different pressure can be obtained. The permeability enhancement factor is the ratio of measured apparent permeability (for a specified pressure) to the non-slip permeability of the rock. This factor gives the level of permeability enhancement due to the gas slippage for that specific pressure. Here, the permeability enhancement factor of P2 in presence of liquid can be compared with the permeability enhancement of P1 which was a dried Pierre shale (describe in section 3.4.1). For example, the permeability enhancement factor of P2 at 750 and 1500 psi were obtained as 1.62 and 1.28, respectively. For P1 (dried Pierre shale) these values were obtained as 1.90 and 1.54 for 750 and 1500 psi, respectively. Based on these results, it can be concluded that the impacts of gas slippage were decreased when the liquid phase presents in the rock matrix. It can be assumed that the liquid phase occupies a fraction of flow paths. In addition, as this shale rock type is strongly oil wet, it is clear that the liquid phase has a tendency to occupy the smaller pores and void spaces. These smaller pores and flow paths have probably more impact on the gas slippage (It is discussed in Chapter 5 with more details). Therefore, it can be assumed that the observed reduction in permeability enhancement can be due to the less contribution of smaller flow paths as some of them may be occupied by liquid phase.

In addition, using the non-slip permeability of E2 and P2 in Figure 3.17, the permeability enhancements for Pierre shale (P2) with 0.44 liquid saturation was bigger than those for Eagle Ford shale (E2) with the liquid saturation of 0.57. Although the permeability enhancements cannot be compared quantitatively, it shows that the gas slippage impact was increased as the liquid saturation was decreased. In other words, by

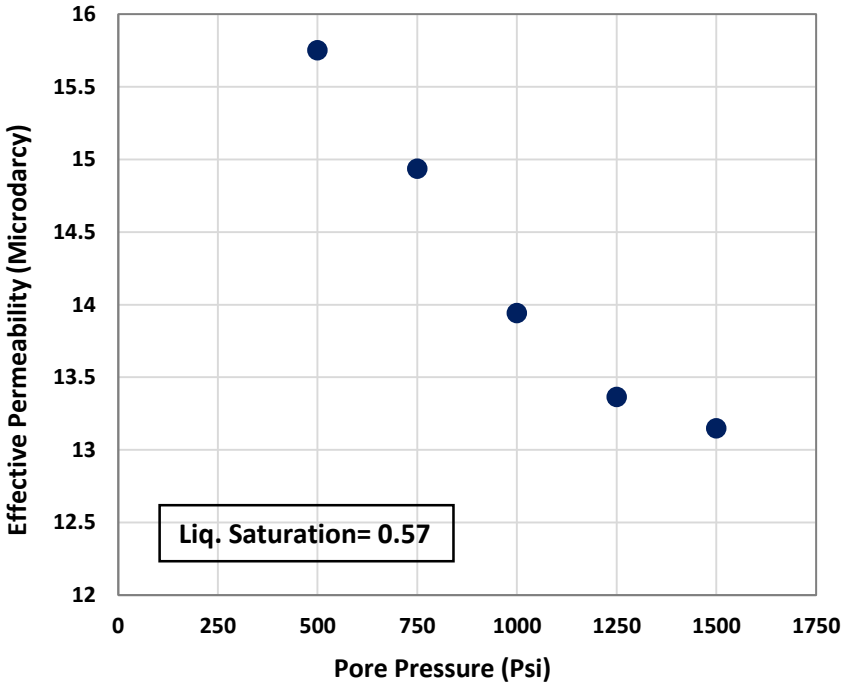

(a)

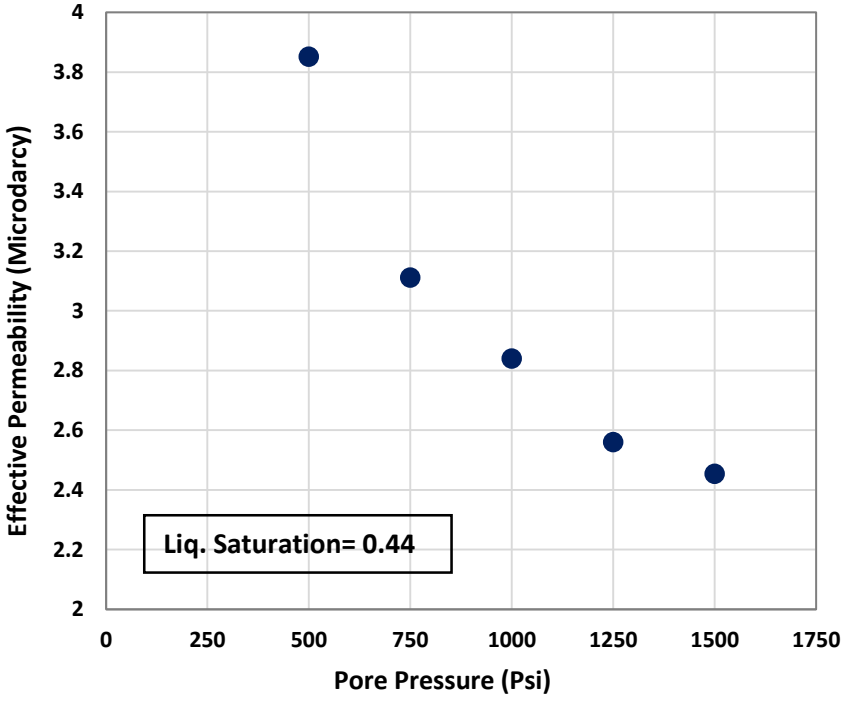

(b)

Figure 3.17: Effective matrix permeability of Eagle Ford (a) and Pierre (b) shale samples at different pore pressure and constant net stress of 1000 psi.

increasing the liquid saturation, the level of permeability enhancement decreases. This also can be linked to the contribution of smaller pores and flow paths in permeability enhancements. In other words, by increasing the liquid saturation, more fraction of smaller pores are occupied with liquid which results in less gas slippage and less permeability enhancement.

3.5 Summary and Conclusions

In this chapter, experimental results of the gas flow in the unconventional shale rocks were presented. The experiments were designed to study the fluid transport in the unconventional shale rocks and investigate some physical phenomena that happen in these reservoirs. The absolute and effective permeability of different shale samples were measured at various pore pressures and net stresses to investigate the effects of gas slippage and geomechanical stress on flow.

To obtain the rock characterization of shale samples, several tests including TOC and Helium porosimetry, XRD analysis, MICP test and SEM image analysis were performed. It was mentioned that the matrix permeabilities were measured using the steady state and unsteady techniques. The procedure of both techniques was also explained.

In the results section, the apparent permeability of gas at five different pore pressures and four net stress values were discussed. It was shown that at any given net stress, the matrix permeability is increased by a reduction of pore pressure. In addition, at any pore pressure, the matrix permeability is decreased as the net stress is increased. From the results, it was concluded that the shale matrix permeability was more sensitive to the applied stress, when the pore pressure was close to the overburden pressure. This sensitivity reduces gradually as the reservoir pore pressure declines.

Furthermore, the Klinkenberg correction was used to find the non-slip permeability at infinite pressure by extrapolating the trend of measured data at high pressures in the plot of apparent permeability versus the inverse of pressure. The obtained non-slip permeability data were used to obtain the level of the permeability enhancement.

It was shown that the stress dependency of non-slip permeabilities followed an exponential relationship. The power exponents of the best-fitted lines are in good agreement with those reported in the literature data. Also, the stress-induced permeability hysteresis of the Eagle Ford and Pierre shale samples was evaluated. It was shown that the permeability of Eagle Ford and Pierre shale sample can be lost up to 84% and 57% of

the original values respectively, when the net stress was increased to 3000 psi and then it was decreased back to the initial net stress value.

Moreover, the effects of liquid phase on gas slippage were investigated by measuring the effective gas permeability at different pressure when a liquid phase is present in the pores. For this purpose, the residual liquid saturation was established in the core and the effective permeabilities were measured. It was shown that the gas slippage plays an important role on gas flow even at two phase conditions. When the pore pressure was decreased, the permeability enhancement was observed for both Eagle Ford and Pierre shale samples with the residual liquid saturation of 0.57 and 0.44, respectively. In addition, the permeability enhancements of the P2 shale (with liquid phase) were compared with those values obtained for P1 shale (dried). It was concluded that the permeability enhancements were decreased when the liquid phase is present in the system. It was discussed that the liquid phase occupies the smaller pores and flow paths. Therefore this behaviour can be due to the less contribution of smaller flow paths as some of them may be occupied by liquid phase. Furthermore, it was shown that the level of enhancement was higher for the Pierre shale sample with the lower liquid saturation. It was concluded that by increasing the liquid saturation, more fraction of smaller pores are occupied with liquid. Therefore the gas slippage intensity is decreased as the liquid saturation is increased.

Chapter 4: Modelling of Flow Regimes and Stress Effects for Shale Matrix Permeability Prediction

4.1 Introduction

In this chapter, the measured permeability data at different pore pressures and net stresses were used to model the flow regimes and the stress effects on matrix permeability. As mentioned before, in unconventional rocks, the Darcy equation may not be valid and a suitable flow model is required for prediction of the flow behaviour (e.g gas flow rate). In addition, poroelasticity properties of shale matrix play an important role in fluid flow. Stress-dependent permeability is among these properties that have a great impact on flow. Considering these simultaneous physical behaviours, a fluid flow model suitable for different flow regimes is required. These models are much more complicated compared to the Darcy equation, which is traditionally used in the petroleum industry.

As an alternative, it is proposed to use an equivalent variable permeability factor. In other words, the Darcy equation can be used with an appropriate permeability factor, which gives the same flow rate. In this way, the gas slippage and the geomechanical effects are taken into account by changing the permeability factor in the Darcy equation with time. However, accurate prediction of this permeability factor for shale/tight gas reservoirs is still challenging due to the presence of several flow regimes in micro and nanoscale systems.

In this chapter, it is aimed to use experimental data and develop a reliable model for prediction of shale matrix permeability. The model should be able to predict the flow regime and gives an accurate permeability factor at different pore pressures. In addition, the poroelasticity properties of shale rocks should be taken into account on the prediction of matrix permeability. Moreover, the model should be easy to implement and simple enough for the industry to use in the reservoir simulators.

In the following, the solution of N-S equation is used to obtain an analytical model for non-Darcian flow to account the slippage effects. Then, the obtained analytical solution is used to determine the TMAC and slip coefficients from the experimental data. These slip coefficients can be used for shale matrix permeability prediction, while the flow regime is different from continuum flow. After that, the effects of stress is incorporated

into the model. Finally, the performance of the model is evaluated using the available experimental data in the literature.

4.2 Solution of N-S Equations with Slip Boundary Conditions

4.2.1 Slip Models in Literature

In the slip flow regime ($10^{-2} < Kn < 10^{-1}$), the prediction of Navier-Stokes equations with no slip boundary conditions fails due to the dominant role of the Knudsen layer (KL). The Knudsen layer is an area near the wall surface with an approximate thickness of ~O(λ) where the momentum diffusivity of the gas is significantly changed due to the presence of the solid boundary. In the Knudsen layer, the number of molecule/wall collisions will be more frequent than gas molecule/molecule collisions. However, in the slip regime, the Knudsen layer covers less than 20% of the characteristic length (assuming KL≤ 2λ). In this regime, the flow can be modelled by Navier–Stokes equations and rarefaction effects can be accounted through the wall velocity slip and temperature jump boundary conditions (Karniadakis et al., 2005). Figure 4.1 shows the Knudsen layer near the wall, which affects the solution of N-S equations. The slip velocity (u_s) is also depicted in this figure. The concept of slip velocity was first introduced by Navier (Zhang et al., 2012c). In his model, slip velocity is proportional to the shear rate of flow at the wall surface. As shown in Figure 4.1, macroscopic slip velocity (streamwise velocity at surface; u_s) can be calculated based on the following equation:

$$u_s = L_s \left(\frac{\partial u}{\partial n}\right)_{sur} \tag{4.1}$$

where u_s is the slip velocity (streamwise velocity at surface), u is the streamwise velocity, n is the coordinate normal to the wall and L_s is the slip length. It is assumed that the wall velocity is zero. It is noted that $\left(\frac{\partial u}{\partial n}\right)_{sur}$ is the derivative of streamwise velocity at surface.

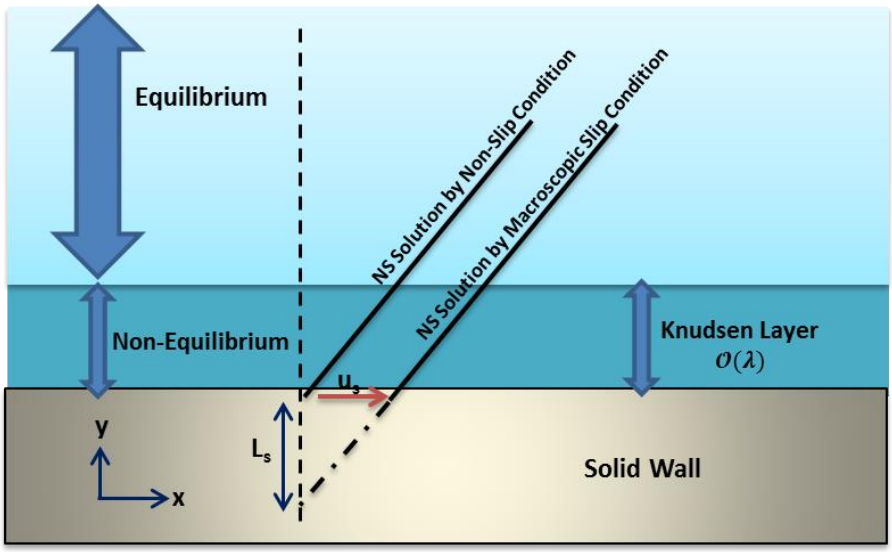

Figure 4.1: A schematic diagram of the Knudsen layer in gas flow near the solid wall; No-slip and macroscopic slip boundary conditions are used in Navier-Stokes equations to predict the velocity profile.

To develop a slip model, there are two different approaches for the gas-surface interaction: kinetic theory and surface adsorption theory. The surface adsorption based models are not considered here. In the kinetic theory, the gas-surface interaction forms a boundary condition between the gas molecules and the solid wall. This interaction can be governed by the typical models, such as the Maxwell model (elastic-diffuse) (Zhang et al., 2012c). Based on the Maxwell model, the first-order slip boundary condition can be written as follows (Here thermal creep effects have been neglected):

$$u_s - u_w = C_1 \lambda \left(\frac{\partial u}{\partial n}\right)_{sur} \tag{4.2}$$

where u_w and u_s are the wall and slip velocities, n is the coordinate normal to the wall and C_1 is the slip coefficient. The slip velocity coefficient is a function of tangential momentum accommodation coefficient (σ_v). The tangential momentum accommodation coefficient or TMAC is an empirical parameter which determines the type of reflection after molecule collision with wall surface. It will be discussed in more details later. The relation between slip coefficient and TMAC can be expressed as:

$$C_1 = \alpha_s \frac{2 - \sigma_v}{\sigma_v} \tag{4.3}$$

where α_s is a constant, which is unity in the Maxwell model. In this research, it is focused on Maxwellian models and hence α_s is assumed to be unity as well. Later, and based on the Maxwell's collision theory, second-order boundary conditions have been proposed and used by many researchers (Karniadakis et al., 2005, Barber and Emerson, 2006, Dongari et al., 2007). In a general form, it can be written as:

$$u_s - u_w = C_1\lambda \left(\frac{\partial u}{\partial n}\right)_{sur} + C_2\lambda^2 \left(\frac{\partial^2 u}{\partial n^2}\right)_{sur} \tag{4.4}$$

where C_1 and C_2 are the first and second order slip coefficients, respectively. Although the first order slip coefficient (C_1) is equal to $\frac{2-\sigma_v}{\sigma_v}$ in many published works, but there are different expressions proposed for the second order slip coefficient (Colin, 2001, Karniadakis et al., 2005, Jie et al., 2000, Roohi and Darbandi, 2009).

In 1999, Beskok and Karniadakis proposed a general slip model in order to circumvent the difficulties in computation of second derivatives of the tangential velocity ($\partial^2 u/\partial n^2$). In addition, their model gives a finite slip as the Knudsen number goes toward infinity. They proposed the dimensionless from of the model with respect to characteristic length and velocity scale (such as mean velocity) as follows:

$$U_s - U_w = \frac{2-\sigma_v}{\sigma_v}\left[\frac{Kn}{1 - b_{BK}\,Kn}\left(\frac{\partial u}{\partial n}\right)_{sur}\right] \tag{4.5}$$

where b_{BK} is a slip coefficient, U_s and U_w are dimensionless slip and wall velocities and Kn is the Knudsen number of the system. b_{BK} which is an empirical parameter can be determined either experimentally or from LBM or DSMC simulation data. They called this model "general model" as it depends on a slip coefficient b_{BK}. For $b_{BK} = 0$, the B-K model is a first-order slip and for $b_{BK} = -0.5$, the B-K model is a second-order (Beskok and Karniadakis, 1999).

In the following, the Maxwell (first order and second order) and Beskok and Karniadakis slip models are used as boundary conditions for flow in porous media to obtain the apparent slip permeability.

4.2.2 Dimensionless Permeability of Porous Media Based on N-S Equations

In the Maxwell slip flow model, Navier-Stokes equations are written for gas flow in a single pipe with slip boundary conditions. The obtained flow rate from this model can be

compared with non-slip flow rate (N-S equations) and an improvement (or enhancement) factor can be calculated. Then, the obtained improvement factor can be used to calculate the apparent permeability of the rock sample assuming the same flow pattern prevails in an idealised porous medium, which is represented as a bundle of capillary tubes. Considering (u_z , u_r) for flow in the pipe, Navier-Stokes equations for isothermal flow in the pipe with large aspect ratio ($L/D \gg 1$) gives

$$\rho \frac{Du_r}{Dt} = \rho g_r - \frac{\partial p}{\partial r} + \frac{\partial}{\partial z}\left[\mu\left(\frac{\partial u_r}{\partial z} + \frac{\partial u_z}{\partial r}\right)\right] + \frac{\partial}{\partial r}\left[\mu r\left(2\mu \frac{\partial u_r}{\partial r} + \zeta\, div\, V\right)\right] \tag{4.6}$$

where μ and ζ are first and second viscosity coefficients. In our experimental condition, the flow can be assumed incompressible. The density difference across the core in each experiment and the calculated Reynolds and Mach numbers are shown in Table 4.1. As shown, the flow can be assumed incompressible. In addition, Karniadakis et al. (2005) have shown that the relative importance of inertial terms in the momentum equations with respect to the diffusion term can be approximated as (Karniadakis et al., 2005):

$$\frac{\rho u \frac{\partial u}{\partial x}}{\mu \frac{\partial^2 u}{\partial y^2}} \approx \frac{\rho u h}{\mu}\left(\frac{h}{L}\right) = Re\left(\frac{h}{L}\right) \tag{4.7}$$

where h is the channel height and L is the length of the channel. Considering the calculated values of Re numbers, the inertial term is negligible in comparison to the diffusion term.

Table 4.1: Calculated density difference, Re and Ma numbers of all experiment pressures performed on Eagle Ford shale.

Ave. Pore Pressure	**Density Difference (%)**	$\boldsymbol{Re = \frac{\rho_{ave} u_{int} d_p}{\mu}}$	$\boldsymbol{Ma = Kn\, Re\sqrt{\frac{\gamma\pi}{2}}}$
250	0.0042	8.71E-7	1.52E-7
750	0.0121	2.52E-6	1.51E-7
1500	0.0119	4.74E-6	1.48E-7
2250	0.0118	6.57E-6	1.45E-7
3000	0.0116	8.00E-6	1.41E-7

Thus assuming steady, incompressible flow and ignoring the gravity effect, the N-S equations can be solved using the following slip boundary conditions:

$$\left(\frac{\partial u_z}{\partial r}\right)_{r=0} = 0 \tag{4.8}$$

$$u_{z\,r=R} = (\alpha_s \frac{2-\sigma_v}{\sigma_v})\lambda \left(\frac{\partial u_z}{\partial r}\right)_{sur} = C_1 \lambda \left(\frac{\partial u_z}{\partial r}\right)_{sur} \tag{4.9}$$

where $\alpha_s = 1$ in the Maxwell model. After some mathematical manipulations, the following analytical solution can be obtained for the velocity profile (See Appendix 2 for derivation):

$$u_z(r) = \left(\frac{R^2}{4\mu}\frac{dp}{dx}\right)\left[\frac{r^2}{R^2} - 1 + 2C_1 Kn\right] \tag{4.10}$$

where R is the pipe radius and Kn is the Knudsen number. The flow rate in a pipe (Q_p) can be obtained by the following integration:

$$Q_p = \int_0^R u_z(r)\, 2\pi r dr \tag{4.11}$$

which gives:

$$Q_p = \left(-\frac{\pi R^4}{8\mu}\frac{dp}{dx}\right)[1 + 4C_1 Kn] \tag{4.12}$$

Assuming flow in a bundle of capillary tubes (N numbers of capillaries), it gives:

$$Q_{Np} = \left(-\frac{N\pi R^4}{8\mu}\frac{dp}{dx}\right)[1 + 4C_1 Kn] \tag{4.13}$$

where $\frac{\pi R^4}{8} = k_{pipe}A_{pipe}$ for a pipe. Then the parameters of the bundle of capillary tubes can be replaced with core parameters. Using the porosity as $\varphi = \frac{NA_{pipe}}{A_{core}}$ and Darcy velocity as $v_{Darcy} = \varphi\, v_{Actual}$, it can be written $k_{core}A_{core} = Nk_{pipe}A_{pipe}$ which gives:

$$Q_{slip} = \left(-\frac{k_{core}A_{core}}{\mu}\frac{dp}{dx}\right)[1 + 4C_1 Kn] \tag{4.14}$$

where $Q_{slip}$is the slip flow rate in a core and N in the number of capillary tubes. Then the Darcy equation can be incorporated into the solution to generalize the equation for fluid flow in pours media. Using Darcy equation, the apparent permeability can be obtained as follows:

$$k_{app} = k_{non-slip}[1 + 4C_1Kn] \tag{4.15}$$

In addition, the solution can be written in dimensionless form to cancel the effects of rock parameters on gas slippage. The permeability improvement factor can be written in a dimensionless form as:

$$k_D = 1 + 4C_1Kn \tag{4.16}$$

where k_D is the dimensionless permeability factor, which is a ratio of slip (apparent) permeability to the non-slip permeability of matrix. It should be noted that, in the above equation, the term $k_{non-slip}$ is measured for a core and k_{app} is also estimated for that rock, which has the same tortuosity and heterogeneity as those in the non-slip flow. Hence there is no need to correct the above equation for rock tortuosity and heterogeneity as the term $k_{non-slip}$ is also measured for the same rock. The obtained equation is used to determine the slip coefficient and TMAC in porous media from the measured k_D.
Similarly, the cylindrical form of the second-order slip model (Equation 4.4) is:

$$u_{z_{r=R}} = \left[C_1\lambda\left(\frac{\partial u_r}{\partial r}\right)_s - C_2\lambda^2\left(\frac{1}{r}\frac{\partial}{\partial r}\left(r\frac{\partial u_z}{\partial r}\right)\right)_{sur}\right] \tag{4.17}$$

Using the same derivation as described above for porous media, the following analytical solution for dimensionless permeability can be obtained:

$$k_D = 1 + 4C_1Kn - 8C_2Kn^2 \tag{4.18}$$

Furthermore, if the general Beskok and Karniadakis (B-K) model is used as the boundary condition, the following equation can be obtained for dimensionless permeability of a steady, and incompressible flow (ignoring the gravity effect):

$$k_D = 1 + 4\left(\frac{2-\sigma_v}{\sigma_v}\right)\frac{Kn}{1 - b_{BK}\,Kn} \tag{4.19}$$

where b_{BK} is general slip coefficient in B-K model.

4.3 Determination of Slip Coefficients from the Experimental Data

As shown in the previous section, the solution of N-S equation with slip boundary conditions can be used to predict the apparent matrix permeability based on the non-slip matrix permeability and the Knudsen number of the system. However, in all models (first order, second order and BK model), slip coefficients are required and needs to be determined. As mentioned in Chapter 2, almost all available slip coefficients in the literature were obtained from gas flow at low pressure in non-porous materials. Hence, to have an accurate prediction for matrix permeability (based on the solution of N-S equation) slip coefficients (C_1, C_2 and b_{BK}) should be determined at high pressure from the gas flow in porous media. In this section, it is aimed to obtain appropriate slip coefficients from the measured apparent permeability presented in Chapter 3. To the best of the author's knowledge, this is the first time that slip coefficients and TMAC are measured for porous media at high pressure.

For this purpose, the dimensionless permeability factors, which is a ratio of apparent permeability to non-slip permeability, were calculated for each single measurement (The measured apparent permeabilities are shown in Figure 3.12 and the calculated non-slip permeability values are reported in Table 3.5). In addition, for each measurement, the Knudsen number of the system was calculated based on the experimental conditions. Then the experimental values of k_D and the corresponding Knudsen numbers were used to determine the slip coefficients and TMAC. The obtained slip coefficients and TMAC are used in the proposed shale permeability prediction model (developed in the second part of this Chapter) and LBM numerical simulations (Chapter 5).

It is noted that, as mentioned before, the dimensionless number of Knudsen number is used for determination of flow regimes. Therefore, the Knudsen number of each experiment should be calculated to estimate the dominant flow regime. To this aim, the mean free path (λ) and a representative characteristic size (D) should be known. It was explained in Chapter 3 that, the average pore size distribution of each rock sample was assumed as a representative characteristic length. It should be noted that, the pore size distribution of a porous media can include a wide range of pore sizes. But here, only a value is required as a representative length for porous media. Therefore the obtained average pore sizes (Chapter 3) is used as characteristic length of rocks under study. However, for mean free path, fluid properties at the experimental condition is required.

In other words, the mean free path of gas molecules is a function of gas pressure. Therefore, for each test, the mean free path should be calculated using the fluid properties at that pressure. Conventionally, the gas mean free path (λ) is calculated based on the following equation (Javadpour et al., 2007):

$$\lambda = \frac{k_B T}{\sqrt{2}\,\pi\sigma^2 P} \tag{4.20}$$

where k_B is the Boltzmann constant (1.3805×10^{-23} J/K), T is the absolute temperature, P is the gas pressure, σ is the collision diameter of gas molecules. Collision diameter can also be estimated from gas viscosity using the following equation (Hildebrand, 1976):

$$\sigma^2 = \frac{2\sqrt{m k_B T}}{3\,\pi^{3/2}\mu} \tag{4.21}$$

where m is the molecule mass and μ is the gas viscosity. All fluid parameters, e.g. gas viscosity, were extracted from the NIST data base (NIST, 2015).

As mentioned, the dimensionless permeability in each experiment was calculated from the measured apparent permeability and the obtained non-slip permeability. In Figure 4.2, the obtained dimensionless permeability factor (k_D) is plotted versus Knudsen number (which is also a dimensionless parameter) for all measurements performed on three shale samples. As shown in this Figure, the experiments cover the entire range of slip flow regime and a small part of the transition flow. The measured k_D values, which are improvement factors, are approximately close to each other for the data points with the same Knudsen number. In other words, the improvement factors (due to gas slippage) are approximately the same for the experiments with the same Kn number. These demonstrate that the improvement factor is a function of the Knudsen number only and independent of the rock type. This kind of non-dimensional plot allows us to obtain the slip coefficients and TMAC regardless of porous media parameters such as porosity, length etc. The corresponding data shown in Figure 4.2 , which is called "general slip plot" in this thesis, is also presented in Table 4.2. The propagation of errors for calculation of Kn and K_D were also reported in this table (see Appendix 1).

As shown in Figure 4.2 the dimensionless permeability data are more scattered when Kn > 0.1. In other words, for transitional regime, more scattered data were obtained. The main reason of this behaviour can be the error of measurements as the experiments are more subject to error when the flow is in this region. In fact, the flow regimes is in

transitional when the matrix permeability of tighter rocks (e.g. Barnett) was measured at lower pressure (e.g. 500 psi). It is evident that the experimental measurements are more difficult and subject to error when the rock sample has lower permeability.

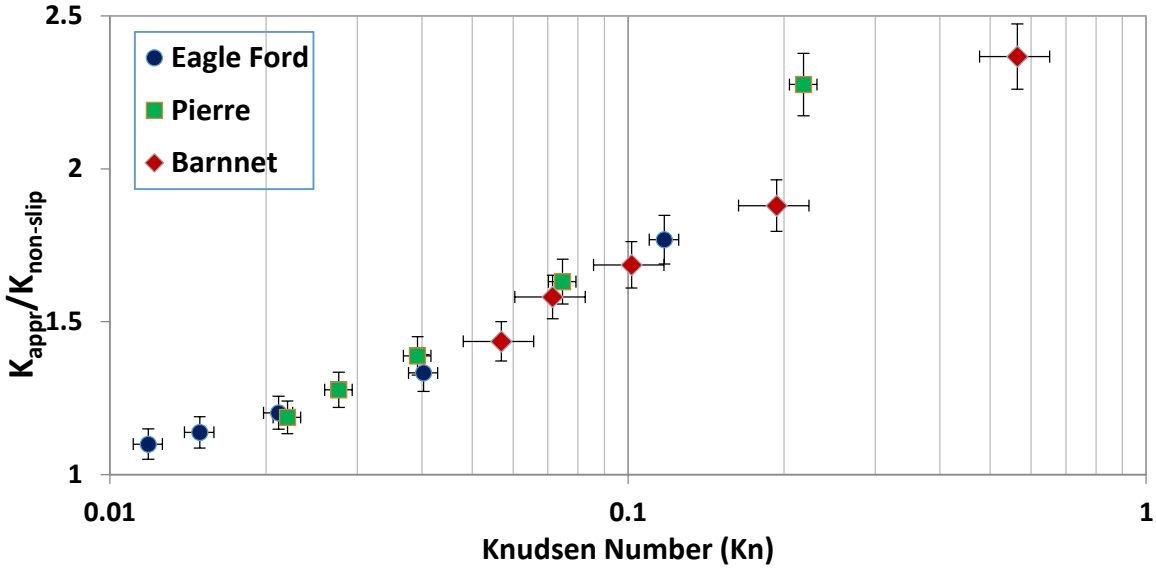

Figure 4.2: Dimensionless permeability versus Knudsen number for three shale plugs.

Table 4.2: The dimensionless permeability (KD) and Knudsen number (Kn) of each measurement for three shale samples.

Eagle Ford		**Pierre**		**Barnett**	
Kn($\pm$6.5%)	**K_D ($\pm$4.5%)**	**Kn($\pm$6.1%)**	**K_D ($\pm$4.5%)**	**Kn($\pm$15.5%)**	**K_D ($\pm$4.5%)**
0.12	1.8	0.22	2.3	0.56	2.4
0.04	1.3	0.07	1.6	0.12	1.9
0.02	1.2	0.04	1.4	0.10	1.7
0.015	1.1	0.03	1.3	0.07	1.6
0.012	1.1	0.02	1.2	0.06	1.4

To obtain the first-order slip coefficient, the dimensionless permeability data are scaled based on Equation 4.16. In Figure 4.3, the data in the slip flow region are used to fit a line by the least square method (linear regression). The first order slip coefficient is determined as $C_1 = 2.10$.

As shown in this figure, the experimental data are approximately predicted by the first-order slip model for Kn<0.07 (blue squares). For the Knudsen number higher than 0.1 (red circles), the experimental data deviate from the first-order linear model. This behaviour is in good agreement with Beskok and Karniadakis findings for the breakdown of slip flow theory based on the first-order slip boundary conditions (Beskok and Karniadakis, 1999). They have shown this deviation from Kn=0.1 using the DSMC and LBE simulation results. Considering this discussion, a higher order slip model should be used to predict the flow behaviour specifically, when Kn>0.1. This observation highlights that the Klinkenberg model, which is a first-order slip model, cannot be used to predict the non-slip permeability, if the flow is in the transition regime. Considering the gas flow in the unconventional reservoir rocks can be in the transition regime, an appropriate model is required which can give more acceptable results for both slip and transition regimes. This can be done using higher order slip models. In other words, higher order slip model can predict accurate behaviour for the flow in the slip regime and also can give acceptable results for flow in the transition region. However, extension of the slip models to be appropriate for transition regime needs more experimental/simulation data performed in this region. It will be explained in the Chapter 5 that the LBM was used to simulate the gas flow in the transition flow regime. The results of such simulations can be used to extend the slip models to be applicable for both slip and transition regimes.

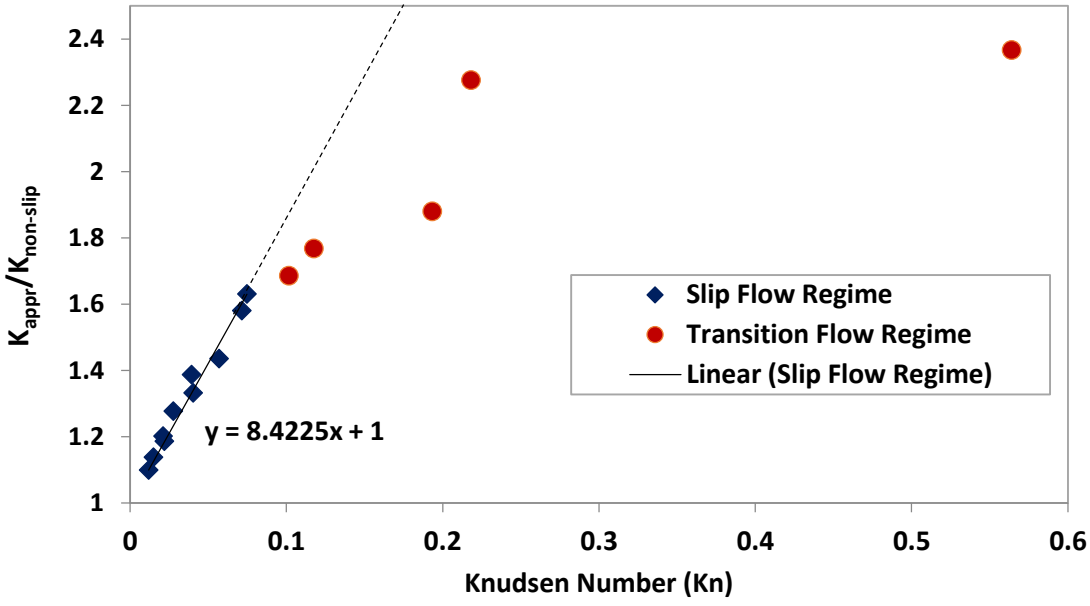

Figure 4.3: Dimensionless permeability versus Knudsen number for three shale rock samples; measured permeabilities enhancement in the slip flow regime are used to find the slip coefficient of the first-order model.

Considering the above discussion, the second-order slip model is used to develop the permeability model for the shale rocks. To obtain the first-order slip (C_1) and second-order slip (C_2) coefficients of the second-order slip model (Equation 4.18), experimental results of the general slip plot were used. Figure 4.4 shows the dimensionless permeability and the best fitted line based on the least squared method. Form equation 4.19, C_1 and C_2 are obtained as 2.390 and 2.392, respectively. In addition, from the obtained slip coefficient, TMAC is also calculated as 0.6. As mentioned before, the first-order slip coefficient (C_1) is equal to $\frac{2-\sigma_v}{\sigma_v}$ in many published works, but there are different reported expressions for the second-order slip coefficient such as $\frac{2-\sigma_v}{\sigma_v}$ (Karniadakis and Beskok, 2002, Roohi and Darbandi, 2009) , $\frac{2-\sigma_v}{\sigma_v}\frac{Re}{Kn}$ (Jie et al., 2000) or 9/8 (Colin, 2001). In this study, we have obtained the same value for both first order and second order slip coefficients ($\sim$ 2.39). This suggests that the expression relating second order coefficient (C_2) to TMAC can be the same as that relating the first order one to TMAC as reported by Karniadakis and Beskok (2002) and Roohi and Darabi (2009) (Karniadakis and Beskok, 2002, Roohi and Darbandi, 2009). It should be noted that, the experimental data in the slip region were used to obtain the slip coefficients. As mentioned before, the slip boundary condition models have been developed to be used in the N-S equation when the flow is in the slip regime. Therefore, the predicted permeability values may not be accurate when the flow is in the transition regime.

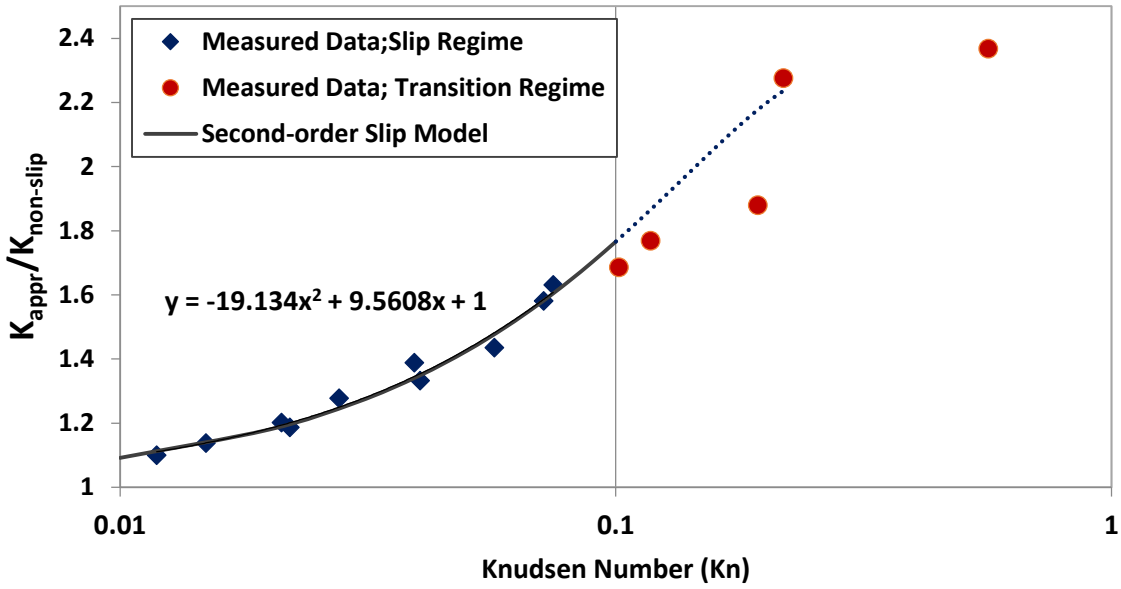

Figure 4.4: Dimensionless permeability versus Knudsen number for three shale rock samples; measured permeabilities in the slip flow regime used to find the slip coefficients of the second-order BK model.

As mentioned earlier, there is no reported document for experimentally measured slip coefficients in porous media; hence, the obtained values in this study are compared with the measured values for non-porous systems. Table 4.3 compares the reported values for the slip coefficients in the literature with obtained values in this study. As shown in this table, the obtained slip coefficients for porous media are higher than the corresponding values for the non-porous system. This means that the gas slippage in porous media is more promoted compared to gas slippage in non-porous conduits. The reason for this phenomenon could likely be having a larger available surface area (walls) and a higher level of surface roughness in porous media. It should be noted that, these slip coefficients were obtained from the experiments performed on three shale samples. As discussed later, more experimental and numerical investigations are required to verify this finding.

Table 4.3: The first slip coefficients in first-order C_1^{1st} and second order slip model C_1^{2nd} reported in literature and this study.

Researchers	**Gas**	**System**	C_1^{1st}	C_1^{2nd}	**Knudsen Range**	**Ref.**
Maurer et al. (2003)	N_2	Channel	1.3	-	0.002-0.59	(Maurer et al., 2003)
	He	Channel	1.2	-	0.06-0.8	(Maurer et al., 2003)
Ewart et al. (2007)	He	Micro tube	1.415	1.066	0.03-0.3	(Ewart et al., 2007)
Graur et al. (2009)	N_2	Micro tube	1.253	1.104	0.007-30.5	(Graur et al., 2009)
	Ar	Micro tube	1.355	1.205	0.009-3.76	(Graur et al., 2009)
Yamaguchi et al. (2011)	N_2	Micro tube	-	1.35	0.05-0.3	(Yamaguchi et al., 2011)
This Study	N_2	Cylindrical Porous Media	2.10	2.392	0.01-0.1	-

In addition to the Maxwell first-order and second-order slip models, the B-K slip model can be used to predict the enhanced flow rate. Equation 4.19 is used to scale the experimental data using $b_{BK} = -0.5$ (for cylindrical tube) as recommended by Beskok and Karniadakis for slip region (Beskok and Karniadakis, 1999). Figure 4.5 presents the experimental data and the predictions based on B-K models with $b_{BK} = -0.5$ and $\sigma_v = 0.6$. As shown in this figure, in the slip region, almost accurate predictions are obtained for $\sigma_v = 0.6$, which confirms our previous finding based on general second-order slip model. However, as shown in this figure, the permeability data of transition region are overestimated by the B-K model.

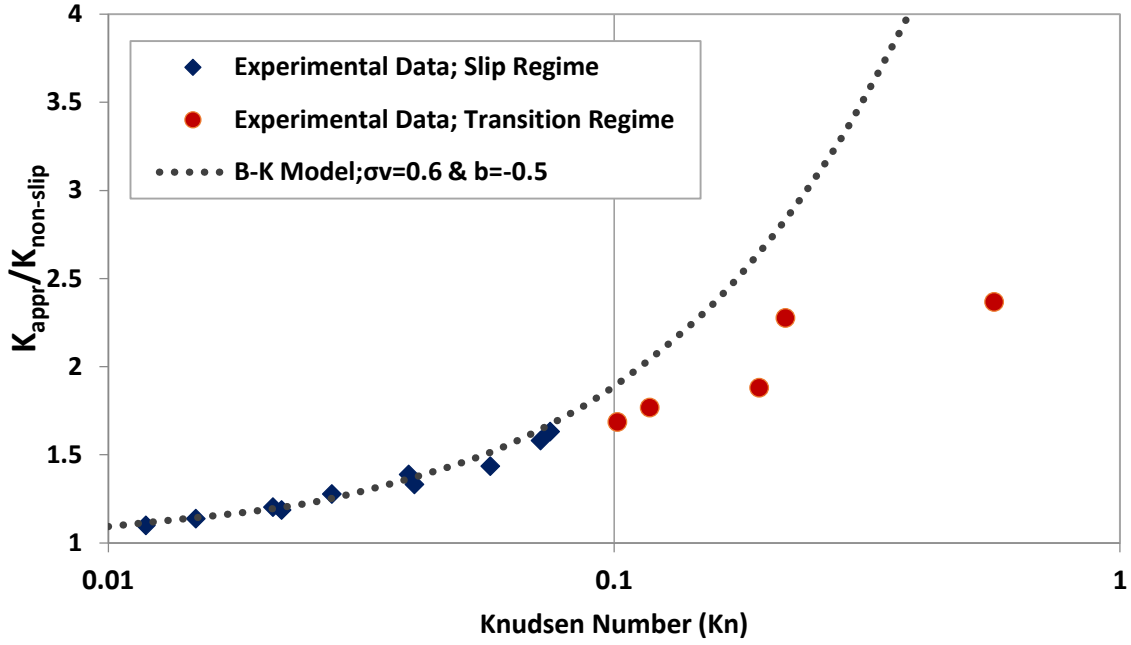

Figure 4.5: The experimental data of dimensionless permeability and the predictions of B-K model using b_{BK}= -0.5 and TMAC=0.6.

In addition to this model, Beskok and Karniadakis (1999) proposed adding a rarefaction coefficient ($C_r = 1 + \alpha\, Kn$) to Equation 4.19 to improve its predictions over the entire range of flow regimes. The corresponding general form of the B-K expression with the rarefaction coefficient is:

$$k_D = (1 + \alpha\, Kn)\,[1 + 4\left(\frac{2-\sigma_v}{\sigma_v}\right)\frac{Kn}{1 - b_{BK}\, Kn}] \qquad (4.22)$$

They mentioned that the α parameter cannot be constant in the entire Knudsen regime and proposed the following relationship:

$$\alpha = \alpha_0 \frac{2}{\pi}\, tan^{-1}(\alpha_1 Kn^{\beta}) \qquad (4.23)$$

where $\alpha_0 = 1.358$, $\alpha_1 = 4.0$ and $\beta = 0.4$. To evaluate the above improvement, the B-K predictions were calculated again with the rarefaction coefficient. Figure 4.6 shows the experimental data and the predictions of the B-K model with and without the rarefaction coefficient (C_r). As shown in this figure, using the rarefaction coefficient in the B-K model for porous media cannot improve the predictions. The rarefaction coefficient

increases the effect of slippage in the transition region and in fact overestimates the permeability enhancement compared to the experimental data. It confirms that the gas slippage in porous media is different from the gas slippage in the non-porous channels. In other words, as shown by Karniadakis and Beskok (2005), their general slip model with rarefaction term can predict the gas flow behaviour in microchannels for both slip and transition regimes. However it overestimates the gas flow in porous media as shown here in Figure 4.6.

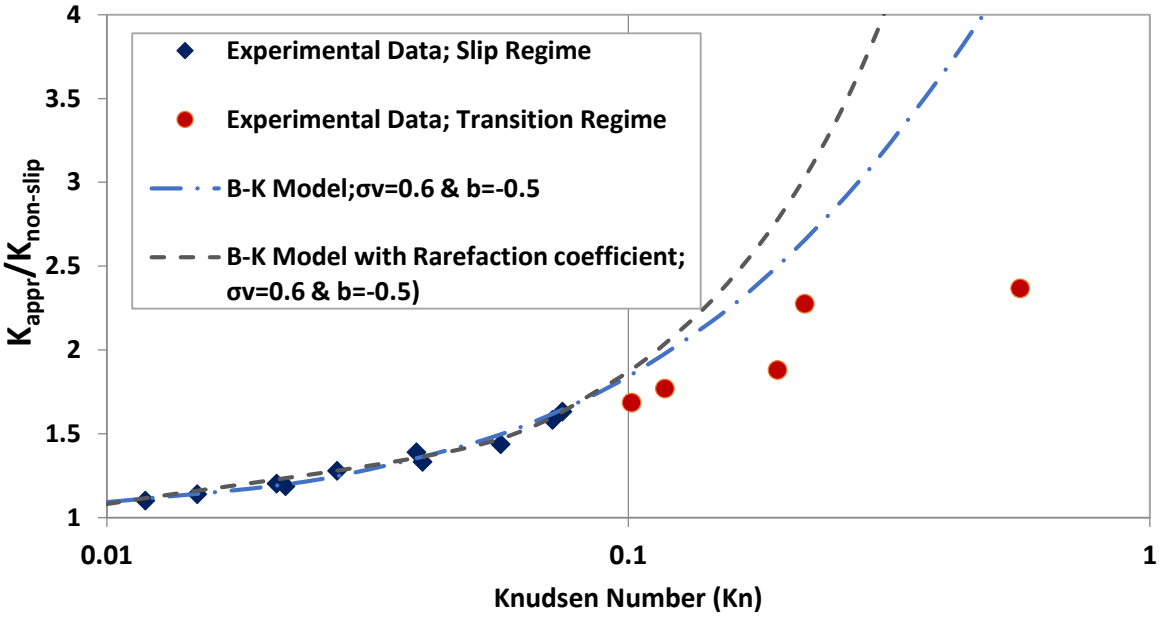

Figure 4.6: The experimental data of dimensionless permeability and the predictions of B-K model with and without rarefaction coefficient for TMAC=0.6 and b_{BK}=-0.5.

4.3.1 Tangential Momentum Accommodation Coefficient (TMAC)

The tangential momentum accommodation coefficient (TMAC) is an empirical parameter, which plays an important role in gas slip models. The amount of gas slippage depends on the type of reflection that gas molecules experience at the wall surface. To quantify the slippage, Maxwell suggested a coefficient to consider the gas reflection from the wall (Maxwell, 1879). This parameter is now frequently referred to as TMAC. Based on its definition, TMAC ranges from 0 for fully specular to 1 for fully diffusive. It means that TMAC with a value of 1 characterises complete tangential momentum transfer to the solid while a TMAC value of zero represents perfect reflection with no tangential momentum transfer to the surface. In other words, this coefficient describes the fluid-wall

interaction and is a function of gas, material and quality of conduit wall; e.g. roughness (Buonomo et al., 2014). Many researchers have shown that the TMAC is a function of these parameters, but the relative impact of each parameter is not well understood.

Table 4.4: The largest and smallest measured TMAC reported in the literature and this study.

Researchers	**Largest Measured TMAC**	**Smallest Measured TMAC**	**Ref.**
Knechtel and Pitts (1969)	0.95	0.45	(Knechtel and Pitts, 1969)
Lord (1977)	0.95	0.35	(Lord, 1977)
Seidl and Steinheil (1974)	1.2	0.2	(Seidl and Steinheil, 1974)
Blanchard and Ligrani (2007)	0.980	0.137	(Blanchard and Ligrani, 2007)
This study	0.6		-

TMAC values normally fall within the range of 0 to 1. However, as reported by Yener et al. (2005) it may be significantly different from unity for light atom gases and closer to unity for heavy atom gases (Yener et al., 2005). In this study, TMAC of ~0.6 has been obtained based on the first- and second-order slip models.

Table 4.4 shows the upper and lower measured values of TMAC in the literature. As shown in this table, the measured TMAC in this study is in between the reported values. It should be noted that the literature data reported in this table were obtained for different system geometries. In addition, there are several papers in the literature, which report TMAC values specifically for gas flow in microchannels. Table 4.5 compares these TMAC values, obtained for microchannels or microtubes, with those obtained in this study. As shown in this table, the measured TMAC in this study is approximately 20-30 % lower than the reported ones for non-porous materials. It means that the specular reflections could be more and need a higher weight for numerical simulation, when considering gas/wall interaction at the boundary. It is discussed in more details in Chapter 5 when simulating gas flow by the LBM. It should be noted that the reported TMAC

values in Table 4.4 are obtained for gas flow in different geometries (e.g. between two disks), while the reported TMAC in Table 4.5 are obtained for gas flow only in microtubes or microchannels.

There are some studies that investigated the effect of roughness on rarefied gas flow (Yan et al., 2015, Zhang et al., 2012b, Rovenskaya, 2013, Chen et al., 2009). .Some researchers considered periodic distributions for surface roughness (to simplify the models)(Cao et al., 2006, Kunert and Harting, 2007) while others dealt with random surface roughness (Croce and D'Agaro, 2004, Yan et al., 2015, Zhang et al., 2012b). It is reported that the TMAC values can change by around 15 % for different surface roughness even for the same surface material (Thomas and Lord, 1974, Jang and Wereley, 2006). Blanchard and Ligrani (2007) measured the TMAC on the walls with different rough surfaces and reported that rougher surfaces have smaller TMAC values (Blanchard and Ligrani, 2007). They performed experiments using rotating disks and stationary surfaces with different roughness and reported TMAC values of 0.885, 0.346 and 0.145 for smooth, medium rough and rough disks, respectively. Considering the presence of multi-scale roughness in porous media, one can conclude that the obtained values of TMAC are lower (compared to micro pipe cases) because of the higher surface roughness of porous rocks. However, to present an explicit relationship between the surface roughness and TMAC more investigations are required. In addition, in porous media, the surface area is several orders of magnitude larger than the non-porous medium with the same pore volume. The presence of higher surface area also suggests that the gas slippage is more likely to happen in porous rocks. However, to present an explicit relationship between these parameters, more investigations are required.

Table 4.5: The measured TMAC reported in literature measured for gas flow in channels and pipes.

Researchers	**Gas**	**System/Materials**	σ_v^{1st}	σ_v^{2nd}	**Kn Range**	**Ref.**
Maurer et al. (2003)	N_2	Microchannel, etched in glass and covered by silicon	0.87	-	0.002-0.59	(Maurer et al., 2003)
	He		0.91	-	0.06-0.8	(Maurer et al., 2003)
Ewart et al. (2007)	He	Micro tube, fused silica	0.77	0.908	0.03-0.3	(Ewart et al., 2007)
Graur et al. (2009)	N_2	Micro tube, silicon	0.889	0.956	0.007-30.5	(Graur et al., 2009)
	Ar		0.848	0.910	0.009-3.76	(Graur et al., 2009)
Yamaguchi et al. (2011)	N_2	Micro tube, deactivated-fused silica	-	0.794	0.05-0.3	(Yamaguchi et al., 2011)
This Study	N_2	Cylindrical Porous Media	0.64	0.6	0.01-0.1	-

4.4 N-S Solution of Rarefied Flow: Incorporation of Stress Effects

In the first part of this chapter, the gas slippage was modelled based on the slip boundary conditions for flow equations. The solution of N-S equation with slip boundary conditions was used to predict the apparent matrix permeability, when the gas slippage is changing due to different flow regimes. In this part, it is explained that the confining pressure effects can be incorporated into this model. In fact, it was aimed to develop a simple model, which considers both slippage and stress effects at the same time. As mentioned earlier, the overall net stress increases as the reservoir pressure declines. This net stress enhancement causes the matrix permeability to reduce. This effect is more pronounced in shale reservoirs due to the higher sensitivity of their rocks to stress. Moreover, in these reservoirs, the slippage phenomenon, which also plays an important role in fluid flow, makes the permeability prediction more difficult.

To consider the stress effects on apparent matrix permeability, the solution of N-S equations solved by the slip boundary conditions was used (Equation 4.18). It should be noted that the pore size distribution changes as the net stress varies during the production period. In other words, the characteristic length of the flow should be also modified as a result of changing the net stress. Therefore, the flow regime may change because of this variation in the characteristic length. In addition, due to the change of net stress, the non-slip permeability also varies. Several authors have shown that the intrinsic permeability decreases as the net stress increases.(Chalmers et al., 2012b, Heller et al., 2014, Ghanizadeh et al., 2014b). Considering the above discussion, it is reasonable to propose that two parameters of "characteristic length" and "non-slip permeability" should be modified simultanously to capture the stress effect on the matrix permeability. In fact, the former should be modified to consider the flow regime variation and the latter should be updated to take into acccout the permeability change. In this study, the experimental data performed at 1000 and 2000 psi net stress values were used to investigate the geomechanical effects (The number of permeability data points measured at 3000 psi net stress was not sufficient to be included in this investigation). To quantify these effects, characteristic length and non-slip permeability of porous media should be determined at each net stress.

As explained in Chapter 3, the non-slip permeability of shale samples are calculated based on the Klinkenberg correction applied to the experimental data performed at high pressures (1500, 2250 and 3000 psi). It was shown that the non-slip permeability changes with variation of the net stress and follows an exponential relationship (Equation 3.1). This exponential behaviour can be used in the slip model (Equation 4.18) to predict the non-slip permeability at different net stress values. In other words, the exponential relationship shown in Equation 3.1 can be incorporated into the equation 4.18 to consider the effects of net stress on non-slip permeability. However, α and ${k^0}_{non-slip}$ should be determined for the rock under study.

Another factor, which should be modified by changing net stress is average pore size, i.e. characteristic length of the flow conduit. It is obvious that the pore size distribution of a rock sample changes if the applied net stress is altered. It happens because the pore throat and pore sizes change due to the variation in applied stress. However, this variation may not be uniform and tend to be more random. Here, as only a single value is required as characteristic length, it is assumed that the average of pore sizes change by variation

of net stress. Therefore, it is aimed to determine a suitable value for the average pore sizes at different net stress conditions. This average value can be used as characteristic length.

To find this characteristic length, the generalised slip plot (Figure 4.2) was used and a tuning process was followed. As mentioned, the general slip plot was generated based on the permeability data measured at 500 psi net stress. Therefore, for the higher net stress values (e.g 1000 or 2000 psi), it is required to obtained a suitable value for characteristic length to have a similar trend. In other words, the assumed characteristic length of the rock at higher net stress values is changed to find the best match on Figure 4.2. The steps for this tuning process can be summarized as follows:

1. Use the measured data at higher net stress and generate slip plot (a graph of dimensionless permeability versus Knudsen numbers)
2. Compared the obtained slip plot with the general slip plot (Figure 4.2)
3. In calculation of Knudsen number, change the assigned characteristic length of the rocks (D) to match the data on the general slip plot.
4. The least square method can be used to obtain the best match.

It was interesting that the all the permeability improvement factors (k_D) at the higher net stresses follow the same trend and matched to the general slip plot when the characteristic length of the rocks were decreased.

Figure 4.7, is similar to Figure 4.2, but also includes the data measured on these three rocks at a net stress of 1000 psi. As seen in this figure, all the data points follow the same trend as that shown in the general slip plot. This suggests that the stress effect can be quantified using an "appropriate" average pore size. In addition, when the permeability enhancement factors measured at 2000 psi net stress (with suitable average pore sizes) are placed on the same graph, (Figure 4.8), all data points measured at different net stresses obey the same trend. Therefore, it can be concluded that the gas slippage (at different net stresses) in these three shale samples can be quantified from the general slip plot provided that the characteristic length (average pore size) at different net stress is determined properly.

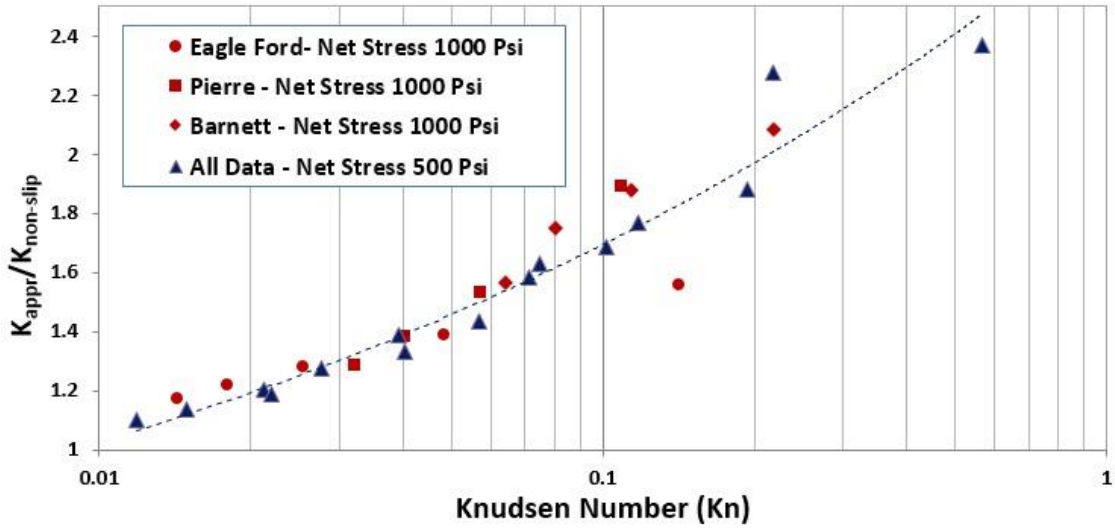

Figure 4.7: Dimensionless permeability factor versus Knudsen number for three shale rock samples at the constant net stress of 500 and 1000 psi; the permeability factors measured at 1000 psi net stress follow the generalised slip plot.

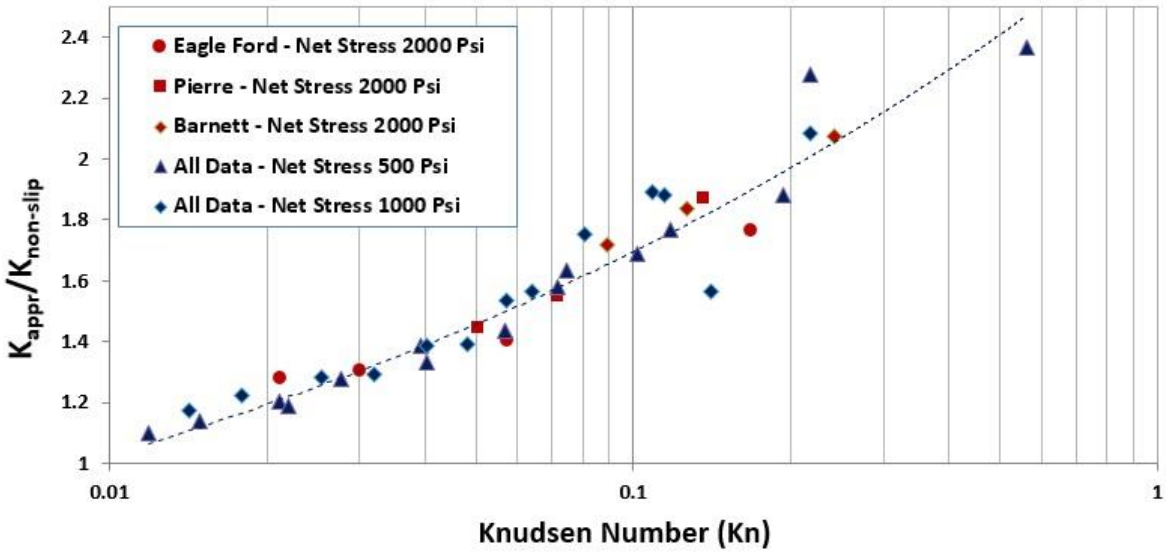

Figure 4.8: Dimensionless permeability factor versus Knudsen number for three shale rock samples at the constant net stress of 500, 1000 and 2000 psi; the permeability factors measured at both 2000 and 1000 psi net stresses follow the generalised slip plot.

Table 4.6 presents the allocated average pore size at different net stresses. As indicated, the average pore size decreases as the net stress increases. The obtained average size are plotted versus net stress in Figure 4.9. The average pore size decreases by increasing the net stress, following an exponential relationship. This exponential relationship can also

be incorporated into the permeability prediction model to consider the effects of stress on the characteristic length (average pore size). As mentioned earlier, the measured MICP data were fitted by a probability distribution functions to find the statistical parameters of the pore size distribution functions. In Figure 4.10, the obtained average pore sizes (mean) at different net stress are used in those fitted functions to plot the pore size distribution. As illustrated in this figure, the pore size distribution plot shifts to the left as the net stress decreases. For generation of these plots, it is assumed that all pores/throats were influenced by the variation of effective stress uniformly. However, as mentioned before, the pore size distribution may not change uniformly in reality, but as only a single value the average pore sizes is required here, this assumption was made.

Table 4.6: The obtained average pore size of shale samples at different net stresses; these data are used as characteristic lengths for calculation of Knudsen number.

Net Stress (Psi)	**Average Characteristic Length (nm)**		
	Eagle Ford	**Pierre**	**Barnett**
500	54	29.1	11.25
1000	45	20	10
2000	38	16	9

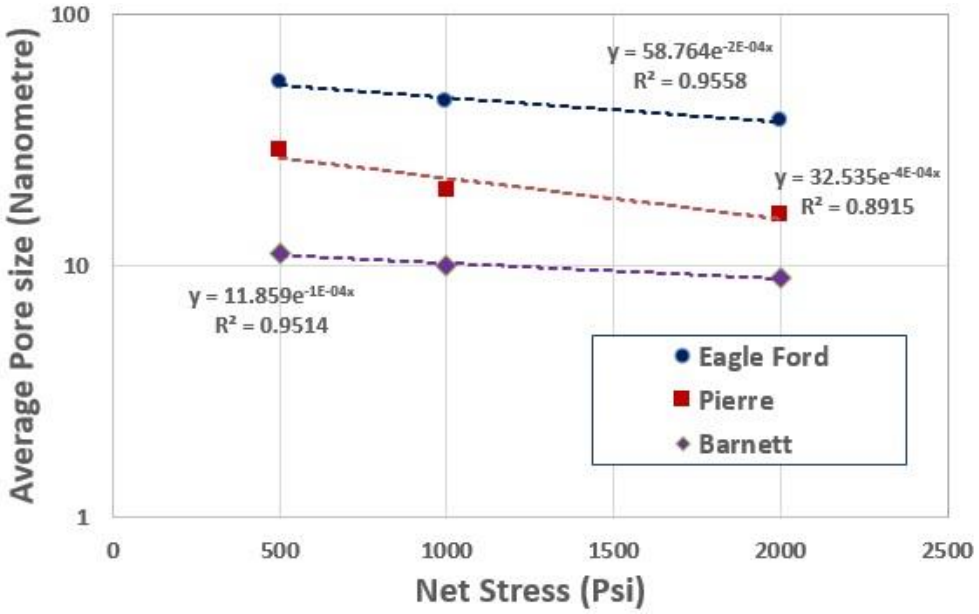

Figure 4.9: Data of average pore size of three shale rock samples at three different net stress obtained through the introduced matching process.

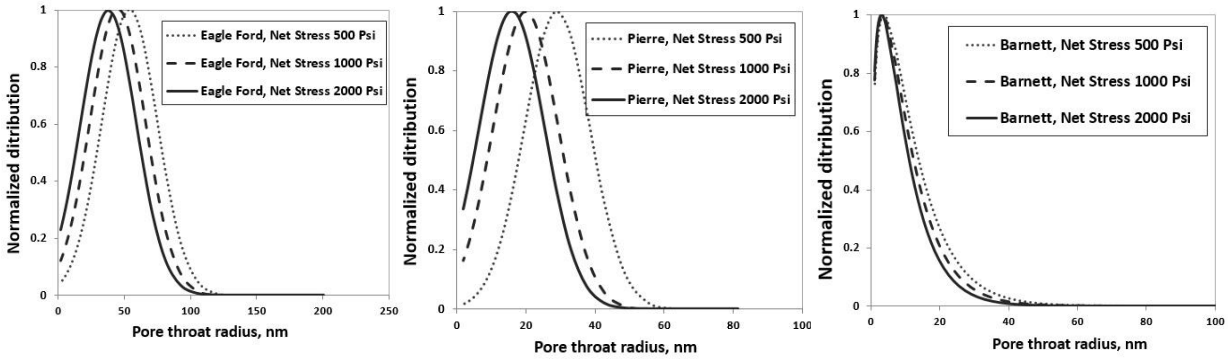

Figure 4.10: The average pore size of shale sample at any net stress was used in the corresponding appropriate probability distribution function.

In summary based on the experimental observations in this study, it is proposed to predict the apparent matrix permeability as a function of net stress assuming exponential reduction for the non-slip permeability and the average pore size. In other words, the slippage can be considered in the flow equations by assuming slip boundary conditions (first or second-order slip model) and the stress effect can be taken into account in the same equation by assuming exponential relationship for the "non-slip permeability" and "average pore size" available in the solution. Hence the final solution has the following form:

$$k_{app} = k_{non-slip}\left[1 + 4C_1\left(\frac{\lambda}{R_c}\right) - 8C_2\left(\frac{\lambda}{R_c}\right)^2\right] \tag{4.24}$$

where

$$k_{non-slip} = {k^0}_{non-slip}[\exp(\alpha \times \Delta P)] \tag{4.25}$$

$$R_c = {R^0}_c[\exp(\beta \times \Delta P)] \tag{4.26}$$

where ${k^0}_{non-slip}$ and ${R^0}_c$ are the non-slip permeability and characteristic radius (average pore radius) at a reference net stress, α and β are fitting parameters, C_1 and C_2 are first- and second-order slip coefficients, respectively and ΔP is the difference between the current net stress and the reference stress. It is noted that the "based non-slip permeability" (i.e. ${k^0}_{non-slip}$) can be assumed as absolute or intrinsic permeability as it is independent from both slippage and net stress. Therefore to predict the apparent matrix

permeability of a rock, the base non-slip permeability ($k^0{}_{non-slip}$) and average pore size ($R^0{}_c$) should be measured in the laboratory. In addition, the exponential parameters (α and β in Equations 4.25 and 4.26) are required, which can be calculated from few permeability measurements at different pore pressure and net stress. It has to be reminded that the slippage intensity is a function of Knudsen number. Hence, slippage is more pronounced, when Knudsen number is high, i.e. the size of flow conduit is small. Therefore, larger flow conduits have less impact on the flow rate in terms of slippage. While larger conduits have greater effects on flow rate in terms of rock permeability. Thus, the fitting coefficients are used in this model to capture such a dependency that would change from rock to rock depending on the pore type, minerology, pore size distribution and etc. Knowing these basic data, the permeability at any net stress and pore pressure can be estimated, based on the proposed model, and used for simulation of gas flow in matrix during the reservoir life. The proposed model can be easily incorporated into the reservoir simulation for the prediction of apparent permeability at different conditions.

4.5 Model Verification

In this section, the performance of the proposed model is evaluated by using a series of experimental data. It is noted that the model also has been developed based on the results of the experiments conducted in the HW-GCR laboratory on the shale samples. However, additional experimental data, measured at a different institution, were used to evaluate the performance of the model. To achieve this aim, series of experimental data were sourced from the literature. Ghanizadeh et al. (2014) reported several matrix permeability measurements on the Scandinavian Alum Shale (Ghanizadeh et al., 2014b). The Cambro-Ordovician Alum Shale is a potential shale gas system occurring at relatively shallow depth along the northern margin of Central Europe, from southern Sweden to southern Denmark (Ghanizadeh et al., 2014b). They investigated the effects of different pertinent parameters including moisture content, permeating fluid, effective stress, and pore pressure. In this work, we used the measured apparent permeability data reported for Alum sample No 2 (Alum#2).

Some of the reported data points at different pore pressure and net stress were used to obtain the base parameters of $k^0{}_{non-slip}$ and α in Equation 4.25 and $R^0{}_c$ and β parameters in Equation 4.26. The obtained $k^0{}_{non-slip}$, α, $R^0{}_c$ and β values were 52 nD,

-2.5E-4, 136.2 and -6.2E-4, respectively. For calculation of these parameters, the non-slip permeabilities were estimated using the Klinkenberg correction. In other words, the measured permeability values at a specified net stress were plotted versus inverse of pore pressure (1/P). Then the data were extrapolated linearly to obtain the permeability at infinite pressure ($1/P \rightarrow 0$). This value is non-slip permeability at that net stress value. After that, the non-slip permeability data obtained for each net stress were plotted versus net stress to obtain the parameters of Equation 4.25. The non-slip permeability data showed a good exponential trend similar to what we have reported for three shale samples in our experiments. To find the parameters in Equation 4.26, the tuning process was used. It means that the Figure 4.2 (general slip plot) was used as reference and the plot of permeability data (K_D versus Kn) were tuned by changing the average of pore sizes (i.e. characteristic length). Then the estimated average pore sizes were plotted versus net stress to obtained parameters of Equation 4.26. The obtained average pore size data for Alum#2 also showed a good exponential trend. Having the non-slip permeability (${k^0}_{non-slip}$ and α) and average pore size (${R^0}_c$ and β) parameters, the apparent permeability at other pore pressures and net stress values can be estimated using Equations 4.24, 4.25 and 4.26. Figure 4.11 shows the predicted values of the apparent matrix permeability based on the Kn number of the experiments at different pore pressures and net stresses. As shown in this Figure, the proposed model can capture both permeability "enhancement" and "reduction" due to the "gas slippage" and "net stress variation", respectively. It should be noted that these data points were not used for obtaining the parameters in Equation 4.25 and 4.26. Table 4.7 indicates the corresponding pore pressure and the net stress in each experiment. The corresponding error for each prediction is also shown in this Table. It has to be added that in this figure, the apparent permeability values plotted versus Knudsen number of the experiments and it is not a general slip plot.

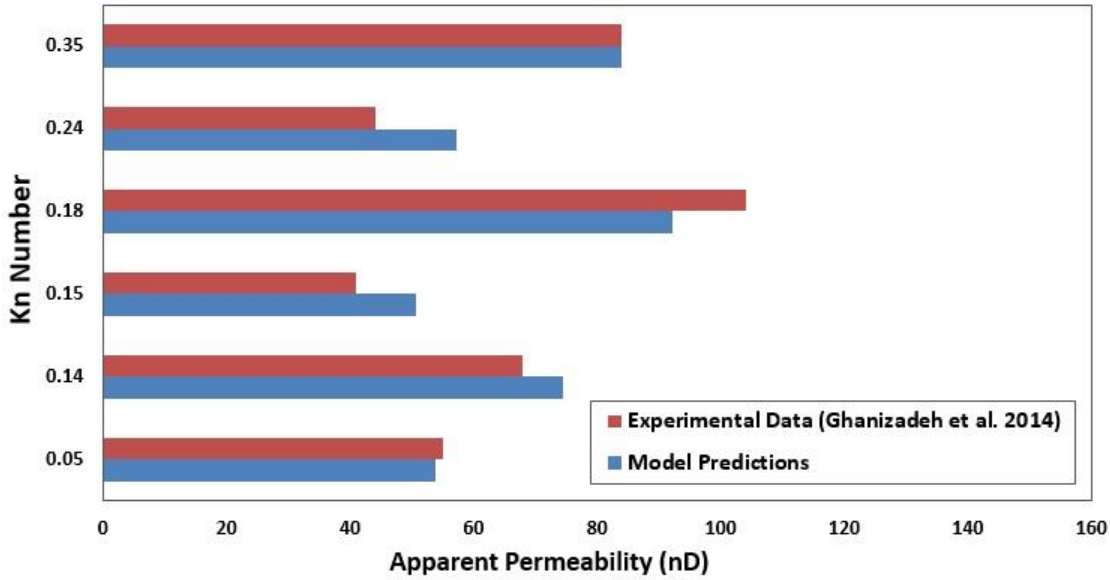

Figure 4.11: Comparison of predicted apparent permeability data of the Alum#2 shale rock sample with the corresponding experimental data reported by Ghanizadeh et al. (2014).

Table 4.7: The predicted apparent permeability data for the Alum#2 shale sample. The predicted values are compared with the corresponding experimental data reported by Ghanizadeh et al. (2014).

Test No	**Pore Pressure (Psi)**	**Net Stress (Psi)**	**Measured Permeability (nD ±5%)**	**Predicted Permeability (nD)**	**Error (%)**	**Kn Number**
1	464	3146	41	50.6	23.4	0.15
2	464	1290	55	53.7	2.3	0.05
3	101.5	1058	104	92.1	11.4	0.18
4	101.5	2088	84	83.8	0.3	0.35
5	319	3306	44	57.3	30.2	0.24
6	174	1566	68	74.5	9.5	0.14

4.6 Summary and Conclusions

In this chapter, the experimental data measured on three different shale rocks were used to develop a model for matrix permeability prediction. For this purpose, the solution of N-S equation with slip boundary conditions was used. The available slip boundary

conditions were reviewed and the Maxwellian first-order, second-order and B-K slip models were applied to N-S equations to capture the permeability enhancement due to the gas slippage. In addition, the obtained non-slip permeability data were used to calculate the dimensionless permeability enhancement factor (k_D) and generate the general slip plot, which is independent of rock and fluid properties. Then, this general slip plot was scaled based on the obtained analytical solution for dimensionless permeability to determine the TMAC and slip coefficients in the analytical solutions. In this study, for the first time, slip coefficients and TMAC were determined experimentally for porous media. The obtained slip coefficients were used in the solution of N-S equation (solved with second-order slip boundary condition) to propose the permeability prediction model for shale rocks. Moreover, the geomechanical effects were incorporated into the model considering the experimental observations. The impacts of net stress variation on the "flow regime" and the "non-slip permeability" were considered by introducing suitable relationships for variation of average pore size and non-slip permeability by net stress. Finally, the performance of the proposed model was evaluated with literature experimental data which were not used for the development of the model. The following observations/conclusions can be made/drawn from this study:

- Based on the solution of N-S equation (solved by the first-order slip boundary condition) and the measured data, the slip coefficient of 2.10 was obtained for the first-order slip model. From the second-order slip model, the first- and second-order slip coefficients were obtained as 2.390 and 2.392, respectively. In addition, it is concluded that to find the second-order coefficient the same expression as the first-order slip coefficient can be used; i.e. $\frac{2-\sigma_v}{\sigma_v}$.

- TMAC was also calculated from the obtained slip coefficients. The TMAC of ~0.6 was obtained from the experimental data of permeability enhancement in porous media.

- The experimental data were used to evaluate the B-K slip model. It is concluded that the experimental data can be accurately predicted using the TMAC of 0.6. In addition, it is concluded that the B-K model overestimates the permeability enhancement when using the rarefaction coefficient in the transition region.

- Comparison of the slip coefficients measured for porous media (this study) and the literature values for microtubes revealed that the higher values of slip coefficients in porous media could be probably due to the much greater surface area and multi-scale roughness of the rocks.

- Based on the experimental results, TMAC value was also calculated, which was lower compared to those value obtained for gas flow in microchannels. It means that the gas slippage is more pronounced in porous media and it needs to be considered when setting appropriate boundary conditions for modelling of gas flow (e.g. Lattice Boltzmann simulations). In addition, as there are lower reported TMAC values for rough surfaces, it is assumed that the lower values of TMAC in porous media could be as a result of their multi-scale roughness. However, these findings need more investigation.
- In addition, the average pore sizes of the shale rocks at the higher net stresses were obtained by matching the permeability enhancement data to the trend of the general slip plot.

- Using the general slip plot, it was demonstrated that the stress effect can be quantified by using an appropriate non-slip permeability and average pore size in the proposed model for matrix permeability prediction. An acceptable permeability enhancement factor (k_D) can be predicted if non-slip permeability and average pore size values corresponding to the desired net stress, are used.

- The performance of the proposed approach was verified using the literature data showing that the proposed model could capture both permeability enhancement and reduction due to the gas slippage and the net stress variations with a reasonable accuracy.

Chapter 5: Lattice Boltzmann Simulation of Gas Flow in Nano and Microscale Systems

5.1 Introduction

In this chapter, the simulation results of gas flow in micro and nanoscale systems are presented. The Lattice Boltzmann method (LBM) was used for this purpose. The Lattice Boltzmann Method (LBM) has received great attention for simulation of non-continuum flow in micro and nanoscale systems. It solves a discretized form of the continuous Boltzmann equation, which is an accepted relationship for modelling the evolution of gas flow based on the kinetic theory of gas particles, for a regular lattice. This technique is computationally efficient as it deals with particle distribution functions. In fact, the intrinsic kinetic nature of the LBM makes it an attractive method for microfluidic flows with high Knudsen numbers similar to gas flow in shale and tight matrices. In the LBM, to account the slippage at the wall surface, the interaction of gas particles with solid surface should be defined properly. As mentioned in Chapter 2, different boundary conditions have been proposed for this purpose including bounce back, specular reflection, diffusive reflection and combinations of them (Nie et al., 2002, Lim et al., 2002, Succi, 2002, Sofonea and Sekerka, 2005). In addition to different boundary conditions, different relaxation time models have been also used in the literature. The relaxation time is a constant which determine the microscopic dynamics towards the local equilibrium and the macroscopic transport coefficients at the same time. In the LBM (a mesoscopic model) the relaxation time is the practical tunable parameter which can be set in order to recover the desired dynamics, both microscopic and macroscopic (Asinari, 2005). Although most of the literature studies were based on the Single-Relaxation-Time (SRT) model (Niu et al., 2004, Zhang et al., 2005, Guo et al., 2006, Homayoon et al., 2011, Shokouhmand and Isfahani, 2011, Tang et al., 2005), Multi-Relaxation-Time (MRT) and Two-Relaxation-Time (TRT) (Guo et al., 2008, Li et al., 2011, Verhaeghe et al., 2009, Ginzburg et al., 2008) have been also used for slip flow studies. The main reason for using TRT and MRT is the deficiency of the SRT model for slip flow simulations as mentioned by Luo (Luo, 2004, Luo, 2011). He argued that slip velocity predicted by SRT with bounce-back boundary condition is merely numerical artefact. Verhaeghe et al.

(2009) have also shown that two relaxation times (TRT) is as efficient as the corresponding STR-LB models. In other words, TRT model is similar to SRT model in simplicity and efficiency, but still retains the advantages of MRT model in terms of accuracy and stability (Verhaeghe et al., 2009). In this study, TRT lattice Boltzmann method was used to simulate the gas flow in micro and nanosystems. Furthermore, different boundary conditions have been used to capture the gas slippage at the wall surface. It was aimed to evaluate the performance of different proposed boundary conditions for the application of gas flow modelling in shale rocks. After development of the code, the simulation results of LBM were verified for slip flow, based on the solution of other simulation techniques (IP and DSMC). Here, after presenting this validation step, the simulation results of slip flow in a single channel with different boundary conditions were compared with the experimental data presented in Chapter 3. The effect of TMAC value was also investigated. In addition, the effects of variable characteristic length in porous media was also investigated. It is clear that the value of the Knudsen number depends on the assigned characteristic length for that porous media. Therefore, to have a closer structure to reality, a system of pore body/throat was modelled and the results were compared with those obtained for a single channel and also experimental data. Furthermore, the LBM simulation results were used to obtain appropriate slip coefficients for a wider range of Knudsen number to capture the permeability enhancement due to the gas slippage. In this study, MATLAB programming language (R2014b version) was used to develop all programs.

5.2 Methodology

5.2.1 Lattice Boltzmann Method (LBM)

The Lattice Boltzmann Method (LBM) was developed from Ludwig Boltzmann's kinetic theory of gases. In this approach, gas consists of a large number of particles moving with random motions. Momentum and energy can be transferred through the streaming and collision of gas particles. The dynamic evolution of gas flow can be modelled by the Boltzmann transport equation (Guo et al., 2006):

$$\frac{\partial f}{\partial t} + \xi . \nabla f = \Omega (f) \qquad (5.1)$$

where $f(\xi, r, t)$ is the density distribution function, ξ is the particle velocity, and Ω is the collision operator. In fact, the density distribution function, f, is the expected number of molecules in the volume d^3r located at r, whose velocities lie in $d^3\xi$ about velocity ξ. In other words, f, is a "number density" of particles whose velocities lie in $d^3\xi$ about velocity ξ. Therefore the local number density (ρ) and the local velocity (u) are defined as:

$$\rho = \int f d\xi \,, \quad \rho u = \int \xi f d\xi \tag{5.2}$$

The collision term (Ω) is usually simplified for practical calculations. The Bhatnagar-Gross-Krook (BGK) model is one of these approximations (Bhatnagar et al., 1954):

$$\Omega = -\frac{1}{\tau}[f - f^{eq}] \tag{5.3}$$

where τ is the relaxation time and f^{eq} is the Boltzmann-Maxwell distribution function as follows:

$$f^{eq} = \rho\,(\frac{m}{2\pi\kappa T})^{3/2}\exp[-\frac{m}{2\kappa T}(\xi - u)^2] \tag{5.4}$$

Note that this definition includes the density ρ, whereas the usual Maxwellian distribution does not include the density in its expression. The Lattice Boltzmann method (LBM) simplifies the Boltzmann's original idea of gas dynamics by considering a reduced number of particles confined in the nodes of a lattice. For example, in a two-dimensional model, a particle is restricted to stream in nine possible directions. These velocities are referred to as the microscopic velocities and denoted by $\overrightarrow{c_\alpha}$, where $\alpha = 1, \ldots, 8, 9$. Figure 5.1 shows this model referred to as D2Q9 for this two dimensional geometry with nine possible paths. As shown, lattice nodes are assumed and the fluid particles can move to the neighbour nodes. For each particle on the lattice, nine discrete distribution functions $f_\alpha(x, t)$ is considered, which describe the probability of streaming in different directions. As shown in this figure, the particle can move to the neighbour nodes (eight nodes and itself) in each streaming step.

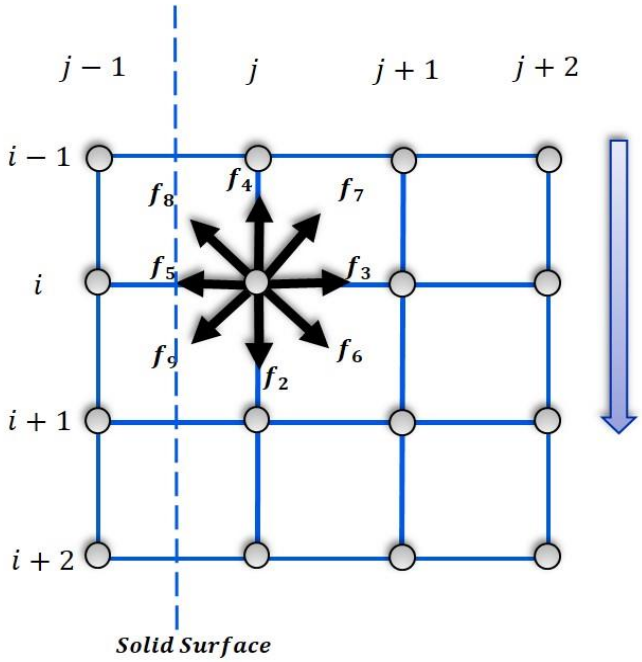

Figure 5.1: The Schematic of the boundary nodes near the wall and the corresponding distributions used for different boundary conditions implemented for gas flow simulations.

The macroscopic fluid density is also defined as a summation of microscopic particle distribution function:

$$\rho(x,t) = \sum_{\alpha=0}^{\alpha=8} f_\alpha(x,t) \tag{5.5}$$

Accordingly, the macroscopic velocity $\vec{u}(x,t)$ is an average of microscopic velocities $\vec{c_\iota}$ weighted by the distribution functions (f_α):

$$u(x,t) = \frac{1}{\rho}\sum_{\alpha=0}^{\alpha=8} \boldsymbol{c}\, f_\alpha\, \vec{c_\iota} \tag{5.6}$$

where $\boldsymbol{c}$ is the lattice speed for fluid particles moving from site to site, expressed as $c = \Delta x/\Delta t$. Therefore, to calculate node density, summation of distribution functions in all nine direction should be used. In addition, Equation 5.6 is also used to calculate the node velocity. It is noted that the bulk density and velocity can be also obtained by averaging all node density and node velocity values.

The equilibrium distribution (f_α^{eq}) in the LBM can be expressed by expanding the exponential function in Equation 5.4 into a Taylor series expansion as (Satoh, 2010):

$$f_\alpha^{eq} = \rho w_\alpha \left[1 + b\frac{c_\alpha . u}{c^2} + e\frac{u^2}{c^2} + h\frac{(c_\alpha . u)^2}{c^4}\right] \tag{5.7}$$

where w_α, b, e and h are the constants, which should be determined based on the model dimensions (e.g. D2Q9, D3Q19, etc). It is noted that these parameters should be determined such that the terms on the right hand sides of Equations 5.5 and 5.6 remain unchanged by a rotation of the whole lattice system by and angle of ϕ (Satoh, 2010). For D2Q9 model, these parametrs are obtained as:

$$w_\alpha = \begin{cases} \frac{4}{9} & for \quad \alpha = 0 \\ \frac{1}{9} & for \quad \alpha = 1,2,3,4 \\ \frac{1}{36} & for \quad \alpha = 5,6,7,8 \end{cases}, \tag{5.8a}$$

and

$$b = 3\ ,\ e = -3/2\ ,\ h = 9/2 \tag{5.8b}$$

The key steps in standard LBM are the streaming and collision processes as given by:

$$f_\alpha(x + \Delta x, t + \Delta t) - f_\alpha(x,t) = -\frac{1}{\tau}[f_\alpha(x,t) - f_\alpha^{eq}(x,t)] \tag{5.9a}$$

or

$$f_\alpha(x + \Delta x, t + \Delta t) = \frac{1}{\tau}\left[f_\alpha^{eq}(x,t)\right] + (1 - \frac{1}{\tau})f_\alpha(x,t) \tag{5.9b}$$

where τ is the relaxation time and it is related to the fluid kinematic viscosity(υ) , which in the D2Q9 geometry is expressed by:

$$\upsilon = \frac{2\tau - 1}{6}\frac{(\Delta x)^2}{\Delta t} \tag{5.10}$$

It is noted that, the term "1/ τ" which is called collision frequency is a weighting factor between the equilibrium distribution function (f_α^{eq}) and the current distribution function f_α.

As mentioned, TRT lattice Boltzmann method was used in this study. In two-relaxation-time (TRT-LBM) scheme, the distribution function is divided into two parts of symmetric and antisymmetric as follow (Ginzburg, 2005, Mohamad, 2011):

$$f_\alpha^S = \frac{1}{2}\,(f_\alpha + f_{-\alpha}) \tag{5.11a}$$

and

$$f_\alpha^{AS} = \frac{1}{2}\,(f_\alpha - f_{-\alpha}) \tag{5.11b}$$

where f_α is the distribution function moving opposite to the $f_{-\alpha}$. Therefore the collision equation can be expressed by:

$$\begin{aligned} & f_\alpha(x+\Delta x, t+\Delta t) - f_\alpha(x,t) \\ &= -\frac{1}{\tau_S}(f_\alpha^S(x,t) - f_{\alpha\,eq}^S(x,t)) - \frac{1}{\tau_{AS}}(f_\alpha^{AS}(x,t) \\ &- f_{\alpha\,eq}^{AS}(x,t)) \end{aligned} \tag{5.12}$$

where

$$\frac{1}{\tau_S} = \omega_S = \frac{1}{3\upsilon + 0.5} \tag{5.13}$$

where ω_S and ω_{AS} are the symmetric and asymmetric collision frequencies, respectively. The asymmetric collision frequency is related to symmetric collision frequency as follows:

$$\omega_S = \frac{8(2-\omega_{AS})}{8-\omega_{AS}} \tag{5.14}$$

In this simulations, the Knudsen number of the system is also calculated based on the definition of Zhang et al. (2005). Based on that, the Knudsen number is related to relaxation time as follows (Zhang et al., 2005):

$$Kn = \sqrt{\frac{8}{3\pi}}\,\frac{\tau - 0.5}{H} \tag{5.15}$$

where H is the characteristic length of the system. In addition, for all simulations in this study, the constant pressure (density) boundary conditions (Zou and He, 1997) were used to be in line with the performed experiments.

5.2.2 Solid-gas Slip Boundary Conditions

As indicated before, to account the molecular slippage on the wall surface, appropriate boundary conditions (BCs) are required to be defined in the lattice Boltzmann simulation of slip flow. It is very important to address how the gas molecule should be reflected after collision with wall surface. For this purpose, after each streaming step, the distribution functions of boundary nodes (i.e. wall surface nodes) should be updated to address the appropriate molecular reflection with slippage. In other words, the discrete distribution functions on the wall boundaries have to be determined in such a way to reflect the macroscopic BCs. In this study, four different types of boundary conditions, proposed for the solid-gas interaction, were used in the simulations. It is aimed to evaluate the pertinence of the existing boundary conditions for the gas slippage modelling in shale rocks.

5.2.2.1 Bounce-Back boundary condition (BB)

If a fluid particle (discrete distribution function) reaches a boundary node and scatters back along its incoming direction, the reflection is a bounce-back. In other words, incident particles are reflected in the opposite direction. Accordingly, for the node (i,j) in Figure 5.1, the following collision process are considered at post stream step :

$$\begin{aligned} f_{3,\ AC}^{i,j} &= f_{5,\ BC}^{i,j} \\ f_{6,\ AC}^{i,j} &= f_{8,\ BC}^{i,j} \\ f_{7.\ AC}^{i,j} &= f_{9,\ BC}^{i,j} \end{aligned} \tag{5.16}$$

where AC and BC refer to “after collision” and “before collision”. It should be noted that f_2 and f_4 are not involved in the boundary condition calculations.

5.2.2.2 Specular Reflection boundary condition (SR)

In this case, the gas particle collides with the wall and specularly reflected such that the angle of incident is equal to the angle of reflection. No shear forces are transmitted and the tangential momentums are conserved. Hence, for the node (i,j) in Figure 5.1, the following distribution function should be considered for collision process to capture the specular reflection boundary condition.

$$\begin{aligned} f_{3,\ AC}^{i,j} &= f_{5\ ,BC}^{i,j} \\ f_{6,\ AC}^{i,j} &= f_{9\ ,BC}^{i-1,j} \\ f_{7.\ AC}^{i,j} &= f_{8\ ,BC}^{i+1,j} \end{aligned} \tag{5.17}$$

5.2.2.3 Diffusive Reflection boundary condition (DR)

In this boundary condition, it is assumed that the gas particles are reflected at random angles unrelated to the angle of incident. In this case, the particle velocities reflected from the wall are assumed to follow the Maxwellian distribution law (Cercignani, 2000). For this boundary condition, the three nodes, which need to be updated can be summarised as follows (Sofonea and Sekerka, 2005):

$$\begin{aligned} f_{3,\ AC}^{i,j} &= f_{5\ ,BC}^{i,j} \\ f_{6,\ AC}^{i,j} &= \frac{f_{7\ ,BC}^{i-1,j} + f_{8\ ,BC}^{i,j} + f_{9\ ,BC}^{i-1,j} - f_{6,\ BC}^{i,j}}{2} \\ f_{7.\ AC}^{i,j} &= \frac{f_{6\ ,BC}^{i+1,j} + f_{9\ ,BC}^{i,j} + f_{8\ ,BC}^{i+1,j} - f_{7,\ BC}^{i,j}}{2} \end{aligned} \tag{5.18}$$

5.2.2.4 Bounce-back Specular Reflection boundary condition (BSR)

This boundary condition, which was proposed by Succi, allows the gas particle to bounce back and to be specularly reflected with probabilities equal to (r) and $(1-r)$, respectively (Succi, 2002). The case $r = 1$ corresponds to the fully bounce-back rule while $r = 0$ captures the fully specular boundary condition. This boundary condition provides a free adjustable parameter to model slip flow phenomena (Zhu et al., 2005, Zhang et al., 2005). Sbragaglia and Succi have shown the relationship between this parameter and the tangential momentum accommodation coefficient (Sbragaglia and Succi, 2005). As shown, the slip coefficient in Maxwellian type slip models can be obtained as follows:

$$A = \frac{c}{c_s}\,\frac{1-r}{r} \tag{5.19}$$

where c and c_s are the lattice speed and speed of sound, respectively, and A is related to the tangential momentum accommodation coefficient, TMAC, (σ_v) as, $A = \frac{2-\sigma_v}{\sigma_v}$.

It is noted that, for all simulations, mid grid configuration was used for modelling the boundary conditions. In this configuration, as can be seen in Figure 5.1, imaginary nodes are assumed (column $j-1$) such that the wall surface is at the centre of these imaginary and boundary nodes. Therefore, the boundary nodes (column j) are the nearest nodes to the wall surface.

5.3 Results and Discussion

5.3.1 Validation of the LBM simulation results

The simulation results of the LBM simulator were initially validated for non-slip gas flow in a channel. To this aim, the obtained velocity profile were compared with the analytical solution of the Navier-Stocks equation for non-slip gas flow. In these simulations, as the flow is in the continuum regime (non-slip), the molecular collisions at the wall boundaries should follow bounce back reflection (BB) which is equivalent to zero slip velocity at the wall surface. Figure 5.2 shows the simulation results of velocity profile in a channel (wall to wall) and the obtained values from the analytical solution of N-S equation (Bao and Meskas, 2011). The width and the length of the channel were 40 and 100 lattice unit (lu), respectively. As can be seen, the velocity profile predicted by LBM simulation is in good agreement with the exact solution of N-S equation. It is noted that the gas velocity at wall surface is zero for both cases. In addition, it has to be added that the LBM velocity profile is obtained from the calculated nodes velocity at the centre (wall to wall). As mentioned, the velocity of nodes is also calculated using Equation 5.6.

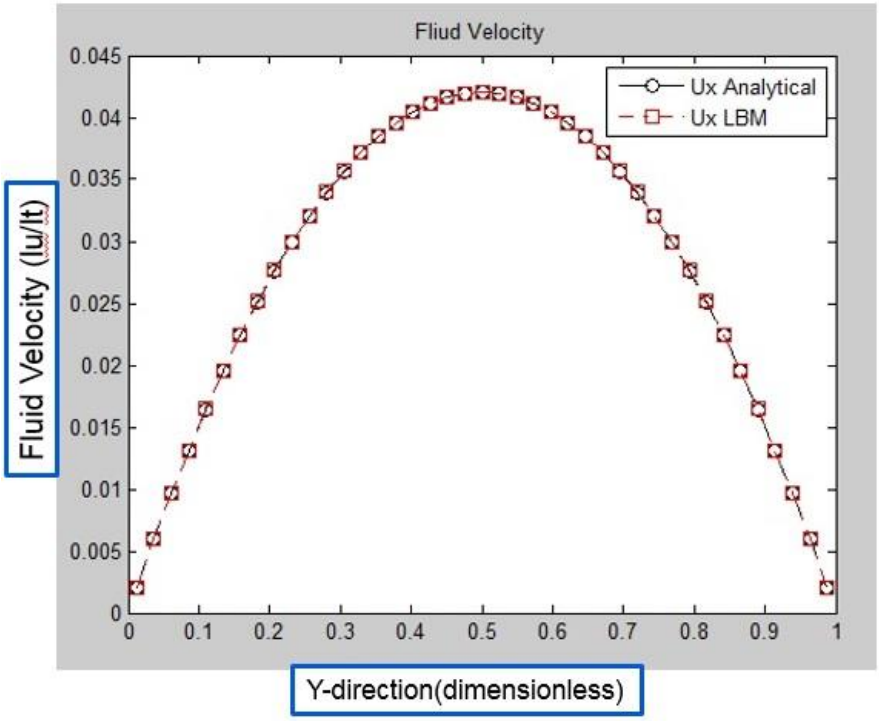

Figure 5.2: The LBM simulation results of the streamwise velocity profile and the obtained profile from the analytical solution of Navier-Stocks equation for incompressible flow in a channel.

The integrity of simulation results were further confirmed when simulating slip gas flow in a long microchannel. As the main purpose of these simulations was the gas slippage study, the simulation results of gas flow in a long microchannel with slip boundary condition should be validated before any other simulation.

To achieve this aim, slip boundary conditions (as described before) should be activated for simulation of gas flow in a microchannel. In these simulations, two different boundary conditions of diffusive reflection (DR) and Bounce back-Specular reflection (BSR) were used. Then the simulation results were compared with the results of other simulation techniques such as Direct Simulation Monte Carlo (DSMC) and Information Preservation (IP) methods reported in the literature (Shen et al., 2004). These methods are suitable for modelling slip flow and have been extensively used for such validation purposes (Verhaeghe et al., 2009, Guo et al., 2006). As mentioned before, the two relaxation time (TRT) scheme has been adapted in these simulations. For these validations, the length to height ratio (l/h) was taken to be 100 and the density ratio was $\frac{\rho_{in}}{\rho_{out}} = 1.4$ for Kn=0.0194

and $\frac{\rho_{in}}{\rho_{out}} = 2$ for Kn=0.194. These particular values of density ratio and Knudsen number were intentionally selected so that the results could be compared by the other methods (Shen et al., 2004). A schematic of the microchannel and the required input data are shown in Figure 5.3. It is noted that the Knudsen number is calculated using Equation 5.15. As shown on this figure, the characteristic length is 11 lattice unit (lu). The inlet and outlet boundary conditions (constant density) are also indicated in this figure. These constant density (pressure) were used to calculate the density and velocity of boundary nodes based on the well-known Zou and He method (Zou and He, 1997).

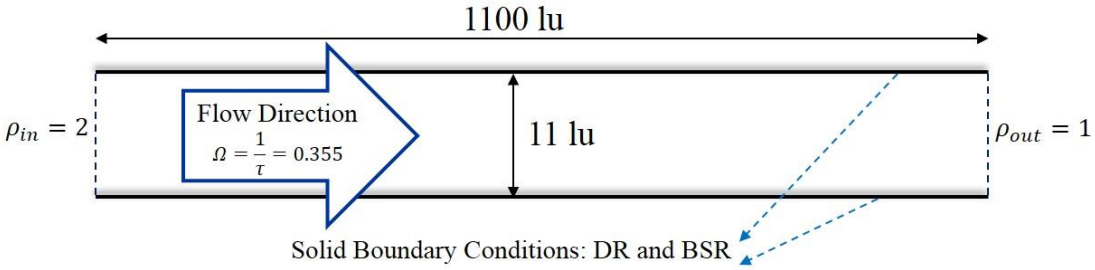

Figure 5.3: Schematic of the microchannel and the required input parameters.

Figure 5.4 presents the results of velocity profile across the channel simulated by DSMC, IP (from the literature) and the LBM-DR and LBM-BSR (in this study). The fluid velocities have been normalised by the maximum streamwise velocity at the centre. As shown in this Figure, the LBM results using both DR and BDR boundary conditions agree well with the results of the other two methods available in the literature, i.e. DSMC and IP, at both Knudsen numbers of 0.0194 and 0.194. It should be noted that the r-factor for the BSR boundary condition, which controls the rate of bounce back and specular reflection, should be given to the simulator as an input. In these simulations, an r-factor of 0.54 was given, which is equivalent to the TMAC of 0.8. This value for TMAC is in the range of measured TMAC values for gas flow in microtubes as descirbed in Chapter 4 (Maurer et al., 2003, Ewart et al., 2007, Graur et al., 2009). In Figure 5.4, it is also shown that in addition to LBM-BSR, the DR boundary condition can also properly capture the slippage in a single microtube for these range of Knudsen numbers. However, it has to be added that the LBM-DR results deviate very slightly from the IP and DSMC results at Kn=0.0194.

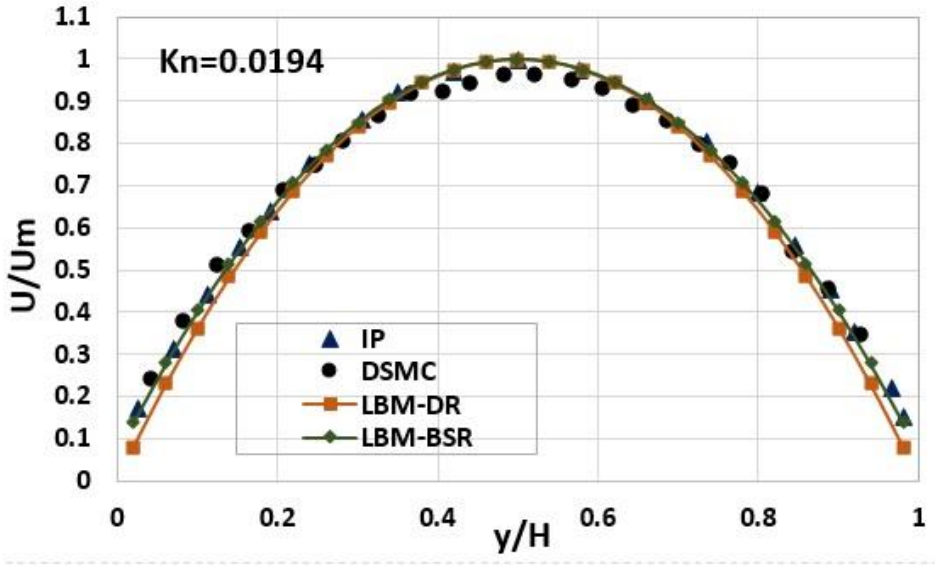

(a)

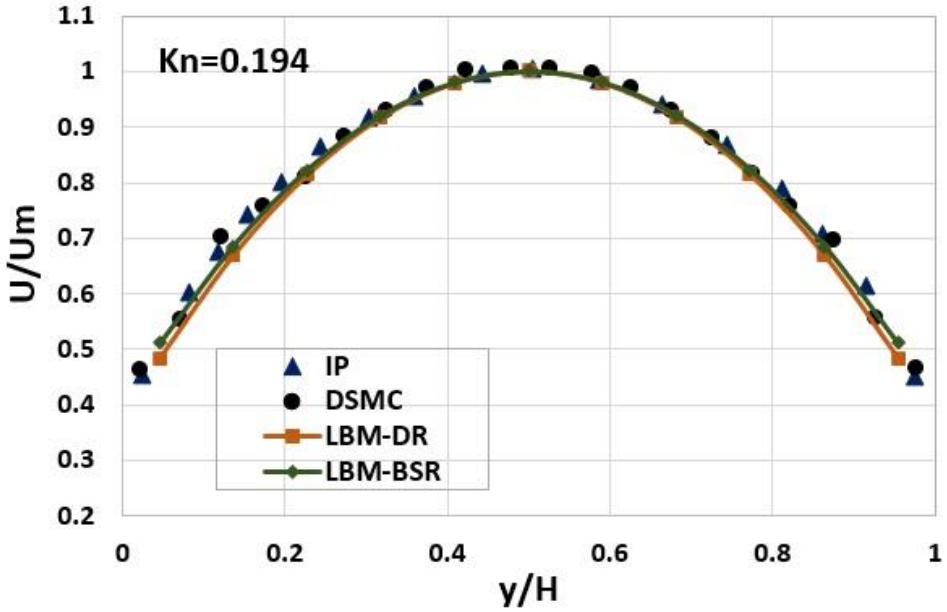

(b)

Figure 5.4: Results of streamwise velocity profile based on Information Preservation (IP), Direct Simulation Monte Carlo (DSMC), LBM-DR and LBM-BSR at a) Kn=0.0194 and b) Kn=0.194.

5.3.2 Slip Flow in a Single Channel and Comparison with Experiential Data

After validation of slip flow simulations for a microchannel, the program was used to generate the general slip plot (Figure 4.2). As mentioned before, general slip plot is a dimensionless graph which relates the permeability enhancement (due to the gas slippage) to the dimensionless Knudsen number of the system. After generation of this plot, it is

possible to compare it with Figure 4.2, which obtained from the experimental measurements for shale rocks samples. From the comparison, the proposed boundary conditions can be evaluated for the lattice Boltzmann modelling of gas flow in shale rocks.

For this purpose, gas flow in a long microchannel was simulated and the DR and BSR boundary conditions were used. To generate the general slip plot, the gas flow was simulated at different Knudsen numbers. The characteristic length of the system (channel width) and gas viscosity were altered to change the Knudsen number of the system. It is noted that the channel width and the gas viscosity are corresponding to the characteristic length of the rock and the pore pressure of the flowing gas (in macroscopic scale), respectively. For each simulation, the permeability of the channel was calculated from the obtained average streamwise velocity. In other words, first, the simulation is performed and the final values of the nodes' velocity were obtained. Then, the average fluid velocity was calculated by averaging the nodes' velocity values across the channel from wall to wall. Having the average velocity, the Darcy law can be used to obtained permeability.

For calculation of permeability enhancement (K_D), the obtained channel permeability for slip and non-slip flow were used. In other words, the gas flow was simulated with and without slip boundary conditions, i.e. the results with DR and BSR boundary conditions representing slip flow were compared with those with the bounce-back (BB) boundary condition describing the non-slip flow. For the non-slip flow case, the simulation results were double checked by the non-slip N-S solution. For all simulations, the inlet/outlet density ratio ($\frac{\rho_{in}}{\rho_{out}}$) was 1.02 and the length and width of channel were 310 and 30 lattice unit (lu), respectively.

Figure 5.4 presents the simulation results of dimensionless permeability of a microchannel at different Knudsen numbers when different boundary conditions were used. As can be seen in this figure, the simulation results of BSR-LBM with $\sigma = 0.8$ are similar to DR-LBM results. However both of them underestimate the permeability of porous media at different Knudsen numbers. As seen in Figure 5.4 the permeability enhancements obtained by these two boundary conditions (DR-LBM and BSR-LBM with $\sigma = 0.8$) are less than the measured values in porous media. In other words, the slippage intensity in porous media is higher than the predicted gas slippage by these two boundary conditions. Therefore, the TMAC value of 0.8, which was suitable for slip flow in a single

microchannel (as shown in Figure 5.4) is not proper for simulation of gas flow in shale rocks. This could be the main reason for poor performance of the available permeability predictions model in the literature since almost all of them have been developed assuming gas flow in a single pipe or a single channel. In addition, these models have never been compared with experimental data performed on porous media.

In order to increase the slippage intensity on wall surface, the input TMAC is reduced to 0.6 (i.e. shifting the gas collisions towards the fully specular). As illustrated in Figure 5.4 the experimental data can be better predicted by $\sigma = 0.6$. It means that, to account the gas slippage in shale rocks, the flow can be approximated by using a single pipe/channel model provided that the TMAC of 0.6 is used. In other words, the TMAC of 0.6 can simulate the solid-gas interaction in shale rocks more accurately, if a single pipe/channel is assumed. However, from Kn>0.1, the predicted permeability enhancements by BSR-LBM with $\sigma = 0.6$ start to deviate from the experimental data and overestimate the permeability. It highlights the difference between the gas flow in a single channel and porous media which is more dominant for the Knudsen numbers greater than 0.1. To investigate this, gas flow in a simple pore body/ pore throat (P/T) system was simulated and the results were compared with those obtained for gas flow in a single channel.

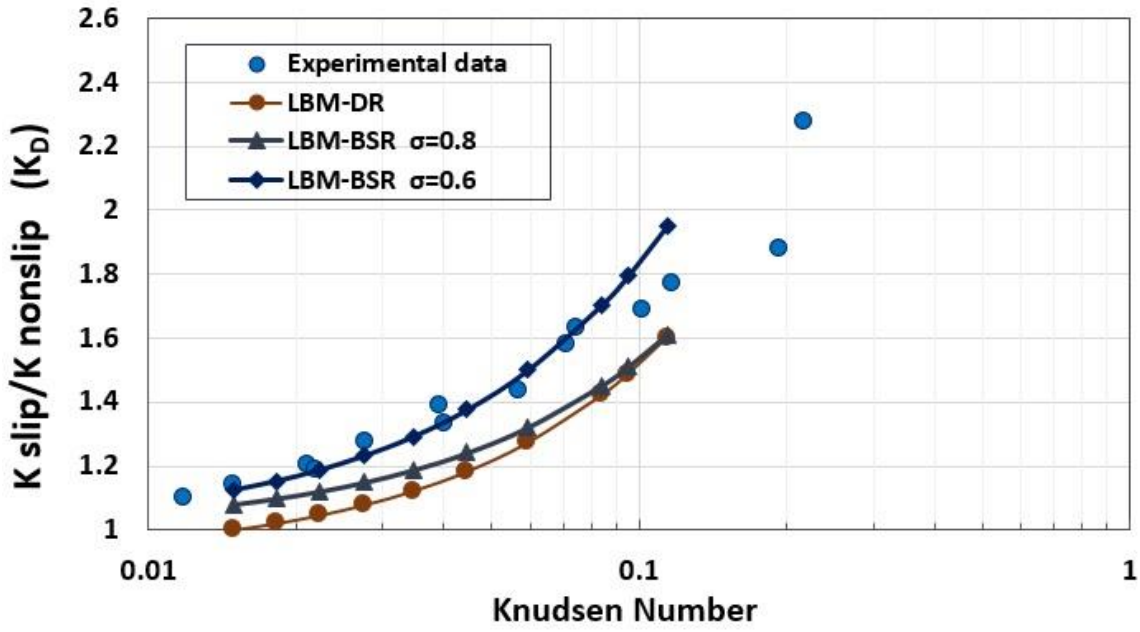

Figure 5.5: Dimensionless permeability versus Knudsen number; comparison of experimental data and simulation results for gas flow in single channel with different boundary conditions.

5.3.3 Modelling of Gas Flow in Pore Body/Throat System

In this section, slip flow is simulated in a "pore body/throat" system (P/T system) to study the gas slippage in non-uniform flow paths which is more close to the gas flow in porous media. As mentioned, it is aimed to determine the possible differences between slip flow in a single channel and a simple porous medium network. The simulation results of slip flow in P/T system were then compared with the obtained results for gas flow in a single channel and experimental data. This kind of comparison can help for better understanding of slip flow in porous media.

When modelling gas flow in porous media, selection of an appropriate characteristic length for the flow conduit attracts many discussions because there are different ranges of pore and throat sizes. The value of the Knudsen number depends on the assigned characteristic length for that porous media. In other words, having variable characteristic length results in variable values of Knudsen number. In this section, this ambiguity is investigated using the simulation results in the P/T system and the experimental data.

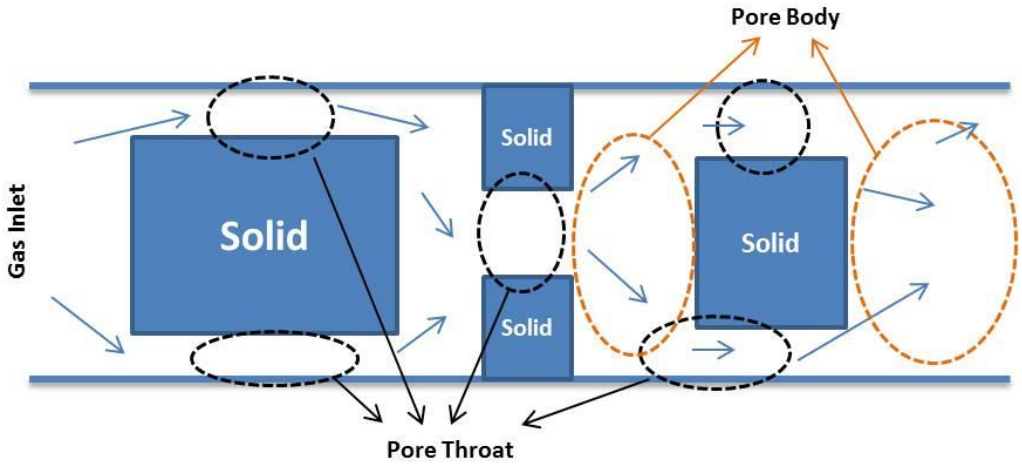

Figure 5.6: Schematic of the pore body/throat system used in this study.

Figure 5.6 shows the schematic of P/T system used in this study. The slippage on wall surface was modelled by using the BSR boundary conditions. The TMAC was also considered as 0.6 based on the discussion presented in the previous section. As mentioned before, the permeability was obtained based on the Darcy law using the total flow rate at the outlet. The dimensionless permeability factor (permeability enhancement) was also calculated from the slip and non-slip flow simulations. In other words, for slip flow, the gas stream in P/T system was simulated with the BSR boundary condition (with $\sigma = 0.6$).

For non-slip flow, bounce back (BB) boundary conditions were used to address the gas-wall interaction. It is noted that the boundary conditions were applied for all wall surfaces including the surface of the solid particles. For all simulations, the density ratio was 1.02 and the length of channel was 112 lattice unit (lu). As shown in Figure 5.6, the dimensions of the solid particles (representative of grains in porous media) were randomly selected to have different pore body and pore throat sizes. Knudsen numbers were also calculated based the obtained characteristic length from 1) pore bodies and 2) pore throats. In other words, for each simulation, the characteristic length of the system is calculated based on 1) the average value of pore body sizes and 2) the average value of pore throat sizes. As mentioned, it is aim to find out which size is suitable for calculation of system's Knudsen number and can capture the slip behaviour accurately.

The velocity profile obtained from a gas flow simulation in the P/T system is shown in Figure 5.7. In this case, the BSR boundary conditions were used and the obtained permeability was twice of that obtained from the non-slip simulation with BB boundary conditions. As seen in this figure, the gas particles' velocity increase when passing through the pore throats. This enhanced velocity can be even increased due to the gas slippage on the wall surface. Since the gas molecules experience more wall collisions in this area, it can be concluded that the gas slippage on the pore throat walls can probably play more important role in the permeability enhancement. For this case shown in Figure 5.7, the Knudsen numbers were calculated as 0.0842 and 0.1892 assuming average pore body sizes and average pore throat sizes, respectively. As obtained, the calculated Kn number from the pore throats can be greater than twice of the calculated Kn number from the pore bodies. However this difference depends on the aspect ratio (ratio of the pore body size to the pore throat size) and can be even higher in real porous media. Therefore, the characteristic length of the rocks should be properly assigned as it may have a great effect on the calculated Knudsen number and the corresponding predicted permeability.

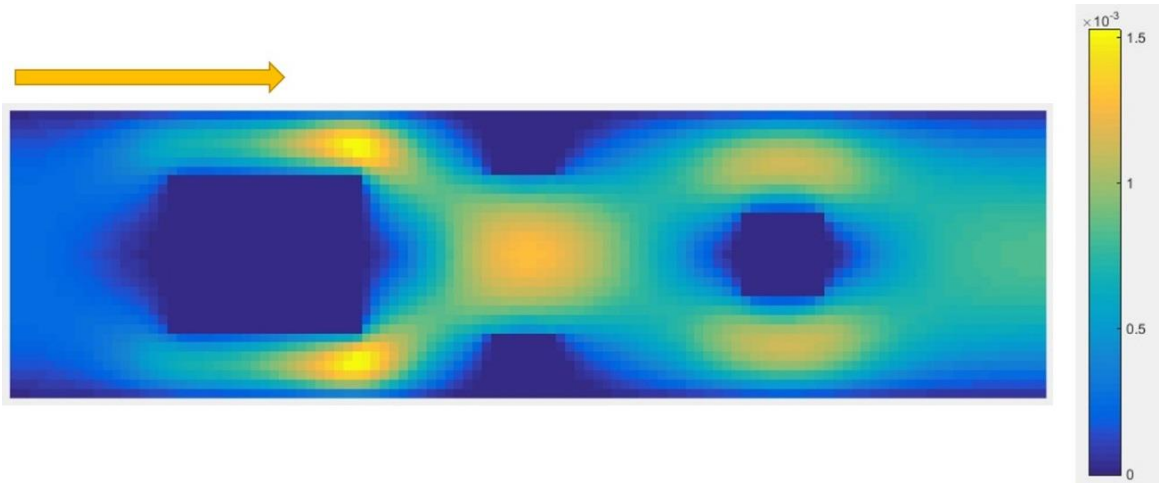

Figure 5.7: The velocity profile of the gas particles obtained from the LBM simulation of slip flow in the P/T system.

The results of LBM simulations of gas flow in the P/T system for different values of Kn numbers are presented in Figure 5.8. As shown in this figure, the obtained permeability enhancement factor (K_D) were plotted versus the calculated Kn numbers from pore bodies and pore throats. In addition, the experimental results are compared with both cases. As can be seen, the experimental data are in good agreement with the predicted permeability enhancements plotted versus Kn numbers obtained from the average pore throats. It means that the matrix permebaility can be better predicted when the system is charactrized based on the pore throat sizes rather than pore body sizes. It indicates that the porous media length scale, which has the dominant effect on the velocity enhancement, is the average of pore throat sizes not the pore body sizes. In addition, the simulation results of the P/T system were in good agreement with the experimental data when the aspect ratio of the P/T system was ~2.5. It can be found that the appropriate aspect ratio for simulation of slip flow in the shale samples under study is ~2.5.

Furthermore, from this exercise, it can be found that the observed permeability enhancement in porous media is mainly because of the gas slippage on throat wall surfaces. In other words, the resistance to pass through the pore throats [which is the main reason of fluid pressure drop (Lei et al., 2007)] is reduced due to the gas slippage. Therefore the gas flow can be alleviated when passing through the pore throats which results in a lower pressure drop and hence a higher permeability.

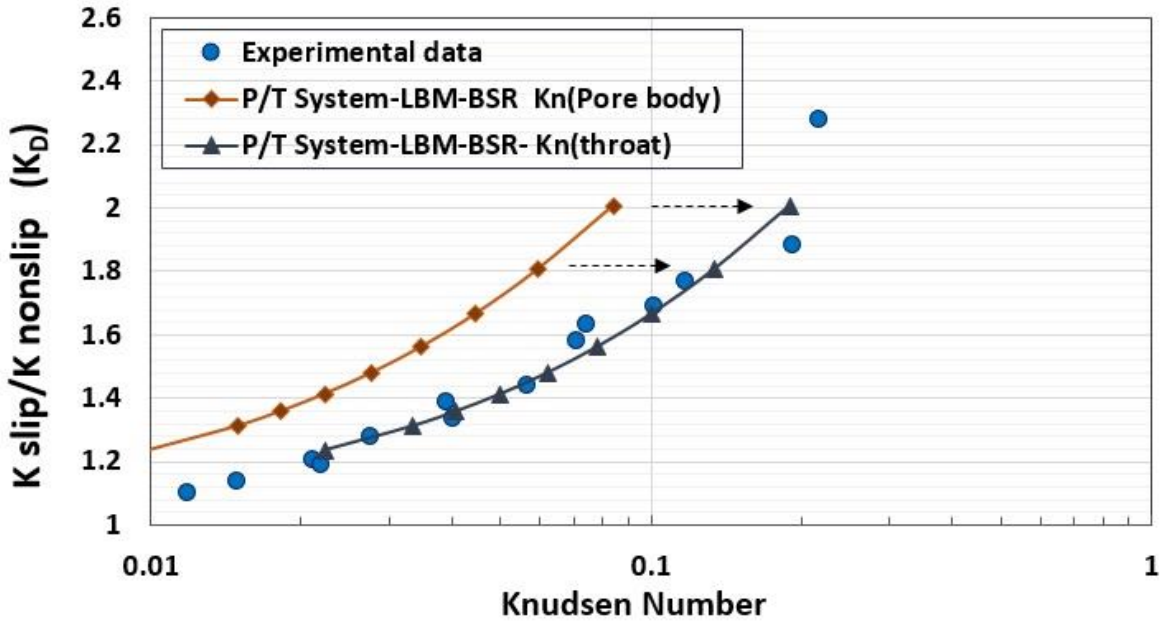

Figure 5.8: Comparison of experimental data and simulation results of dimensionless permeability as a function of Knudsen number obtained from LBM modelling of the pore body/throat system with different characteristic length.

In addition, the simulation results of the P/T system were compared with the reulsts obtained from the gas flow simulation in a single channel when the system's Knudsen number is the same for both cases. It should be noted that for the P/T system, the Knudsen number is calculated based on the averag throat sizes.

Figure 5.9 shows the simulated permeability enhacment factor (K_D) versus Knudsen number of the system for a single channel and for the P/T system. As illustrated in this figure, for Kn>0.05 , the predicted permeability for a single channel is higher than the predicted values for the P/T ststem. This could be the main reason for the permeability overstimation of the literature models (e.g. B-K model, see Figure 4.6). In other words, as these models are originally developed based on assumption of flow in a single pipe/channel, they always overstimate the permeability of porous media.

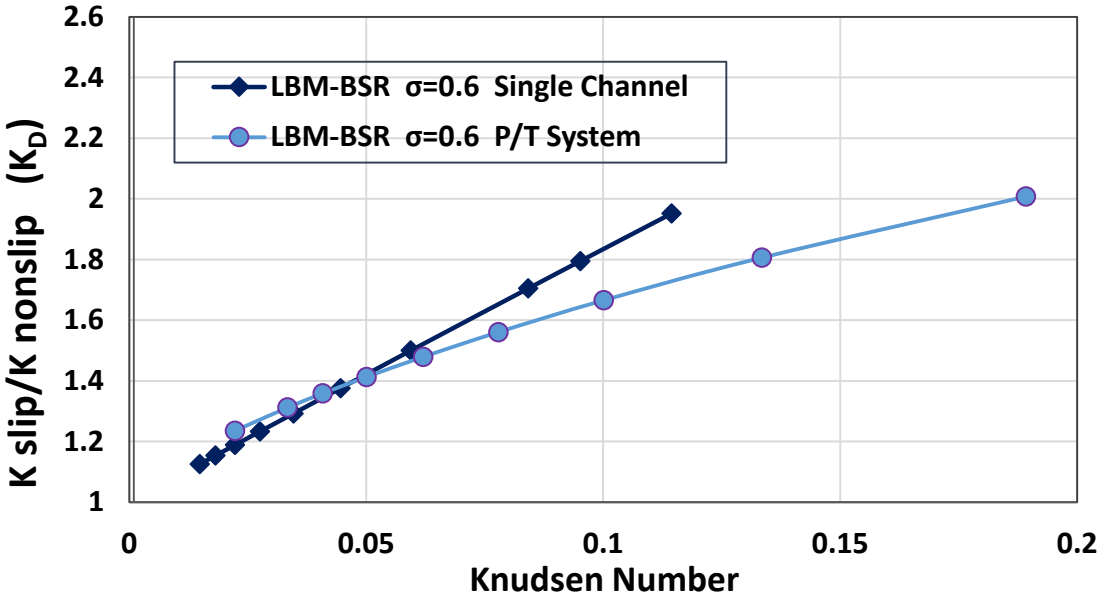

Figure 5.9: The LBM predicted permeability enhancements versus Knudsen number of the system for a single channel (rotated squares) and the P/T system (circles). For all simulations the BSR (with TMAC=0.6) boundary condition was used.

In addition, in Figure 5.10, the experimental data of permeability enhancements are compared with the predicted values obtained from LBM simulation of slip flow in a single channel and in the P/T system. As can be seen in this figure, for higher Knudsen numbers (i.e. Kn>0.1), the flow behaviour in these shale rocks can be better captured when a system of pores/throats are considered. In other words, the permeability enhancement is overestimated for Kn>0.1 when the gas flow is simulated in a single micropipe or microchannel. This overestimation is also given when the analytical models (which are originally developed for a single pipe) are used for shale matrix permeability prediction.

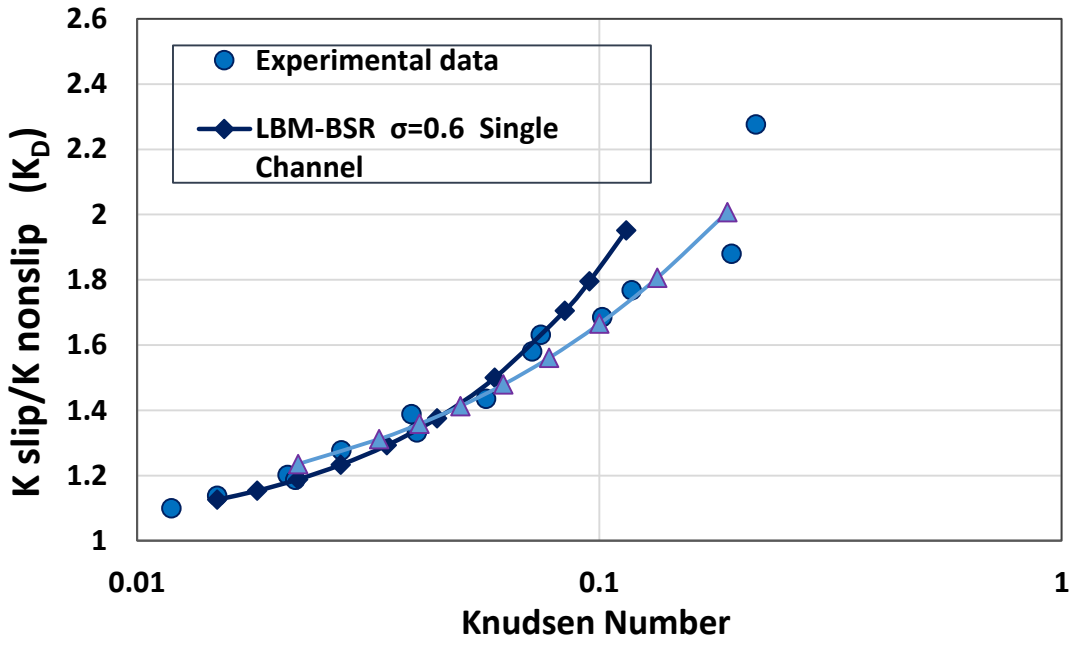

Figure 5.10: The measured permeability enhancement in shale rocks compared with the predicted values using LBM simulation of gas flow in a single channel and in the T/P system.

5.3.3.1 Effects of P/T Structure on the Simulation Results

In this section, the gas flow in different configurations of the P/T system were simulated using the BSR boundary conditions. It was aimed to evaluate the effects of the P/T structure on the obtained simulation results. To generate different configurations, the dimensions of the solid particles (see Figure 5.6) were changed. In all cases, the density ratio (inlet/outlet) and the aspect ratio were 1.02 and 2.5, respectively. The velocity profiles obtained for a typical simulation in these three structures are shown in Figure 5.11. As shown, different velocity profiles were obtained when the gas flow was simulated in these three P/T configurations. To evaluate the effects of pore structure on the permeability enhancement factor, the gas flow was simulated in these three configurations using bounce-back (for non-slip flow) and BSR boundary conditions (for slip flow). The obtained permeability were used to calculate the dimensionless permeability factor (K_D). The obtained permeability enhancements factors were plotted versus the Knudsen number of the system to generate the general slip plot. It is noted that boundary conditions were applied for the wall surfaces of solid particles.

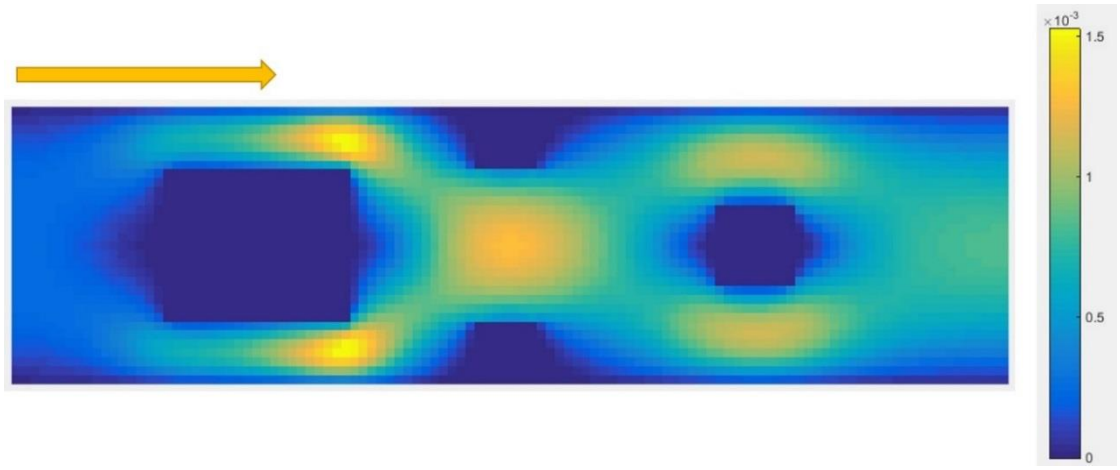

(a)

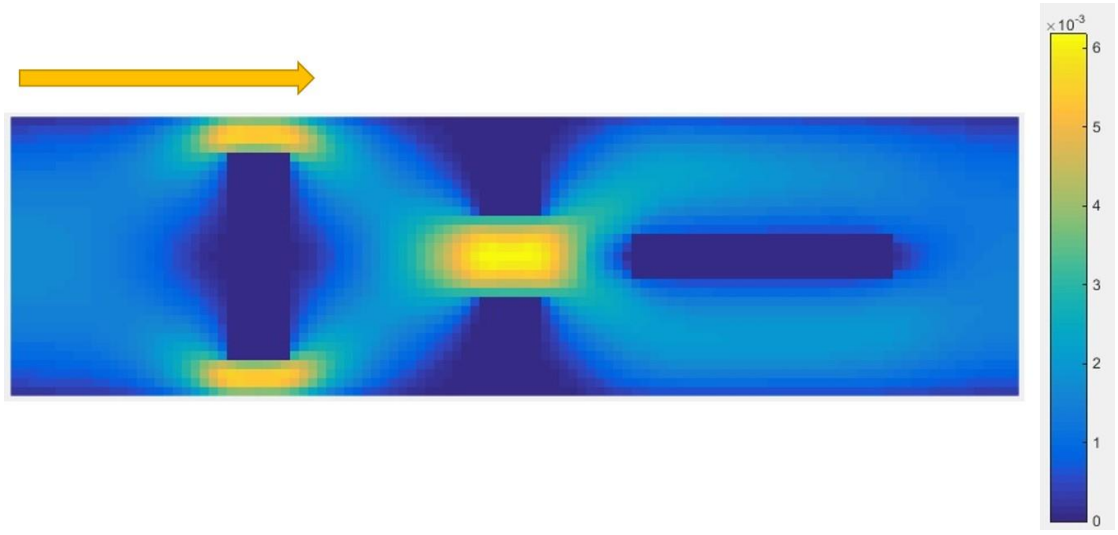

(b)

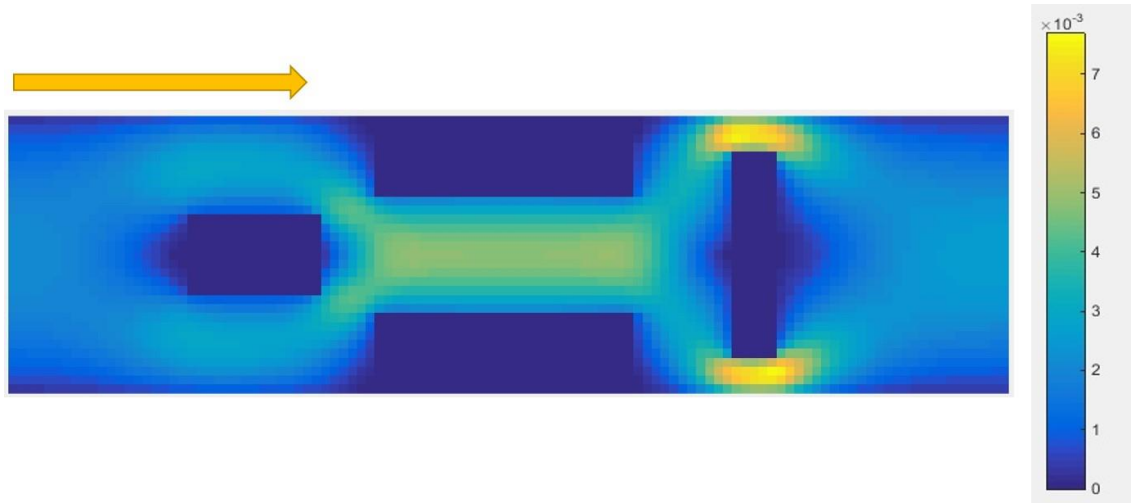

(c)

Figure 5.11: The velocity profile of the gas flow in three different configurations generated to study the effect of P/T structure on the permeability enhancement factors.

The obtained permeability enhancement factors (K_D) were plotted versus Knudsen number of the system in Figure 5.12. As shown in this figure, similar permeability enhancement factors were obtained for three cases. It shows that the impact of P/T structure on the permeability enhancement factors are minimal.

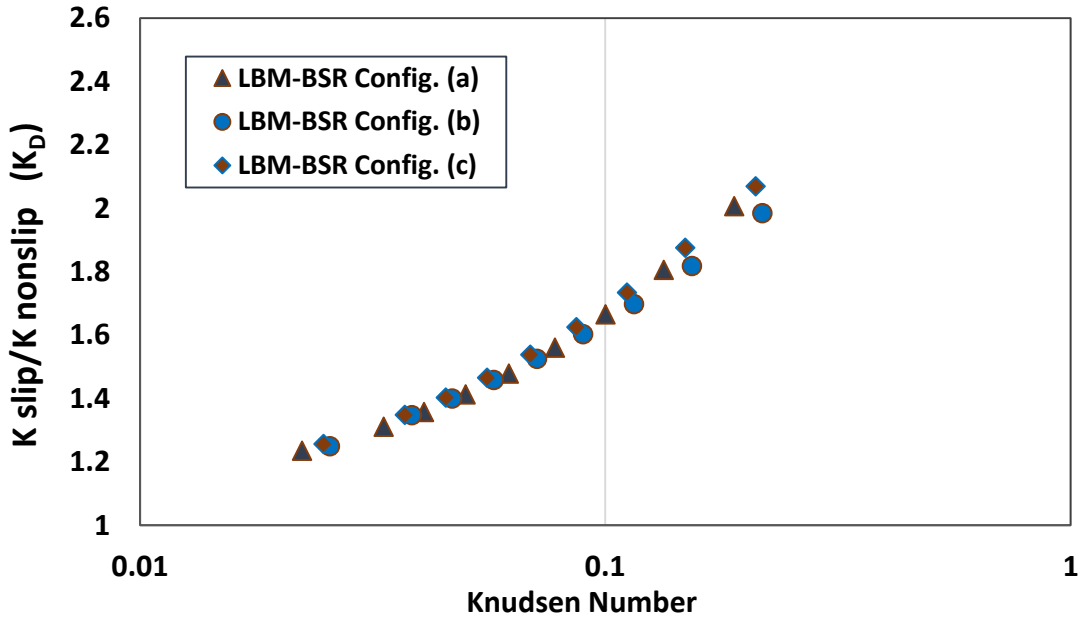

Figure 5.12: The dimensionless permeability factors versus Knudsen numbers obtained from the LBM-BSR simulations of gas flow in three different P/T configurations shown in Figure 5.10.

5.3.4 Slip Coefficients of N-S Equations from LBM-BSR Results

In this section, the LBM simulation results of gas flow in the pore body/throat system with slip boundary conditions were used to obtain the slip coefficient in the N-S equation. As extensively discussed in the literature (Barisik and Beskok, 2011, Zhang et al., 2010, Roy et al., 2003, Lockerby and Reese, 2008, Dongari et al., 2007), the N-S equations with slip boundary conditions can approximately predict the flow behaviour in the slip flow regime. As the gas flow in shale and tight reservoirs are mainly within the slip and transition regimes, the N-S equation can be used to predict the permeability enhancement in such systems. Solving the N-S equation with a second-order slip boundary condition gives the following dimensionless permeability expression (Eq 4.18):

$$K_D = \frac{k_{app}}{k_{non-slip}} = [1 + 4C_1Kn - 8C_2Kn^2] \quad (5.14)$$

where C_1 and C_2 are the first and second order slip coefficients, respectively. These coefficients can be obtained from the results of gas flow simulations. As shown in Figure 5.10, the LBM simulation results of gas flow in the P/T system are reasonably validated by the experimental data. Afterwards, the simulation results performed for a wider range of Knudsen number can be used for determination of slip coefficients in Equation 5.14. It is noted that more data for a wider range of Knudsen numbers can be obtained by performing LBM simulations. These results are shown in Figure 5.13. From the fitted line of the simulation results in Figure 5.13, the first and second order slip coefficients are found as 2 and 1.54, respectively. As indicated, these slip coefficients can be used for gas flow prediction when Kn<0.3. Considering the obtained slip coefficients above, the following slip boundary condition is proposed for using the N-S equation to describe the slip flow in these shale rocks:

$$u_s = 2\lambda \left(\frac{\partial u_s}{\partial n}\right)_s - 1.5\,\lambda^2 \left(\frac{\partial^2 u_s}{\partial n^2}\right)_s \quad (5.15)$$

where u_s is the slip velocity, n is the coordinate normal to the wall and λ is the gas mean free path. In addition, the predicted permeability enhancement factors obtained from LBM were compared with those obtained from the Klinkenberg model. As illustrated in this figure, the Klinkenberg model, which is a first-order slip model, overestimates the permeability enhancement. That is, as shown, for Kn>0.05, the first order slip models (e.g. Klinkenberg model) cannot be applied on the experimental data. In other words, for those experiments performed at the pressure conditions with Kn>0.05, the Klinkenberg model cannot be applied to extract the non-slip permeability. Therefore, for using Klinkenberg model, it is required to perform the experiments above a certain pressure (depending on the characteristic length of the system) which gives the system's Knudsen number less than 0.05.

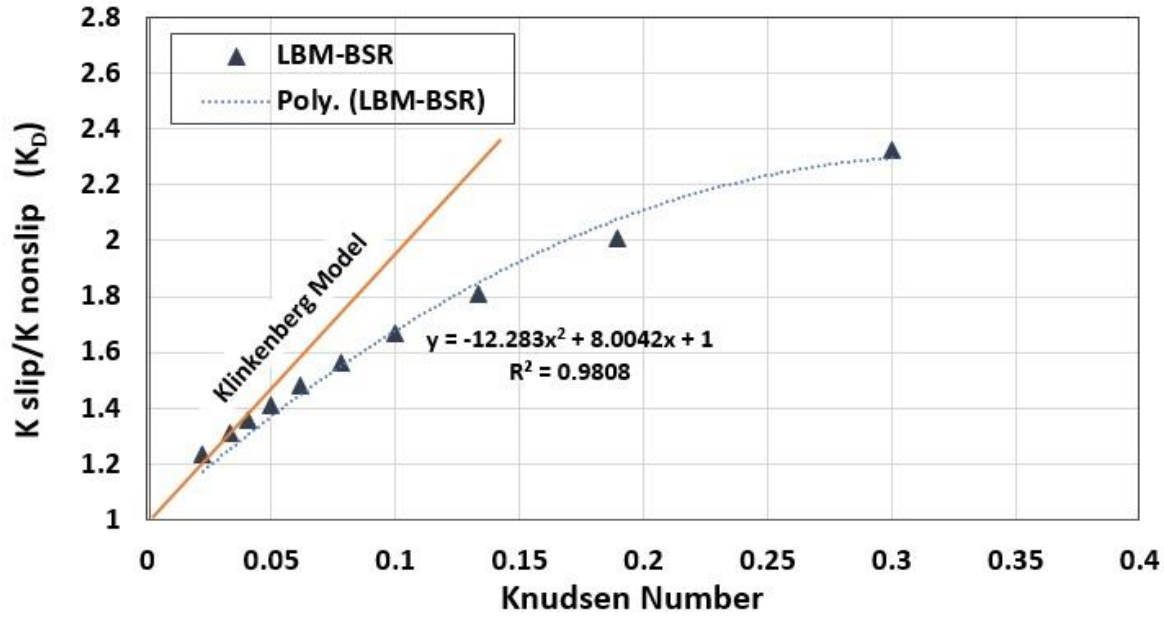

Figure 5.13: Simulation results of dimensionless permeability as a function of Knudsen number obtained from LBM modelling of a pore body/throat system. The second-order slip coefficients can be obtained from the results.

5.4 Summary and Conclusion

In this chapter, Two-relaxation-time based Lattice Boltzmann Method (TRT-LBM) was used to simulate the gas flow in shale rock samples. Different boundary conditions were applied to capture the gas slippage at the wall surface. First, the simulation results of LBM for non-slip flow were validated based on the solutions of N-S equations. In addition, for slip flow, the reliability of the LBM results with DR and BSR boundary conditions were also confirmed based on the solution of other methods found in the literature (IP and DSMC). After validation, slip gas flow was simulated and compared with the available apparent permeability experimental data of three shale rocks in slip and transition flow regimes. The effects of different slip boundary conditions and various accommodation coefficients were studied. In addition, a system of pore body/throat (P/T) was modelled and the simulation results were compared with those obtained for gas flow in a single channel. Furthermore, the simulation results of gas flow in the P/T system were compared with the experimental data. Finally, the LBM simulation results were used to propose appropriate slip coefficients for N-S equation for a wider range of Knudsen numbers. The following observations/conclusions can be made/drawn from this study:

- It was shown that the diffusive reflection (DR) boundary condition could not be used to capture the slip flow in these three shale rocks. That is, the results of LBM-DR underestimated the permeability enhancement and hence, using this boundary condition is not suggested.

- The gas slippage modelling with the BSR boundary condition with the literature value of TMAC=0.8 also underestimates the permeability enhancement of these shale rocks. It was found that the TMAC of 0.6 could better estimate the permeability enhancement if the gas flow is simulated in a single channel.

- It was shown that the characteristic length of porous media can be better described by the average of pore throat sizes rather than average of pore body sizes. In addition, it was concluded that the gas slippage on the wall surface of pore throats has significant effects on the flow enhancement. This is mainly because of the pressure drop reduction across the pore throat which is due to the relative ease of flow with slippage.

- Furthermore, the simulation results of slip flow in a single channel were compared with those obtained for flow in the P/T system when the Knudsen number of the system is the same. From the comparison, it was found that, for Kn>0.05, the LBM simulation of slip flow in a single channel gives higher permeabilities compared to those values obtained from the LBM simulation in the P/T system.

- Moreover, the experimental data could be better simulated when the system of pore body/throat was considered. It means that the permeability enhancement is overestimated for Kn>0.1 when the gas flow is simulated in a single micropipe or microchannel. It was concluded that the main reason for the overestimation of the literature models can be due to the assumption of flow in a single pipe/channel.

- From the fitted line to the simulation results (up to Kn=0.3), the first and second order slip coefficients of the N-S boundary condition were found as 2 and 1.54, respectively. Also, it was shown that the Klinkenberg model can give significant errors when it applies on the experimental data measured at the pressure conditions which gives Kn>0.05.

Chapter 6: Relative Permeability Measurements of Two-Phase Flow in Shale Matrix

6.1 Introduction

Relative permeability (kr) functions are among the required data for simulation of multiphase flow in porous media. Such data are crucial for the estimation of productivity, ultimate recovery, formation injectivity and planning various engineering operations, including EOR and diagnosing formation damage (Honarpour and Mahmood, 1988).

Relative permeability measurement of shale samples is extremely difficult due to several unconventional processes which have been discussed in the previous chapters. In addition to the effects of mechanisms explained in these chapters on the relative permeability data, further difficulties can be encountered during the kr measurements because of the low porosity and permeability of these rock types. For example, injection at high flow rates is not practical for fluid displacement in shale/tight samples. In addition, the low pore volume of unconventional samples makes all measurements difficult and subject to error. Hence, special facilities are required when dealing with such low pore volume core samples. Moreover, conducting displacement experiments is mostly time-consuming, as the fluid has to be injected at a low rate.

The non-Darcian flow regimes can also be among the unconventional mechanisms which make the kr measurements more difficult. The presence of these regimes means that all measured kr data should be corrected for gas slippage, if the relative permeabilities were measured under different pore pressure conditions. Likewise, the effective confining stress can also have significant impacts on the measured data. Therefore, the relative permeability measurements should be conducted at the same effective stress, otherwise the values need to be corrected.

In addition to the effects of these natural mechanisms, experimental artefacts can distort extremely the measurements. The capillary end effect (CEE) is the most dominant one during such relative permeability measurements. As explained in Chapter 2, capillary end effects are more significant in tight/shale formations, due to the higher capillary pressure in these rock types compared to those in conventional rocks.

In this chapter, the results of measuring relative permeability of a tight sandstone and three shale samples are presented. To overcome the difficulties regarding the kr

measurements of shale rocks, a special setup was designed and used for these measurements. The reliability of the experimental apparatus was also evaluated by kr measurements of a tight sandstone core. The effects of gas slippage and net stress were minimised by performing all the experiments at the same pore pressure and net stress. In addition, a fluid system with low viscosity was used for all measurements, to increase the injectivity and reduce the pressure drop created across the core. To handle the CEEs, a new technique has been proposed to correct the experimental kr data. In this method, four different flow rates are required to be injected for each flow rate ratio. For all flow rates, the pressure drop across the core and the measured wetting phase saturations (obtained by material balance) are used to solve the four pressure and four saturation equations simultaneously. From the results, the CEE length at each flow rate, corrected wetting phase saturation, average wetting phase saturation in the CEE region and the corresponding kr values can be obtained. It should be noted that, the correction of the kr data means that more accurate values are obtained through the modification of kr calculations. In other words, by this corrections (or improving the calculations), the influence of CEE can be removed during the SS kr measurements.

To examine the integrity of the proposed method, two theoretically generated data sets were used. The results obtained from this technique were compared with the original kr input data to evaluate the prediction error. In addition, as will be discussed in the last part of this chapter, the proposed technique has been applied to the experimental data, from measurements performed on an Eagle Ford and a Pierre shale sample to obtain the actual kr functions.

6.2 Tight/ Shale Relative Permeability Measurements

6.2.1 Experiments: Materials and Method

Relative permeability data are usually measured in the laboratory using different techniques, including centrifuge, steady state, and unsteady state displacements. In a steady-state displacement, a constant total flow rate of liquid and gas is usually injected, while their ratio can be changed. In this method, it is necessary to reach to the equilibrium state across the core. After equilibrium, the pressure drop and flow rate data are used to calculate the individual phase kr values, according to Darcy's law. The measured kr data is then related to the average saturation in the core, determined by material balance.

Among the methods developed for kr measurements, the most reliable technique is the steady state method (Shen and Bae, 1987, Maini et al., 1990). In this technique, kr curves can be determined for a wider range of saturation compared to the other methods. However, this method has some disadvantages, including the long time required to attain the steady state and the capillary end effects (Richardson et al., 1952, Virnovsky et al., 1995). Nevertheless, considering the non-uniqueness and unreliability of the results obtained by the other techniques, the steady state method is still the most reliable one for relative permeability measurements.

In this study, the feasibility of shale relative permeability measurements by steady state method is investigated. It is noted that the standard procedure with small changes was followed to measure the steady state relative permeability of tight and shale samples. In other words, in standard procedure, the test is started at the lowest LGR and completed at the highest LGR with several LGR measurements in between. However, in this study, for the measurements on tight and shale rock samples, after reaching equilibrium state for each LGR, the test was finished and the initial condition was restored (Except in some cases that the test was continued by injection of single phase to obtain effective permeability at end points). Then the same procedure was repeated for the next LGR test. This procedure was followed since the experiments were time consuming and the equilibrium condition was stabilized after a long time. For each LGR experiment, depending on the injection rate and the absolute permeability of the rock under study, it could take up to 5 days to reach the equilibrium state.

The basic properties of the shale rock samples used in this study are shown in Table 6.1. As shown, a Scioto sandstone, two Eagle Ford and a Pierre shale sample were used. The Scioto sandstone core was washed with methanol and dried for 12 hours in the oven. The shale rock samples were also dried overnight at 105 ℃ while connected to the vacuum pump. All absolute permeabilities of core samples were measured at the effective stress of 1000 Psi (assuming an effective stress coefficient of unity). For these measurements, a fluid system of Butane/Nitrogen (C4/N2) at 1500 Psi and 22 ℃ was used. The fluid PVT properties were obtained using PVTi - Eclipse Software. The interfacial tension (IFT) of the system was estimated as 5.5 mN/m under the experimental conditions. As mentioned above, this fluid system (with low viscosities) was intentionally selected to minimise the pressure difference across the core. For fluid preparation, pure nitrogen (N2) and butane (C4) were mixed in the recombination cell and shaken for 24

hours to reach the equilibrium state. Then, the liquid and gas were separated into gas and liquid injection cells.

Table 6.1: Basic properties of the tight sandstone and the shale rock samples used in this study.

Sample	Length (cm)	Diameter (cm)	Porosity (%)	Abs. Permeability (μD)	Moisture
Scioto Sandstone (S1)	14.1	3.80	17.7	455	Fully Dry
Eagle Ford Shale (E3)	4.61	3.77	13.5	9.9	Fully Dry
Pierre Shale (P3)	5.08	3.77	31.8	8.5	Fully Dry
Eagle Ford Shale (E4)	5.09	3.80	13.0	16.6	Fully Dry

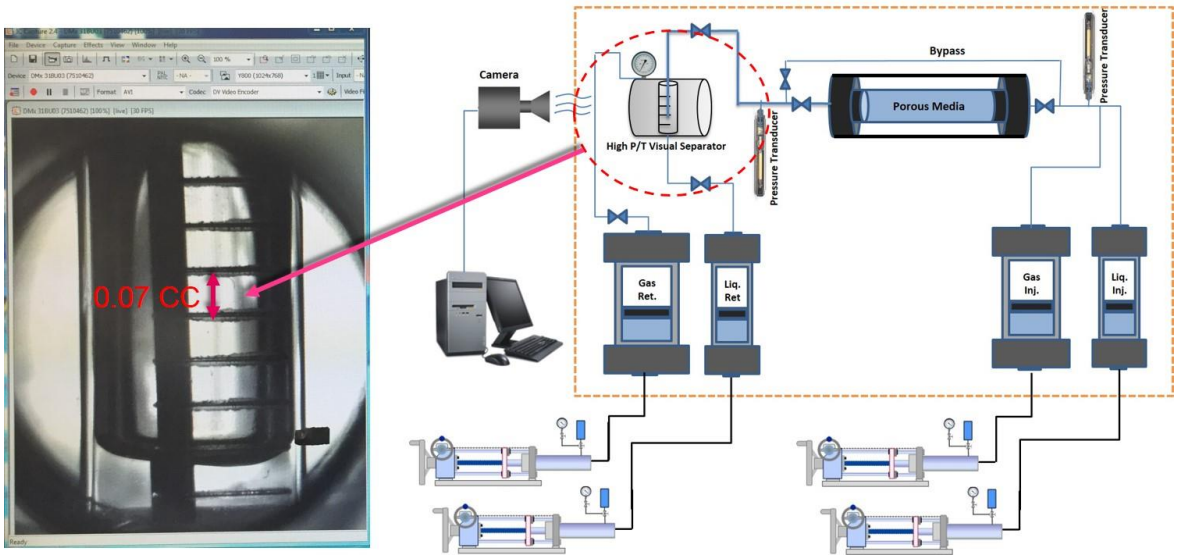

Figure 6.1: The schematic diagram of the steady state relative permeability measurement setup equipped with a high-pressure visual separator with an accuracy of 0.07 cc.

The schematic diagram of the steady state setup is shown in Figure 6.1. As illustrated, two cells were used for simultaneous injection of equilibrated gas and liquid. Two retract (extraction) cells were also used to collect the fluids. These cells were positioned after a High Pressure High Temperature (HPHT) separator. The fluids were extracted after passing through the HPHT separator. The pressures were measured across the core at the inlet and outlet using a Quartzdyne pressure transducer. The accuracy of these pressure transducers is ±0.015% FS. Four accurate Quizix pumps were used at the same time for fluid injection and retraction. Prior to each experiment, a gas leakage test at high pressure was performed on the system. In addition, the dead volumes of all lines and valves were measured based on the Boyle two-cell method, using nitrogen at low pressure. The measured dead volume was double-checked by using a standard core, which had a known pore volume of 0.4 cc.

The procedure followed in the SS kr measurements in this research can be summarized as below. First, the core sample was fully saturated with gas. Then the liquid and gas was injected simultaneously through the core and continued to reach the equilibrium state. Gas and liquid were injected into the core at the selected value of LGR (liquid to gas ratio, volume liquid/volume gas, at test conditions). The equilibrium state was achieved when the rate of gas and liquid injection was equal to rate of gas and liquid retractions. In addition, the pressure drop across the core sample was stable when the steady state condition was achieved. Then, the average saturation of the core was calculated based on an accurate material balance, benefiting from the HPHT visual separator, which enabled the gas and liquid production to be measured at test conditions. In other words, the error caused by fluid expansion/contraction was removed when the measurements were performed under the experimental conditions. Furthermore, since the pore volumes of shale samples are generally low, the material balance calculations are subject to significant error without accurate measurement of fluid production. The accuracy of the visual separator used in this study was ±0.07 cc, which allows an error of <1% for saturation measurements. This value depends on the accuracy of the pumps, the accuracy of the HPHT visual separator and the total pore volume of the rock under study. Finally, the recorded pressure drop was used in the Darcy law to obtained relative permeability values for both liquid and gas phases. As mentioned, fluid properties were also estimated using PVTi - Eclipse Software.

It has to be added that the effective permeability values at the end points were obtained by injection of a single phase at the end of the SS-kr measurements with highest and

lowest LGR. In other words, after completion of SS kr measurements with the lowest LGR, the liquid injection was stopped and only gas was injected into the core. The single phase gas injection was continued until no liquid was produced. At that points, the pressure drop was recorded and used for calculation of effective gas permeability. Similar procedure was followed to obtained effective oil permeability.

After each measurement, to restore the initial conditions, the core was left at atmospheric pressure and room temperature overnight. In addition, the core was cleaned by injection of several pore volumes methane to remove any remained liquid butane. The core absolute permeability was measured before each test to ensure that the original conditions had been restored.

6.2.2 Experimental Results

6.2.2.1 Scieto Sandstone Relative Permeability

The reliability of the measurement facilities was checked by performing steady state relative permeability (SS-kr) measurements on a long tight sandstone core. The results are shown in Figure 6.2. As shown, for the two pressures of 500 psi (IFT of 9.3 mN/m) and 1500 psi (IFT of 5.5 mN/m), almost similar kr data were obtained. It should also be mentioned that, for each pressure, the measurements were repeated twice to check the repeatability of the results. In addition, it was found that the CEE was not dominant in this core, because for each LGR, the kr data were measured by injection of different total flow rates and the same data points were obtained. It is noted that the error of $\pm 4.5\%$ was expected for all relative permeability measurements (See Appendix 1).

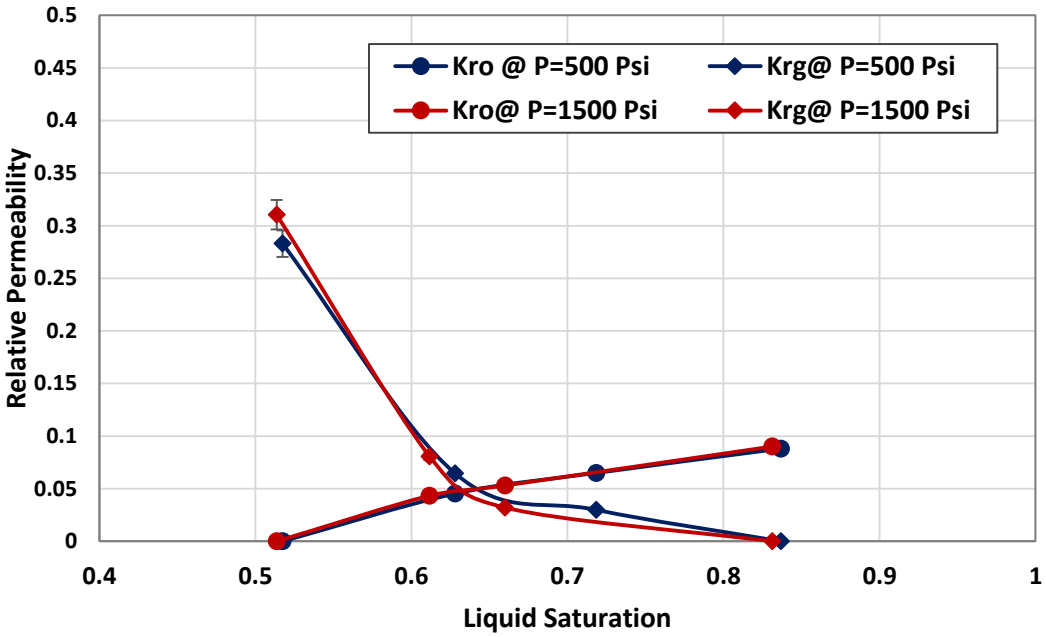

Figure 6.2: Gas/oil SS-kr data of Scioto sandstone measured at two different pressures of 500 psi (9.3 mN/m) and 1500 psi (5.5 mN/m) using Butane/Nitrogen fluid system.

6.2.2.2 Relative Permeability of Shale Samples

The relative permeabilities of Eagle Ford (E3) and Pierre shale (P3) were measured following the steady-state method explained earlier. For the Eagle Ford sample (E3), four total flow rates of 10 cc/hr (equivalent to 1.6 m/day), 13 cc/hr (2.1 m/day), 16 cc/hr (2.5 m/day) and 20 cc/hr (3.2 m/day) were injected. As the SS-kr experiments are tedious and time-consuming, the experiments were performed at two LGRs. To have a wider range of saturation, LGRs of 0.08 and 0.25 were selected. It is noted that, compared to conventional samples, the equilibrium state for unconventional rocks is achieved after a longer period of time. This is because of their ultra-low permeability and low injection rates used for displacement. To determine the end points, the relative permeability of oil and gas were measured at residual liquid and residual gas saturation, respectively.

The measured SS-kr data of the Eagle Ford (E3) sample are shown in Figure 6.3. As illustrated, different relative permeability curves were obtained for different flow rates. As reported by many researchers (Osoba et al., 1951, Rapoport and Leas, 1953, Honarpour et al., 1986), in the absence of CEE, the relative permeability data are not a function of flow rate. Therefore, it can be stated that these results have been affected by CEE. As explained before, for unconventional rocks, the capillary pressure is much higher compared to conventional samples. This high capillary pressure enhances the effect of

CEE on measured data. In fact, the liquid hold-up at the core outlet depends on the competition of capillary forces and viscous force. In addition, as higher flow rates cannot be injected into such a tight matrix (injection at high rates results in a very unsustainably high pressure drop across the core) the viscous forces are small and the capillary forces are dominant. For example, for the core samples under study, the maximum practical injection rate is assumed to be 20 cc/hr, considering core physical properties and fluid viscosities at the experimental conditions. Injecting at higher flow rates creates a high pressure drop across the core, which results in an intensive stress change along the core. In addition, rock and fluid properties may change significantly, when a high pressure difference is applied across the core.

As can be seen in Figure 6.3, for almost all flow rates, different saturation and SS-kr values were obtained, which confirms the presence of the capillary end effect (CEE). In these tests, and even at the highest injection flow rate, the CEE had a significant impact on the measured data. This discrepancy in the measured kr increased as the LGR was decreased towards lower liquid saturation. It further confirms that the capillary end effect is the main reason for this observation. In other words, by reducing LGR, the end effects become more dominant. Here, at the left-hand side of Figure 6.3, significant differences are observed between the measured SS-kr at the lower LGR which confirms the dominant influence of CEE on the measured data. In addition, as seen in this figure, the difference in the measured residual gas saturation and the SS-kr value at different flow rates is negligible at higher LGR (right-hand side of Figure 6.3). Therefore, it is more necessary to correct the experimental kr data for CCE at the lower LGRs. This behaviour is also observed in the CEE simulation results described in the next section.

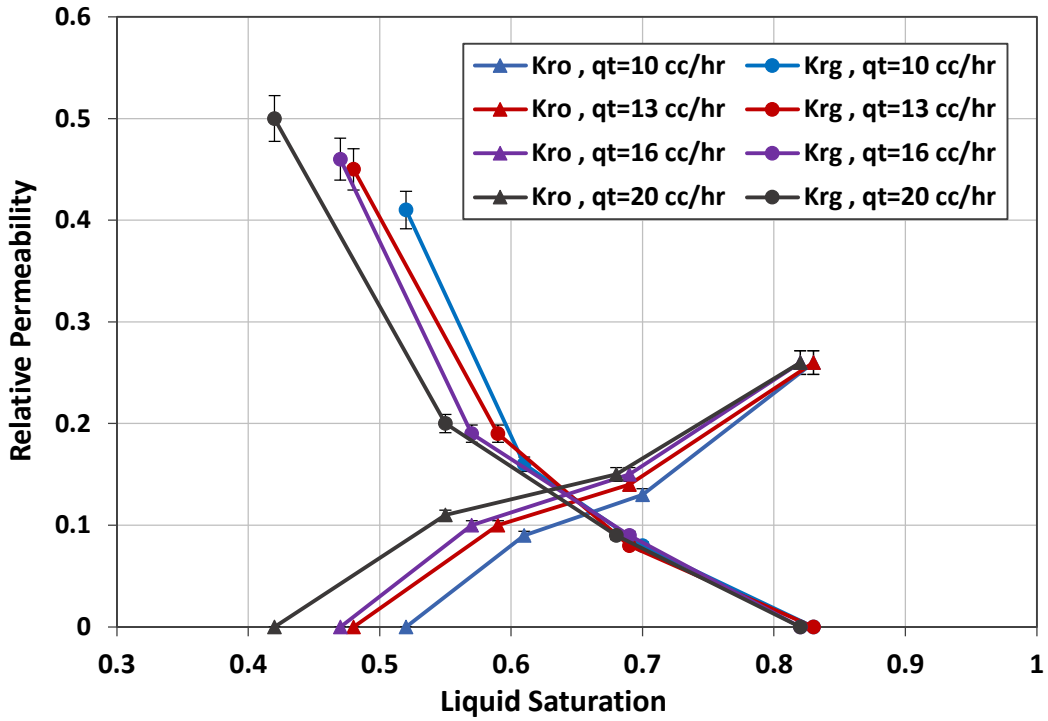

Figure 6.3: Gas/oil SS-kr data of Eagle Ford sample (E3) for different total flow rates measured at 1500 psi, corresponding to IFT of 5.5 mN/m.

Figure 6.4 shows the relative permeability data obtained for the Pierre shale sample. The experiments were performed with the same fluids and experimental conditions. For this core sample, the fluids were injected at four total flow rates of 9 cc/hr , 12 cc/hr, 15 cc/hr and 18 cc/hr. As seen in Table 6.1, the absolute permeability of the Pierre (P3) sample was 8.5 μD, which was very close to the permeability of E3 sample. However, as discussed in Chapter 3, the measured capillary pressure of the Pierre shale was higher than that of the Eagle Ford shale samples.

A difference in the measured relative permeability data can also be observed for the P3 sample. Similarly to the case for E3, the measured kr data show more discrepancy for different flow rates, especially at the lower LGR. This confirms the dominant role of the CEE in all measurements. However, there are some differences when comparing the measured data from E3 (shown in Figure 6.3) and P3 (shown in Figure 6.4). Despite similar absolute permeability and total injection rates for both E3 and P3, the difference in the measured kr and saturation data at different rates is higher for P3. For example, the differences between the measured end point liquid saturations for the highest and lowest rate (at residual liquid saturation) are 10% and 17% for E3 and P3, respectively, showing

that the capillary end effects were more dominant for P3 compared to E3 measurements. This greater capillary end effect is expected, due to the higher capillary pressure of P3 compared to E3.

In addition, the measured residual gas saturation for E3 was higher than the residual gas saturation obtained for P3. As seen in Figure 6.3 and Figure 6.4, the residual gas saturations obtained were 18% for E3 and 8% for P3. The level of residual gas saturation can be linked to the heterogeneity of the samples. At similar conditions, the greater the heterogeneity, the higher the residual gas saturation. Assuming strong wettability of both shale rocks with respect to oil, it seems that the Pierre shale sample is more homogeneous compared to the Eagle Ford sample. It is noted that, from the pore size distributions measured for these two shale samples (Figure 3.3), a wider range of pore size was also obtained for E3, which is consistent with this assumption.

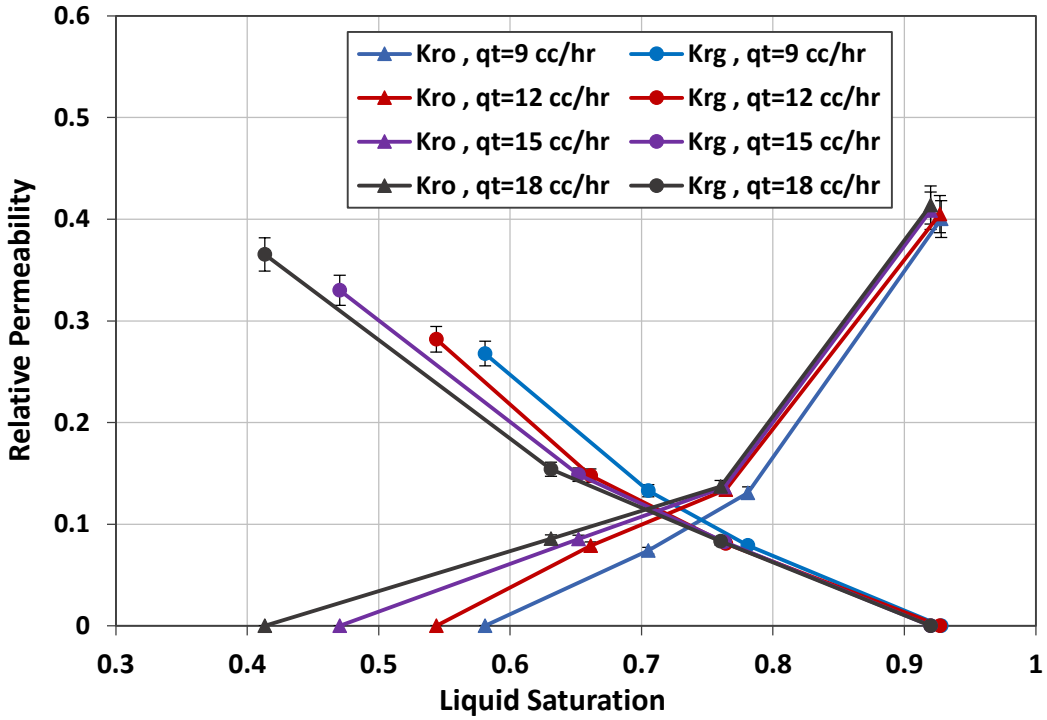

Figure 6.4: Gas/oil SS-kr data of Pierre sample (P3) for different total flow rates measured at 1500 psi, corresponding to IFT of 5.5 mN/m.

6.2.2.3 Effects of Net Stress on Relative Permeability Data

As discussed in the previous chapters, the effective stress can strongly affect the absolute matrix permeability of shale samples. However, the impact of effective stress on relative permeability of shale samples has not yet been investigated. In this research the relative permeability of an Eagle Ford shale sample (E4) was measured at two different net stress values of 1000 and 3000 psi. All other experimental conditions were kept constant for both experiments. The measurements were performed at 1500 psi pore pressure using the fluid system of N2/C4 described earlier. The steady-state technique was also used for these measurements, using the same equipment illustrated in Figure 6.1. The absolute permeability and porosity of shale sample E4 were measured as 16.6 μD and 13% at 1000 psi net stress. After kr measurements at the net stress of 1000 psi, the original condition (dried clean core) was restored and the net stress was then increased gradually to 3000 psi. The system was left for 24 hours to reach the equilibrium state and the porosity and absolute permeability were measured again. The porosity and absolute permeability were obtained as 12.75 μD and 12.3 % at 3000 psi net stress. The kr measurements were then repeated at the same pore pressure (1500 psi) with the same procedure and fluid mixture. For both measurements, a total flow rate of 10 cc/hr was used. Figure 6.5 shows the relative permeability data for the E4 shale sample measured at two different net stress values of 1000 and 3000 psi.

As illustrated in this figure, increasing the net stress shifts the plot toward the right-hand side, which means an increase in the measured liquid saturation for the same LGR. As explained in the previous section, the measured relative permeability data of shale samples are strongly influenced by CEEs. In this rock type, due to the high capillary pressure, the viscous forces could not overcome the capillary forces entirely. Hence the CEE was dominant, as a result of competition between capillary and viscous forces.

In this experiment, the average of pore and throat sizes were decreased by increasing the effective (net) stress. Thus, the capillary pressure was increased and the CEE became more pronounced. Variation of capillary pressure with net stress also were reported and quantified in the literature (Wu, 2015, Wu and Fakcharoenphol, 2011). As seen in Figure 6.3 and Figure 6.4, for the same LGR, the measured liquid saturation was increased when the CEE was magnified by reduction of injection flow rate. Here, the CEE was magnified by increasing the capillary pressure in the shale matrix, as a result of net stress increase; therefore, the liquid hold-up became more pronounced and the plot shifted

toward the right-hand side. In other words, the CEE affected kr data more significantly at 3000 psi net stress compared to those measured at 1000 psi net stress.

However, no significant change was observed for measured kr data, which indicates the same relative permeability (kr) values at different net stresses, while the absolute permeabilities are different. In other words, by increasing the net confining stress, the relative permeability remained constant, which means that the effective flow paths remained the same. It can be assumed that the sizes of all pore bodies and pore throats have been reduced uniformly. In addition, it can be concluded that there was no macro-channel (macro-fracture) inside the matrix, as the macro-channels play an important role in fluid conductivity and are extremely sensitive to the net confining stress (Wang et al., 2015). It should be noted that these macro-fractures have much more impact on fluid flow compared to the natural microfractures that may exist in the texture of the rock. However, this behaviour was observed for the Eagle Ford shale rock (E4) but it could be different in other shale samples, depending on the presence of macro-fractures, rock heterogeneity, net stress and other factors.

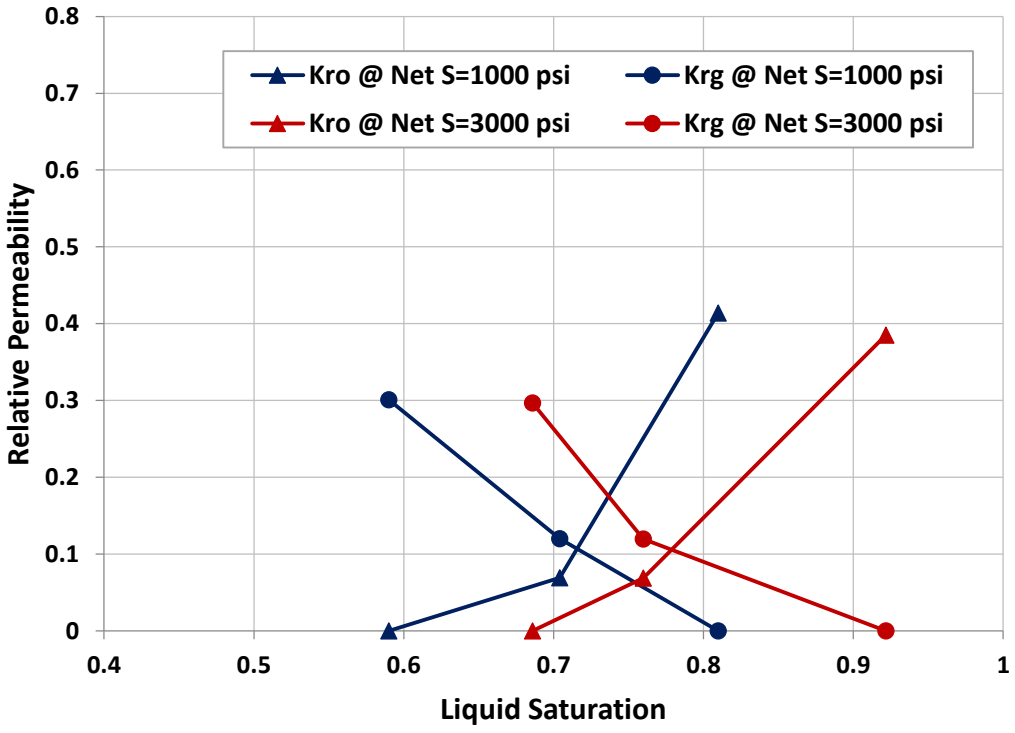

Figure 6.5: Relative permeability of Eagle Ford shale (E4) measured at 1500 psi (5.5 mN/m) at two different net stresses of 1000 and 3000 psi.

As discussed in section 6.2, the CEE is an important artefact which significantly affects the measured data during kr measurements of tight/shale samples. As shown, the CEE was dominant in almost all experiments, even for the test with a high injection rate. To obtain reliable kr data, the CEE should be minimised or the experimental data should be corrected for CEEs. In the next section, the fluid flow in a SS-kr experiment is modelled to obtain the liquid saturation profile. Based on the simulation results with CEE and the observations from the experimental measurements, a new model is developed to correct the CEEs. The new technique can be used to extract the actual kr data from the measured data when the CEEs are dominant.

6.3 Multi-Rate Method for Capillary End Effect Correction

6.3.1 Capillary End Effect for SS Displacement

For the first time, Richardson et al. (1952) used the capillary end effect formulation in two immiscible fluid injection into horizontal porous media. They have conducted a series of gas-displacing-oil experiments using a Berea sandstone to study capillary end effects.

Richardson et al. compared their experimental results with the obtained analytical solutions and demonstrated excellent agreements between measurements and predictions (Richardson et al., 1952).

Later, Huang and Honarpour (1998) used the same formulation to discuss an experiment of co-injecting oil and water into a water pre-saturated, water-wet core sample. They used capillary end effect formulation in steady state displacement to show how the relative permeability and capillary pressure can be estimated from the non-uniform liquid saturation profile. In the following, same formulation was used to obtain the liquid saturation profile when capillary end effects are not negligible (Huang and Honarpour, 1998).

In a SS-kr measurement experiment, assuming incompressible and immiscible fluids, the following equations can be used for one-dimensional flow of gas and liquid (oil), including the capillary pressure:

$$q_g = \frac{-K k_{rg} A}{\mu_g} \frac{\partial P_g}{\partial x} \tag{6.1}$$

$$q_o = \frac{-Kk_{ro}A}{\mu_o}\frac{\partial P_o}{\partial x} \tag{6.2}$$

$$P_c = P_g - P_o \tag{6.3}$$

The gradient of capillary pressure can be stated as:

$$\frac{\partial P_c}{\partial x} = \frac{1}{KA}\left(\frac{q_o\mu_o}{k_{ro}} - \frac{q_g\mu_g}{k_{rg}}\right) \tag{6.4}$$

and

$$\frac{\partial P_c}{\partial x} = \frac{dP_c}{dS_o}\frac{\partial S_o}{\partial x} \tag{6.5}$$

$$\frac{1}{KA}\left(\frac{q_o\mu_o}{k_{ro}} - \frac{q_g\mu_g}{k_{rg}}\right) = \frac{dP_c}{dS_o}\frac{\partial S_o}{\partial x} \tag{6.6}$$

Hence at steady state conditions:

$$dx = \frac{\frac{dP_c}{dS_o}\,dS_o}{\frac{1}{KA}\left(\frac{q_o\mu_o}{k_{ro}} - \frac{q_g\mu_g}{k_{rg}}\right)} \tag{6.7}$$

The above equation can be integrated along the core from x to L, i.e. from S_o to $1 - S_{gr}$ (Honarpour et al., 1986):

$$x = L - KA\int_{S_o}^{1-S_{gr}}\left[\frac{\frac{dP_c}{dS_o}}{\left(\frac{q_o\mu_o}{k_{ro}} - \frac{q_g\mu_g}{k_{rg}}\right)}\right]dS_o \tag{6.8}$$

It should be noted that S_{gr} is the residual gas saturation, which is assumed to be constant.

The saturation profile along the core can be obtained analytically from the above equation if the capillary pressure and relative permeability functions are known. It is noted that the reliability of this equation were confirmed before (Richardson et al., 1952). As an example for the application of this equation, it was used with known Pc and kr data (shown in Figure 6.6) to produce a typical saturation profile. Figure 6.7 shows a theoretical saturation profile generated by Equation 6.8 for two different flow rates at the same liquid/gas flow rate ratio (F). As shown in this Figure, by increasing the flow rate,

the length of the CEE region is decreased and the effect of the boundary is reduced. Hence, various flow rates give different CEE lengths (L_{CEE}). This solution clearly supports the conclusion that, at higher flow rates, the CEE is reduced. In addition, it is shown that the wetting phase (liquid) saturation ($S_o{}^*$) in the unaffected region of the core is not influenced by the capillary end effect and it is the same at both flow rates: i.e. at the same flow rate ratio (F), the wetting phase saturation in the unaffected zone is constant and independent of the flow rates. In this study, these two regions (unaffected and CEE) will be used later in the proposed method to capture CEEs during SS-kr measurements.

It should be noted that, the core is assumed to be homogenous to have sharp difference between unaffected and CEE regions. In other words, if the core is homogenous, the transition between the CEE region and unaffected region is relatively sharp. In the case of heterogeneous rock, this difference may not be sharp and followed by a transition region. Even in this case, two regions can be detected. However, the accuracy of the predicted values maybe be less in case of heterogeneous rock due to this transitional region.

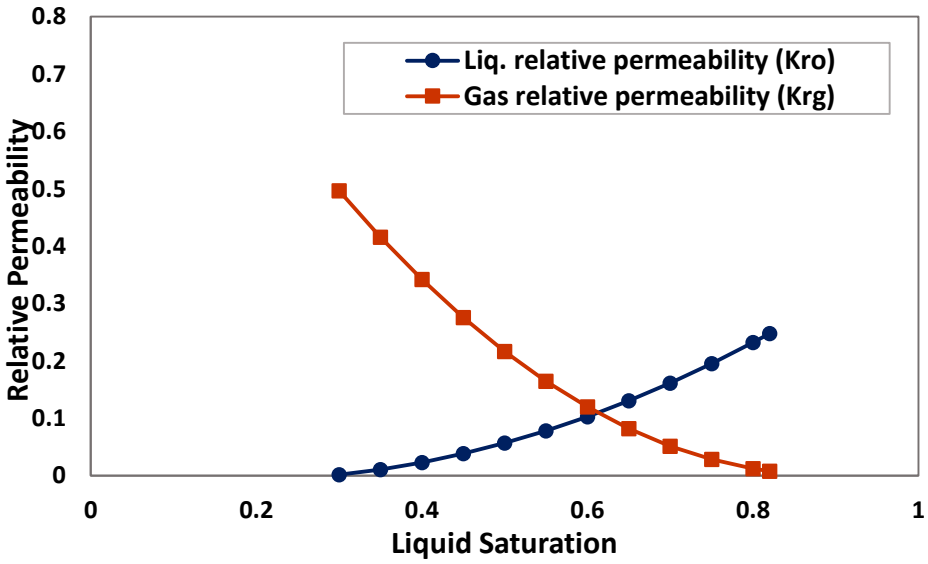

(a)

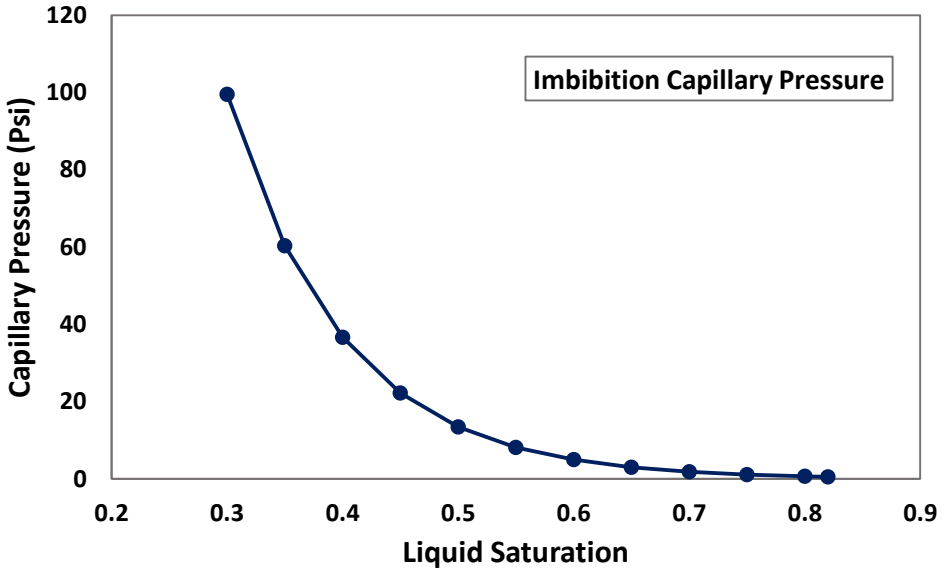

(b)

Figure 6.6:(a) Imbibition relative permeability and (b) imbibition capillary pressure data used in the analytical solution.

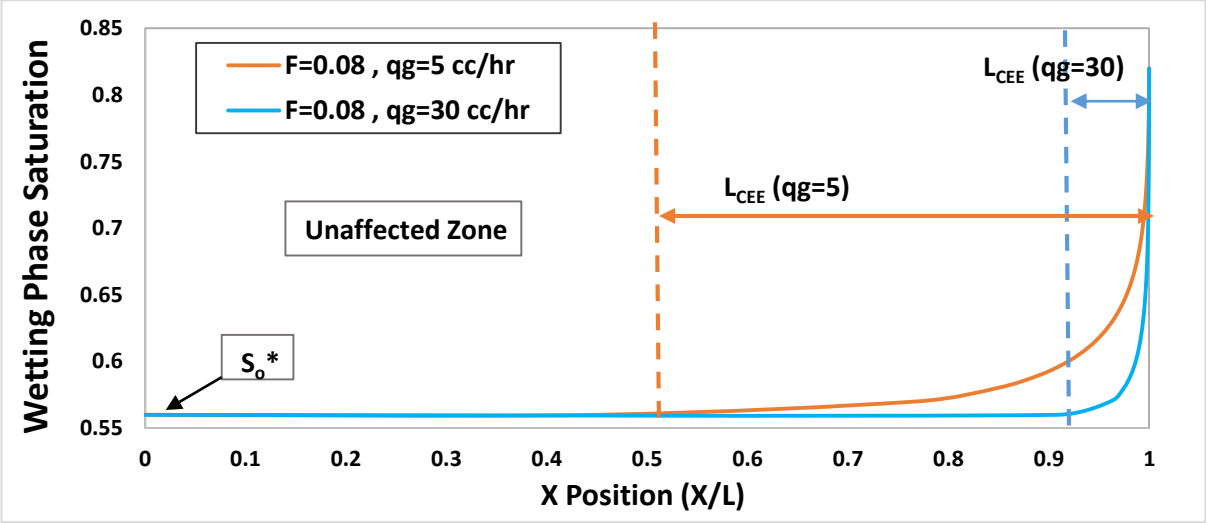

Figure 6.7: Theoretical wetting phase saturation profile for constant LGR of 0.08 and at different gas flow rates of 5 and 30 cc/hr.

6.3.2 Method Development

In the steady state relative permeability (SS-kr) measurements, the saturation profile can give valuable information regarding the capillary end effect (CEE). Among available techniques for the determination of saturation profile, the X-ray computed tomography method (X-ray CT) is the most popular one (Withjack, 1988, Iglauer et al., 2010, Maloney

et al., 1999). Magnetic resonance imaging (MRI) is also a well-established method for such purposes (Romanenko and Balcom, 2013). In the steady-state experiments, the measured saturation profile together with a pre-determined Pc function can be used to obtain the SS-kr data using a history matching technique. However, the SS-kr values obtained may not be unique. In addition, obtaining saturation profile measurements with the current techniques make the experiment more complicated and expensive. In the method proposed in this research, only a conventional steady state setup is required with no additional modifications. In this technique, data of different rates are needed for each fractional flow, to correct SS-kr and saturation data obtained from the experiments.

As explained previously, the saturation profile along the core can be divided into two separate regions of CEE and unaffected zone. In the unaffected zone, the wetting phase saturation is constant while in the CEE region, the wetting phase saturation changes from the $S_o{}^*$ to $(1 - S_{gr})$, where S_{gr} is the residual gas saturation. It is noted that the kr data is constant in the unaffected zone, as it is only a function of fluid saturation, which is constant in that region.

In addition, knowing the saturation profile along the core, the gas pressure can be calculated as follows:

$$\int dP_g = \frac{q_g \mu_g}{KA} \int \frac{dx}{k_{rg}} \tag{6.9}$$

For the CEE region, the pressure drop can be obtained as:

$$\int_{P_{L_{CCE}}}^{P_{out}} dP_g = \frac{q_g \mu_g}{KA} \int_{L_{CCE}}^{L} [\frac{dx}{k_{rg}(S_o)}] \tag{6.10}$$

Using Equation 6.7, gives:

$$\int_{P_{L_{CCE}}}^{P_{out}} dP_g = \frac{q_g \mu_g}{KA} \int_{S_o{}^*}^{1-S_{gr}} [\frac{\frac{dP_c}{dS_o}}{\frac{1}{KA}(\frac{q_o \mu_o}{k_{ro}} - \frac{q_g \mu_g}{k_{rg}})}] dS_o \tag{6.11}$$

After some manipulations it gives:

$$\Delta P_{CEE} = \int_{S_o{}^*}^{1-S_{gr}} \frac{\frac{dP_c}{dS_o}\, dS_o}{(F\, \frac{\mu_o k_{rg}}{\mu_g k_{ro}} - 1)} \tag{6.12}$$

where F is the liquid/gas flow rate ratio (LGR):

$$F = \frac{q_o}{q_g} \tag{6.13}$$

As mentioned before and shown in Figure 6.7, in the CEE region the wetting phase saturation changes from $S_o{}^*$ at the beginning to $(1 - S_{gr})$ at the end of the core. From Equation 6.12, the pressure drop across the CEE region (ΔP_{CEE}) is not a function of the flow rate. That is, (ΔP_{CEE}) is constant at the same LGR (F) irrespective of the total flow rates. In other words, it is proved in Equation 6.12 that the ΔP_{CEE} is constant for all SS-kr measurements performed at different flow rates but with the same LGR.

However, the length of the CEE region (L_{CCE}) is not constant for all flow rates. Considering the constant ΔP_{CEE} for different total flow rates at the same LGR, the pressure drop across the core can be written as follows:

$$\Delta P_{core} = \frac{q_g\, \mu_g\, (L - L_{CEE})}{K k_{rg}(S_o{}^*) A} + \Delta P_{CEE} \tag{6.14}$$

In Eq. 6.14, when applied to the results of an experiment, the values of L_{CCE}, $k_{rg}(S_o{}^*)$ and ΔP_{CEE} are unknown, which are going to be determined.

In a similar way, it can be shown that the "average liquid saturation" at the CEE region is also constant for different flow rates with the same LGR. That is, the average saturation is defined as:

$$\bar{S}_{o\ CEE} = \frac{\int_{L_{CCE}}^{L} S_o\, dx}{\int_{L_{CCE}}^{L} dx} \tag{6.15a}$$

which can also be written as follows, if Equation 6.7 is used:

$$\bar{S}_{o\,CEE} = \frac{\int_{L_{CCE}}^{L} S_o\, dx}{\int_{L_{CCE}}^{L} dx} = \frac{\int_{S_o}^{1-S_{gr}} \frac{S_o \frac{dP_c}{dS_o}\, dS_o}{\frac{1}{KA}\left(\frac{q_o\mu_o}{k_{ro}} - \frac{q_g\mu_g}{k_{rg}}\right)}}{\int_{S_o}^{1-S_{gr}} \frac{\frac{dP_c}{dS_o}\, dS_o}{\frac{1}{KA}\left(\frac{q_o\mu_o}{k_{ro}} - \frac{q_g\mu_g}{k_{rg}}\right)}} \tag{6.15b}$$

$$= \frac{q_g \int_{S_o}^{1-S_{gr}} \frac{S_o \frac{dP_c}{dS_o}\, dS_o}{\left(\frac{q_o\mu_o}{k_{ro}} - \frac{q_g\mu_g}{k_{rg}}\right)}}{q_g \int_{S_o}^{1-S_{gr}} \frac{\frac{dP_c}{dS_o}\, dS_o}{\left(\frac{q_o\mu_o}{k_{ro}} - \frac{q_g\mu_g}{k_{rg}}\right)}} = \frac{\int_{S_o}^{1-S_{gr}} \frac{S_o \frac{dP_c}{dS_o}\, dS_o}{\left(F\frac{\mu_o}{k_{ro}} - \frac{\mu_g}{k_{rg}}\right)}}{\int_{S_o}^{1-S_{gr}} \frac{\frac{dP_c}{dS_o}\, dS_o}{\left(F\frac{\mu_o}{k_{ro}} - \frac{\mu_g}{k_{rg}}\right)}}$$

As shown in this equation, the average oil saturation in the CEE region ($\bar{S}_{o\,CEE}$) is also independent of flow rates and it is constant for all SS-kr experiments performed at different flow rates with the same LGR (F). Therefore, the saturation equation for the core, considering the two separate regions, can be written as follows:

$$\overline{S_o}\,\mathrm{L} = S_o^{*}(L - L_{CEE}) + \bar{S}_{o\,CEE}\, L_{CEE} \tag{6.16}$$

where $\overline{S_o}$ is the average wetting phase saturation inside the entire core, which is measured during the SS-kr experiment, S_o^{*} is the wetting phase saturation in the unaffected zone, L_{CCE} is the length of the CEE region and $\bar{S}_{o\,CEE}$ is the average saturation in the CEE region. It should be noted that, in Equation 6.16, when applied to the results of a SS-kr experiment, S_o^{*}, L_{CCE} and $\bar{S}_{o\,CEE}$ are again unknowns which are going to be determined.

During the experiments, the pressure drop across the core (ΔP_{Exp}) and the average saturation ($\bar{S}_{Exp}$) can be measured at each flow rate. It is noted that this measured average saturation ($\bar{S}_{Exp}$) is the average wetting phase saturation in the entire core ($\overline{S_o}$).

Assuming performing SS-kr experiments at four different flow rates (with constant LGR), the following equations can be written for pressure and wetting phase saturations:

$$\begin{cases} \Delta P^1_{Exp} = \dfrac{q^1_g\ \mu_g\ (L - L^1_{CEE})}{K k_{rg}(S_o{}^*) A} + \Delta P_{CEE} \\ \Delta P^2_{Exp} = \dfrac{q^2_g\ \mu_g\ (L - L^2_{CEE})}{K k_{rg}(S_o{}^*) A} + \Delta P_{CEE} \\ \Delta P^3_{Exp} = \dfrac{q^3_g\ \mu_g\ (L - L^3_{CEE})}{K k_{rg}(S_o{}^*) A} + \Delta P_{CEE} \\ \Delta P^4_{Exp} = \dfrac{q^4_g\ \mu_g\ (L - L^4_{CEE})}{K k_{rg}(S_o{}^*) A} + \Delta P_{CEE} \end{cases} \quad (6.17)$$

and

$$\begin{cases} \bar{S}^1_{Exp} L = S_o{}^*\ (L - L^1_{CEE}) + \bar{S}_{CEE}\ L^1_{CEE} \\ \bar{S}^2_{Exp} L = S_o{}^*\ (L - L^2_{CEE}) + \bar{S}_{CEE}\ L^2_{CEE} \\ \bar{S}^3_{Exp} L = S_o{}^*\ (L - L^3_{CEE}) + \bar{S}_{CEE}\ L^3_{CEE} \\ \bar{S}^4_{Exp} L = S_o{}^*\ (L - L^4_{CEE}) + \bar{S}_{CEE}\ L^4_{CEE} \end{cases} \quad (6.18)$$

where L^1_{CEE}, L^2_{CEE}, L^3_{CEE}, L^4_{CEE},$S_o{}^*$, $k_{rg}(S_o{}^*)$,$\bar{S}_{CEE}$ and ΔP_{CEE} are unknowns. The above eight equations can be solved simultaneously for these unknowns. After solving the equations, the wetting phase saturation $S_o{}^*$ and non-wetting relative permeability $k_{rg}(S_o{}^*)$ are known. Thus, the only unknown value for plotting the relative permeability data is $k_{ro}(S_o{}^*)$. This values can be calculated using the Darcy law as follows. After solving the equations (Equation 6.17 and 6.18), the pressure drop across the CEE region is obtained. Therefore, the value of the pressure drop across the "unaffected zone" can be also calculated ($\Delta P_{unaf.} = \Delta P_{Exp} - \Delta P_{CEE}$). Having the pressure drop across the unaffected zone and the liquid rate, the $k_{ro}(S_o{}^*)$ can be easily calculated using Darcy law. Therefore, the corrected kr data corresponding to a single LGR are obtained. The procedure should then be repeated for the next LGR.

In the following sections, the proposed technique is evaluated, using both theoretical and experimental data.

6.4 Validation of the Proposed Method

6.4.1 CEE Correction by the Multi-Rate Method: Theoretical Data

In this section, the integrity of the proposed technique is evaluated using two sets of theoretically generated data. To achieve this aim, known functions of Pc and kr data were employed in the corresponding analytical equation to simulate a steady-state two-phase

displacement through a core. The theoretically generated experimental data (i.e. pressure drop (ΔP_{EXP}) from Equation 6.9, and average saturation ($\bar{S}_{Exp}$) from Equation 6.15) were then obtained. For generation of these data, the input parameters were selected in such way to have dominant end effects. In the next step, to evaluate the proposed technique, the generated experimental data (with CEEs) were used to predict the corrected kr data. Finally, the corrected data obtained by the proposed method were compared with the actual known kr functions. The predicted CEE length and pressure drop were also compared with the analytically calculated values. In this study, the imbibition kr and Pc functions, shown in Figure 6.6 were used. Table 6.2 shows the PVT and the core properties used for this exercise.

Table 6.2: Rock and PVT properties used in the numerical solution to generate experimental data.

Property	**Test 1**	**Test 2**
LGR	0.08	0.02
Gas flow rate (cc/hr)	4,5,15,30	11,15,25,30
Abs. Permeability (μD)	16	16
Area (cm^2)	11.4	11.4
Gas viscosity (cP)	0.0192	0.0192
Liquid viscosity (cP)	0.1268	0.1268
Core length (cm)	4.61	4.61
S_{oi} and S_{gr}	0.3, 0.18	0.3, 0.18

As mentioned before, using the kr and Pc data in Figure 6.6 and input parameters shown in Table 6.2, the saturation profile at different flow rates can be numerically obtained using Equation 6.8. Figure 6.8 shows these obtained saturation profiles along the core for the two tests conducted at various LGRs. When LGR=0.08, the dimensionless CEE lengths (L_{CEE}/L) for the gas flow rates of 4, 5, 15 and 30 are 0.689, 0.232, 0.184 and 0.092, respectively. When LGR=0.02, the dimensionless CEE lengths (L_{CEE}/L) for the gas flow rates of 11, 15, 25 and 50 are 0.921, 0.676, 0.405 and 0.203 respectively.

As mentioned before, at constant LGR the wetting phase saturation in the unaffected zone ($S_o{}^*$) is constant at all flow rates. In these results from numerical solutions, the $S_o{}^*$

value at the higher LGR of 0.08 is 0.56 and at the lower LGR of 0.02, it is 0.45. It is clear that, by decreasing the LGR, $S_o{}^*$ decreases.

Another point that should be noted here is the CEE length for different LGRs at the same flow rate. When LGR=0.08, $L_{CEE}/L = 0.184$ for the gas flow rate of 15, while it is $L_{CEE}/L = 0.676$ for the same gas flow rate when LGR=0.02. It can be concluded that the CEE is more dominant at lower LGR. For example, in this case, the CEE has occupied the 18.4 % of the core length when LGR is 0.08, while it has occupied 67.6% of it, when LGR is equal to 0.02. Hence, at lower LGR, the CEE is more dominant.

As mentioned above, from the numerical solution for a SS core flood, the measured pressure drop and measured wetting phase average saturation can be calculated. In other words, knowing the saturation profile along the core (from Equation 6.8), the pressure drop across the core can be calculated using Equation 6.9. In real SS kr experiments, this pressure drop is usually measured across the core by the pressure transducers. The average saturation in the core can be also calculated using Equation 6.15. In real SS kr experiments, this average saturation is obtained using the material balance. These data (pressure drop and average saturation) were used in the proposed procedure to obtain the corrected gas and oil kr data. Table 6.3 and Table 6.4 show these parameters obtained from the numerical solutions.

Table 6.3: The pressure drop, measured k_{rg} and measured average saturation in an artificial steady-state relative permeability experiment with LGR of 0.08.

$\boldsymbol{q_g}$	**4** $\boldsymbol{cc/hr}$	**5** $\boldsymbol{cc/hr}$	**15** $\boldsymbol{cc/hr}$	**30** $\boldsymbol{cc/hr}$
$\Delta P_{Exp}\ (Psi)$	57.99	70.77	198.52	390.14
$k_{rg\ Exp}$	0.136	0.139	0.149	0.152
$\bar{S}_{Exp}$	0.574	0.571	0.564	0.562

Table 6.4: The pressure drop, measured k_{rg} and measured average saturation in an artificial steady-state relative permeability experiment with LGR of 0.02.

$\boldsymbol{q_g}$	**11** $\boldsymbol{cc/hr}$	**15** $\boldsymbol{cc/hr}$	**25** $\boldsymbol{cc/hr}$	**50** $\boldsymbol{cc/hr}$
$\Delta P_{Exp}(Psi)$	95.00	123.74	195.57	375.15
$k_{rg\ Exp}$	0.229	0.240	0.253	0.264
$\bar{S}_{Exp}$	0.478	0.470	0.462	0.456

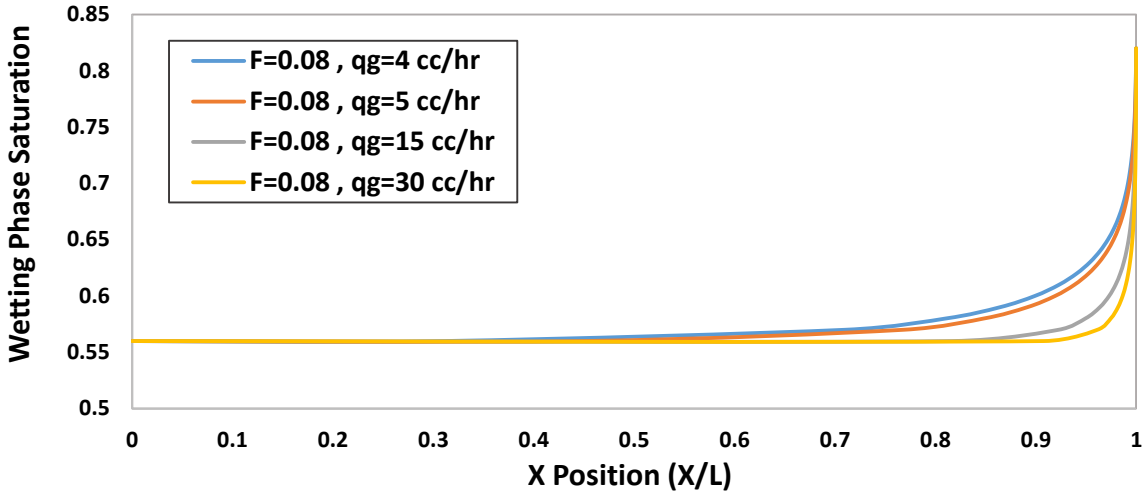

(a)

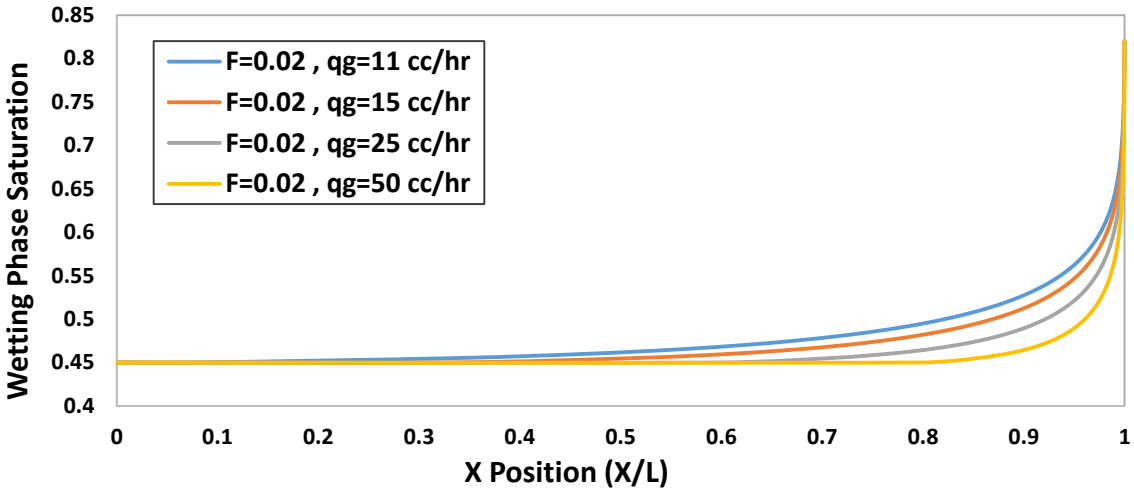

(b)

Figure 6.8: The saturation profile for two LGRs of (a) 0.08 and (b) 0.02 obtained from the simulation of core flooding experiments at four different flow rates.

For test 1 (LGR of 0.08), the artificial experimental data (ΔP_{Exp} and $\bar{S}_{Exp}$) shown in Table 6.3 were used in Equations 6.17 and 6.18 to obtain the unknowns, which are L^1_{CEE}, L^2_{CEE}, L^3_{CEE}, L^4_{CEE}, ${S_o}^*$, $k_{rg}({S_o}^*)$, $\bar{S}_{CEE}$ and ΔP_{CEE}. The data shown in Table 6.4 were also used with the same procedure to obtain the unknowns in test 2 (LGR of 0.02).

After using the proposed method for correction of CEE, the obtained results were compared with the actual values, as shown in Table 6.5. It should be noted that the actual data are obtained from the input kr functions and the results of Eq. 6.8, 6.12 and 6.15b. As shown in this table, the predicted values are in good agreement with the actual data.

In addition, benefiting from the proposed technique, some valuable information about the saturation profile and pressure drop along the core can be obtained. The wetting phase relative permeability, $k_{ro}(S_o{}^*)$, can be simply calculated by the Darcy equation when the length of the unaffected zone and the pressure drop across it are known. Figure 6.9 shows the gas and oil kr obtained from the artificial experiment (with CEE) compared with the actual data (from the known function) and corrected data (using the proposed technique). In this figure, the experimental data for the smallest flow rate are shown. It has to be borne in mind that the measured kr and saturation values can be corrected using the proposed method, as long as the experimental data for four different flow rates at each LGR are available.

It should also be noted that, in this approach, it is necessary for the CEE region to be smaller than the core length. In other words, the core should not be entirely covered by the CEE region and the unaffected zone should be still available. Hence, if $L_{CEE} > L$ is obtained for a test, then a higher flow rate is required to shorten the CEE region.

Another advantage of this technique is that the proposed method can be applied to the experimental data before going to the next LGR. This means that, during the experiments, if $L_{CEE} > L$ is obtained for a set of flow rates at a specified LGR, the experiments can be repeated with higher flow rates before moving to the next LGR.

It is noted that, as mentioned before, for generation of saturation profile, the imbibition kr and Pc functions, shown in Figure 6.6 were used. Although the data in Figure 6.6 were generated based on the known functions, in reality, the measured data are more scattered and using a known fitted function may introduce error in the integration (Equation 6.8). However, the integration is not required in the proposed model in this study as all eight equations involved in the model (Equation 6.17 and 6.18) are developed based on the Darcy's law and the material balance.

Table 6.5: The actual and predicted values of CEE length, CEE pressure, wetting phase saturation and corresponding non-wetting relative permeability.

Parameter	Test 1 (LGR=0.08)			Test 2 (LGR=0.02)		
	Predicted	True value	Rel. Error (%)	Predicted	True value	Rel. Error (%)
L_{CEE}^{1}/L	0.7264	0.68911	5.41 %	0.9130	0.9211	0.88 %
L_{CEE}^{2}/L	0.5807	0.5513	5.33 %	0.6629	0.6755	1.87 %
L_{CEE}^{3}/L	0.1924	0.1838	4.68 %	0.3878	0.4053	4.32 %
L_{CEE}^{4}/L	0.0954	0.0919	3.78 %	0.1815	0.2026	10.41 %
$k_{rg}(S_o^*)$	0.1553	0.1550	0.21 %	0.2826	0.2758	2.47 %
ΔP_{CEE}	44.030	42.116	4.55 %	88.2944	88.7721	0.54 %
$\bar{S}_{CEE}$	0.5793	0.5803	0.17 %	0.4808	0.4805	~0%
S_o^*	0.5600	0.5600	0 %	0.4500	0.4507	~0%

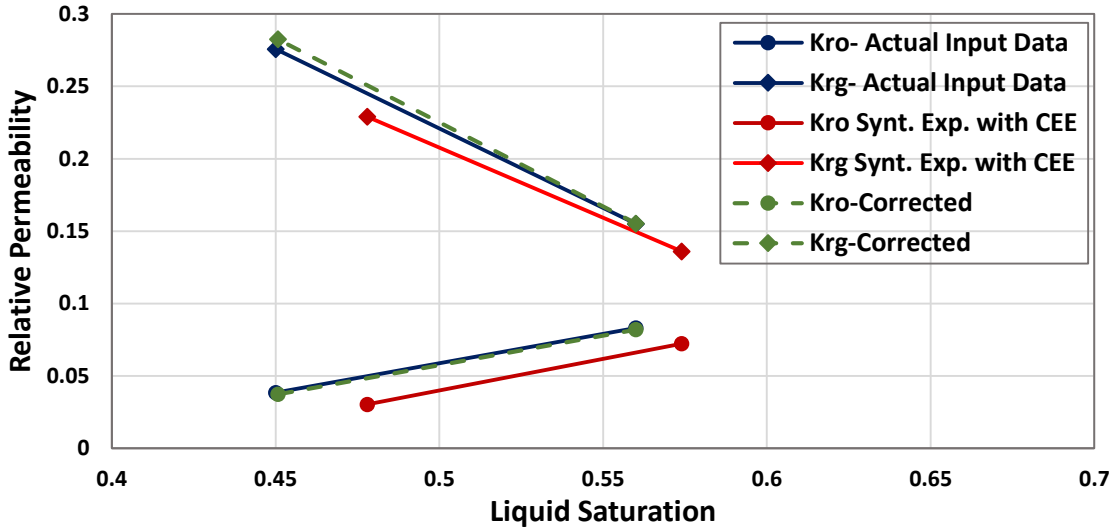

Figure 6.9: The gas and oil relative permeability obtained from the artificial experiment compared with actual and corrected data using the proposed technique.

In Table 6.5, the pressure drop values across the CEE zone are also presented. As shown in Eq. 6.12, this pressure is not a function of the flow rate. Hence, a certain value is obtained for each LGR, regardless of the injected flow rate. As mentioned before, Gupta

and Maloney (2015) proposed a method to obtain this pressure drop (ΔP_{CEE}) from the non-zero intercept when plotting the measured pressures versus total flow rates (based on the assumption of a constant CEE length). However, as shown in Equation 6.14, the CEE length changes as flow rate changes, hence plotting measured pressure versus flow rate gives a wrong value for ΔP_{CEE}. The results of following their proposed procedure are shown in Figure 6.10. As indicated, the predicted ΔP_{CEE} values are 6.9 and 18.9 Psi for tests with LGR of 0.08 and 0.02, respectively, while the true values are 42.1 and 88.8 Psi. In other words, ignoring the variation of the CEE length has resulted in a significant error in prediction of ΔP_{CEE} and hence, the calculated kr values.

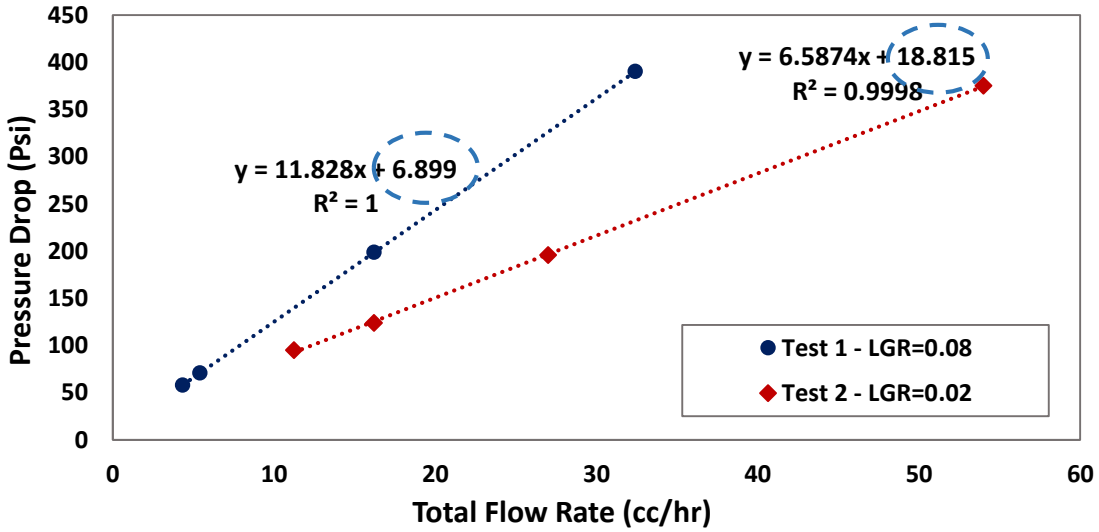

Figure 6.10: Experimental pressure drop versus total flow rate of two tests at two different LGRs used to follow the proposed procedure by Gupta and Maloney (2015) to obtain relative permeability data corrected for the capillary end effect.

It has to be noted that, to solve the equations 6.17 and 6.18, any numerical solver can be used. Based on the degree of freedom analysis, the number of unknowns are equal to independent algebraic equations, hence the problem is uniquely solvable. However, using numerical solver may introduce numerical errors. It is noted that these errors are in addition to the experimental errors of pressure drop and saturation measurements during SS kr experiments. In this study, a numerical solver in MATLAB with the Levenberg-Marquardt algorithm (LMA) was used. The LMA interpolates between the Gauss–Newton algorithm (GNA) and the method of gradient descent. However, as for many

fitting algorithms, the LMA finds only a local minimum, which is not necessarily the global minimum. Therefore it is dependent on the initial guess selected for the iterations. However, for the problem under study, the initial guess can be easily selected. For instance, considering the parameters in Table 6.5, the first four parameters, which are the dimensionless CEE lengths, should be selected between 0 and 1. In addition, these value can be better selected depending on the injection rate (it is known that the higher the injection rate, the lower the CEE length). The initial guess for gas relative permeability can be also given using the obtained k_{rg} from the experiment performed at the highest injection rate. The guess for CEE pressure drop can be also selected using the experimental pressure drop performed at the lowest injection rate. Similarly, for the average wetting saturation of CEE region ($\bar{S}_{CEE}$) and the average wetting saturation in the unaffected zone ($S_o{}^*$), the measured wetting saturation obtained from the experiments performed at the lowest and the highest injection rate can be used, respectively.

6.4.2 CEE Correction by the Multi-Rate Method: Experimental Data

6.4.2.1 Eagle Ford Shale (E3)

In addition to the verification of the method by theoretical data, the proposed technique was applied to the measured experimental data to correct the CEE. To this aim, the pressure drop and saturations obtained during SS-kr measurements of E3 shale (shown in Figure 6.3) were used in Equations 6.17 and 6.18 to estimate the CEE length, relative permeability data and the corresponding saturations for each LGR. To solve the equations, a numerical solver in MATLAB with the Levenberg-Marquardt algorithm was used.

Table 6.6 presents the results obtained for all flow rates, measured at two LGRs of 0.08 and 0.25. As shown, the estimated CEE length (L_{CEE}) is longer for the lower flow rates, which confirms that the CEE decreases as the injection rate increases.

In addition, as seen in Table 6.6, the CEE region covers a significant area of the E3 shale during the SS-kr measurements. This confirms the prevailing effect of the CEE on the experimental data when measuring SS-kr of Eagle Ford shale. It is also shown that the corrected gas kr value is 0.28, which is 8% greater than 0.2, which was the value obtained at the highest flow rate. This means that the CEE may cause errors, even in measured kr data with the highest possible flow rate.

Furthermore, at LGR of 0.25, a smaller CEE length was estimated compared to that at the same flow rate and LGR of 0.08. At LGR of 0.25, the corrected gas kr is 0.11, which is 2 % higher than the value obtained at the highest flow rate. It also proves that the corrections are more necessary for the experimental data measured at lower LGRs. In addition, the wetting phase saturation in the unaffected zone was obtained at each LGR. As shown in Table 6.6, at LGR of 0.08, the wetting phase saturation ($S_o{}^*$) was 0.49, which is 6% smaller than the average saturation obtained at the highest flow rate. This difference is 3% at the highest LGR of 0.25. This further confirms the necessity of CEE correction for experimental data measured at lower LGR.

Table 6.6: The actual and predicted values of CEE length, CEE pressure, wetting phase saturation and corresponding non-wetting relative permeability for E3 shale sample.

LGR	**Total Flow Rate (cc/hr)**	L_{CEE}	$k_{rg}(S_o{}^*)$	ΔP_{CEE} **(psi)**	$\bar{S}_{CEE}$	$S_o{}^*$
0.08	10	0.85	0.28	174	0.63	0.49
	13	0.74				
	16	0.59				
	20	0.41				
0.25	10	0.53	0.11	184	0.74	0.65
	13	0.43				
	16	0.42				
	20	0.37				

Using the estimated CEE length, the oil relative permeability can be calculated using the Darcy equation applied to the unaffected zone (i.e. non-CEE length), based on the oil viscosity and pressure difference. The corrected SS-kr data are shown in Figure 6.11, together with the uncorrected values from the experiments. As shown, uncorrected experimental data give underestimated relative permeability values. In addition, liquid build-up due to the CEE causes higher wetting phase saturation along the core. However, for the Eagle Ford shale sample, the corrections were not required for the experimental data measured at residual gas saturation, as there were no significant changes at different rates.

As mentioned before, the proposed method can be applied to correct the experimental data as long as the CEE region is smaller than the core length. In other words, if the CEE region covers the entire core, the proposed technique cannot be applied and negative values will be obtained for the non-CEE length. This means that the viscous forces are not strong enough to compete with capillary end effect and thus the CEE region covers the entire core. Considering this point, it should be added that the proposed method cannot be applied to correct the experimental data for residual oil saturation, since the CEE region is extended all along the core. As shown in Table 6.6, at LGR of 0.08, the CEE zone extended up to 85% of the core length, at the total flow rate of 10 cc/hr. It is evident that at lower LGRs (towards the residual liquid saturation), the CEE covers the entire core length and the proposed technique cannot be applied. However, based on the corrections performed on the experimental data at LGRs of 0.25 and 0.08, a trend with major differences in kr and wetting phase saturations is expected, shown as a green dotted line in Figure 6.11.

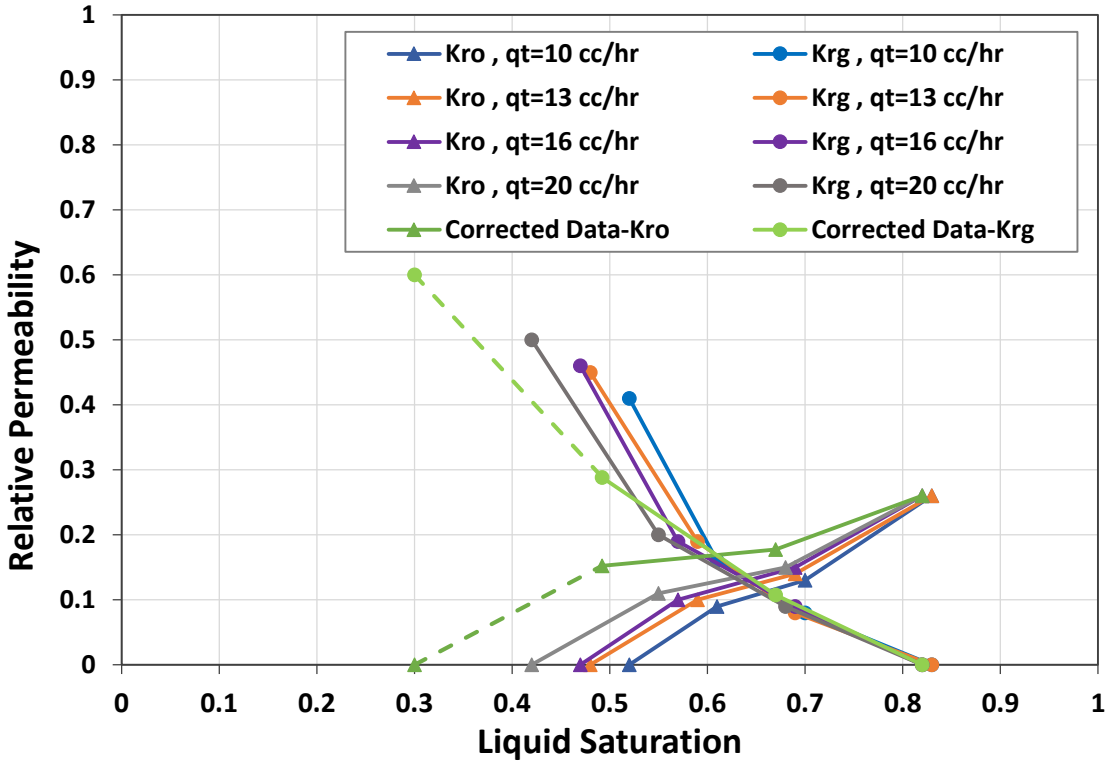

Figure 6.11: Experimental and predicted relative permeability data measured on the Eagle Ford shale samples at 1500 psi, corresponding to IFT of 5.5 mN/m.

6.4.2.2 Pierre Shale (P3)

The relative permeability data measured for the P3 shale sample were also corrected by the proposed method. Table 6.7 presents the results obtained for all flow rates at each LGR. As shown, the estimated CEE length (L_{CEE}) is longer at the lower flow rate, which confirms the higher impacts of CEEs on kr data measured at lower injection rates.

In addition, comparison of the corrected data at LGR of 0.08 and 0.25 reveals that CEEs were more prevalent at the lower LGR. As shown in Table 6.7, the estimated CEE lengths at LGR of 0.08 are greater than the estimated values for the corresponding flow rate at LGR of 0.25. It is noted that the corrected gas kr data are 0.18 and 0.09 for LGRs of 0.08 and 0.25, respectively, while the measured values for the highest flow rate were 0.15 and 0.08.

Furthermore, the wetting phase saturation in the unaffected zone (non-CEE) was obtained at each LGR. As shown in Table 6.7, at LGR of 0.08, the wetting phase saturation ($S_o{}^*$) is 0.54, which is 9% smaller than the average saturation obtained at the highest flow rate. This difference is 5% at the highest LGR of 0.25.

The corrected SS-kr data are shown in Figure 6.12, together with the uncorrected values from the experiments. As shown, the CEE shifts the relative permeability data to the right hand side of the figure. In fact, higher fluid saturations were measured because of the liquid hold-up in the core due to the CEE. As shown for P3, this liquid hold-up can be significant and has great impact on both oil and gas relative permeabilities.

Furthermore, as mentioned before, the proposed technique here cannot be applied for all LGRs or low flow rates. If the injection flow rate is less than a certain value (critical flow rate), the liquid hold-up or CEE can cover the entire core length and the proposed method gives negative values for the non-CEE length. This means that the capillary forces are fully dominant and the injection flow rate (i.e. viscous force) needs to be increased. It is noted that the critical flow rate depends on several factors, including LGR, rock and fluid properties, and capillary pressure function. Considering this point, as with the CEE corrections for the E3 kr data, the proposed method cannot be applied to correct the P3 experimental data measured at residual oil saturation. It is noted that, in Figure 6.12, the green dotted line is also expected and it is not obtained by the proposed method.

Table 6.7: The actual and predicted values of CEE length, CEE pressure, wetting phase saturation and corresponding non-wetting relative permeability for P3 shale sample.

LGR	Total Flow Rate (cc/hr)	L_{CEE}	$k_{rg}(S_o^*)$	ΔP_{CEE} (psi)	$\overline{S}_{CEE}$	S_o^*
0.08	9	0.67	0.18	192	0.78	0.54
	12	0.57				
	15	0.44				
	18	0.39				
0.25	9	0.58	0.09	197	0.83	0.71
	12	0.49				
	15	0.43				
	18	0.38				

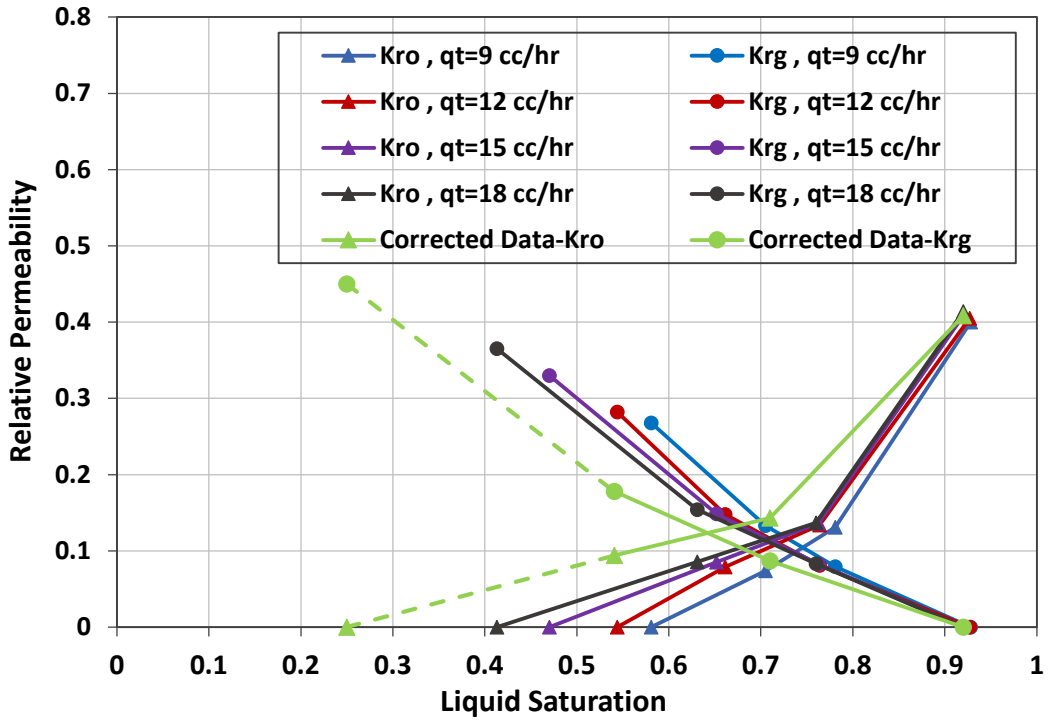

Figure 6.12: Experimental and predicted relative permeability data measured on the Pierre shale samples at 1500 psi, corresponding to IFT of 5.5 mN/m.

6.5 Summary and Conclusions

In this chapter, the two-phase flow in shale rock samples was investigated. The main difficulties for SS-kr measurements of shale samples were explained and the capillary end effects (CEEs) were described as the main challenging artefacts during the SS-kr

measurements of shale rocks. The relative permeability data of four rock samples (a tight sandstone and three shale samples) were measured using the steady-state technique. In addition, the effects of net confining stress were also investigated by measuring the relative permeability of the Eagle Ford shale (E4) at two net stress values of 1000 and 3000 psi. It was observed that the CEEs have significant impacts on the measured SS-kr data.

In the second part of this chapter, a new technique was proposed to correct the steady state relative permeability (SS-kr) data affected by capillary end effects (CEE). In the proposed technique, steady state displacements at four different flow rates are required to estimate the CEE length, oil/gas relative permeability, fluid saturations and pressure drop in the unaffected zone. It was mathematically shown that, for a constant LGR, the pressure drop and the average wetting phase saturation within the CEE region are constant and independent of flow rate.

In addition, the integrity of the proposed method was evaluated using series of artificially generated experimental data. For this purpose, a set of capillary pressure (Pc) and kr data were assumed and used in the analytical solution of two-phase flow coupled with Pc. The analytical solutions were then used to generate artificial experimental data for pressure drop and average saturation during the SS-kr measurements. The generated data were then utilised in the proposed technique to estimate the kr data and the fluid saturations corrected for CEEs. In addition, the proposed technique was used to correct the SS-kr data of two shale samples (E3 and P3). The data from SS displacement experiments conducted at four different flow rates were used to obtain the corrected SS-kr data. The following observations and conclusions can be drawn from this study:

- The SS-kr data of the Eagle Ford shale (E3) showed a significant variation when measured at different injection rates. This variation was significant for lower LGR and decreased by increasing LGR. It was concluded that the CEE is the main reason for this observation, as a similar behaviour was shown in the results from the numerical solutions.
- The SS-kr data measured for Pierre shale (P3) presented the same behaviour, which further confirms the dominant role of the CEE during SS-kr measurements. In addition, it was observed that the CEE was more dominant in SS-kr experiments on Pierre (P3), compared to those performed on Eagle Ford (E3), because the kr data showed more discrepancies with respect to the injection rate. It was concluded

that this behaviour was due to the higher capillary pressure of Pierre shale compared to Eagle Ford shale.

- In addition, compared to the Pierre shale experimental kr data, higher values for residual gas saturations were obtained from the SS-kr experiments on Eagle Ford (E3). It was mentioned that this higher residual gas saturation could be due the greater heterogeneity of Eagle Ford shale (E3) compared to the Pierre shale sample (P3).

- From the SS-kr experiments performed at two different net stress values, it was found that the CEEs become more pronounced with increasing net stress. This is mainly because of the increase in capillary pressure, which could be due to the reduction of pore/throat sizes.

- In addition, no significant change was observed for measured kr data at different net stress values. This observation confirmed that there was no macro-channel (macro-fracture) inside the matrix, since the macro-channels play important roles in fluid conductivity and are extremely sensitive to the net confining stress.

- The simulation results of SS two-phase flow showed that the CEE is more significant during the SS-kr experiment performed at lower LGR. In addition, the dominant role of the CEE increases as the injection rate is decreased.

- The proposed model was validated by artificially generated data. It was shown that the corrected SS-kr data obtained by the proposed method were in good agreement with the actual known kr data of the input.

- Comparison of the measured kr data and the corrected values showed that ignoring CEEs during SS-kr measurements of tight and shale rocks can be highly erroneous.

- The proposed technique can be used to estimate reliable kr data without any saturation profile measurement equipment, such as CT-scan or MRI. In addition, the proposed technique can be simply applied to the measured data during the experiment and, if required, the test can be repeated before going on to the next LGR.

Chapter 7: Summary, Conclusions and Recommendations for Future Studies

7.1 Summary

The unconventional resources have received great attention recently mainly because of the growing global energy demand and also the continuance of fossil fuels as the main source of energy. Despite this, recent production from these resources reveals a number of technical challenges mainly due the significant impacts of the unconventional mechanisms. In fact, these unconventional mechanisms and their effects on the fluid flow is not well understood.

The main objective of this research was to study the impacts of certain mechanisms on fluid flow in the unconventional reservoir rocks with an emphasis on shale rocks. Among them, the effects of flow regimes, geomechanical stress and the impacts of high capillary pressure on fluid flow were investigated. In this research, the effects of these mechanisms on fluid flow are investigated by performing several single-phase and two-phase experiments and also numerical simulations. The experimental results were used to develop a model for matrix permeability predictions. In addition, results of the experiments were used to validate the numerical simulations performed by the Lattice Boltzmann method. Furthermore, the effects of high capillary pressure were investigated on two-phase flow in the shale rocks. For this purpose, the steady state relative permeability of three shale samples were measured. The displacement process was also simulated assuming the dominant effects of capillary pressure inside the core. The experimental data and simulation results were used to develop a model for correction of capillary end effect (CEE) which is the main challenge when measuring SS-kr of the shale samples. In the following, the conducted experiments and simulations were briefly summarized.

First, several experiments were designed to study the effects of flow regimes and effective stress on matrix permeability. For this purpose, the apparent permeability of three shale samples were measured at various pore pressures and net stresses to investigate the effects of gas slippage and geomechanical stress on the single-phase gas flow. The permeabilities of shale samples were measured using the steady state (for the sample with high permeability, $k > 50\ \mu D$) and unsteady techniques (for the samples

with lower permeability, $k < 50\ \mu D$). In addition, to have a better understanding about the rock characterization of shale samples under study, results of several performed experiments including TOC and Helium porosimetry, XRD analysis, contact angle measurements, MICP test and SEM image analysis were used. In addition, the level of permeability hysteresis of the shale samples was evaluated. To this aim, the apparent permeability of two shale samples (E1 and P1) were measured when the net stress was increased from 500 to 3000 psi. Then the measurements were repeated while the net stress was decreased from 3000 psi to 500 psi. Furthermore, the effects of presence of a liquid phase on the gas slippage was investigated for two different shale samples. In these experiments, after establishment of the residual liquid saturation, the apparent permeability of the shale samples were measured at different pore pressures. All these experiments have been reported in Chapter 3.

After experimental evaluation of the flow regimes and the stress effects on the fluid flow in shale matrix, the obtained results were used to develop a model for matrix permeability prediction. For this purpose, the N-S equation was used to model the gas flow in a bundle of capillary tubes. The gas slippage was taken into account by using slip boundary conditions. The Maxwellian first-order, second-order and B-K slip boundary models were applied to N-S equations to capture the permeability enhancement due to the gas slippage. Then the Darcy equation was incorporated into the solution to generalize the equation for fluid flow in porous media. Next, the dimensionless form of the solution was used to cancel the effects of rock heterogeneity and tortuosity.

In the next step, the measured apparent permeability data and the calculated non-slip permeability values were used to determine the dimensionless permeability factor (k_D). These dimensionless factors were plotted versus the Knudsen number to generate the general slip plot. Then, the general slip plot and the solution obtained from the N-S equation (with slip boundary conditions) were used to determine the slip coefficients. The experimental data in the general slip plot were also compared with the predicted results of the other slip models, e.g. B-K slip model. Then to develop a general permeability prediction model, the geomechanical effects were incorporated into the solution of N-S equation. In this approach, the impacts of net stress variation on the "flow regime" and the "non-slip permeability" were considered by introducing suitable relationships for variation of average pore size and non-slip permeability by net stress. These mathematical modelling and model development have been explained in Chapter 4.

In Chapter 5, the gas flow in micro- and nanoscale systems was simulated using the Lattice Boltzmann Method (LBM). The main purpose of these simulations was to investigate the application of the LBM for gas flow modelling in the shale rocks. In addition, it was aimed to determine the appropriate TMAC in the LBM simulations to predict the measured matrix permeability values from the Knudsen number of the system. As the LBM is a simulation technique in the mesoscopic level, the slip flow results should be nondimensionalized to be comparable with the experimental data. The nondimensionalization were performed using the simulation results for the same system without gas slippage. In this exercise, the Two-Relaxation-Time based Lattice Boltzmann Method (TRT-LBM) was used to simulate the gas flow. Different boundary conditions were applied to capture the gas slippage at the wall surface. For validation, the simulation results of LBM for non-slip flow were compared with those obtained from the solution of the N-S equation. In addition, for slip flow, the reliability of the LBM results with Diffusive Reflection (DR) and Bounce-back Specular Reflection (BSR) boundary conditions were also confirmed based on the solution of other methods found in the literature. Afterwards, gas flow in a single channel was simulated and the dimensionless from of the results were compared with the scaled measured permeability of three shale rocks. The effects of different slip boundary conditions and various accommodation coefficients were investigated. In addition, to study the impact of conduit size variations (similar to flow path in porous media), the gas flow was simulated in a simple pore body/throat (P/T) system. The simulation results were compared with those obtained for gas flow in a single channel. Furthermore, the simulation results of gas flow in the P/T system were compared with the experimental data. Finally, the LBM simulation results of gas flow in the P/T system were used to obtain appropriate slip coefficients for N-S equation for a wider range of Knudsen numbers (both slip and transition regimes). These simulation have been reported in Chapter 5.

In addition to single phase flow studies, the impact of high capillary pressure on the two-phase flow were investigated. To this aim, the relative permeability of three shale samples were measured using the steady state technique. It was explained that the main challenging artefact for the SS-kr measurements of the shale samples are the capillary end effect (CEE) due to the high capillary pressure. In these measurements, the relative permeability data of two shale samples were measured at four different injection rates. These measurements were performed to improve our understanding of the CEE during SS-kr measurements of the shale rocks. In addition, the effects of net stress were also

investigated by measuring relative permeability of the Eagle Ford shale (E4) at two net stress values of 1000 and 3000 psi. Moreover, the steady state displacement process was also simulated when the capillary pressure is not negligible. The results from numerical solutions were also used to study the impacts of CEE on the saturation profile of the wetting (liquid) phase. Then, the experimental data and the simulation results were used to develop a model to correct the CEE on the SS-kr data. To develop this method, it was mathematically shown that, for a constant LGR, the pressure drop and the average wetting phase saturation within the CEE region are constant and independent of the flow rate. Therefore, the experimental pressure drop and the measured wetting phase saturations have been related to the actual relative permeability values. In the proposed technique, steady state displacements at four different flow rates are required to estimate the CEE length, oil/gas relative permeability, fluid saturations and pressure drop in the unaffected zone. Furthermore, the integrity of the proposed method was evaluated using a series of artificially generated experimental data. For this purpose, a set of capillary pressure (Pc) and kr data were assumed and used in the analytical solution of two-phase flow. The analytical solutions were then used to generate artificial experimental data for pressure drop and average saturation during the SS-kr measurements. Then, the generated data were used as inputs and the proposed technique was hired to estimate the corrected kr data. Furthermore, the proposed technique was used to correct the SS-kr data of two shale samples (E3 and P3). The kr data from SS displacement experiments conducted at four different flow rates were used to obtain the corrected SS-kr data.

7.2 Conclusions

In this section, the observations and conclusions obtained from this research are briefly summarized. In addition, it is also tried to elaborate more on the main conclusions that relates to the fluid flow in the shale reservoirs at a larger scale.

- From the single-phase experiments performed on three shale rocks, it was shown that at any given net stress, the matrix permeability is increased by a reduction of pore pressure. In addition, at any pore pressure, the matrix permeability is decreased as the net stress is increased.
- It was concluded that the shale matrix permeability was more sensitive to the applied stress, when the pore pressure was close to the overburden pressure. This sensitivity reduces gradually as the reservoir pore pressure declines.

- It was shown that the stress dependency of non-slip permeabilities followed an exponential relationship. In addition, from the study of stress-induced permeability hysteresis, it was found that the permeability of Eagle Ford and Pierre shale sample can be lost up to 84% and 57% of the original values respectively, when the net stress was increased to 3000 psi and then it was decreased back to the initial net stress value.
- From the experimental results obtained for permeability hysteresis of shale samples, it was also concluded that the level of this stress-induced permeability hysteresis should be considered when designing a production plan (pressure drowdown) for an unconventional shale well. It means that the matrix permeability around the wellbore can be significantly damaged if it is exposed to a high net stress due to an excessive reduction of bottomhole pressure.
- It was shown that the gas slippage plays an important role on gas flow even at two-phase conditions. However, it was concluded that the permeability enhancements (in presence of liquid phase) are less compared to those values in a dried single-phase flow. It was discussed that this behaviour can be due to the less contribution of smaller flow paths as some of them may be occupied by liquid phase. However, more investigations are required to verify this behaviour. These results highlight the significant role of slippage in gas production from shale reservoirs.
- From the comparison of the analytical solution of N-S equation for slip flow and the experimental data, the slip coefficient of 2.10 was obtained for the first-order slip model. From the second-order slip model, the first- and second-order slip coefficients were obtained as 2.390 and 2.392, respectively. In addition, it was concluded that to find the second-order slip coefficient the same expression as the first-order slip coefficient can be used; i.e. $\frac{2-\sigma_v}{\sigma_v}$. In this study, the slip coefficients in porous media were measured for the first time. Such slip coefficients can be used in the slip model for accurate prediction of matrix permeability during the production period.
- The TMAC value, which is an important factor for simulation of slip flow, was also calculated based on the analytical slip flow model and the experimental data. The TMAC of ~0.6 was obtained from the experimental data performed on three shale samples at different pore and confining pressures. In addition, it was shown

that the B-K model overestimates the permeability enhancement when using the proposed rarefaction coefficient in the transition region. Therefore, using this model is not recommended for matrix permeability predictions.

- It was found that the obtained TMAC value in this study (from the three shale samples) was lower than those value obtained for gas flow in microchannels. It was concluded that the gas slippage was more pronounced in porous media and it needed to be considered when setting appropriate boundary conditions for modelling of gas flow (e.g. Lattice Boltzmann simulations).
- As an outcome of this research, a permeability prediction model was developed which considers the effects of slippage and stress on shale matrix permeability. The proposed model is simple and easy to implement in the commercial software such as Eclipse. The model can be tuned for any specific shale rock if the constants of the model are determined by performing a limited number of experiments.
- In addition, from the LBM simulation results, it was found that the LBM-BSR with the literature value of TMAC=0.8 underestimates the permeability enhancement of these shale rocks. It was concluded that the TMAC of 0.6 could better estimate the permeability enhancement. Such findings can help other researchers who work on the slip flow modelling in shale rocks by using the LBM.
- It was shown that the characteristic length of porous media can be better described by the average of pore throat sizes rather than average of pore body sizes. In addition, it was concluded that the gas slippage on the wall surface of pore throats has significant effects on the flow enhancement.
- Furthermore, simulation results of gas flow in a single channel and in the P/T system showed that, for Kn>0.05, the LBM simulation of slip flow in a single channel gives higher permeabilities compared to those values obtained from the LBM simulation in the P/T system. It was concluded that this bahaviour can be the main reason for the shale rocks permeability overestimation of the literature models (e.g. B-K model) as these models are originally developed based on the assumption of flow in a single pipe/channel.
- Moreover, it was shown that the experimental data can be better simulated when the system of pore body/throat was considered. It was discussed that assuming gas flow in a single pipe/channel cannot be a good representative of the gas flow in

porous media since gas molecules experience variable size flow conduits in shale reservoirs.

- From the fitted line to the simulation results (up to Kn=0.3), the first and second order slip coefficients of the N-S boundary condition were found as 2 and 1.54, respectively. Also, it was shown that the Klinkenberg model can give significant errors when it applies on the experimental data measured at the pressure conditions which gives Kn>0.05.
- From the experiments performed for two-phase flow study, it was found that the relative permeability data of the Eagle Ford shale (E3) are function of total injection rate. It was observed that the variation in the measured kr data was significant at the lower LGR. It was concluded that the CEE is the main reason for this observation. Similar behaviour was shown in the results from numerical solutions.
- In addition, it was observed that the CEE was more dominant in SS-kr experiments of Pierre (P3) compared to those performed on Eagle Ford (E3) because the kr data showed more discrepancies with respect to the injection rate. It was concluded that this behaviour was due to the higher capillary pressure of Pierre shale compared to Eagle Ford shale.
- In addition, compared to Pierre shale experimental kr data, higher values for residual gas saturations were obtained from the SS-kr experiments on Eagle Ford (E3). It was concluded that this higher residual gas saturations could be due the greater heterogeneity of Eagle Ford shale (E3) compared to the Pierre shale sample (P3).
- From the SS-kr experiments performed at two different net stress values, it was found that the CEEs become more pronounced with increasing net stress. This is mainly because of the increase in capillary pressure which could be due to the reduction of pore/throat sizes.
- In addition, since no significant change was observed for measured kr data at different net stress values, it was concluded that there was no macro-channel (macro-fracture) inside the matrix.
- The simulation results of SS two-phase flow showed that the CEE was more significant during the SS-kr experiment performed at the lowest LGR. In addition, the dominant role of the CEE increased as the injection rate was decreased.

- Finally, as an outcome of this research, a new model was proposed for correction of the CEE during SS-kr measurements of shale samples. Using this new method, kr data of shale samples can be measured by the steady-state technique without an expensive equipment for saturation profile determination such as CT-scan apparatus. The model was validated by artificially generated data. It was shown that the corrected SS-kr data by the proposed method were in good agreement with the actual known kr data of the input.

7.3 Recommendations for future studies

In this section, some recommendations are presented for the researchers who would like to contribute to this new line of research by improving the available understanding of fluid flow in the unconventional reservoir rocks. As mentioned, there are some dominant unconventional mechanisms which were not investigated in this study. In addition, some simplifying assumptions were made which can be relaxed in the future studies. These recommendations can be numbered as follows:

- Among the unconventional mechanisms mentioned in the Chapter 2, the sorption/desorption process are the dominant mechanism which has great impacts on fluid flow. In the experiments performed in this research, nitrogen gas was used to cancel the effects of sorption/desorption of the flowing gas to the organic materials. While in the unconventional reservoirs, methane is the main component of the gas stream which shows a significant rate of sorption/desorption to the available organic materials. Therefore it is suggested to quantify the impact of sorption/desorption mechanism on the flow using experimental data. Then the permeability model developed in this study can be modify to include the effects of sorption/desorption mechanism.
- The effects of liquid phase (residual saturation) on the gas slippage were not investigated quantitatively in this research. It is recommended to quantify the impacts of liquid saturation (using experimental data) and include it in the proposed permeability prediction model.
- After improving the model for adsorption mechanism and the effects of liquid saturation, the model can be implemented into commercial reservoir simulators. To this aim, based on the pore pressure and the liquid saturation of each grid block,

the absolute permeability should be estimated. The model considers the permeability of block assuming the simultaneous effects of slippage, stress, adsorption and the liquid saturation. However, in the commercial simulators, the pressures and the saturations are unknowns which have to be determined at each time step. Therefore, it is recommended to use pressure and saturation of the previous time steps to calculate the matrix absolute permeability.

- As indicated in Chapter 4, based on the obtained TMAC and slip coefficients, a higher slippage rate is expected in porous media. The reasons behind this behaviour are not well understood which needs more experimental and simulation studies. These reasons can be surface roughness or presence of higher surface area in porous media.
- The LBM simulations were performed for single-phase gas flow in a simple P/T system. As seen in Chapter 5, the geometries selected for pore body/ pore throat study were simple and symmetric. The squared (sharp corner) bodies were used as obstacle. It is recommended to investigate the effects of random shaped and round corner bodies in the fluid stream. For example, the simulations can be performed for more complex geometries benefiting from the SEM images of shale samples. However, implementation of DR and BSR boundary conditions are difficult if the obstacles are not symmetric. In other words, based on the SEM, the coordination of the solid and fluid nodes should be established first. Then the boundary condition rules should be given for solid nodes in the system. However, as the direction of distribution functions are important, the neighbour nodes should be also considered when setting up the boundary conditions. Although it would be difficult and time consuming to set-up the models based on SEM images, the simulation results are more reliable and the developed structure can be for simulation of two-phase fluid flow.
- As mentioned, the LBM simulations can be extended for two-phase flow to study the impacts of liquid phase. The effects of liquid on the slip flow were not investigated quantitatively in this study. Moreover, the developed program can be used to obtain the kr data as an alternative for SS kr measurements.
- The relative permeability of unconventional reservoir rocks are rarely measured and the effects of pertinent parameters are not investigated yet. Hence, more

studies should be performed to improve our understanding of the behaviour of two-phase flow in the unconventional reservoir rocks.

- As mentioned in Chapter 6, there are some limitations for using the proposed method in this study to correct the CEE during the SS-kr measurements. The main one is that the injection rate should be higher above a certain value to have an unaffected region (non-CEE region). In some cases for the ultralight samples, the CEE region covers the entire core due to the significant effects of capillary forces. It is suggested to extend the proposed method here to be applicable for these experiments as well.

APPENDIX 1: ERROR CALCULATIONS

In this research, the absolute permeability (Chapter 3), dimensionless permeability (Chapter 4), Knudsen numbers (Chapter 4) and relative permeability (Chapter 6) values were calculated using the measured data and the Darcy's law as follows:

$$k = \frac{q\mu L}{A\,\Delta P} \tag{A1.1}$$

and

$$k_D = \frac{k}{k_{non-slip}} = \frac{q\mu L}{k_{non-slip}\,A\,\Delta P} \tag{A1.2}$$

and

$$k_r = \frac{q\mu L}{k\,A\,\Delta P} \tag{A1.3}$$

The propagation of the errors should be calculated for estimation of errors for calculated absolute, dimensionless and relative permeability values.

It is known that, if

$$Q = \frac{ab\,\ldots.c}{xy\,\ldots.z} \tag{A1.4}$$

then the corresponding error in calculation of Q can be written as follows:

$$\frac{\delta Q}{|Q|} = \sqrt{(\frac{\delta a}{a})^2 + (\frac{\delta b}{b})^2 + \cdots + \left(\frac{\delta c}{c}\right)^2 + \left(\frac{\delta x}{x}\right)^2 + \left(\frac{\delta y}{y}\right)^2 + \cdots (\frac{\delta z}{z})^2} \tag{A1.5}$$

In practice, it is usually easier to convert all of the uncertainties into percentages before applying the formula. Therefore, to calculate the errors corresponding to the calculated absolute and relative permeability values, the error percentages of the measured length, area, viscosity, pressure drop and flow rate should be known.

The percentage error for the length and area measurements were 0.2 % and 0.28 %, respectively. For pressure measurements, the error is 0.3 % assuming the measurements were performed at 500 psi. For fluid viscosity, the error of 0.25 % was reported by NIST (Marvin, 1971). In addition, as mentioned before, a Quizix pump (Q5000-5K) was used

in the setup. Based on the specifications of the pump, the percentage error of measurements is 3.15 % for the minimum injection rate of 0.2 cc/hr.

Therefore, the error of absolute permeability measurements can be calculated as follows:

$$\frac{\delta k}{|k|}(\%) = \sqrt{(0.2\%)^2 + (0.28\%)^2 + (0.3\%)^2 + (0.25\%)^2 + (3.15\%)^2} = 3.2\ \% \quad \text{(A1.6)}$$

And for the calculated dimensionless and relative permeability values, the obtained error for absolute permeability (Equation A1.6) can be used. Hence

$$\frac{\delta k_r}{|k_r|}(\%) = \sqrt{(0.2\%)^2 + (0.28\%)^2 + (0.3\%)^2 + (0.25\%)^2 + (3.15\%)^2 + (3.193\%)^2} = 4.5\ \% \quad \text{(A1.7)}$$

These calculated errors were used to plot the error bars in Figure 3.12, 4.2, 6.2, 6.3 and 6.4.

The propagation of the error for calculation of the Knudsen numbers can be also obtained if the error percentage for the measurements of viscosity, pressure, temperature and the characteristic length scale are known. In other words, as equations 4.20 and 4.21 were used for calculation of mean free paths, it is required to know the percentage errors for viscosity, gas pressure and temperature measurements. Also, as for calculation of Knudsen number, equation 2.1 was used, the percentage error of measurement for characteristic length should be determined. It was mentioned that the percentage error for viscosity measurements can be assumed 0.25 %. Considering the error of $\pm 0.1\%\ C$ for the oven, the percentage error of measurement for absolute temperature was 0.03%. For calculation of error percentage for characteristic length, the following equation was used.

$$Standard\ Error = \frac{\sigma}{\sqrt{n}} \quad \text{(A1.8)}$$

where σ is standard deviation and n is the number of measurement points during the MICP test. From the best identified probably distribution functions, the standard deviations were reported on Table 3.3. The number of measurement points during the

MICP tests were 36, 29 and 28 for Eagle Ford, Pierre and Barnett shale, respectively. Using the above values, the percentage errors for the characteristic lengths were obtained as 6.48%, 6.06% and 15.45% for Eagle Ford, Pierre and Barnett, respectively.

Considering the above values, the propagation error for Knudsen number calculations are as follow.

For Eagle Ford:

$$\frac{\delta Kn}{Kn}(\%) = \sqrt{(0.25\%)^2 + (0.3\%)^2 + (0.03\%)^2 + (6.48\%)^2} = 6.5\ \% \qquad \text{(A1.9)}$$

For Pierre:

$$\frac{\delta Kn}{Kn}(\%) = \sqrt{(0.25\%)^2 + (0.3\%)^2 + (0.03\%)^2 + (6.06\%)^2} = 6.1\ \% \qquad \text{(A1.10)}$$

For Barnett:

$$\frac{\delta Kn}{Kn}(\%) = \sqrt{(0.25\%)^2 + (0.3\%)^2 + (0.03\%)^2 + (15.45\%)^2} = 15.5\ \% \qquad \text{(A1.11)}$$

APPENDIX 2: SOLUTION OF NAVIER–STOKES EQUATION FOR INCOMPRESSIBLE FLOW WITH SLIP BOUNDARY CONDITIONS

In this appendix, the solution of N-S equation for incompressible flow in a single pipe was obtained by assuming first-order slip boundary condition. Figure A2.1 demonstrates the coordination used in the following derivations.

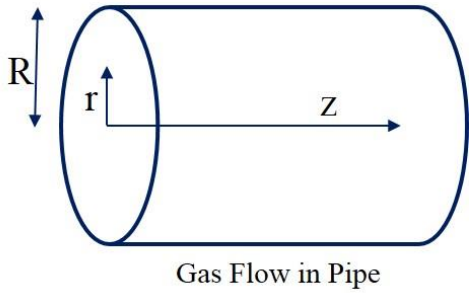

Figure A2.1: coordination in schematic of gas flow in a pipe

Assuming steady state, incompressible flow and ignoring the gravity effect, the N-S equations can be written as follows:

$$\frac{1}{r}\frac{\partial}{\partial r}\left(r\frac{\partial u_z}{\partial r}\right)=\frac{1}{\mu}\frac{\partial p}{\partial z} \tag{A2.1}$$

The first order slip boundary conditions are:

$$\left(\frac{\partial u_z}{\partial r}\right)_{r=0}=0 \tag{A2.2}$$

$$u_{z\,r=R}=(\alpha_s\frac{2-\sigma_v}{\sigma_v})\lambda\left(\frac{\partial u_z}{\partial r}\right)_{sur}=C_1\lambda\left(\frac{\partial u_z}{\partial r}\right)_{sur} \tag{A2.3}$$

Equation A2.1 can be integrated with respect to r, as follows:

$$\left(r\frac{\partial u_z}{\partial r}\right)=\frac{r^2}{2\mu}\frac{\partial p}{\partial z}+A \tag{A2.4}$$

where A is a constant and should be determined based on the boundary conditions. Using Equation A2.2, the term A is equal to zero. Hence:

$$\frac{\partial u_z}{\partial r} = \frac{r}{2\mu}\frac{\partial p}{\partial z} \tag{A2.5}$$

Equation A2.5 can be integration again with respect to r, as follows:

$$u_z(r) = \frac{r^2}{4\mu}\frac{\partial p}{\partial z} + B \tag{A2.6}$$

where B is a constant and should be determined based on the boundary conditions. Using Equation A2.3, B is equal to:

$$B = C_1\lambda \left(\frac{\partial u_z}{\partial r}\right)_R - \frac{R^2}{4\mu}\frac{\partial p}{\partial z} \tag{A2.7}$$

using Equation A2.5, B can be obtained as:

$$B = C_1\lambda \frac{R}{2\mu}\frac{\partial p}{\partial z} - \frac{R^2}{4\mu}\frac{\partial p}{\partial z} = \frac{R}{2\mu}\frac{\partial p}{\partial z}(C_1\lambda - \frac{R}{2}) \tag{A2.8}$$

Therefore, the velocity profile can be written as:

$$u_z(r) = \frac{r^2}{4\mu}\frac{\partial p}{\partial z} + B = \frac{r^2}{4\mu}\frac{\partial p}{\partial z} + \frac{R}{2\mu}\frac{\partial p}{\partial z}(C_1\lambda - \frac{R}{2}) \tag{A2.9}$$

which is

$$u_z(r) = \frac{1}{2\mu}\frac{\partial p}{\partial z}\left[\frac{r^2}{2} - \frac{R^2}{2} + C_1\lambda R\right] = \frac{R^2}{4\mu}\frac{\partial p}{\partial z}\left[\frac{r^2}{R^2} - 1 + C_1\frac{\lambda}{R}\right] \tag{A2.10}$$

As $Kn = \lambda/R$, the velocity profile can be written as:

$$u_z(r) = \left(\frac{R^2}{4\mu}\frac{dp}{dx}\right)\left[\frac{r^2}{R^2} - 1 + 2C_1Kn\right] \tag{A2.11}$$

REFERENCES

AL- WARDY, W. & ZIMMERMAN, R. W. 2004. Effective stress law for the permeability of clay- rich sandstones. *Journal of Geophysical Research: Solid Earth,* 109.

AL HINAI, A., REZAEE, R., ESTEBAN, L. & LABANI, M. 2014. Comparisons of pore size distribution: a case from the Western Australian gas shale formations. *Journal of Unconventional Oil and Gas Resources,* 8**,** 1-13.

ARYA, G., CHANG, H.-C. & MAGINN, E. J. 2003. Molecular simulations of Knudsen wall-slip: effect of wall morphology. *Molecular Simulation,* 29**,** 697-709.

ASINARI, P. 2005. *Multi-Scale Analysis of Heat and Mass Transfer in Mini/Micro-Structures.* Ph. D. Dissertation.

BAO, Y. B. & MESKAS, J. 2011. Lattice boltzmann method for fluid simulations. *Department of Mathematics, Courant Institute of Mathematical Sciences, New York University*.

BARBER, R. W. & EMERSON, D. R. 2006. Challenges in modeling gas-phase flow in microchannels: from slip to transition. *Heat Transfer Engineering,* 27**,** 3-12.

BARISIK, M. & BESKOK, A. 2011. Molecular dynamics simulations of shear-driven gas flows in nano-channels. *Microfluidics and nanofluidics,* 11**,** 611-622.

BARISIK, M. & BESKOK, A. 2014. Scale effects in gas nano flows. *Physics of Fluids (1994-present),* 26**,** 052003.

BESKOK, A. & KARNIADAKIS, G. E. 1999. Report: a model for flows in channels, pipes, and ducts at micro and nano scales. *Microscale Thermophysical Engineering,* 3**,** 43-77.

BHATIA, S. K., BONILLA, M. R. & NICHOLSON, D. 2011. Molecular transport in nanopores: a theoretical perspective. *Physical Chemistry Chemical Physics,* 13**,** 15350-15383.

BHATIA, S. K. & NICHOLSON, D. 2003. Molecular transport in nanopores. *The Journal of Chemical Physics,* 119**,** 1719-1730.

BHATNAGAR, P. L., GROSS, E. P. & KROOK, M. 1954. A model for collision processes in gases. I. Small amplitude processes in charged and neutral one-component systems. *Physical review,* 94**,** 511.

BHATTACHARYA, D. & LIE, G. 1991. Nonequilibrium gas flow in the transition regime: a molecular-dynamics study. *Physical Review A,* 43**,** 761.

BIOT, M. & WILLIS, D. 1957. The elastic coefficients of the theory of consolidation. *Journal of Applied Mechanics,* 24**,** 594-601.

BIOT, M. A. 1956. Theory of propagation of elastic waves in a fluid-saturated porous solid. II. Higher frequency range. *the Journal of the Acoustical Society of America,* 28**,** 179-191.

BIRD, G. A. 1994. *Molecular gas dynamics and the direct simulation of gas flows,* Clarendon Press.

BLANCHARD, D. & LIGRANI, P. 2007. Slip and accommodation coefficients from rarefaction and roughness in rotating microscale disk flows. *Physics of Fluids* 19**,** 063602.

BOURBIE, T. & WALLS, J. 1982. Pulse Decay Permeability: Analytical Solution and Experimental Test. *Society of Petroleum Engineers Journal,* 55.

BRACE, W. F., WALSH, J. & FRANGOS, W. 1968. Permeability of granite under high pressure. *Journal of Geophysical research,* 73**,** 2225-2236.

BUONOMO, B., MANCA, O. & LAURIAT, G. 2014. Forced convection in micro-channels filled with porous media in local thermal non-equilibrium conditions. *International Journal of Thermal Sciences,* 77**,** 206-222.

BURGDORFER, A. 1958. The Influence of the Molecular Mean Free Path on the Performance of Hydrodynamic Gas Lubricated Bearings. Franklin Inst. Labs. for Research and Development, Philadelphia.

BUSTIN, A. M. & BUSTIN, R. M. 2012. Importance of rock properties on the producibility of gas shales. *International Journal of Coal Geology,* 103**,** 132-147.

BUSTIN, A. M., BUSTIN, R. M. & CUI, X. Importance of fabric on the production of gas shales. SPE Unconventional Reservoirs Conference, 2008. Society of Petroleum Engineers.

BYRNES, A., CLUFF, R. & WEBB, J. 2009. Analysis of critical permeability, capillary pressure, and electrical properties for Mesaverde tight gas sandstones from western US basins: Final report submitted by Kansas Geological Survey for United States Department of Energy (DOE) contract DE-FC26-05NT42660. Technical Report: pdf document and spreadsheets downloaded February 2013 from website: http://www. kgs. ku. edu/mesaverde.

CAO, B.-Y., CHEN, M. & GUO, Z.-Y. 2006. Effect of surface roughness on gas flow in microchannels by molecular dynamics simulation. *International Journal of Engineering Science,* 44**,** 927-937.

CERCIGNANI, C. 2000. *Rarefied gas dynamics: from basic concepts to actual calculations,* Cambridge University Press.

CHALMERS, G. R., BUSTIN, R. M. & POWER, I. M. 2012a. Characterization of gas shale pore systems by porosimetry, pycnometry, surface area, and field emission scanning electron microscopy/transmission electron microscopy image analyses: Examples from the Barnett, Woodford, Haynesville, Marcellus, and Doig units. *AAPG bulletin,* 96**,** 1099-1119.

CHALMERS, G. R., ROSS, D. J. & BUSTIN, R. M. 2012b. Geological controls on matrix permeability of Devonian Gas Shales in the Horn River and Liard basins, northeastern British Columbia, Canada. *International Journal of Coal Geology,* 103**,** 120-131.

CHEN, A. & WOOD, A. Rate effects on water-oil relative permeability. Proceedings of the International Symposium of the Society of Core Analysts, Edinburgh, Scotland, 2001. 17-19.

CHEN, C.-C. & RAJAGOPAL, R. 1997. A multiply-fractured horizontal well in a rectangular drainage region. *SPE Journal,* 2**,** 455-465.

CHEN, T. & STAGG, P. W. 1984. Semilog Analysis of the Pulse-Decay Technique of Permeability Measurement. *Society of Petroleum Engineers Journal,* 24.

CHEN, Y., ZHANG, C., SHI, M. & PETERSON, G. 2009. Role of surface roughness characterized by fractal geometry on laminar flow in microchannels. *Physical Review E,* 80**,** 026301.

CIVAN, F. 2010. Effective correlation of apparent gas permeability in tight porous media. *Transport in porous media,* 82**,** 375-384.

COLIN, C. A., STÉPHANE 2001. High-order boundary conditions for gaseous flows in rectangular microducts. *Microscale Thermophysical Engineering,* 5**,** 41-54.

CROCE, G. & D'AGARO, P. 2004. Numerical analysis of roughness effect on microtube heat transfer. *Superlattices and Microstructures,* 35**,** 601-616.

CUI, X., BUSTIN, A. & BUSTIN, R. M. 2009. Measurements of gas permeability and diffusivity of tight reservoir rocks: different approaches and their applications. *Geofluids,* 9**,** 208-223.

CURTIS, M. E., AMBROSE, R. J., SONDERGELD, C. H. & RAI, C. S. Transmission and scanning electron microscopy investigation of pore connectivity of gas shales

on the nanoscale. North American Unconventional Gas Conference and Exhibition, 2011. SPE 144391.
DARABI, H., ETTEHAD, A., JAVADPOUR, F. & SEPEHRNOORI, K. 2012. Gas flow in ultra-tight shale strata. *Journal of Fluid Mechanics,* 710**,** 641-658.
DENG, J., ZHU, W. & MA, Q. 2014. A new seepage model for shale gas reservoir and productivity analysis of fractured well. *Fuel,* 124**,** 232-240.
DEWHURST, D. N. & SIGGINS, A. F. 2006. Impact of fabric, microcracks and stress field on shale anisotropy. *Geophysical Journal International,* 165**,** 135-148.
DICKER, A. I. & SMITS, R. M. 1988. A Practical Approach for Determining Permeability From Laboratory Pressure-Pulse Decay Measurements. *International Meeting on Petroleum Engineering.* Tianjin, China: Society of Petroleum Engineers.
DONG, J.-J., HSU, J.-Y., WU, W.-J., SHIMAMOTO, T., HUNG, J.-H., YEH, E.-C., WU, Y.-H. & SONE, H. 2010. Stress-dependence of the permeability and porosity of sandstone and shale from TCDP Hole-A. *International Journal of Rock Mechanics and Mining Sciences,* 47**,** 1141-1157.
DONGARI, N., AGRAWAL, A. & AGRAWAL, A. 2007. Analytical solution of gaseous slip flow in long microchannels. *International Journal of Heat and Mass Transfer,* 50**,** 3411-3421.
EIA 2013. Technically Recoverable Shale Oil and Shale Gas Resources: An Assessment of 137 Shale Formations in 41 Countries Outside the United States. *Analysis and projections. United States Energy Information Administration*.
EIA 2015. Annual Energy Outlook 2015 with Projections to 2040
EIA 2016. ENERGY IN BRIEF. *U.S Energy Information Administration,* https://www.eia.gov/energy_in_brief/article/shale_in_the_united_states.cfm.
EVANS, J. P., FORSTER, C. B. & GODDARD, J. V. 1997. Permeability of fault-related rocks, and implications for hydraulic structure of fault zones. *Journal of Structural Geology,* 19**,** 1393-1404.
EWART, T., PERRIER, P., GRAUR, I. & MÉOLANS, J. G. 2007. Tangential momemtum accommodation in microtube. *Microfluidics and Nanofluidics,* 3**,** 689-695.
FATHI, E. & AKKUTLU, I. Y. 2013. Lattice Boltzmann Method for Simulation of Shale Gas Transport in Kerogen. *Society of Petroleum Engineers Journal,* 18.
FIROUZI, M., ALNOAIMI, K., KOVSCEK, A. & WILCOX, J. 2014. Klinkenberg effect on predicting and measuring helium permeability in gas shales. *International Journal of Coal Geology,* 123**,** 62-68.
FLORENCE, F. A., RUSHING, J., NEWSHAM, K. E. & BLASINGAME, T. A. 2007. Improved Permeability Prediction Relations for Low Permeability Sands. *Rocky Mountain Oil & Gas Technology Symposium.* Denver, Colorado, U.S.A.: Society of Petroleum Engineers.
FREEMAN, C., MORIDIS, G. & BLASINGAME, T. 2011. A numerical study of microscale flow behavior in tight gas and shale gas reservoir systems. *Transport in porous media,* 90**,** 253-268.
GAD-EL-HAK, M. 1999. The fluid mechanics of microdevices—the Freeman scholar lecture. *Journal of Fluids Engineering,* 121**,** 5-33.
GHABEZLOO, S., SULEM, J., GUÉDON, S. & MARTINEAU, F. 2009. Effective stress law for the permeability of a limestone. *International Journal of Rock Mechanics and Mining Sciences,* 46**,** 297-306.
GHANIZADEH, A., AMANN-HILDENBRAND, A., GASPARIK, M., GENSTERBLUM, Y., KROOSS, B. M. & LITTKE, R. 2014a. Experimental study of fluid transport processes in the matrix system of the European organic-

rich shales: II. Posidonia Shale (Lower Toarcian, northern Germany). *International Journal of Coal Geology,* 123**,** 20-33.

GHANIZADEH, A., GASPARIK, M., AMANN-HILDENBRAND, A., GENSTERBLUM, Y. & KROOSS, B. M. 2014b. Experimental study of fluid transport processes in the matrix system of the European organic-rich shales: I. Scandinavian Alum Shale. *Marine and Petroleum Geology,* 51**,** 79-99.

GINZBURG, I. 2005. Equilibrium-type and link-type lattice Boltzmann models for generic advection and anisotropic-dispersion equation. *Advances in Water resources,* 28**,** 1171-1195.

GINZBURG, I., VERHAEGHE, F. & D'HUMIERES, D. 2008. Study of simple hydrodynamic solutions with the two-relaxation-times lattice Boltzmann scheme. *Communications in computational physics,* 3**,** 519-581.

GRAUR, I., PERRIER, P., GHOZLANI, W. & MÉOLANS, J. 2009. Measurements of tangential momentum accommodation coefficient for various gases in plane microchannel. *Physics of Fluids* 21**,** 102004.

GUO, C., XU, J., WU, K., WEI, M. & LIU, S. 2015. Study on gas flow through nano pores of shale gas reservoirs. *Fuel,* 143**,** 107-117.

GUO, Z., ZHAO, T. & SHI, Y. 2006. Physical symmetry, spatial accuracy, and relaxation time of the lattice Boltzmann equation for microgas flows. *Journal of Applied physics,* 99**,** 074903.

GUO, Z., ZHENG, C. & SHI, B. 2008. Lattice Boltzmann equation with multiple effective relaxation times for gaseous microscale flow. *Physical Review E,* 77**,** 036707.

GUPTA, R. & MALONEY, D. R. 2015. Intercept Method--A Novel Technique To Correct Steady-State Relative Permeability Data for Capillary End Effects. *SPE Reservoir Evaluation & Engineering*.

GUTIERREZ, M., KATSUKI, D. & TUTUNCU, A. 2014. Determination of the continuous stress-dependent permeability, compressibility and poroelasticity of shale. *Marine and Petroleum Geology*.

GUTIERREZ, M., ØINO, L. & NYGÅRD, R. 2000. Stress-dependent permeability of a de-mineralised fracture in shale. *Marine and Petroleum Geology,* 17**,** 895-907.

HELLER, R., VERMYLEN, J. & ZOBACK, M. 2014. Experimental investigation of matrix permeability of gas shales. *AAPG bulletin,* 98**,** 975-995.

HELLER, R. & ZOBACK, M. 2014. Adsorption of methane and carbon dioxide on gas shale and pure mineral samples. *Journal of Unconventional Oil and Gas Resources,* 8**,** 14-24.

HILDEBRAND, J. 1976. Viscosity of dilute gases and vapors. *Proceedings of the National Academy of Sciences,* 73**,** 4302-4303.

HOMAYOON, A., ISFAHANI, A. M., SHIRANI, E. & ASHRAFIZADEH, M. 2011. A novel modified lattice Boltzmann method for simulation of gas flows in wide range of Knudsen number. *International Communications in Heat and Mass Transfer,* 38**,** 827-832.

HONARPOUR, M., KOEDERITZ, F. & HERBERT, A. 1986. *Relative permeability of petroleum reservoirs*, C.R.C. Press, 1986.

HONARPOUR, M. & MAHMOOD, S. 1988. Relative-permeability measurements: An overview. *Journal of Petroleum Technology,* 40**,** 963-966.

HSIA, Y. T. & DOMOTO, G. 1983. An experimental investigation of molecular rarefaction effects in gas lubricated bearings at ultra-low clearances. *Journal of Tribology,* 105**,** 120-129.

HSIEH, P., TRACY, J., NEUZIL, C., BREDEHOEFT, J. & SILLIMAN, S. A transient laboratory method for determining the hydraulic properties of 'tight'rocks—I.

Theory. International Journal of Rock Mechanics and Mining Sciences & Geomechanics Abstracts, 1981. Elsevier, 245-252.
HUANG, D. D. & HONARPOUR, M. M. 1998. Capillary end effects in coreflood calculations. *Journal of Petroleum Science and Engineering,* 19**,** 103-117.
IGLAUER, S., FAVRETTO, S., SPINELLI, G., SCHENA, G. & BLUNT, M. J. 2010. X-ray tomography measurements of power-law cluster size distributions for the nonwetting phase in sandstones. *Physical Review E,* 82**,** 056315.
JANG, J. & WERELEY, S. T. 2006. Effective heights and tangential momentum accommodation coefficients of gaseous slip flows in deep reactive ion etching rectangular microchannels. *Journal of Micromechanics and Microengineering,* 16**,** 493.
JAVADPOUR, F. 2009. Nanopores and Apparent Permeability of Gas Flow in Mudrocks (Shales and Siltstone). *Journal of Canadian Petroleum Technology,* 48.
JAVADPOUR, F., FISHER, D. & UNSWORTH, M. 2007. Nanoscale gas flow in shale gas Sediments. *Journal of Canadian Petroleum Technology,* 46**,** 55-61.
JENNINGS, D. S., ANTIA, J., CAMP, W., DIAZ, E. & WAWAK, B. 2013. Petrographic characterization of the Eagle Ford Shale, South Texas: Mineralogy, common constituents, and distribution of nanometer-scale pore types. *Electron microscopy of shale hydrocarbon reservoirs: AAPG Memoir,* 102**,** 101-114.
JIE, D., DIAO, X., CHEONG, K. B. & YONG, L. K. 2000. Navier-Stokes simulations of gas flow in micro devices. *Journal of Micromechanics and Microengineering,* 10**,** 372.
JONES, F. O. & OWENS, W. 1980. A laboratory study of low-permeability gas sands. *Journal of Petroleum Technology,* 32**,** 1,631-1,640.
JONES, S. 1997. A technique for faster pulse-decay permeability measurements in tight rocks. *SPE Formation Evaluation***,** 19-26.
KALANTARI-DAHAGHI, A. 2011. Systematic approach to numerical simulation and modelling of shale gas reservoirs. *International Journal of Oil, Gas and Coal Technology,* 4**,** 209-243.
KARNIADAKIS, G. & BESKOK, A. 2002. Micro flows: fundamentals and simulation. New York, NY: Springer Verlag.
KARNIADAKIS, G., BESKOK, A. & ALURU, N. 2005. *Microflows and nanoflows: fundamentals and simulation,* Springer Science & Business Media.
KAZEMI, M. & TAKBIRI-BORUJENI, A. 2015. An analytical model for shale gas permeability. *International Journal of Coal Geology,* 146**,** 188-197.
KLINKENBERG, L. J. 1941. The Permeability Of Porous Media To Liquids And Gases. American Petroleum Institute.
KNECHTEL, E. D. & PITTS, W. C. 1969. Experimental momentum accommodation on metal surfaces of ions near and above earth-satellite speeds. *Rarefied Gas Dynamics,* 5**,** 1257-1266.
KUHLTHAU, A. 1949. Air friction on rapidly moving surfaces. *Journal of Applied Physics,* 20**,** 217-223.
KUNERT, C. & HARTING, J. 2007. Roughness induced boundary slip in microchannel flows. *Physical review letters,* 99**,** 176001.
KWON, O., KRONENBERG, A. K., GANGI, A. F. & JOHNSON, B. 2001. Permeability of Wilcox shale and its effective pressure law. *Journal of Geophysical Research: Solid Earth,* 106**,** 19339-19353.
KWON, O., KRONENBERG, A. K., GANGI, A. F., JOHNSON, B. & HERBERT, B. E. 2004. Permeability of illite-bearing shale: 1. Anisotropy and effects of clay content and loading. *Journal of Geophysical Research: Solid Earth (1978–2012),* 109.

LEI, Q., XIONG, W., YUANG, J., CUI, Y. & WU, Y.-S. Analysis of stress sensitivity and its influence on oil production from tight reservoirs. Eastern Regional Meeting, 2007. Society of Petroleum Engineers.
LEVERETT, M. 1941. Capillary behavior in porous solids. *Transactions of the AIME,* 142**,** 152-169.
LI, Q., HE, Y., TANG, G. & TAO, W. 2011. Lattice Boltzmann modeling of microchannel flows in the transition flow regime. *Microfluidics and nanofluidics,* 10**,** 607-618.
LIM, C., SHU, C., NIU, X. & CHEW, Y. 2002. Application of lattice Boltzmann method to simulate microchannel flows. *Physics of Fluids (1994-present),* 14**,** 2299-2308.
LOCKERBY, D. A. & REESE, J. M. 2008. On the modelling of isothermal gas flows at the microscale. *Journal of Fluid Mechanics,* 604**,** 235-261.
LORD, R. 1977. Tangential momentum accommodation coefficients of rare gases on polycrystalline metal surfaces. *Rarefied gas dynamics***,** 531-538.
LOUCKS, R., REED, R., RUPPEL, S. & HAMMES, U. 2010. Preliminary classification of matrix pores in mudrocks: Gulf Coast Association of Geological Societies Transactions, v. 60. *ndash,* 441**,** 435.
LOYALKA, S. & HAMOODI, S. 1990. Poiseuille flow of a rarefied gas in a cylindrical tube: solution of linearized Boltzmann equation. *Physics of Fluids A: Fluid Dynamics (1989-1993),* 2**,** 2061-2065.
LUO, L.-S. 2004. Comment on "Discrete Boltzmann equation for microfluidics". *Physical review letters,* 92**,** 139401.
LUO, L.-S. 2011. Comment on "Heat transfer and fluid flow in microchannels and nanochannels at high Knudsen number using thermal lattice-Boltzmann method". *Physical Review E,* 84**,** 048301.
MAINI, B., COSKUNER, G. & JHA, K. 1990. A Comparison Of Steady-State And Unsteady-State Relative Permeabilities Of Viscocities Oil And Water In Ottawa Sand. *Journal of Canadian Petroleum Technology,* 29.
MALONEY, D., WEGENER, D. & ZORNES, D. 1999. New x-ray scanning system for special core analyses in support of reservoir characterization. *Paper SCA,* 9940**,** 1-4.
MARVIN, R. S. 1971. The accuracy of measurements of viscosity of liquids. *J. Res. Natl. Bur. Stand. A,* 75.
MAURER, J., TABELING, P., JOSEPH, P. & WILLAIME, H. 2003. Second-order slip laws in microchannels for helium and nitrogen. *Physics of Fluids,* 15**,** 2613-2621.
MAXWELL, J. C. 1879. On stresses in rarified gases arising from inequalities of temperature. *Philosophical Transactions of the royal society of London***,** 231-256.
MITSUYA, Y. 1993. Modified Reynolds equation for ultra-thin film gas lubrication using 1.5-order slip-flow model and considering surface accommodation coefficient. *Journal of Tribology,* 115**,** 289-294.
MOHAMAD, A. A. 2011. *Lattice Boltzmann method: fundamentals and engineering applications with computer codes,* Springer Science & Business Media.
NAZARI MOGHADDAM, R. & JAMIOLAHMADY, M. An Investigation into Free-Imbibition of Sessile Drop when Measuring Contact Angle on Porous Substrates. 77th EAGE Conference and Exhibition 2015, 2015 Madrid, Spain.
NIE, X., DOOLEN, G. D. & CHEN, S. 2002. Lattice-Boltzmann simulations of fluid flows in MEMS. *Journal of Statistical Physics,* 107**,** 279-289.
NING, Y., JIANG, Y., LIU, H. & QIN, G. 2015. Numerical modeling of slippage and adsorption effects on gas transport in shale formations using the lattice Boltzmann method. *Journal of Natural Gas Science and Engineering,* 26**,** 345-355.
NIST 2015. National Institute of Standards and Technology. *http://webbook.nist.gov/chemistry/fluid/*.

NIU, C., HAO, Y.-Z., LI, D. & LU, D. 2014. Second-Order Gas-Permeability Correlation of Shale During Slip Flow. *Society of Petroleum Engineers Journal* 19(05)**,** 786-792.

NIU, X., SHU, C. & CHEW, Y. 2004. A lattice Boltzmann BGK model for simulation of micro flows. *EPL (Europhysics Letters),* 67**,** 600.

NOBAKHT, M., CLARKSON, C. R. & KAVIANI, D. 2013. New type curves for analyzing horizontal well with multiple fractures in shale gas reservoirs. *Journal of Natural Gas Science and Engineering,* 10**,** 99-112.

OSOBA, J., RICHARDSON, J., KERVER, J., HAFFORD, J. & BLAIR, P. 1951. Laboratory measurements of relative permeability. *Journal of Petroleum Technology,* 3**,** 47-56.

QADEER, S., DEHGHANI, K., OGBE, D. & OSTERMANN, R. 1991. *Correcting oil-water relative permeability data for capillary end effect in displacement experiments*, Springer.

RAPOPORT, L. & LEAS, W. 1953. Properties of linear waterfloods. *Journal of Petroleum Technology,* 5**,** 139-148.

REN, J., GUO, P., GUO, Z. & WANG, Z. 2015. A Lattice Boltzmann Model for Simulating Gas Flow in Kerogen Pores. *Transport in Porous Media,* 106**,** 285-301.

RICHARDSON, J., KERVER, J., HAFFORD, J. & OSOBA, J. 1952. Laboratory determination of relative permeability. *Journal of Petroleum Technology,* 4**,** 187-196.

ROMANENKO, K. & BALCOM, B. J. 2013. An assessment of non-wetting phase relative permeability in water-wet sandstones based on quantitative MRI of capillary end effects. *Journal of Petroleum Science and Engineering,* 110**,** 225-231.

ROOHI, E. & DARBANDI, M. 2009. Extending the Navier–Stokes solutions to transition regime in two-dimensional micro-and nanochannel flows using information preservation scheme. *Physics of Fluids (1994-present),* 21**,** 082001.

ROVENSKAYA, O. 2013. Kinetic analysis of surface roughness in a microchannel. *Computers & Fluids,* 77**,** 159-165.

ROY, S., RAJU, R., CHUANG, H. F., CRUDEN, B. A. & MEYYAPPAN, M. 2003. Modeling gas flow through microchannels and nanopores. *Journal of applied physics,* 93**,** 4870-4879.

RP40, A. 1998. Recommended practices for core analysis. *Feb*.

SAKHAEE-POUR, A. & BRYANT, S. 2012. Gas Permeability of Shale. *SPE Reservoir Evaluation & Engineering,* 15(04)**,** 401-409.

SANAEI, A., JAMILI, A., CALLARD, J. & MATHUR, A. Production Modeling in the Eagle Ford Gas Condensate Window: Integrating New Relationships between Core Permeability, Pore Size, and Confined PVT Properties. SPE Western North American and Rocky Mountain Joint Meeting, 2014. SPE 169493.

SATOH, A. 2010. *Introduction to practice of molecular simulation: molecular dynamics, Monte Carlo, Brownian dynamics, Lattice Boltzmann and dissipative particle dynamics*, Elsevier.

SBRAGAGLIA, M. & SUCCI, S. 2005. Analytical calculation of slip flow in lattice Boltzmann models with kinetic boundary conditions. *Physics of Fluids (1994-present),* 17**,** 093602.

SCHMOKER, J. W. & HALLEY, R. B. 1982. Carbonate porosity versus depth: a predictable relation for south Florida. *AAPG Bulletin,* 66**,** 2561-2570.

SEIDL, M. & STEINHEIL, E. 1974. Measurement of momentum accommodation coefficients on surfaces characterized by Auger spectroscopy, Sims and LEED. *Rarefied gas dynamics,* 9.

SHEN, C., TIAN, D.-B., XIE, C. & FAN, J. 2004. Examination of the LBM in simulation of microchannel flow in transitional regime. *Microscale Thermophysical Engineering,* 8**,** 423-432.

SHEN, J. & BAE, J. 1987. An Automated Steady-State Relative Permeability Measurement System. *paper SPE,* 17217**,** 0.012-0.02.

SHOKOUHMAND, H. & ISFAHANI, A. M. 2011. An improved thermal lattice Boltzmann model for rarefied gas flows in wide range of Knudsen number. *International Communications in Heat and Mass Transfer,* 38**,** 1463-1469.

SINGH, S. K., SINHA, A., DEO, G. & SINGH, J. K. 2009. Vapor− liquid phase coexistence, critical properties, and surface tension of confined alkanes. *The Journal of Physical Chemistry C,* 113**,** 7170-7180.

SINHA, S., BRAUN, E., DETERMAN, M., PASSEY, Q., LEONARDI, S., BOROS, J., WOOD III, A., ZIRKLE, T. & KUDVA, R. Steady-state permeability measurements on intact shale samples at reservoir conditions-effect of stress, temperature, pressure, and type of gas. SPE Middle East Oil and Gas Show and Conference, 2013. Society of Petroleum Engineers.

SOFONEA, V. & SEKERKA, R. F. 2005. Boundary conditions for the upwind finite difference Lattice Boltzmann model: Evidence of slip velocity in micro-channel flow. *Journal of Computational Physics,* 207**,** 639-659.

SUCCI, S. 2002. Mesoscopic modeling of slip motion at fluid-solid interfaces with heterogeneous catalysis. *Physical review letters,* 89**,** 064502.

SWAMI, V. & SETTARI, A. A pore scale gas flow model for shale gas reservoir. SPE Americas Unconventional Resources Conference, 2012. Society of Petroleum Engineers.

TANG, G., TAO, W. & HE, Y. 2005. Lattice Boltzmann method for gaseous microflows using kinetic theory boundary conditions. *Physics of Fluids (1994-present),* 17**,** 058101.

THOMAS, L. B. & LORD, R. 1974. Comparative measurements of tangential momentum and thermal accommodations on polished and on roughened steel spheres. *Rarefied gas dynamics,* 8**,** 405-412.

TOKUMASU, T. & MATSUMOTO, Y. 1999. Dynamic molecular collision (DMC) model for rarefied gas flow simulations by the DSMC method. *Physics of Fluids,* 11**,** 1907-1920.

UN 2015. World Population Prospects. *http://www.un.org/popin/*, United Nations Population Division.

VERHAEGHE, F., LUO, L.-S. & BLANPAIN, B. 2009. Lattice Boltzmann modeling of microchannel flow in slip flow regime. *Journal of Computational Physics,* 228**,** 147-157.

VIRNOVSKY, G., SKJAEVELAND, S., SURDAL, J. & INGSOY, P. Steady-state relative permeability measurements corrected for capillary effects. SPE Annual Technical Conference and Exhibition, SPE 30541, 1995. Society of Petroleum Engineers.

VIRNOVSKY, G., VATNE, K., SKJAEVELAND, S. & LOHNE, A. Implementation of Multirate Technique to Measure Relative Permeabilities Accounting. SPE Annual Technical Conference and Exhibition, 1998. Society of Petroleum Engineers.

VISHNYAKOV, A., PIOTROVSKAYA, E., BRODSKAYA, E., VOTYAKOV, E. & TOVBIN, Y. K. 2001. Critical properties of Lennard-Jones fluids in narrow slit-shaped pores. *Langmuir,* 17**,** 4451-4458.

WANG, C., WU, Y.-S., XIONG, Y., WINTERFELD, P. H. & HUANG, Z. Geomechanics coupling simulation of fracture closure and its influence on gas

production in shale gas reservoirs. SPE Reservoir Simulation Symposium, 2015. Society of Petroleum Engineers.
WANG, F. P. & REED, R. M. Pore networks and fluid flow in gas shales. SPE annual technical conference and exhibition, 2009. Society of Petroleum Engineers.
WARPINSKI, N. & TEUFEL, L. 1992. Determination of the effective-stress law for permeability and deformation in low-permeability rocks. *SPE formation evaluation,* 7**,** 123-131.
WITHJACK, E. 1988. Computed tomography for rock-property determination and fluid-flow visualization. *SPE formation evaluation,* 3**,** 696-704.
WU, K., LI, X., WANG, C., CHEN, Z. & YU, W. 2015. A model for gas transport in microfractures of shale and tight gas reservoirs. *AIChE Journal,* 61**,** 2079-2088.
WU, Y.-S. 2015. *Multiphase Fluid Flow in Porous and Fractured Reservoirs*, Gulf Professional Publishing.
WU, Y.-S. & FAKCHAROENPHOL, P. A unified mathematical model for unconventional reservoir simulation. SPE EUROPEC/EAGE Annual Conference and Exhibition, 2011. Society of Petroleum Engineers.
XIE, W., LI, X., ZHANG, L., WANG, J., CAO, L. & YUAN, L. 2014. Two-phase pressure transient analysis for multi-stage fractured horizontal well in shale gas reservoirs. *Journal of Natural Gas Science and Engineering,* 21**,** 691-699.
YAMAGUCHI, H., HANAWA, T., YAMAMOTO, O., MATSUDA, Y., EGAMI, Y. & NIIMI, T. 2011. Experimental measurement on tangential momentum accommodation coefficient in a single microtube. *Microfluidics and nanofluidics,* 11**,** 57-64.
YAN, H., ZHANG, W.-M., PENG, Z.-K. & MENG, G. 2015. Effect of random surface topography on the gaseous flow in microtubes with an extended slip model. *Microfluidics and Nanofluidics,* 18**,** 897-910.
YENER, Y., KAKAC, S., AVELINO, M. & OKUTUCU, T. 2005. Single-Phase Forced Convection in Microchannels. *Microscale Heat Transfer Fundamentals and Applications.* Springer.
YVES, G., AMIN, G., ROBERT, C. J., AMANN-HILDENBRAND, A., KROOSS, B. M., CLARKSON, C. R., HARRINGTON, J. F. & ZOBACK, M. D. 2015. Gas storage capacity and transport in shale gas reservoirs–A review. Part A: Transport processes. *Journal of Unconventional Oil and Gas Resources*.
ZHANG, H., ZHANG, Z., ZHENG, Y. & YE, H. 2010. Corrected second-order slip boundary condition for fluid flows in nanochannels. *Physical Review E,* 81**,** 066303.
ZHANG, R., NING, Z., YANG, F., WANG, X., ZHAO, H. & WANG, Q. 2015. Impacts of nanopore structure and elastic properties on stress-dependent permeability of gas shales. *Journal of Natural Gas Science and Engineering*.
ZHANG, T., ELLIS, G. S., RUPPEL, S. C., MILLIKEN, K. & YANG, R. 2012a. Effect of organic-matter type and thermal maturity on methane adsorption in shale-gas systems. *Organic Geochemistry,* 47**,** 120-131.
ZHANG, W.-M., MENG, G., WEI, X.-Y. & PENG, Z.-K. 2012b. Slip flow and heat transfer in microbearings with fractal surface topographies. *International Journal of Heat and Mass Transfer,* 55**,** 7223-7233.
ZHANG, W.-M., MENG, G. & WEI, X. 2012c. A review on slip models for gas microflows. *Microfluidics and nanofluidics,* 13**,** 845-882.
ZHANG, X., XIAO, L., SHAN, X. & GUO, L. 2014. Lattice Boltzmann simulation of shale gas transport in organic nano-pores. *Scientific reports,* 4.
ZHANG, Y., QIN, R. & EMERSON, D. R. 2005. Lattice Boltzmann simulation of rarefied gas flows in microchannels. *Physical Review E,* 71**,** 047702.

ZHU, L., TRETHEWAY, D., PETZOLD, L. & MEINHART, C. 2005. Simulation of fluid slip at 3D hydrophobic microchannel walls by the lattice Boltzmann method. *Journal of Computational Physics*, 202**,** 181-195.

ZIARANI, A. S. & AGUILERA, R. 2012. Knudsen's permeability correction for tight porous media. *Transport in porous media*, 91**,** 239-260.

ZOU, Q. & HE, X. 1997. On pressure and velocity boundary conditions for the lattice Boltzmann BGK model. *Physics of Fluids (1994-present)*, 9**,** 1591-1598.